Max Planck Institute of Immunobiology and Epigenetics

Computational epigenomics study of the Male-Specific Lethal complex in flies and mammals

Inaugural-Dissertation

Author:
Vivek BHARDWAJ

Supervisor:
Dr. Asifa AKHTAR

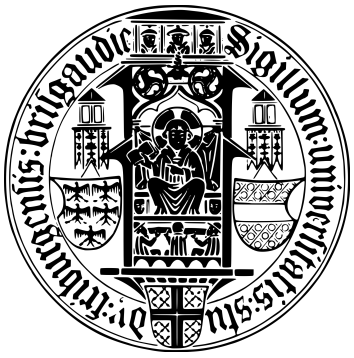

to obtain the Doctoral Degree at the

Faculty of Biology

Albert-Ludwigs-Universität Freiburg im Breisgau

20 September, 2018

Dekan der Fakultät für Biologie: Mr. Decan
Promotionsvorsitzender: Dr. Someone
Betreuer der Arbeit: Dr. Asifa AKHTAR
Referent: Dr. Asifa AKHTAR
Koreferent: Dr. Thomas Manke
Drittprüfer: Dr. Giorgos Pyrowolakis
Datum der mündlichen Prüfung:

Acknowledgements

This thesis would not be complete without the help and support of people from both the Akhtar Lab and Manke group at the MPI-IE. I am grateful to both my supervisors Dr. Asifa Akhtar and Dr. Thomas Manke for trusting my abilities and allowing me to work with them. Asifa provided me with all the independence I desired to work on my projects and to collaborate with the people in the lab. Discussions with her provided me the motivation and ability to see the significance of the work I was doing. Thomas has always been available for me to discuss all sorts of issues and provided me with the support and encouragement I needed to improve my skills and prepare for the next steps in my career. Opting for this co-supervision was the best choice I could have made for my PhD.

All of my works presented here have been done in collaboration, and would not be completed without the efforts and insights of those involved. I would like to thank :

Fidel, who taught me HiC analysis and mentored me during our collaboration on the HiC project. Due to HiCExplorer and deepTools projects, I was pushed out of my comfort zone to learn Python and to adopt reproducible workflows for my analysis. I glady cherish all the discussions with Fidel during work as well as during our Sunday morning run. Giuseppe, for initiating the wonderful collaborations on the Drosophila projects, and for all the helpful discussions over the years. Raed, for working with me on the mammalian MSL2 project. Ibrahim and Tugce for initiating the collaboration on the mammalian MLE project, and finally Bilal and Ken for other independent projects. I would like to thank all the people at the Bioinformatics Unit for providing me with such a wonderful and interactive working environment, useful discussions, and fun collaborations. The deep-sequencing unit for producing the great quality data, and people in the Akhtar lab for all the discussions as well as fun activities outside work. Finally I want to thank my TAC members Ritwick Sawarkar and Michael Stadler for the support and discussions during my TAC.

Contents

List of Figures

Summary

In various species, sex determination is associated with an imbalance in the number of sex chromosomes between males and females. In Drosophila, this imbalance is corrected by an chromosome-level epigenetic phenomenon resulting in the upregulation of gene expression on the single male X chromosome. This phenomenon, referred to as dosage compensation, requires the Male-specific lethal (MSL) complex. The 3D conformation of the X-chromosome guides the spreading of the MSL complex, depositing histone (H4K16) acetylation on genes. On the other hand, mammalian dosage compensation occurs via X inactivation in females, and the role of MSL complex in mammals is poorly understood.

The aim of my project was to provide insights into the functions of the MSL complex in flies and mammals through computational epigenomics approach. This involved development of methods and tools for analysis of chromosome conformation and promoter-profiling data, and their integration with other transcriptomic and epigenetic data. Softwares such as HiCExplorer, icetea and deepTools2 were developed to facilitate this, and workflows for reproducible analysis were implemented as part of the snakePipes package. Application of our methods on HiC data in flies revealed that chromatin domains influence gene transcription, and validated previous observation on clustering of MSL2 sites in 3D space. Analysis of the MSL complex member MLE through promoter profiling identified a catalogue of MLE sensitive and insensitive promoters at the male X-chromosome and the difference in MLE action between sexes. Analysis of mammalian ortholog of MLE revealed it's novel function in regulation of Alu transposons independent of the MSL complex, while the analysis of other members of the mammalian MSL complex showed that MSLs are involved in transcriptional regulation of genes on X chromosome in an allele-specific manner.

In summary, we gained new insights into the functions of the MSL complex through analysis and integration of multiple epigenomic and transcriptomic data. This study would motivate further studies utilizing integrative epigenomics to understand the functions of MSLs as well as other regulators of transcription.

Abbreviations

Term	Abbreviation
Long-term memory	LTM
Short-term memory	STM
Working memory	WM

1. Introduction

2. Results and discussion

A. Publications and Manuscripts

A.1 Analysis of chromosome conformation in flies

I contributed to the development of HiCExplorer and HiCBrowser (led by Fidel Ramirez), and developed the Chorogenome Navigator resource. I performed the analysis of motif combinations and boundary strength, prediction of motifs, and relationship of TAD boundary and transcription (Fig 2, S2, 4, S4, 5 and S5). Together with Fidel Ramirez and Thomas Manke I devised, wrote, and revised the manuscript.

nature COMMUNICATIONS

ARTICLE

DOI: 10.1038/s41467-017-02525-w OPEN

High-resolution TADs reveal DNA sequences underlying genome organization in flies

Fidel Ramírez[1], Vivek Bhardwaj[1,2], Laura Arrigoni[1], Kin Chung Lam[1], Björn A. Grüning[3], José Villaveces[4], Bianca Habermann[4], Asifa Akhtar[1] & Thomas Manke[1]

Despite an abundance of new studies about topologically associating domains (TADs), the role of genetic information in TAD formation is still not fully understood. Here we use our software, HiCExplorer (hicexplorer.readthedocs.io) to annotate >2800 high-resolution (570 bp) TAD boundaries in *Drosophila melanogaster*. We identify eight DNA motifs enriched at boundaries, including a motif bound by the M1BP protein, and two new boundary motifs. In contrast to mammals, the CTCF motif is only enriched on a small fraction of boundaries flanking inactive chromatin while most active boundaries contain the motifs bound by the M1BP or Beaf-32 proteins. We demonstrate that boundaries can be accurately predicted using only the motif sequences at open chromatin sites. We propose that DNA sequence guides the genome architecture by allocation of boundary proteins in the genome. Finally, we present an interactive online database to access and explore the spatial organization of fly, mouse and human genomes, available at http://chorogenome.ie-freiburg.mpg.de.

[1] Max Planck Institute of Immunobiology and Epigenetics, Stübeweg 51, 79108 Freiburg, Germany. [2] Faculty of Biology, University of Freiburg, Schänzlestraße 1, 79104 Freiburg, Germany. [3] University of Freiburg, Department of Computer Science, Georges-Köhler-Allee 106, 79110 Freiburg, Germany. [4] Max Planck Institute of Biochemistry and Computational Biology, Am Klopferspitz 18, 82152 Martinsried, Germany. Fidel Ramírez and Vivek Bhardwaj contributed equally to this work. Correspondence and requests for materials should be addressed to T.M. (email: manke@ie-freiburg.mpg.de)

How the DNA packs into the nucleus and coordinates functional activities is a long-standing question in biology. Recent studies have shown that the genome of different organisms is partitioned into chromatin domains, usually called topologically associated domains (TADs), which are invariable between cell types and evolutionary conserved in related species[1].

To understand TAD formation, researchers had focused on the proteins found at TAD boundaries[2–4]. In mammalian cells, the CCCTC-binding factor (CTCF) protein has been shown to be enriched at chromatin loops, which also demarcate a subset of TAD boundaries (referred to as "loop domains")[5]. A proposed mechanism, based on the extrusion of DNA by cohesin, suggests that the DNA-binding motif of CTCF and its orientation determine the start and end of the loop[6,7]. In line with this hypothesis, deletions of the CTCF DNA-motif effectively removed or altered the loop[6] or caused changes in gene–enhancer interactions that lead to developmental abnormalities in mouse embryos[8]. Additionally, acute depletion of CTCF leads to loss-of-TAD structure on CTCF containing boundaries[9]. However, CTCF-cohesin loops only explain a fraction (<39%) of human TAD boundaries[5], while plants and bacteria lack CTCF homologs but also show TAD-like structures. Thus, it is possible that additional factors are involved in the formation of TADs.

In contrast to mammals, the genetic manipulation tools available in flies have allowed the characterization of several proteins that, like CTCF, are capable of inhibiting enhancer-promoter interactions. Throughout the manuscript, we will refer to these proteins as "insulator proteins" and their binding motifs as "insulators" or "insulator motifs". In flies, apart from CTCF, the following DNA-binding insulator proteins have been associated to boundaries[3,10]: Boundary Element Associated Factor-32 (Beaf-32), Suppressor of Hairy-wing (Su(Hw)), and GAGA factor (GAF). Also, Zest white 5 (Zw5) has been proposed to bind boundaries[11]. These insulator proteins recruit co-factors critical for their function, such as Centrosomal Protein-190 (CP190) and Mod(mdg4)[12]. Recently, novel insulator proteins have been described as binding partners of CP190: the zinc finger protein interacting with CP190 (ZIPIC), Pita[13] which appear to have human homologs and localizes to TAD boundaries[11], and the Insulator binding factors 1 and 2 (Ibf1 and Ibf2)[14]. Except for CP190 and Mod(mdg4), all previously characterized boundary associated proteins bind to specific DNA motifs, suggesting that the 3D conformation of chromatin can be encoded by these motifs.

In this study, we sought to identify the DNA encoding behind TAD boundaries in flies. First, we develop software (HiCExplorer) to obtain boundary positions at 0.5 kilobase resolution based on published Hi-C sequencing data from *Drosophila melanogaster* Kc167 cell line[15,16]. Using these high-resolution TAD boundaries, we identify eight significantly enriched DNA-motifs. Five of these motifs are known to be bound by the insulator proteins: Beaf-32, CTCF, the heterodimer Ibf1 and Ibf2, Su(Hw) and ZIPIC. We find that a large fraction of boundaries contain the motif bound by the motif-1 binding protein (M1BP)[17], a protein associated to constitutively expressed genes. This motif has recently been found at boundaries[18,19]. The two remaining DNA-motifs have not been associated to boundaries before. Surprisingly, we find that depletion of Beaf-32 has no major effect on chromosome organisation, while the depletion of M1BP leads to cell arrest in M-phase and dramatically affects the Hi-C results. Using machine learning methods based on the acquired DNA-motif information, we could accurately distinguish boundaries from non-boundaries and identify TAD boundaries that were missed when using only Hi-C data. Our results suggest that the genome architecture of flies can be explained predominantly by the genetic information. We have implemented the methods for Hi-C data processing, TAD calling and visualization into an easy to use tool called HiCExplorer (hicexplorer.readthedocs.io). To facilitate exploration of available Hi-C data, we also provide an interactive online database containing processed high-resolution Hi-C data sets from fly, mouse and human genome, available at http://chorogenome.ie-freiburg.mpg.de.

Results

High-resolution TAD boundaries in flies. We obtained Hi-C data for Kc167 cells from two recent studies[15,16] and processed them to obtain corrected Hi-C contact matrices at restriction fragment resolution (Methods section). These data sets contain the most detailed contact maps in flies, compared to other data sets (Methods section), due to high-sequencing depth (over 246 million valid read pairs) and the use of DpnII, a restriction enzyme with short-restriction fragment size (mean ~570 bp). We found 2852 TADs having a median size of 26 kb (Fig. 1a, Supplementary Figure 1a). We corroborated the precision of our boundaries by comparing their overlap with CP190 peaks (p-value = 1.8E − 20, Fisher's exact test, Fig. 1b) and the separation of histone marks (Fig. 1c, Supplementary Figure 2b). We classified TADs (Supplementary Data 1) using modENCODE histone marks[3] as active (enriched for either H3K36me3, H3K4me3, and H4K16ac), polycomb group silenced (PcG) (enriched for H3K27me3), HP1 (enriched for H3K9me3) and inactive (not enriched for any of the marks, see Methods section and Supplementary Figure 1c). A significant fraction of the genome (43%) is covered by large inactive TADs having a mean length of 63 kb (Fig. 1d). In contrast, active chromatin TADs have a mean length of 23 kb and occupy 29% of the genome. PcG chromatin occupies 25% of the genome with TADs that are on average 61 kb. The largest TADs are found for HP1 repressed chromatin, which together occupy 3% of the genome and have a mean length of 74 kb. We also find that active TADs tend to be assembled one after the other due to their higher number (Fig. 1e). Interestingly, the TAD separation score varied significantly (p-value <7.8E − 5, Wilcoxon rank-sum test) between the TAD types (Fig. 1f). The stronger boundaries (low-TAD-separation score) are found between active and inactive or PcG TADs. While the weakest boundaries are found between PcG TADs. Similarly, we find that the TAD-separation score between larger TADs (mostly inactive) is significantly larger than the TAD separation score for smaller TADs (mostly active) (p-value = 9.9E − 7, Wilcoxon rank-sum test).

While most of our boundaries overlap with those from previous studies[3,16], our method allowed us to identify a larger set of boundaries (Supplementary Figure 1d, e) with increased precision (as measured by distance to CP190, Supplementary Figure 1f–h), which mostly subdivide active TADs from previous studies. We observed that the majority of the boundaries (77%) are located at gene promoters (henceforth referred to as promoter-boundaries. Figure 1g). Promoter-boundaries are different from non-promoter boundaries (23%), since they associate significantly with active chromatin (Fig. 1h, H3K4me3 p-value = 4.43E − 144 Wilcoxon rank-sum test, other histone marks can be seen in Supplementary Figure 1i), have lower TAD separation score representing stronger boundaries (p-value = 8.5E − 35, Wilcoxon rank-sum test, Fig. 1i), and show higher DNAse sensitivity (Fig. 1j).

Specific gene orientation and transcription marks boundaries. Next we correlated our promoter boundaries with gene orientation and transcription. Most promoter-boundaries (70%, p-value = 2.5E − 88 Fisher's exact test), are marked by divergently

oriented gene promoters on either side, while genes in convergent or tandem orientation tend to be inside the TADs. To correlate TADs with gene transcription, we analysed the RNA-Seq data from 14 stages of *Drosophila* development along with the expression in the Kc167 cell line obtained from modENCODE (Supplementary Figure 2a, Methods section). We found that 95.6% of genes which have a TAD boundary at their promoter are expressed in Kc167 cells (1244 out of 1300) compared to 75.3% of genes which do not have a boundary at their promoter (6892 out of 9149, p-value = 2.19E − 80, Fisher's exact test). Higher

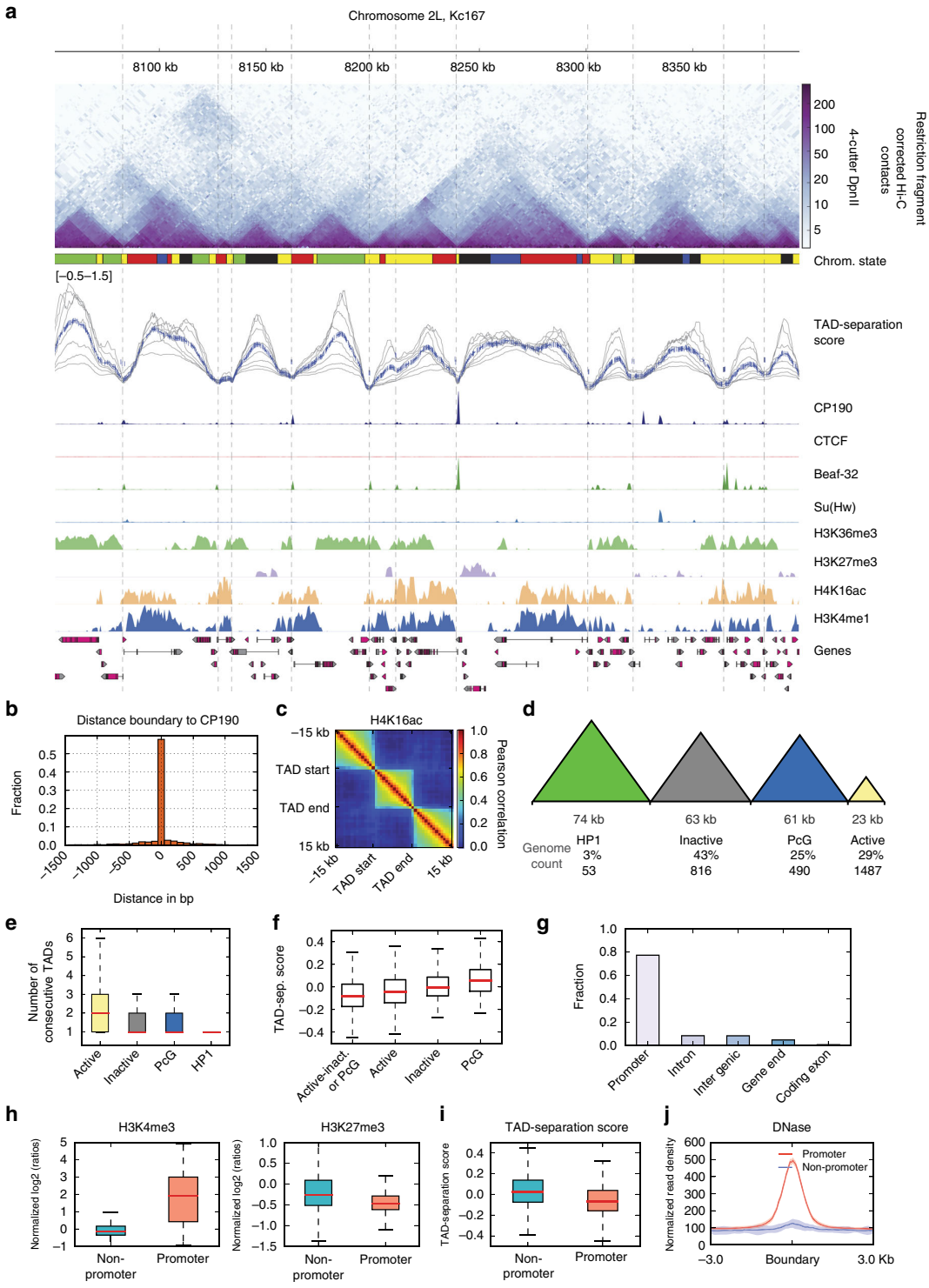

correlation was observed between gene expression inside TADs than between neighboring TADs (Fig. 2a, Supplementary Figure 2c). When we investigated the expression of genes at TAD boundaries we found that these genes show significantly higher expression than the expressed genes which do not have a TAD boundary at their promoters (Fig. 2b, p-value = 6.08E − 21, t-test). Boundary associated genes also show a more stable expression across development than other genes (Fig. 2c, Supplementary Figure 2b), suggesting that these genes are ubiquitously transcribed. Furthermore, we find that for a pair of genes lying next to each other, the variability in their gene expression tend to be correlated during development if these genes are within same TAD, while this correlation is lost if there is a TAD boundary in between (Fig. 2d, Methods section). This is true for gene-pairs in any orientation (convergent, divergent, or tandem, Supplementary Figure 2d).

Taken together, these results suggest that specific gene orientation and level of transcription could be associated with TAD formation.

A comprehensive list of boundary associated DNA motifs. We followed the strategy outlined in (Fig. 3a) to create a comprehensive list of motifs frequently found at boundaries. First, we performed de novo motif calling using MEME-chip[20] (Methods section) on our promoter-boundaries and non-promoter boundaries. To filter out motifs that are frequently found at promoters or open chromatin but are not specific to boundaries, we performed an enrichment analysis using two different methods: Ame[21] and TRAP[22]. As a second approach, we tested boundaries for the motifs of known insulator proteins and core-promoter motifs from a previous study[23]. In contrast to de novo motif detection, searching for known motifs allows additional sensitivity to detect low frequency motifs. After filtering for only consistent results, we could identify 5 motifs enriched at promoter-boundaries and 3 motifs enriched at non-promoter boundaries (Fig. 3b).

The promoter boundary motifs we identified belong to the list of core-promoter motifs 1, 2, 6, 7, and 8 from Ohler et al.[23]. Motif-1 is recognized by the recently described 'motif-1 binding protein' (M1BP), a protein found at the promoters of transiently paused Pol-II of constitutively expressed genes[17]. Motif-2 (also called DRE motif) is recognized by the insulator protein Beaf-32 and DREF[24]. Motif-7 (also called DMv3) is recognized by the insulator protein ZIPIC. The binding proteins for motif-6 (also known as DMv5) and motif-8 (also known as DMv2) are, to the best of our knowledge, not known. De novo motif calling also identified other core-promoter motifs but they were not found enriched at boundaries. The three motifs that we find enriched on non-promoter boundaries, correspond to the binding sites of Su (Hw), CTCF and Ibf (Fig. 3b). We could not find an enrichment for motifs of other insulator proteins like GAF, Pita, and Zw5. For clarity, we will refer to the boundary motifs by the name of the insulator protein that binds to them, except for motif-6 and 8.

As an independent validation we find that our three predicted boundary motifs (M1BP motif, motif-6, and motif-8) are also enriched at the binding sites of CP190 and Cap-H2 (condensin II complex) (Supplementary Table 1). We repeated our analysis using the TAD boundaries from previous studies[3,15,16] and found similar enrichments (Supplementary Table 2).

To better understand the distribution of the motifs on boundaries we performed hierarchical clustering of the binding affinity (TRAP score) for the eight motifs enriched at boundaries (Fig. 3c left panel, Supplementary Figure 3a). We then plotted the ChIP-seq signal of the DNA-binding proteins (Fig. 3c second panel, Supplementary Figure 3b), along with CP190, Cap-H2, Rad21 (Fig. 3c third panel) and RNA Pol-II, over the clusters. The results show that the boundary motifs are usually associated with their corresponding proteins, except for motifs 6 and 8 for which the binding proteins are not known (Fig. 3c second panel). ZIPIC and Ibf show ChIP-seq enrichment at many regions that do not have the motif although their enrichment is higher when the motif is present. This could indicate indirect binding of the proteins as seen for CP190 or could also indicate antibody cross-reactivity or other problems with ChIP-seq experiments[25,26]. Examples of the boundaries with their motifs and corresponding proteins can be seen in Supplementary Figure 3c–g.

We discover that promoter boundaries are primarily associated with Beaf-32 and M1BP motifs. Promoter boundaries also tend to be associated with condensin II (Cap-H2), RNA polymerase II and housekeeping enhancers. Interestingly, Rad21 (cohesin) ChIP-seq peaks mostly associate with M1BP motif (Fig. 3c–d) and de novo motif calling on Rad21 peaks identified a clear enrichment for M1BP motif (MEME[27] E-value = 4.2E − 97) (Supplementary Table 1). Furthermore, M1BP ChIP-seq signal correlates well with Rad21 ChIP-seq (Supplementary Figure 3h). Thus, while Cap-H2 is found together with all boundary promoter motifs, Rad21 is closely associated with M1BP. We found that specific boundaries containing M1BP, as well as ZIPIC and Motif-6 are also associated with paused Pol-II (Fig. 3e) (previously, only M1BP was associated to paused Pol-II[17]).

Ibf1, CTCF and Su(Hw) are the most common insulator motifs found at non-promoter boundaries, and tend to be associated with enhanced binding of CP190 co-factor (Fig. 3c–d). The ChIP-Seq signals for these proteins follows this observation, showing that promoter and non-promoter boundary proteins are correlated within their group (Supplementary Figure 3h).

We then searched for association of all the transcription factors from modENCODE consortium[28], as well as from the

Fig. 1 High-resolution TAD boundaries in flies. **a** Example region of 350 kb showing Hi-C TADs from Kc167 cells. Top panel: Hi-C contact matrix obtained from refs. [15,16]. The size of the bins is variable (mean 570 bp) and depends on the genomic location of the DpnII restriction sites. The chromatin state track contains the five classifications from ref. [29]: Active chromatin, red and yellow; inactive chromatin, black; PcG, blue; HP1, green. The TAD separation score track (Methods section) depicts a normalized measure of the contacts between two flanking regions (10–40 kb, depicted by gray line, blue line depict mean score). The boundaries, estimated using the TAD separation score are shown as vertical lines. The following tracks show normalized ChIP-seq coverage for the known boundary proteins CP190, Beaf-32, and Su(Hw) on Kc167[39] and CTCF[15]. The following tracks contain ChIP-chip data for histone modifications from modEncode[28]. The image was generated using HiCExplorer. This particular region was selected because many different TADs could be seen; other regions can be browsed at http://chorogenome.ie-freiburg.mpg.de. **b** Histogram of the distance of a boundary to the nearest CP190 (common insulator protein co-factor) peak. **c** Correlation of histone marks within and between TADs. Each pixel in the matrix represent the Pearson correlation of the histone mark in all TADs at different distances (Methods section). **d** TAD classification based on histone marks. The numbers below each TAD type represent respectively: mean length, percentage of genome occupied by the TAD and number of TADs of that type. **e** Boxplot of consecutive TAD of each type. **f** TAD-separation score between: active and inactive or PcG, active–active, inactive–inactive, and PcG–PcG. The differences between the groups are all significant (p-value < = 7.8E − 5, Wilcoxon rank-sum test). **g** Classification of TAD boundaries. TAD boundaries are classified at promoter if they are within 1000 bp of the annotated TSS. **h** Histone marks at non-promoter and promoter boundaries. Further marks can be seen in Supplementary Figure 1i. **i** TAD-separation score for non-promoter and promoter boundaries. **j** DNase accessibility at non-promoters and promoter boundaries

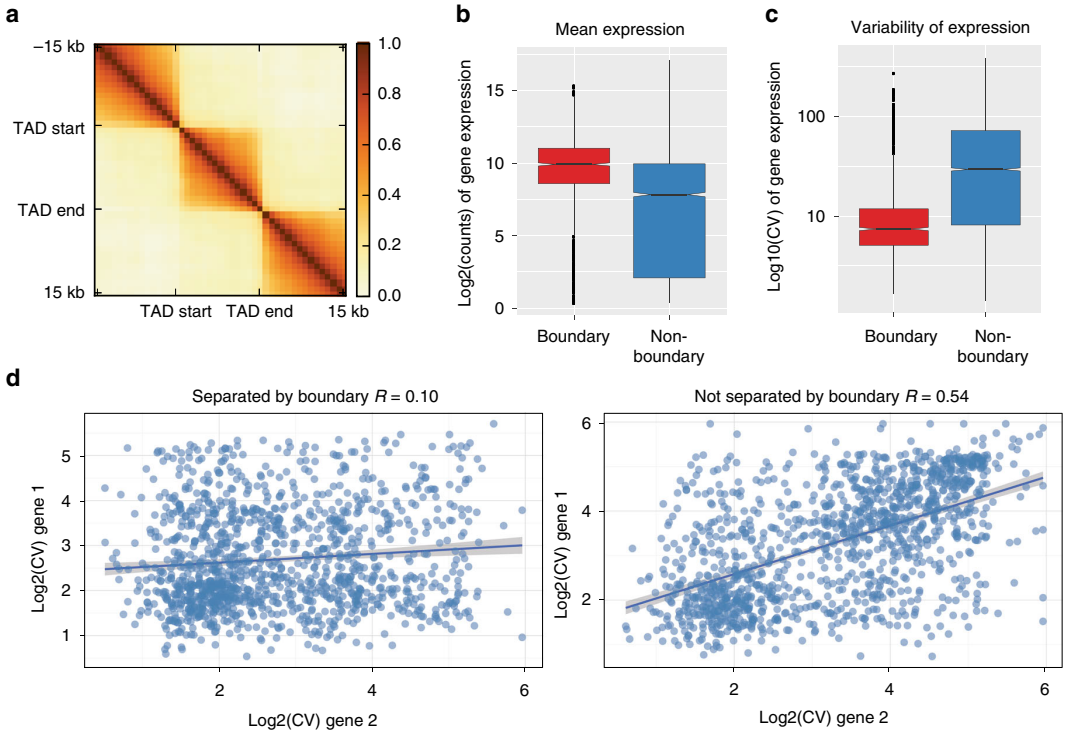

Fig. 2 TAD boundaries are marked by specific gene orientation and transcription. **a** Correlation of mean expression across developmental stages inside TADs vs. outside. Region inside TADs was scaled to 15 kb. Each pixel in the matrix contains the pearson correlation at different distances. **b**–**c** Mean expression (in Kc167 cells) and variability of expression (during development) for genes whose promoters are at a TAD boundary vs. genes whose promoters are not at boundaries. **d** Coefficient of variation (across developmental stages) between pairs of adjacent genes either separated by a TAD boundary (left) or not separated by a boundary (right). Line shows the linear model fit (shaded region: std. error)

comprehensive collection of ChIP-seq data from refs. [15,16] with our boundary motifs. Interestingly, our screen for proteins associated to boundary motifs showed that Nup98, a component of the nuclear pore complex, is associated with motif-6 and Pita, along with CTCF (Fig. 3d and Supplementary Figure 3i). Further validation using de novo motif calling on Nup98 peaks identified motif 6 and Pita motif as the most enriched motifs (MEME[27] *E*-value = 3.4E − 4 and 3.3E − 9, respectively).

We observed that ChIP-seq peaks of DNA-binding proteins are often found in regions not containing their motif (Fig. 3d). For example, ZIPIC peaks can be seen together with motif 6 or CTCF although ZIPIC motif does not overlap with any of them (Fig. 4a). Similar observations can be made for CTCF ChIP-seq experiments (Supplementary Figure 3j, see discussion), suggesting that motif sequences should be considered along with ChIP-Seq binding sites as more reliable functional predictors of an insulator protein.

Motif combinations reflect boundary strength. Next we looked at motif combinations at boundaries in relation to boundary strength. Using ChIP-Seq analysis it has been reported that boundary strength increases with the number of proteins bound at the boundary[10]. When we looked for motif combinations at boundaries that overlap with their corresponding protein, we did not observe any significant differences in boundary strength between boundaries containing one, two, or three motifs (we only found eight boundaries having more than three motifs, Supplementary Figure 4b), although we could replicate earlier results based on ChIP-seq peaks (Supplementary Figure 4c). We found that specific motifs or their combinations are associated with boundary strength (Fig. 4a). Boundaries containing the motif for Ibf, Su(Hw) or the combination of the two motifs are weaker than average while the combination of the Beaf-32 motif with either Pita, ZIPIC, or motif-6 result in the strongest boundaries.

We also looked at the association of motifs with active, inactive, PcG and HP1 TADs from Fig. 1d. We observe that the promoter-boundary motifs are mostly found between active TADs or between active and inactive (including PcG) TADs. Conversely, the non-promoter boundary motifs are rarely found between active TADs, and mostly separate active from inactive TADs or are between inactive TADs (Fig. 4b). We find the same trend when analysing the ChIP–chip log2 ratios of the active histone mark H3K36me3 and the repressive histone mark H3K27me3 surrounding the boundaries (Supplementary Figure 4d). Most promoter-boundary motifs separate active-inactive marks, while most non-promoter boundary motifs lie within inactive marks.

Additionally, we analyzed the chromatin state[29] that overlaps with the boundary motifs and found that promoter-boundary motifs lie mostly within active chromatin while non-promoter boundary motifs lie within both active and inactive chromatin (Fig. 4c).

Boundaries can be predicted using motifs. To better characterize boundaries at promoters we used three standard classification methods and ranked features by their relevance to distinguish boundaries from other promoters (Methods section). The features included the TRAP score of all motifs studied along

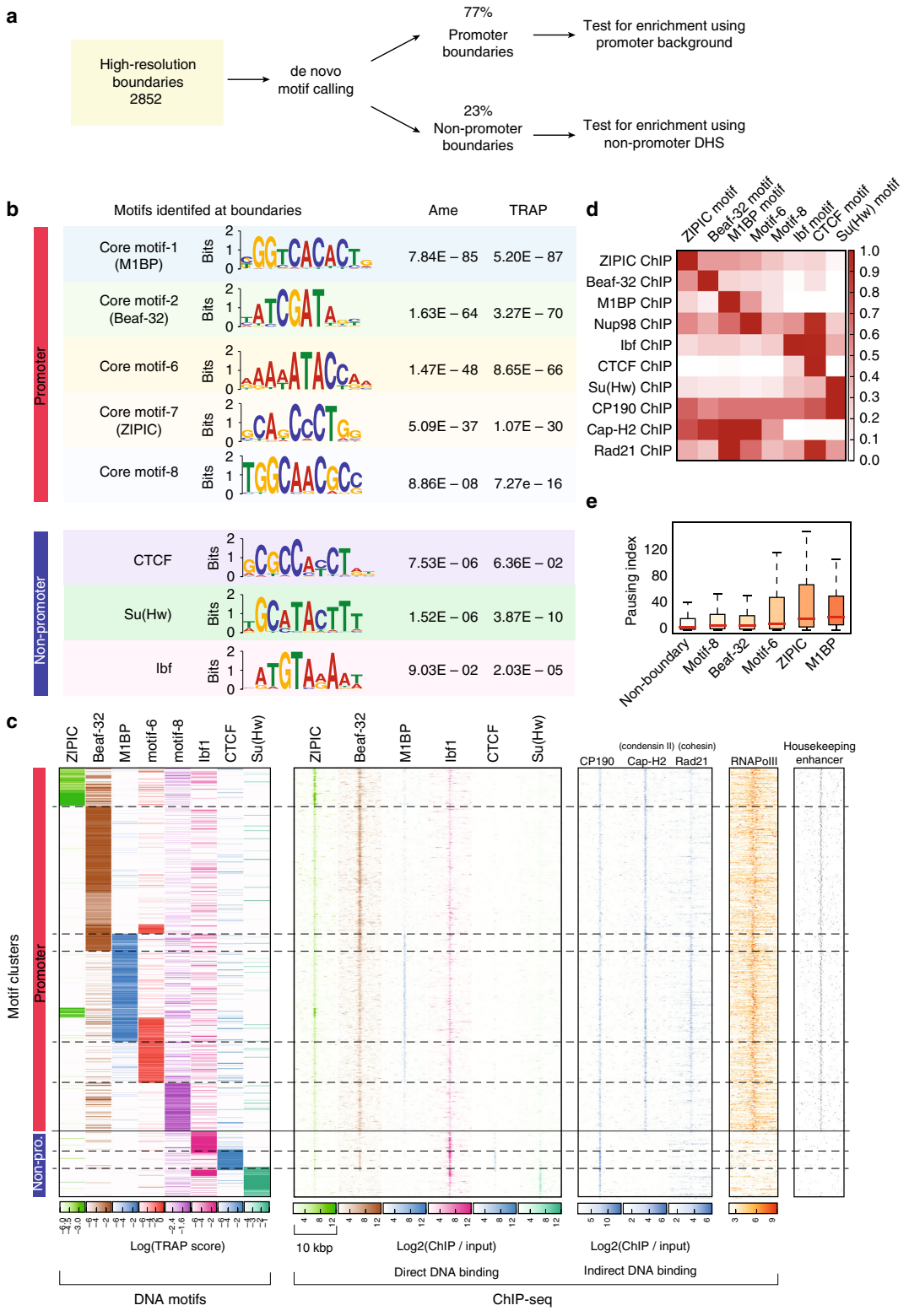
a
High-resolution boundaries 2852
de novo motif calling
77%
Promoter boundaries
Test for enrichment using promoter background
23%
Non-promoter boundaries
Test for enrichment using non-promoter DHS
b
Motifs identifed at boundaries
Ame
TRAP
Promoter
Core motif-1 (M1BP)
7.84E – 85
5.20E – 87
Core motif-2 (Beaf-32)
1.63E – 64
3.27E – 70
Core motif-6
1.47E – 48
8.65E – 66
Core motif-7 (ZIPIC)
5.09E – 37
1.07E – 30
Core motif-8
8.86E – 08
7.27e – 16
Non-promoter
CTCF
7.53E – 06
6.36E – 02
Su(Hw)
1.52E – 06
3.87E – 10
Ibf
9.03E – 02
2.03E – 05
Bits
d
ZIPIC motif
Beaf-32 motif
M1BP motif
Motif-6
Motif-8
Ibf motif
CTCF motif
Su(Hw) motif
ZIPIC ChIP
Beaf-32 ChIP
M1BP ChIP
Nup98 ChIP
Ibf ChIP
CTCF ChIP
Su(Hw) ChIP
CP190 ChIP
Cap-H2 ChIP
Rad21 ChIP
e
Pausing index
Non-boundary
Motif-8
Beaf-32
Motif-6
ZIPIC
M1BP
c
Motif clusters
Promoter
Non-pro.
ZIPIC
Beaf-32
M1BP
motif-6
motif-8
Ibf1
CTCF
Su(Hw)
(condensin II)
(cohesin)
CP190
Cap-H2
Rad21
RNAPolIII
Housekeeping enhancer
Log(TRAP score)
10 kbp
Log2(ChIP / input)
Direct DNA binding
Indirect DNA binding
DNA motifs
ChIP-seq

with other known insulator motifs. We also used DNase hypersensitive sites (DHS) as a feature to identify open promoters, considering that protein binding to a motif requires an accessible promoter. The ranking of feature importance showed that indeed open promoters are required for boundaries (Fig. 5a). For the motifs, the feature importance ranking follows the abundance of the motifs at boundaries: M1BP and Beaf-32 show the highest importance scores, followed by motif-6, ZIPIC, and motif-8. Some features, like GAF and Pita motifs were found to be negatively associated with boundaries at promoters (Supplementary Figure 5a).

Although regularized models used here are less prone to overfitting compared to other machine learning methods, we further protect against overfitting by 10-fold cross validation during training. We then tested model accuracy on an independent test data set. The classifiers showed a sensitivity and specificity over 71% on the test data (Fig. 5b). We also classified open chromatin regions distant from promoters, using only motif scores on these sites as features (Fig. 5c). This resulted in a sensitivity and specificity over 60% (Fig. 5d). The motif binding affinity can also be used as a linear predictor of boundary strength (Supplementary Figure 5b, d). Interestingly, we find the motif bound by GAF, a protein recognized to bind insulators[30,31], to be negatively associated with both promoter and non-promoter boundaries (Supplementary Figure 5c, e).

The machine learning predictions can complement the Hi-C derived boundaries at the promoters, as some boundaries predicted by our model are missed by our boundary detection method based on the TAD-separation score (Fig. 5e).

Depletion of Beaf-32 protein does not affect TAD boundaries. Our analysis showed that Beaf-32 and M1BP motifs are enriched at *Drosophila* boundaries. We further explored the effect of depletion of the proteins that bind these motifs on chromosome organisation by performing siRNA mediated depletion of Beaf-32, M1BP or both, followed by in situ Hi-C protocol (Methods section). We used the knockdown of GST as a negative control and two biological replicates for each condition. We first observed that while Beaf-32 depletion has no effect on M1BP protein levels, M1BP knockdown leads to downregulation of Beaf-32 (Supplementary Figure 6a). We therefore expected M1BP knockdown to produce either similar, or more exacerbated effects compared to those in Beaf-32 knockdown. Surprisingly, Hi-C analysis showed no global change in chromosome conformation upon knockdown of Beaf-32 compared to GST control (Supplementary Figure 6b). This effect was highly reproducible (Supplementary Figure 6c-f). Depletion of M1BP showed a dramatic effect on the distribution of Hi-C contacts in which short range contacts decrease and inter-chromosomal interactions increase (Supplementary Figure 6d, h). We further found that M1BP knockdown cells were arrested in M-phase (Supplementary Figure 6g), yet the contact distributions are different than those observed for fly mitotic cells from Hug et. al.[18] (Supplementary Figure 6h). The fraction of inter-chromosomal contacts is often used as a quality measure for Hi-C data[32]. For healthy cells it had been suggested that this fraction should be <20% of all valid reads. This assumes that chromosomes occupy their own territories which may not be true for perturbed cells. Our data from wild-type cells and Beaf-32 knockdown show an average of 8% inter-chromosomal interactions. The samples from M1BP knockdown and double knockdown show a replicable high fraction of inter-chromosomal contacts (~45%, Supplementary Figure 6d). Since they were identically processed in the same batch and alongside the wild type and Beaf-32 samples, we argue that this is not a technical artifact and the large number of inter-chromosomal contacts probably reflects a biological effect on chromatin.

Resources to explore TADs and associated genomic features. During our research, we developed processing and analysis tools for chromosome conformation. Our tool-suite, called HiCExplorer, simplifies the Hi-C data pre-processing, quality controls, contact matrix transformation, and TAD calling into a few easy steps (Fig. 6a). HiCExplorer is open source and is available at https://github.com/deeptools/HiCExplorer/. Importantly, HiCExplorer can be used with other pipelines and processing tools as we have built-in import/export functions covering commonly used Hi-C data formats. To facilitate analysis, we have integrated HiCExplorer into the Galaxy platform[33]. With HiCExplorer, we made available our efforts to create meaningful and accurate visualizations of Hi-C data that can integrate other data sources, examples of which can be seen throughout this manuscript. Further information can be found at the associated documentation (http://hicexplorer.readthedocs.io), which includes a full analysis workflow and detailed description of the tools.

Our tools would be beneficial to users that do not routinely perform expensive and technically challenging Hi-C experiments. They enable quick visualization of specific genes or regions of interest in the context of TADs and loops, to understand gene regulation. We provide a resource called the Chorogenome Navigator (Fig. 6b) (http://chorogenome.ie-freiburg.mpg.de/), which includes *Drosophila*, Mouse, and Human Hi-C data sets, already processed by HiCExplorer, along with associated gene annotations, histone marks and other TAD/boundary annotations. The underlying program called HiCBrowser (https://github.com/deeptools/HiCBrowser/), is also freely available to be used as a standalone browser, where users can include their own genomic tracks. With these resources, we hope to make Hi-C analysis a routine part of genomics workflows.

Discussion

In this study, we used high resolution (DpnII restriction enzyme) and deeply sequenced (~246 million reads) Hi-C data[15,16] to map the genomic positions of TAD boundaries within ~600 bp in *D.*

Fig. 3 Eight motifs are enriched at boundaries. **a** Overview of the strategy used to identify de novo motifs. **b** Motifs enriched at promoter and non-promoter boundaries (along with Bonferroni-corrected *p*-values). Two methods were used to estimate enrichment (Methods section): Ame[21] and TRAP[22]. **c** Clustering of boundaries by motif binding affinity (Methods section). Each row represents one boundary. Left panel: clustering of motif binding affinity using the TRAP score[22]. Higher scores indicate stronger predicted binding. Dashed lines delineate the clusters. Following panels: using the motif clustering results, we show the heatmaps corresponding to ChIP-seq enrichments for insulator proteins binding the DNA (second panel), other proteins that bind indirectly (third panel) and RNA Pol-II. Last panel shows housekeeping enhancers from ref. [69]. For boundaries at promoters, heatmaps are centered at the gene promoter, for non-promoter boundaries, heatmaps are centered at the nearest CP190 peak within 2000 bp. ChIP-seq signal was computed in 50 bp bins for 5000 bp from the center. The scale of each heatmap goes from 1 to 12 for the direct DNA-binding ChIPs and from 1 to the max ChIP-seq value for the indirect binding ChIPs (based on Supplementary Figure 3b). **d** Relationship between motif presence and ChIP-seq peak fold change at boundaries. Each cell in the matrix contains the mean fold change of all respective ChIP-seq peaks having the motif. For each row, the maximum fold change was scaled to 1. **e** Pausing index at different boundary-promoters containing one of the boundary motifs. Non-boundary promoters are plotted as control

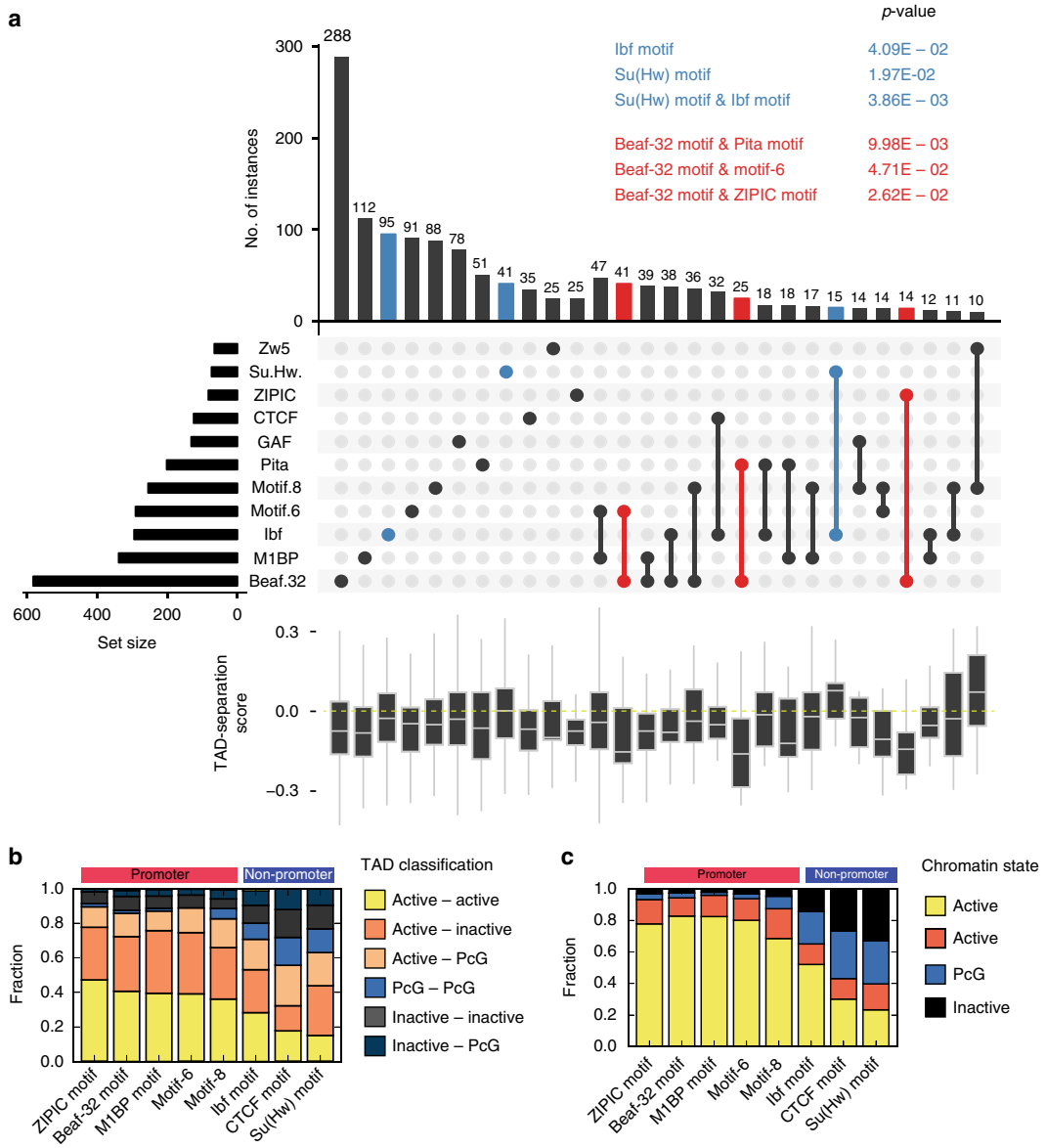

Fig. 4 Promoter and non-promoter boundary motifs show marked differences. **a** TAD-separation score at boundaries grouped by the motif presence. For this analysis we considered a motif to be present if the motif overlaps with a ChIP-seq peak (Methods section). The bars show the overlap between the indicated motifs below. The boxplots show the distribution of the respective TAD-separation score. The sets highlighted in blue have a TAD-separation score distribution significantly larger than the overall TAD-separation score. The *p*-values (Wilcoxon rank-sum test) are shown above the figure. Similarly, the sets highlighted in red have a distribution significantly smaller. Only motif combinations having >10 instances are shown. Motif combinations with three or more motifs were rare. The intersections were plotted using UpSetR[70]. An overview of the motif overlaps can be seen in Supplementary Figure 4a. **b** Frequency of flanking TAD types (as classified in Fig. 1d) per boundary motif. **c** Frequency of the chromatin state from ref. [29]

melanogaster. Our analysis revealed a larger number of TADs, including many small active TADs (23 kb mean length), that were absent in previous reports[3,4,34]. We characterized TAD size, boundary strength, chromatin marks, gene orientation, and transcription at the TADs. We perform motif calling at boundaries, validating the presence of known insulators, along with M1BP motif, which recently has also been shown to be associated to boundaries[18,19] and core promoter motif 6 and motif 8, which have not been associated to boundaries before. Using different machine learning methods, we find that DNA motifs and open chromatin are sufficient to accurately predict a major fraction of fly boundaries. Finally, we present a set of useful tools and a resource for visualization and annotation of TADs in different organisms.

Our study verifies various properties of fly boundaries indicated in previous publications. We detect that most boundaries associate with promoters and active chromatin (Fig. 1g, h)[4] and that various known insulator proteins are enriched at boundaries (Fig. 3b,c)[3,4]. We also detect a comprehensive set of core promoter motifs at boundaries, including the newly discovered

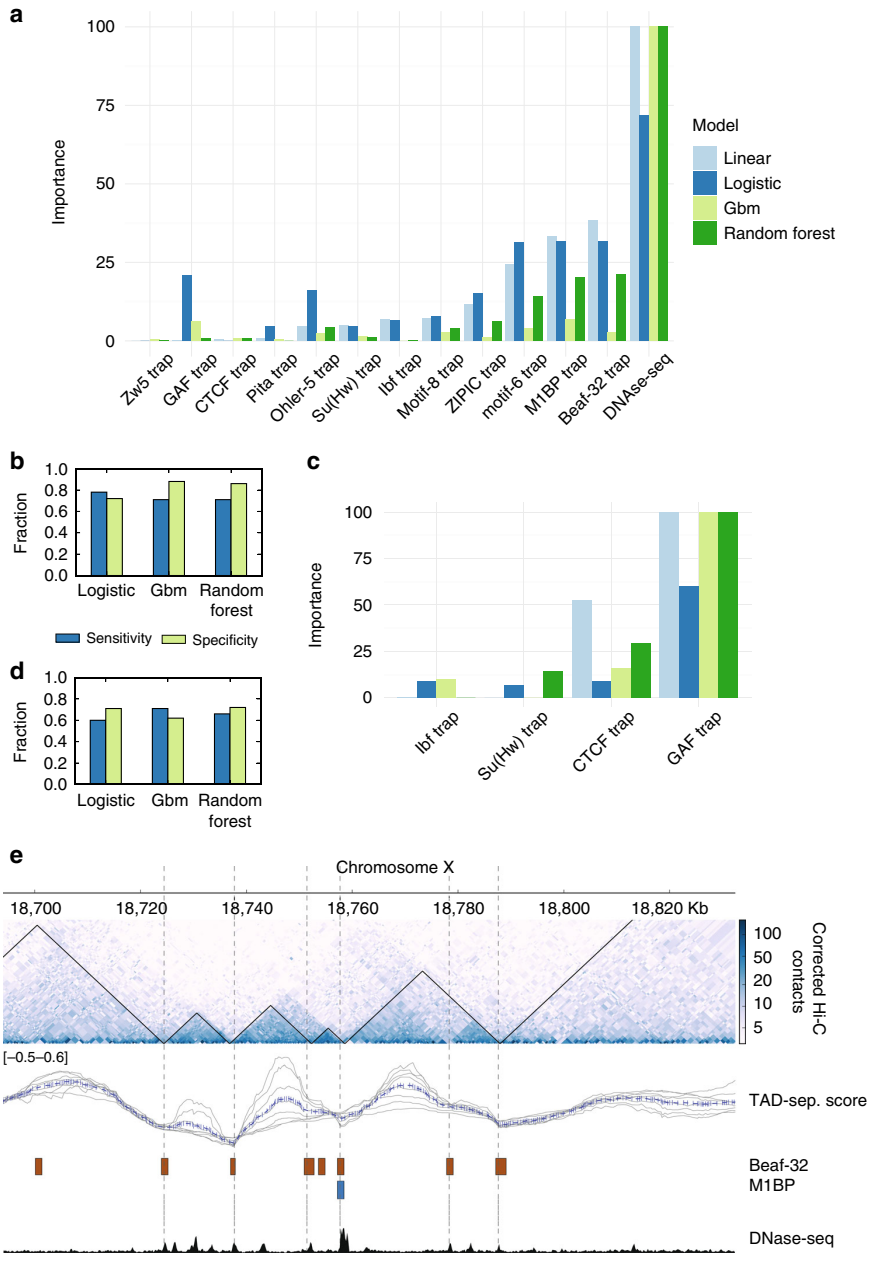

Fig. 5 Prediction of boundaries using machine learning. **a** Feature importance for promoter boundaries computed using four different methods: linear model, logistic regression, gradient boost model (gbm), and random forest. Importance scores of each method were scaled from 0 to 100. Except for DNAse-seq, each feature represents the binding affinity (TRAP score) of the respective motif. **b** Sensitivity and specificity for promoter boundaries measured for logistic regression, gradient boost model and random forest. The output of the linear model can be seen in Supplementary Figure 5b. **c** Feature rankings, as in **a**, for non-promoter boundaries. **d** Sensitivity and specificity for non-promoter boundaries. **e** Examples of high-resolution boundaries and predicted boundaries. The high-resolution boundaries (based on the TAD-separation score) are depicted as black triangles on top of the Hi-C heatmap. The predicted boundaries are shown as dotted vertical lines. The tracks below the Hi-C contact map contain the instances of the motifs that overlap with promoters. To aid the visualization of the short motifs, their genomic location was extended by 500 bp in each direction. The last track depicts regions of open chromatin based on DNase-seq from modEncode[28]

M1BP motif[17–19], and motifs which have been associated to housekeeping gene expression[35,36]. However, some of our results contradict previous observations. For example, we find that genes at boundaries have higher expression and lower variability of expression throughout fly development (Fig. 2b, c, Supplementary Figure 2b). This in line with Ulianov et al.[18,34] and Hug et al.[18,34] but in contrast with Hou et al.[4], who suggest that gene density and not the transcriptional state is important for boundary formation. Unlike Hou et al.[4] we find that genes at boundaries tend to be divergently transcribed. In contrast to various earlier

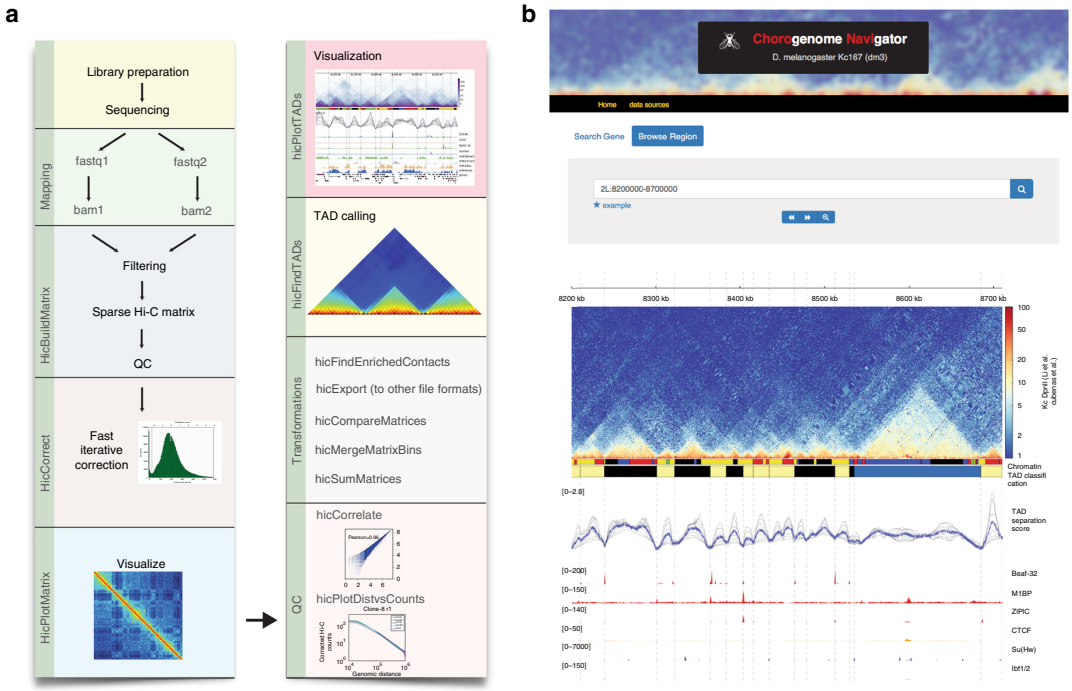

Fig. 6 HiCExplorer and Chorogenome navigator. **a** Pipeline of Hi-C processing and the commands used by HiCExplorer. HiCExplorer is easy to install (*conda install hicexplorer*), easy to use, tested (automatic tests and numerous data sets processed), well documented (https://hicexplorer.readthedocs.io/) and is ready to be used within the Galaxy framework[33]. **b** The Chorogenome navigator aims to be a repository for available Hi-C data. Currently, we host data from fly, mouse and human. Customized tracks can be created using the HiCBrowser (https://github.com/deeptools/HiCBrowser/)

studies[3,4,37], CTCF does not appear to be a major boundary associated insulator in flies (Figs. 3c, 4a). We also show that the number of insulator motifs at boundaries correlates very little with boundary strength (Supplementary Figure 4b), in contrast to Van Bortle et al.[10].

Most of these differences are due to the increased resolution of detected boundaries (Fig. 1b, Supplementary Figure 1f–h) and the combined analysis of DNA motifs with ChIP-seq data, rather than ChIP-Seq peaks alone. We show that correlating boundaries with ChIP-Seq peaks alone is not a good measure when it comes to determinants of boundary formation. Many DNA-binding proteins show co-localization in ChIP-Seq data without presence of the corresponding DNA motifs (Fig. 3d, Supplementary Figure 3j). This is possible due to cross-linking artifacts and indirect binding, which is, in fact, aggravated at boundaries, which tend to contact each other in 3D space[38].

Another argument for considering motifs is the contradicting case of CTCF at boundaries. In contrast to earlier studies based on CTCF ChIP-seq[3,4], we find that the CTCF motif is rarely associated to boundaries. This difference is caused by the quality of the ChIP-seq data that can produce spurious peaks. For example, we could observe a significant enrichment of CTCF at boundaries in the ChIP-Seq data from Wood et al.[39] but not in the CTCF ChIP-seq data from Li et al.[15]. On the other hand, both ChIP-seq data sets show significant enrichment if we only consider ChIP-seq peaks that contain the CTCF motif, (Supplementary Figure 3j). For CTCF, and in general for ChIP-seq experiments in flies, 'phantom peaks' are known to occur at active promoters[25]. Thus, to avoid misleading results our analyses are based on motif presence when possible and for ChIP-Seq data sets, we use significance threshold along with motif binding affinity for analysis (instead of taking a significance cutoff alone).

We observe that boundary strength is associated with the chromatin states of flanking TADs and particular motif combinations, but is not associated with the number of co-occurring boundary motifs. Boundary strength is higher between active and inactive/PcG TADs while is lower at boundaries separating two TADs within the same state (e.g., active–active, inactive–inactive, Fig. 1f). Boundaries containing Beaf-32 are stronger when present together with either motif 6, Pita, or ZIPIC motif while weaker with motif 8 (Fig. 4a). Although, the mechanism by which combinations of insulators alter the boundary strength still remains unclear, we observe an association of Nup98 with Pita motif, motif 6, and CTCF (Fig. 3d and Supplementary Figure 3i), suggesting that association with nuclear pore proteins may result in stronger boundaries. Nup98 has now been shown to be functionally important in mediating enhancer-promoter looping in the *Drosophila* genome[40].

Our results indicate that the two sets of boundary motifs (promoter and non-promoter) participate in the compartmentalization of different types of chromatin. Boundaries containing core promoter motifs are either flanking, or surrounded by active chromatin regions (Fig. 4b). In contrast, the boundaries containing non-promoter motifs tend to be within or at the borders of inactive or repressed chromatin (Fig. 4b). This finding is in line with previous reports showing an enrichment of CTCF at the borders of H3K27me3 domains[3,37] and an enrichment of Beaf-32 in active chromatin[3]. This indicates that insulator proteins might serve different functions guided by the DNA sequence. For example, we observe that GAF motif, whose presence is negatively associated with TAD boundaries (Supplementary Figure 5a, c), is rather detected alone at "loop domains"[5] (Supplementary Figure 5e).

Our analyses indicate that the depletion of the well-studied insulator protein Beaf-32, has no significant effect on the chromosome conformation. However, in *Drosophila melanogaster*, both the Beaf-32 and DREF proteins bind exactly the same DNA motif[24]. Thus, our results, as well as others[41–43] point out that DREF, a protein that unlike Beaf-32 is conserved in humans, might have a more prominent role in genome organization than previously thought.

On the other hand, cells under M1BP knockdown grow slower in culture and get arrested in M-Phase, probably because M1BP is a transcription factor of constitutively expressed genes[17]. Since M1BP depleted cells show cell cycle defects, it is difficult to separate the direct role of M1BP at boundaries from the indirect effects caused by deregulation of thousands of genes. To study the direct role of M1BP at boundaries, it would be useful to perform either deletion of M1BP motif on boundaries using CRISPR, as shown for CTCF in mammals[44,45] or through acute and complete depletion of M1BP[9].

In this study, we present evidence that the DNA sequence contains features that can guide the formation of higher order chromosome organisation. The association of boundary types with a combination of motifs (Fig. 4a), and the fact that we can predict boundaries using DNA sequence alone, in absence of any information about associated protein or histone marks (Fig. 5 and Supplementary Figure 5a–d), leads us to propose a DNA-guided chromatin assembly model. In this model, the boundary elements are recognized by their proteins, which help loading TAD assembly factors onto chromatin. Promoter and non-promoter boundaries can thus have different mechanisms of formation. DNA motifs at inactive regions can attract proteins that may establish TAD domains by setting up barriers for chromatin marks[46]. Although overall barrier activity of insulator proteins have been controversial[10,43], it is plausible that the barrier mechanism is active only at a subset of boundaries (like those of inactive TAD domains). DNA motifs at gene promoters can associate with core-promoter proteins which then guide the assembly of Pol-II pre-initiation complex. The pre-initiation complex can then recruit condensins[47]. Once recruited, condensins can perform loop extrusion independent of Pol-II transcriptional activity[18,48,49], leading to emergence of TADs[6,50]. Condensins can also remain associated to chromatin during mitosis, to re-establish TADs after the cell division. In general, our results indicate that active transcription and chromosome conformation are related, in-line with a recent study[51]. Future studies investigating the association of Pol-II pre-initiation complex and condensin activity on gene promoters would advance our understanding of mechanism of TAD formation.

Methods

Hi-C processing. Different Hi-C data available for *D. melanogaster* were downloaded from GEO and processed using HiCExplorer (http://hicexplorer.readthedocs.io/). The list of data sources can be seen in Supplementary Table 3.

Each mate of the Hi-C sequencing read pairs was aligned separately using bwa mem with parameters '-E50 -L0'. The E parameter is the gap extension penalty, which is set high to avoid gapped alignments. This is because a fraction of the reads from a Hi-C experiment contain sequences from two distinct genomic positions. By increasing the gap extension penalty we promote the aligner to map the two parts of the read separately instead of trying to map the read to a single location. The L parameter is the penalty for 5′ and 3′ clipping which we set to zero to favor such clipping for the same reason as before.

To create the contact matrices, HiCExplorer divides the genome into bins of unequal size demarcated by the genomic positions of the restriction site and a matrix was created having these bins as rows and columns. The mapped reads were processed to count the number of times any two bins were connected by the Hi-C reads pairs. The following reads were discarded: read pairs that were not uniquely mapped or had a mapping score lower than 15, were within 800 bp to each other, were duplicated, contained a dangling end indicative of defective re-ligation or when one of the fragment mates was farther than 1500 bp from the restriction site.

In our processing of the data, we observed that restriction enzymes do not cut with the same efficiency at all sites or sometimes do not cut at all. Because of this, after the creation of the contact matrices, rows, and columns with zero or small total counts were removed. To define a sample-specific lower cutoff, we analyzed the bimodal distribution of total counts per rows, which is a convolution of two distinct distributions. The distribution with lower counts contains all bins with zero reads, mostly from repetitive regions, and also bins with low number of reads, probably from inefficient digestion of restriction sites. We chose as count threshold the position of the local minimum between the two modes. After filtering low count bins, the matrices were corrected following the iterative procedure from ref. [52].

For the 4-cutter DpnII restriction enzyme the mean fragment length after removing low coverage bins is 570 bp. For the 6-cutter HindIII the average was 4500 bp.

Identification of boundaries. TAD boundaries were identified using an improved version of TAD-separation score method from ref. [53] which is similar to TopDom[54]. The method works by first transforming the Hi-C contact matrix into a *z*-score matrix $\mathbf{A} = (\boldsymbol{a}_{ij})$. For this, each contact frequency in the matrix is transformed into a *z*-score based on the distribution of all contacts at the same genomic distance. For a bin l, the contacts between an upstream and downstream region of length w are in the *z*-score submatrix of $\mathbf{A}[\boldsymbol{\alpha}_l, \boldsymbol{\beta}_l]$, such that $\alpha_l \in \{l - w, ..., l\}$and $\beta_l \in \{l, ..., l + w\}$. This submatrix corresponds to the 'diamond' seen in Supplementary Fig. 1a. For each matrix bin we compute the TAD-separation score(w) as the mean overall $\mathbf{A}[\boldsymbol{\alpha}_l, \boldsymbol{\beta}_l]$ values.

To reduce noise, a multi-scale version of the TAD-separation score is computed for different values of w that are averaged per bin, $w \in${10,000, 12,000, 18,000, 25,000, and 40,000}. Genomic bins with a low-TAD-separation score with respect to neighboring regions (local minima) are indicative of TAD boundaries (Supplementary Figure 1a) and stronger boundaries will have lower scores. To assign a statistical significance to each local minimum we compare, the distribution of the *z*-scores for the submatrices $\mathbf{A}[\boldsymbol{\alpha}_l, \boldsymbol{\beta}_l]$ having $l \in \{i, i - v, i + v\}$, where i is the bin of the local minima, and $i - v$ and $i + v$ are the bins at distance v =1000 bp upstream and downstream of i, respectively. We use the Wilcoxon rank-sum test to compare the values of $\mathbf{A}[\boldsymbol{\alpha}_i, \boldsymbol{\beta}_i]$ with the values of each of the other two matrices and the highest of the two p-values is used. Finally, we correct the p-values using the Bonferroni method, and report boundaries with $p < 0.001$.

We also used a minimum local minima depth of 0.01. Depth of local minima (referred to as delta) can be considered similar to "fold change" of any minimum, with respect to the neighboring TAD-score average. These parameters were selected by maximizing the AUC for ROC curves in which the positive set contained CP190 binding sites and the negative set contained inactive regions (black chromatin state from ref. [29])

In contrast to other published methods to call TADs, this procedure has several advantages: (i) Each boundary is associated to a TAD-separation score and a p-value, that are useful to characterize strong vs. weak boundaries, (ii) the TAD score can be easily visualized (e.g., as an genome browser track), which is always useful for visual inspection, and (iii) the computation of boundaries takes only minutes, scaling linearly with the length of the genome). Our method differs from the TopDom method in the following aspects: (i) we compute TAD-separation scores using a *z*-score matrix while TopDom uses the corrected counts matrix, (ii) we use multiple length (w) sizes to compute our TAD-separation score while TopDom uses a single-$w$value, (iii) we compute p-values using the 'diamond' $\mathbf{A}[\boldsymbol{\alpha}_l, \boldsymbol{\beta}_l]$ submatrices values in contrast to the 'diamond and triangle' distributions used in TopDom. The triangle distribution contain the intra *z*-score values between bin $l - w$ and l, and the intra *z*-score values between bin l and $l + w$.

Validation of boundary quality. We used the following functional signatures to validate the quality of our boundaries:

Distance to known insulator co-factor CP190: since all studied insulators proteins bind to CP190[11,12,14], a sensible quality measure is the overlap of boundaries with CP190 ChIP-seq peaks. For this, we computed the distance of the boundaries to CP190 peaks using bedtools[55] closestBed (Fig. 1b, Supplementary Figure 1h). For comparison, we randomized our boundary positions using bedtools shuffleBed (Supplementary Figure 1h) and estimated the new distances to CP190. ShuffleBed simply assigns a new random position for each boundary anywhere in the genome (excluding heterochromatic and unplaced regions. Finally, we computed the background probability of obtaining the observed overlap between CP190 peaks and Hi-C boundaries using bedtools Fisher's exact test.

Separation of histone marks: as boundaries are expected to separate histone marks we used the method described by ref. [5] to quantify the correlation of marks within TADs and between TADs. For this, each TAD was scaled to 15 kb, flanked with a 15 kb region and divided into 1 kb bins. For each bin the mean histone ChIP–chip value was recorded, thus generating a matrix of 2852 TADs (rows) and 45 bins (columns). For this we used computeMatrix from deepTools2. The pairwise pearson correlation value of each column was then computed to produce a matrix of size 45 × 45.

Classification of TADs. The following histone marks for Kc167 from modEncode[28] were used: H3K36me3, H3K4me3, H3K9me3, and H3K27me3. Other marks that correlate closely to these marks were not included. For example,

H3K9me2 correlates closely with H3K9me3, H3K4me2 with H3K4me3, and so on. The average intensity of the marks over the TAD length was computed using multiBigwigSummary from deepTools2[56]. The resulting matrix was clustered by computing Euclidean distances between the histone marks and applying hierarchical clustering using the complete method. Five clusters were detected (Supplementary Figure 1c) that correspond to the presence of H3K36me3, H3K9me3, H3K4me3, H3K27me3, or none. Analysis of the TADs containing H3K36me3 and H3K4me1 in the genome revealed that that H3K36me3 is present at exons of active genes while H3K4me1 is mostly present at introns and intergenic regions of active genes and less abundant at exons. Thus, noticing that these two marks are complementary for active regions we classified TADs having predominantly these marks as 'active'. For the other clusters we used the same categories as[29]: the cluster of TADs with H3K9me3 was labeled as 'HP1' (Heterochromatin Protein 1); the cluster with H3K27me3 was labeled 'repressed' or 'PcG' (Polycomb group) and the cluster with no mark was labeled as inactive.

Analysis of transcription at boundaries. In order to analyse transcription at boundaries, we downloaded ribo-depleted RNA-Seq data from modENCODE[57]. All data were mapped to the *Drosophila* (dm3) genome using HISAT2 (v2.0.4)[58] and the reads were summarized per gene using featureCounts (v1.5.0.p1)[59] using options '-p --primary -Q 10'. We used data from Kc167 cells, along with 14 different developmental stages, ranging from embryo to adult. We only used data produced in 2014 in order to avoid batch effects and further confirmed the data quality by clustering the samples by Euclidean distance (Supplementary Figure 2a). We normalized each sample by library size, averaged the counts for replicates, and finally used log transformed counts for all the analysis.

In order to be able to compare all samples from mixed sex, genes on sex chromosomes were excluded for analysis. In total 10,449 autosomal genes were used for expression and variability analysis. Genes were considered expressed if they have a normalized log-count >0. Similar results were obtained using the more stringent cutoff of log counts ≥10, genes with boundary promoters = 45.84% and non-boundary promoter 18.36% (p-value = 1.58E − 96, Fisher's exact test). Variability was assessed using coefficient of variation of a gene across all developmental stages along with Kc167 cells. To measure the effect of boundary on nearby gene expression, we first define pairs of adjacent genes in different orientation (convergent, divergent, or tandem) and record the coefficient of variation for each gene in the pair. Then we obtain the scatterplots for all such gene-pairs and compare the results for two different scenarios: (a) where the pairs are separated by a boundary and (b) where there is no such separation. We further tested whether in Kc167 cells, genes within TADs tend to be more correlated in expression amongst them compared to genes lying in the nearby TADs. For this we used a subset of consecutively arranged TADs that have more than one gene inside them. We then used ANOVA to test whether variability gene expression within TADs is different from variability between TADs. As seen in Supplementary Figure 2c, many TADs pairs are significantly different from each other, while very few TADs are significantly different if we randomly assign genes to TADs.

Identification of boundary motifs. We took the list of boundaries and expanded them by 500 bp on each side. To avoid false positives, repetitive regions from the sequences of those boundaries were replaced by 'N's and any region with >10% of 'N's was removed. We used MEME-chip[20] to identify enriched DNA motifs; MEME-chip internally computes motifs using two methods, DREME[60] and MEME[27]. DREME aims to quickly identify short motifs while MEME identifies larger overrepresented sequences (at the expense of significantly longer processing times).

To obtain the position-weight matrices of insulator motifs we ran MEME-chip[20] on the peaks called using MACS2[61]. We selected the highest scoring motif for each case which invariably corresponded to the motif reported for the protein. ChIP-seq data sources are found in Supplementary Table 4.

Enrichment of motifs using control background. For promoter boundaries a control background composed of all *Drosophila* gene promoters was used to test the enrichment. We downloaded *Drosophila* genes (dm3 assembly) from UCSC table browser[62] and selected the sequences 200 bp upstream and 50 bp downstream of the transcription start site as core promoter sequences.

We classified these promoter sequences as boundary if they were within 500 bp of a boundary, or non-boundary (control background) if they were farther than 2000 bp from a boundary. Repetitive regions from the sequences of those promoters were replaced by 'N's and any region with >10% of 'N's was removed. In total, 10,529 background promoters and 1944 boundary promoters were used.

We used two different methods to assess the enrichment of the de novo and known motifs in boundary promoters with respect the control background, namely Ame[21] from the MEME-suite and a method based on the predicted binding affinity given by TRAP[22] that works as follows: for each motif, the log(TRAP score) distribution was computed for both the background and the boundary promoters. The Wilcoxon rank-sum test was then used to test for differences in the distributions. The p-values obtained were corrected using FDR. For Ame, we use total hits as scoring method and Fisher's test for estimating enrichments. We tested all de novo motifs identified either by MEME or by DREME and all known motifs associated to insulators and CP190 co-factors, as well as all core-promoter motifs.

We also used as control active genes in Kc167. To make this control, we selected those genes that overlapped with the yellow and red chromatin states from ref. [29] that are indicative of active chromatin in *Drosophila* Kc cells. The enrichment results were similar to the ones using a more broader list of genes for background.

For the boundaries that are not at promoters we used non-promoter open chromatin sequences obtained from DNase-seq[28] as control. In this case, we used 1665 background open chromatin regions and 655 non-promoter boundaries.

Pausing index. Pausing index for all *D. melanogaster* promoters was computed as the ratio of Pol-II ChIP-seq coverage at promoter over coverage at gene body. We used the ChIP-seq data for RNA Pol-II from Li et al.[15]. The promoter region was defined as in the previous section (200 bp downstream, 50 bp upstream of transcription start site). The gene body was defined as the region between 50 bp downstream of the transcription start site and the gene end. We used the maximum coverage for the promoters and the median coverage for the gene body.

Processing of ChIP-seq data. The data sources are listed in Supplementary Table 4. For each ChIP-seq data used, we downloaded the respective fastq files and aligned them in the dm3 assembly using Bowtie2[63]. MACS2 was used to identify peaks for each of the proteins[61]. For the respective data sources we downloaded input sequences and aligned them as the ChIP-seq data. bamCompare and bamCoverage from deepTools2[56] were used to create normalized coverage bigwig files.

MEME-chip[20] was used to identify motifs based on the MACS2 peaks. The resulting motifs can be seen in Supplementary Table 1.

Clustering of motifs. We used the promoters (200 bp upstream 50 bp downstream) annotated as boundaries and computed the log(TRAP score) for the Beaf-32 motif, motif-1 (M1BP), motif-6, motif-7 (ZIPIC), and motif-8. The scores for each motif were converted to bigwig files and clustered using hierarchical clustering from deepTools2[56].

All boundaries that were further than 2000 bp of a promoter were centered at the nearest CP190 ChIP-seq peaks within 2000 bp, otherwise the boundary position was not modified. Log(TRAP score) for CTCF, Ibf, and Su(Hw) were computed for these regions and clustered as previously described.

We used hierarchical clustering based on Euclidian distance and the Ward method. The cluster number used was 13 for promoter boundaries and 9 for non-promoter boundaries. In each case, the group composed only of low-TRAP scores was removed. After clustering, the groups were manually ordered to produce the left panel of Fig. 3c. Scale of each heatmap was manually adjusted based on the range of TRAP scores found at the clusters for each motif (Supplementary Figure 3a). The log2 ratio of ChIP-seq/input for the different proteins was used for the center and right panels of Fig. 3c. Each heatmap is centered on the boundary and extended ±5000 bp. Scale of the heatmaps was adjusted based on the log2 ChIP/input for the protein in the respective cluster (Supplementary Figure 3b).

Motif presence. In general, sequence motifs occur with different strengths at different genomic loci, and the notion of presence/absence is largely dependent on arbitrary thresholds. Therefore much of our analysis is based on binding scores of motifs rather than their binary presence, which we invoke only for the purpose of visualization (Fig. 5e, Supplementary Figure 3c) and combinatorial motif analysis (Fig. 4). For Fig. 3d and Supplementary Figure 3, we considered a motif as present at a boundary if the TRAP score was equal or higher than the minimum log(TRAP score) identified for the clusters in Fig. 3c (the distribution of the log(TRAP scores) can be seen in Supplementary Figure 3a). The thresholds used were: ZIPIC motif −4.7, Beaf-32 −5, M1BP −4.5, motif-6 −3, motif-8 −2, Ibf −4, CTCF −4, and Su (Hw) −3. For GAF, Pita and Zw5 motifs we used FIMO[64] with the following parameters: '--max-strand --thresh 1e − 3'. For analysis of motif combinations at boundaries, we also require that the motifs are accompanied by the corresponding ChIP-seq peaks. For motif-6 and motif-8 whose binding proteins are not known, we require that the motif is on an accessible region. For this we use the peaks from the DNAse-seq data[28].

Boundary prediction and feature ranking. We performed boundary prediction at all *Drosophila* promoters using motif TRAP scores for various transcription factors and DNAse-seq signals as features. We utilized methods ranging from simple to complex (linear models, logistic regression, random forest, and stochastic gradient boosting), with the primary purpose to rank the features by importance in boundary prediction. Pre-filtering was done to remove highly correlated features (pearson $R >$ 40%). Linear model and random forest was performed using the package Caret[65], while logistic regression was performed using package glmnet[66] in R.

Linear model was used with stepwise feature selection algorithm to predict boundary score from features by selecting the combination of features that minimizes the Akaike Information Criteria (AIC). Logistic regression, Random forest, and gradient boosting were used to classify the promoters into boundary and non-boundary, with additional feature selection performed using lasso, for logistic regression. We performed 10-fold cross validation while training all classification models. To evaluate model accuracy, the data were randomly divided

into training (60%) and test (40%) data sets and the sensitivity and specificity was calculated for test predictions. Lasso and gradient boosting models show highly similar sensitivity and specificity when used on an independent test data set, compared to when same data set was used for prediction, suggesting they are robust and less prone to overfitting.

Linear model predicted the boundary scores on the test data set with overall Spearman correlation of 37.6%, while logistic regression and random forest performed predictions with around 73–78% accuracy. After obtaining the best model in each scenario, we ranked the features by their importance in prediction, using the 'varImp' function from Caret. 'varImp' selects a variable importance predictor based on the model type, which is calculated for each parameter in the model (https://topepo.github.io/caret/variable-importance.html). Briefly, the importance score for linear model is the absolute value of the *t*-statistic for the model parameter, for lasso, it is the absolute value of final coefficients, for gbm it is the relative influence score as described in Friedman[67], and for random forest it is the difference between the classification error-rate for the out-of-bag portion of data and a permuted predictor variable, averaged over all trees and normalized by the standard deviation of the differences (https://www.stat.berkeley.edu/~breiman/RandomForests/cc_home.htm#varimp). All importance scores are then scaled between 0 and 100 to compare them together.

Knockdown of M1BP and Beaf-32. S2 cells (obtained from Michael Boutros lab) were cultured in Express Five SFM (Thermo Fisher Scientific) supplemented with glutamax, at 27 °C at a density of 1–16 million/ml. All cell lines are regularly checked for the absence of mycoplasma by PCR detection kit (Jena Bioscience PP-401). dsRNA was generated using HiScribe T7 High Yield RNA Synthesis Kit (NEB) and purified with MEGAclear (Ambion). The dsRNA was heated to 65 °C for 5 min and left to cool to room temperature. Primers used for generating M1BP dsRNA are from ref. [17]. Primers used for generating Beaf-32 and GST dsRNABeaf-32_fwd 5′-ttaatacgactcactatagggAATCACGAGGAGCTCACCAA-3′

Beaf-32_rev 5′-ttaatacgactcactatagggCTACTCATCCTTGGCAAGCG-3′

GST_fwd 5′-ttaatacgactcactatagggAGATATCAATTTGTGGGATAGCT-3′

GST_rev 5′-ttaatacgactcactatagggAGATTTTGGATATTAGATACGGT-3′

For knockdown experiments, 7.5 million cells were transfected with 100 µg of dsRNA on 10 cm dishes, using Lipofectamine RNAiMAX Reagent (Thermo Fisher Scientific). The M1BP knockdown lasted for 7 days while that of Beaf-32 lasted for 4 days. For M1BP-Beaf-32 double knockdown, cells were first treated with M1BP dsRNA at day 1, followed by treatment with Beaf-32 dsRNA at day 3, and were collected at day 7. All knockdown experiments were performed in two biological replicates and samples were processed in the same batch.

Western blot to determine knockdown efficiency. Protein depletion efficiencies were verified with western blot using specific antibodies against Beaf-32 (1:2000, Creative Diagnostics, CABT-BL422), M1BP (1:1000, gift from David Gilmour, PennState) and Actin (1:2000, Santa Cruz Sc-1616). Blots were incubated overnight at 4 degrees. HRP-coupled goat Anti-Rabbit IgG (1:10,000, GE healthcare) was used as secondary antibody, followed by incubation for 1 h at room temperature. Results were measured using ChemiDoc Imaging system (Bio Rad).

In situ Hi-C of knockdown and control cells. We used a modified version of the in situ Hi-C protocol[5] to generate our Hi-C maps. All samples were processed in the same batch. S2 cells were fixed with 2% formaldehyde for 10 min at room temperature. Glycine at 125 mM final concentration was added to the plates followed by 5 min incubation. After two washes in PBS, cells were scraped off the plate and pelleted. Each pellet (10–50 million of cells) was resuspended in 1 ml of lysis buffer (10 mM Tris-HCl, pH 8, 10 mM NaCl, 0.2% IGEPAL CA-630) and nuclei were extracted by sonication following the NEXON protocol[68] (Covaris E220 sonicator, settings: 75 W peak power, 2% duty factor, 200 cycles/burst, for 60–90 s until about 70% of intact nuclei were released). Nuclei were pelleted and resuspended in 0.5% SDS to permeabilize the nuclear membrane and to make chromatin accessible for restriction digestion. After 10 min incubation at room temperature, SDS was quenched adding 1% Triton X-100 (final concentration) and 1X of NEBuffer 3.1 (NEB, B7203S). Nuclei were digested overnight at 37 °C on a rocking platform using DpnII (NEB, R0543M, ~1–5 units per million cells). Prior and after digestion, an aliquot of nuclei was set aside for digestion quality control and DNA quantification. Biotin incorporation was carried out in a final volume of 150 µl using these reaction conditions: 50 mM of each dNTPs, replacing dCTP with biotin-14-dCTP (Life Technologies, 19518-018), 1 U of Klenow (NEB, M0210L) per microgram of DNA, at 25 °C for 1 h to promote fill-in. Ligase mix was added (1X Ligation buffer NEB B0202, 0.8% Triton X-100, 0.1 mg/ml BSA, 2000 U T4 DNA ligase NEB M0202S, final sample volume 1.2 ml) and samples were incubated for 4 h at room temperature under rotation. Nuclei were pelleted, resuspended in SDS buffer (10 mM Tris-HCl, pH 8, 1 mM EDTA, 1% SDS), lysed, de-crosslinked and de-proteinized overnight at 68 °C. DNA was precipitated and sonicated to the size range of 100–600 bp. Biotinylated Hi-C DNA in 1X binding buffer (5 mM Tris-HCl, pH 8, 0.5 mM EDTA, 1 M NaCl) was pulled down using Dynabeads MyOne Streptavidin C1 (Life Technologies, 650.01), using 5 µl of beads per microgram of DNA, pre-washed in 1X binding buffer. Beads were washed twice in Tween wash buffer (5 mM Tris-HCl, pH 8, 0.5 mM EDTA, 1 M NaCl, 0.05% Tween-20) and twice in EB (10 mM Tris-HCl, pH 8). A small aliquot of beads-bound DNA was kept to measure the DNA concentration, eluting the DNA by incubation at 98 °C for 10 min. Quantity of 10–50 ng of DNA bound to beads was used for library preparation using a modification of the NEBNext Ultra II DNA library preparation workflow (NEB, E7645). DNA bound to beads was then end-repaired, A-tailed, adaptor-ligated using manufacturer's instruction. Beads were reclaimed on a magnet, washed once in EB and eluted at 98 °C for 10 min. DNA was USER-treated to open the adapters in meantime to PCR amplification. Libraries were sequenced paired-end, with a read length of 75 bp, on Illumina HiSeq 3000.

Cell cycle analysis using FACS. Formaldehyde-fixed cells (2% for 10 min) were resuspended in 500 µl of permeabilization buffer (1% BSA, 0.5% Triton X-100 in PBS) and incubated for 15 min at room temperature under mixing. Cells were then incubated overnight at 4 °C with a 1:500 dilution of anti-H3 Ser10 phosphorylated antibody (Abcam, ab5176) and washed twice with permeabilization buffer. Cells were pelleted and resuspended in 400 µl of permeabilization buffer. One microliter of secondary antibody (anti-rabbit conjugated with Alexa 633 fluorophore, A21070, Life Technologies) was added and cells were incubated for 2 h at room temperature (protected from light). After two washes using the permeabilization solution, cells were resuspended in 500 µl of PBS and treated with 5 µl of RNase A for 30 min at room temperature. Nuclei were stained using 1 µg/ml of DAPI prior sorting. Samples were analyzed by flow cytometry using BD LSRFortessa instrument. The data have been analyzed using FACSDiva.

Hi-C processing of Beaf-32 and M1BP knockdowns. Hi-C samples for GST control and knockdowns were processed as all other Hi-C samples using HiCExplorer. The bins are based on the restriction fragments for DpnII. The statistics of data processing are shown in Supplementary Figure 6d-f and Supplementary Table 5.

Code availability. HiCExplorer code is available online at: https://github.com/deeptools/HiCExplorer/. HiCBrowser code is available at: https://github.com/deeptools/HiCBrowser

Data availability. The processed data from ChIP-Seq and Hi-C samples obtained from online sources can be found at: http://chorogenome.ie-freiburg.mpg.de/data_sources.html. Sequencing data for the in situ Hi-C experiments described in this article are available at NCBI GEO under accession: GSE97965.

Received: 26 June 2017 Accepted: 6 December 2017
Published online: 15 January 2018

References

1. Dixon, J. R., Gorkin, D. U. & Ren, B. Chromatin domains: the unit of chromosome organization. *Mol. Cell* **62**, 668–680 (2016).
2. Dixon, J. R. et al. Topological domains in mammalian genomes identified by analysis of chromatin interactions. *Nature* **485**, 376–380 (2012).
3. Sexton, T. et al. Three-dimensional folding and functional organization principles of the Drosophila genome. *Cell* **148**, 458–472 (2012).
4. Hou, C., Li, L., Qin, Z. S. & Corces, V. G. Gene density, transcription, and insulators contribute to the partition of the Drosophila genome into physical domains. *Mol. Cell* **48**, 471–484 (2012).
5. Rao, S. S. P. et al. A 3D map of the human genome at kilobase resolution reveals principles of chromatin looping. *Cell* **159**, 1665–1680 (2014).
6. Sanborn, A. L. et al. Chromatin extrusion explains key features of loop and domain formation in wild-type and engineered genomes. *Proc. Natl Acad. Sci. USA* **112**, E6456–E6465 (2015).
7. Nichols, M. H. & Corces, V. G. A CTCF code for 3D genome architecture. *Cell* **162**, 703–705 (2015).
8. Lupiáñez, D. G. et al. Disruptions of topological chromatin domains cause pathogenic rewiring of gene-enhancer interactions. *Cell* **161**, 1012–1025 (2015).
9. Nora, E. P. et al. Targeted degradation of CTCF decouples local insulation of chromosome domains from genomic compartmentalization. *Cell* **169**, 930–944. e22 (2017).
10. Van Bortle, K. et al. Insulator function and topological domain border strength scale with architectural protein occupancy. *Genome Biol.* **15**, R82 (2014).
11. Zolotarev, N. et al. Architectural proteins Pita, Zw5,and ZIPIC contain homodimerization domain and support specific long-range interactions in Drosophila. *Nucleic Acids Res.* **44**, 7228–7241 (2016).
12. Ong, C.-T. & Corces, V. G. CTCF: an architectural protein bridging genome topology and function. *Nat. Rev. Genet.* **15**, 234–246 (2014).
13. Maksimenko, O. et al. Two new insulator proteins, Pita and ZIPIC, target CP190 to chromatin. *Genome Res.* **25**, 89–99 (2015).

14. Cuartero, S., Fresán, U., Reina, O., Planet, E. & Espinàs, M. L. Ibf1 and Ibf2 are novel CP190-interacting proteins required for insulator function. *EMBO. J.* **33**, 1–11 (2014).
15. Li, L. et al. Widespread rearrangement of 3D chromatin organization underlies polycomb-mediated stress-induced silencing. *Mol. Cell* **58**, 216–231 (2015).
16. Cubeñas-Potts, C. et al. Different enhancer classes in Drosophila bind distinct architectural proteins and mediate unique chromatin interactions and 3D architecture. *Nucleic Acids Res.* **45**, 1714–1730 (2017).
17. Li, J. & Gilmour, D. S. Distinct mechanisms of transcriptional pausing orchestrated by GAGA factor and M1BP, a novel transcription factor. *EMBO J.* **32**, 1829–1841 (2013).
18. Hug, C. B., Grimaldi, A. G., Kruse, K. & Vaquerizas, J. M. Chromatin architecture emerges during zygotic genome activation independent of transcription. *Cell* **169**, 216–228.e19 (2017).
19. Mourad, R., Li, L. & Cuvier, O. Uncovering direct and indirect molecular determinants of chromatin loops using a computational integrative approach. *PLoS Comput. Biol.* **13**, e1005538 (2017).
20. Ma, W., Noble, W. S. & Bailey, T. L. Motif-based analysis of large nucleotide data sets using MEME-ChIP. *Nat. Protoc.* **9**, 1428–1450 (2014).
21. McLeay, R. C. & Bailey, T. L. Motif Enrichment Analysis: a unified framework and an evaluation on ChIP data. *BMC Bioinform.* **11**, 165 (2010).
22. Thomas-Chollier, M. et al. Transcription factor binding predictions using TRAP for the analysis of ChIP-seq data and regulatory SNPs. *Nat. Protoc.* **6**, 1860–1869 (2011).
23. Ohler, U., Liao, G.-C., Niemann, H. & Rubin, G. M. Computational analysis of core promoters in the Drosophila genome. *Genome Biol.* **3**, RESEARCH0087 (2002).
24. Gurudatta, B. V., Yang, J., Van Bortle, K., Donlin-Asp, P. G. & Corces, V. G. Dynamic changes in the genomic localization of DNA replication-related element binding factor during the cell cycle. *Cell Cycle* **12**, 1605–1615 (2013).
25. Jain, D., Baldi, S., Zabel, A., Straub, T. & Becker, P. B. Active promoters give rise to false positive 'Phantom Peaks' in ChIP-seq experiments. *Nucleic Acids Res.* **43**, 6959–6968 (2015).
26. Landt, S. G. et al. ChIP-seq guidelines and practices of the ENCODE and modENCODE consortia. *Genome Res.* **22**, 1813–1831 (2012).
27. Bailey, T. L. & Elkan, C. Fitting a mixture model by expectation maximization to discover motifs in biopolymers. *Proc. Int. Conf. Intell. Syst. Mol. Biol.* **2**, 28–36 (1994).
28. Celniker, S. E. et al. Unlocking the secrets of the genome. *Nature* **459**, 927–930 (2009).
29. Filion, G. J. et al. Systematic protein location mapping reveals five principal chromatin types in Drosophila cells. *Cell* **143**, 212–224 (2010).
30. Belozerov, V. E., Majumder, P., Shen, P. & Cai, H. N. A novel boundary element may facilitate independent gene regulation in the Antennapedia complex of Drosophila. *EMBO J.* **22**, 3113–3121 (2003).
31. Schweinsberg, S. et al. The enhancer-blocking activity of the Fab-7 boundary from the Drosophila bithorax complex requires GAGA-factor-binding sites. *Genetics* **168**, 1371–1384 (2004).
32. Kalhor, R., Tjong, H., Jayathilaka, N., Alber, F. & Chen, L. Genome architectures revealed by tethered chromosome conformation capture and population-based modeling. *Nat. Biotechnol.* **30**, 90–98 (2011).
33. Goecks, J., Nekrutenko, A. & Taylor, J. Galaxy: a comprehensive approach for supporting accessible, reproducible, and transparent computational research in the life sciences. *Genome Biol.* **11**, R86 (2010).
34. Ulianov, S. V. et al. Active chromatin and transcription play a key role in chromosome partitioning into topologically associating domains. *Genome Res.* **26**, 70–84 (2016).
35. Lam, K. C. et al. The NSL complex regulates housekeeping genes in Drosophila. *PLoS Genet.* **8**, e1002736 (2012).
36. Feller, C. et al. The MOF-containing NSL complex associates globally with housekeeping genes, but activates only a defined subset. *Nucleic Acids Res.* **40**, 1509–1522 (2012).
37. Van Bortle, K. et al. Drosophila CTCF tandemly aligns with other insulator proteins at the borders of H3K27me3 domains. *Genome Res.* **22**, 2176–2187 (2012).
38. Liang, J. et al. Chromatin immunoprecipitation indirect peaks highlight long-range interactions of insulator proteins and Pol II pausing. *Mol. Cell* **5**, 1–10 (2014).
39. Wood, A. M. et al. Regulation of chromatin organization and inducible gene expression by a Drosophila insulator. *Mol. Cell* **44**, 29–38 (2011).
40. Pascual-Garcia, P. et al. Metazoan nuclear pores provide a scaffold for poised genes and mediate induced enhancer-promoter Contacts. *Mol. Cell* **66**, 63–76. e6 (2017).
41. Emberly, E. et al. BEAF regulates cell-cycle genes through the controlled deposition of H3K9 methylation marks into its conserved dual-core binding sites. *PLoS Biol.* **6**, 2896–2910 (2008).
42. Tue, N. T. et al. DREF plays multiple roles during Drosophila development. *Biochim. Biophys. Acta* **1860**, 705–712 (2017).
43. Schwartz, Y. B. et al. Nature and function of insulator protein binding sites in the Drosophila genome. *Genome Res.* **22**, 2188–2198 (2012).
44. Narendra, V. et al. CTCF establishes discrete functional chromatin domains at the Hox clusters during differentiation. *Science* **347**, 1017–1021 (2015).
45. Guo, Y. et al. CRISPR inversion of CTCF sites alters genome topology and enhancer/promoter function. *Cell* **162**, 900–910 (2015).
46. Cuddapah, S. et al. Global analysis of the insulator binding protein CTCF in chromatin barrier regions reveals demarcation of active and repressive domains. *Genome Res.* **19**, 24–32 (2009).
47. Iwasaki, O. et al. Interaction between TBP and condensin drives the organization and faithful segregation of mitotic chromosomes. *Mol. Cell* **59**, 755–767 (2015).
48. Strick, T. R., Kawaguchi, T. & Hirano, T. Real-time detection of single-molecule DNA compaction by condensin I. *Curr. Biol.* **14**, 874–880 (2004).
49. Alipour, E. & Marko, J. F. Self-organization of domain structures by DNA-loop-extruding enzymes. *Nucleic Acids Res.* **40**, 11202–11212 (2012).
50. Fudenberg, G. et al. Formation of chromosomal domains by loop extrusion. *Cell Rep.* **15**, 2038–2049 (2016).
51. Rowley, M. J. et al. Evolutionarily conserved principles predict 3D chromatin organization. *Mol. Cell* **67**, 837–852.e7 (2017).
52. Imakaev, M. et al. Iterative correction of Hi-C data reveals hallmarks of chromosome organization. *Nat. Methods* **9**, 999–1003 (2012).
53. Ramírez, F. et al. High-affinity sites form an interaction network to facilitate spreading of the MSL complex across the X chromosome in Drosophila. *Mol. Cell* **60**, 146–162 (2015).
54. Shin, H. et al. TopDom: an efficient and deterministic method for identifying topological domains in genomes. *Nucleic Acids Res.* **44**, e70 (2016).
55. Quinlan, A. R. & Hall, I. M. BEDTools: a flexible suite of utilities for comparing genomic features. *Bioinformatics* **26**, 841–842 (2010).
56. Ramírez, F. et al. deepTools2: a next generation web server for deep-sequencing data analysis. *Nucleic Acids Res.* **44**, W160–W165 (2016).
57. Graveley, B. R. et al. The developmental transcriptome of Drosophila melanogaster. *Nature* **471**, 473–479 (2011).
58. Pertea, M., Kim, D., Pertea, G. M., Leek, J. T. & Salzberg, S. L. Transcript-level expression analysis of RNA-seq experiments with HISAT, StringTie and Ballgown. *Nat. Protoc.* **11**, 1650–1667 (2016).
59. Liao, Y., Smyth, G. K. & Shi, W. FeatureCounts: an efficient general purpose program for assigning sequence reads to genomic features. *Bioinformatics* **30**, 923–930 (2014).
60. Bailey, T. L. DREME: motif discovery in transcription factor ChIP-seq data. *Bioinformatics* **27**, 1653–1659 (2011).
61. Feng, J., Liu, T., Qin, B., Zhang, Y. & Liu, X. S. Identifying ChIP-seq enrichment using MACS. *Nat. Protoc.* **7**, 1728–1740 (2012).
62. Karolchik, D. et al. The UCSC table browser data retrieval tool. *Nucleic Acids Res.* **32**, D493–D496 (2004).
63. Langmead, B. & Salzberg, S. L. Fast gapped-read alignment with Bowtie 2. *Nat. Methods* **9**, 357–359 (2012).
64. Grant, C. E., Bailey, T. L. & Noble, W. S. FIMO: scanning for occurrences of a given motif. *Bioinformatics* **27**, 1017–1018 (2011).
65. Kuhn, M. Building Predictive Models in R Using the caret Package. *J. Stat. Softw. Artic.* **28**, 1–26 (2008).
66. Friedman, J., Hastie, T. & Tibshirani, R. Regularization paths for generalized linear models via coordinate descent. *J. Stat. Softw.* **33**, 1–22 (2010).
67. Friedman, J. H. Greedy function approximation: a gradient boosting machine. *Ann. Stat.* **29**, 1189–1232 (2001).
68. Arrigoni, L. et al. Standardizing chromatin research: a simple and universal method for ChIP-seq. *Nucleic Acids Res.* **44**, e67 (2016).
69. Zabidi, M. A. et al. Enhancer-core-promoter specificity separates developmental and housekeeping gene regulation. *Nature* **518**, 556–559 (2015).
70. Lex, A., Gehlenborg, N., Strobelt, H., Vuillemot, R. & Pfister, H. UpSet: visualization of intersecting sets. *IEEE Trans. Vis. Comput. Graph.* **20**, 1983–1992 (2014).
71. Gaszner, M., Vazquez, J. & Schedl, P. The Zw5 protein, a component of the scs chromatin domain boundary, is able to block enhancer-promoter interaction. *Genes Dev.* **13**, 2098–2107 (1999).

Acknowledgements

We would like to thank David Gilmour (PennState University) for providing the M1BP antibody. Also, we would like to thank Ulrike Bönisch and her team at the Deep-Sequencing Facility and Andreas Würch from the FACS facility of the MPI-IE. We further thank Wilhelm Rüsing for IT support, Diana Santacruz for critical reading of the manuscript and Gina Renschler for the help in interpreting FACS results. We also thank Victor Corces Lab whose published data have been instrumental in this research. This work was supported by the German Research Foundation [SFB 992 "Medical Epigenetics"] awarded to A.A. and T.M. and a grant from the Federal Ministry of Education and Research through the German Epigenome Programme DEEP [01KU1216G] awarded to T.M.

Author contributions

F.R. developed HiCExplorer, HiCBrowser and the Chorogenome navigator with support from V.B., B A.G. and J.V. F.R. and V.B. performed all the analysis and designed the experiments, with inputs from T.M. L.A. and K.C.L. performed the experiments. T.M. supervised all aspects of the analysis, while B.H. and A.A. supervised J.V. and K.C.L., respectively. F.R. and V.B. wrote the manuscript with input from all other authors.

Additional information

Supplementary Information accompanies this paper at https://doi.org/10.1038/s41467-017-02525-w.

Competing interests: The authors declare no competing financial interest.

Reprints and permission information is available online at http://npg.nature.com/reprintsandpermissions/

Publisher's note: Springer Nature remains neutral with regard to jurisdictional claims in published maps and institutional affiliations.

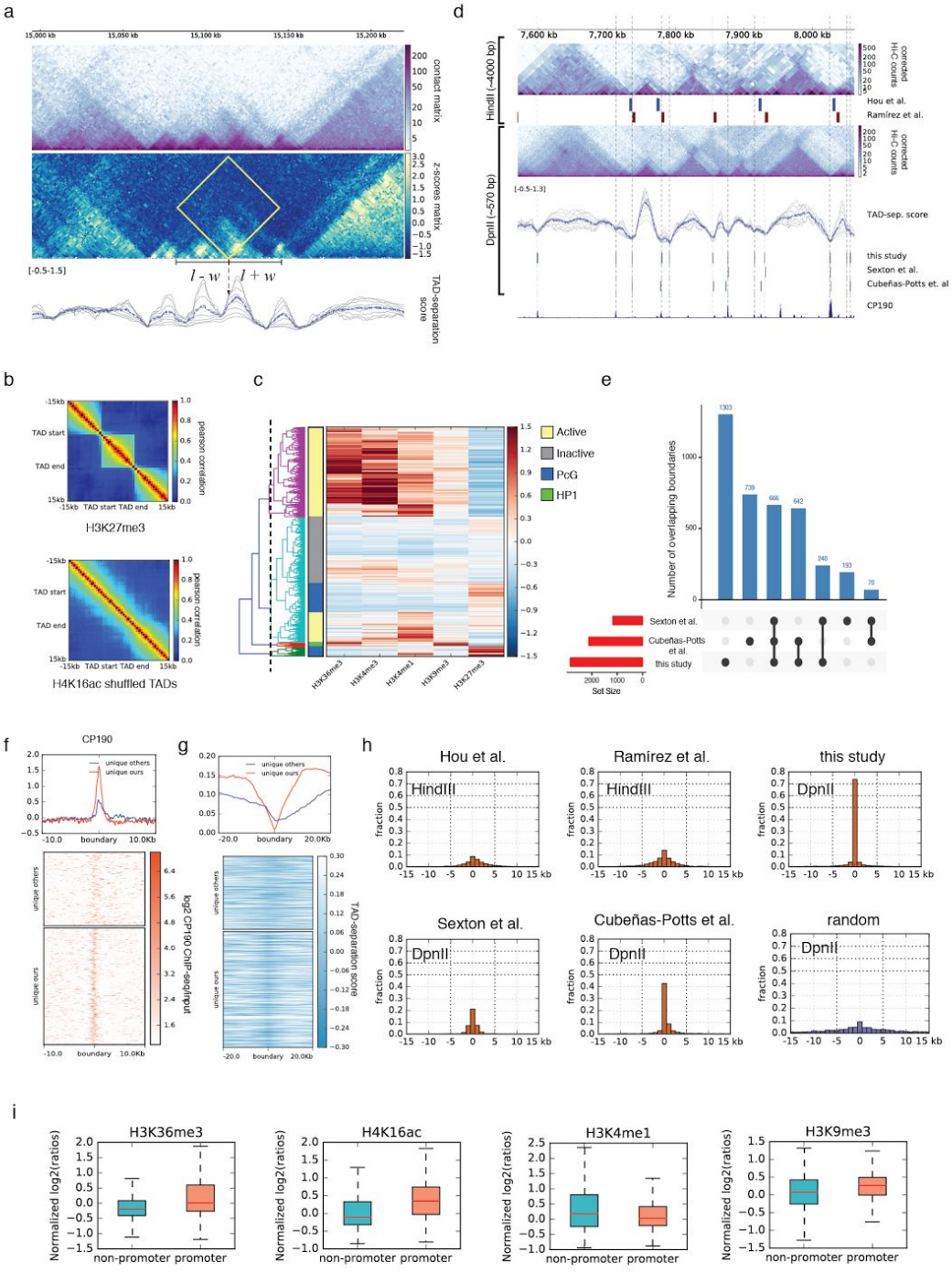
a
d
b
c
e
f
g
h
i
contact matrix
z-scores matrix
TAD-separation score
HindIII (~4000 bp)
DpnII (~570 bp)
Hou et al.
Ramírez et al.
TAD-sep. score
this study
Sexton et al.
Cubeñas-Potts et. al
CP190
H3K27me3
H4K16ac shuffled TADs
pearson correlation
Active
Inactive
PcG
HP1
Number of overlapping boundaries
Set Size
unique others
unique ours
log2 CP190 ChIP-seq/Input
boundary
Hou et al.
Ramírez et al.
this study
Sexton et al.
Cubeñas-Potts et al.
random
fraction
H3K36me3
H4K16ac
H3K4me1
H3K9me3
Normalized log2(ratios)
non-promoter
promoter

Supplementary Figure 1. **Detection of TAD boundaries and assessment of their quality**. **a.** Method to identify boundaries (see 'methods' for details). Top, Hi-C contact matrix counts. Middle, z-score transformed matrix. Last: TAD-separation score at different window lengths (gray lines) and mean score (blue line). The TAD-separation score at bin (l) corresponds to the mean values of the z-scores inside the 'diamond', which correspond to the contacts between a region of width w on left and on right. **b.** Similar to Fig. 1c, Pearson correlations of histone marks within and outside TADs (+15kb flanking regions) and for a random placement of boundaries. **c.** Hierarchical clustering of TADs based on modENCODE histone marks for Kc167 cells. Manual annotations for active, inactive, PcG and HP1 are based on the clustering results (see methods). **d.** Example genomic location comparing published boundaries with the ones generated in this study. Top, HindIII based Hi-C contact matrix counts for S2 cell line [1] and boundaries reported by Hou et al.[2] (Kc167) and Ramirez et al.[1] (S2). Bottom, DpnII based Hi-C contact matrix and the boundaries from this study, Sexton et al.[3] and Cubeñas-Potts et al. [4]. Below the Hi-C heatmap is the TAD-separation score as in Fig. 1a. The last track shows CP190 ChIP-seq signal [5].The vertical lines correspond to the boundaries in this study. **e.** Overlap of boundaries based on Hi-C DpnII experiments. The bars show the overlap between the indicated sets below (black dots). Two boundaries were considered overlapping if they were within 2000 bp from each other. The intersections were plotted using UpSetR [1]. **f.** Comparison of unique boundaries in our study with the unique boundaries in previous studies [2,3] with respect to CP190. Our unique boundaries overlap more frequently with CP190. **g.** Similar to f, but comparing TAD separation score. **h.** Histograms of the distance of our boundaries and other published boundary sets to CP190 peaks. The 'random' dataset contains our boundary set randomly shuffled (see methods). **i.** As in Fig. 1h, modENCODE histone marks at non-promoter and promoter boundaries. In all cases the promoter boundaries are associates significantly to the active marks (H3K36me3 and H4K16ac, p-value <=3.106261e-17 Wilcoxon rank-sum test).

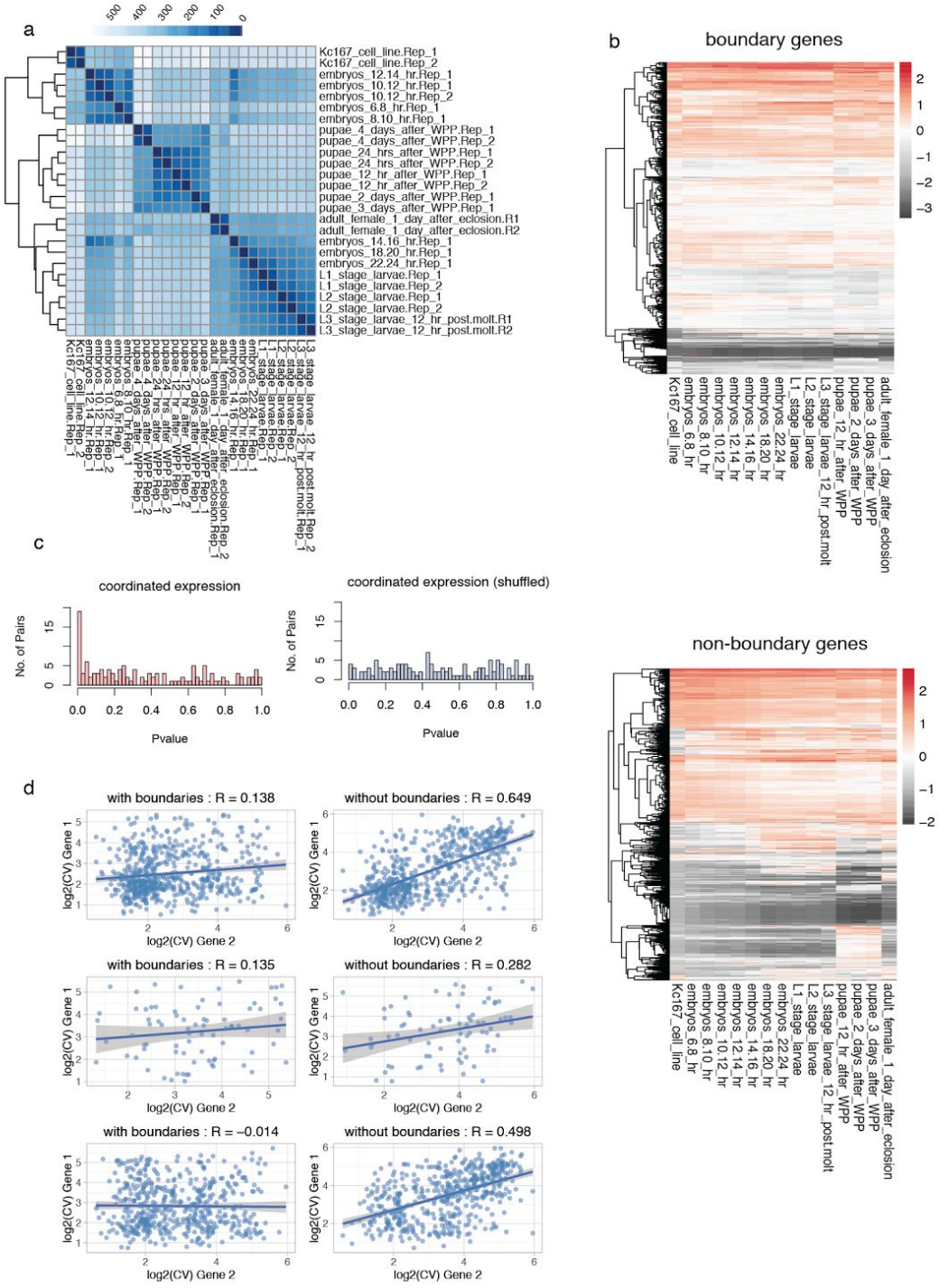
a
500
400
300
200
100
0
Kc167_cell_line.Rep_1
Kc167_cell_line.Rep_2
embryos_12.14_hr.Rep_1
embryos_10.12_hr.Rep_1
embryos_10.12_hr.Rep_2
embryos_6.8_hr.Rep_1
embryos_8.10_hr.Rep_1
pupae_4_days_after_WPP.Rep_1
pupae_4_days_after_WPP.Rep_2
pupae_24_hrs_after_WPP.Rep_1
pupae_24_hrs_after_WPP.Rep_2
pupae_12_hr_after_WPP.Rep_1
pupae_12_hr_after_WPP.Rep_2
pupae_2_days_after_WPP.Rep_1
pupae_3_days_after_WPP.Rep_1
adult_female_1_day_after_eclosion.R1
adult_female_1_day_after_eclosion.R2
embryos_14.16_hr.Rep_1
embryos_18.20_hr.Rep_1
embryos_22.24_hr.Rep_1
L1_stage_larvae.Rep_1
L1_stage_larvae.Rep_2
L2_stage_larvae.Rep_1
L2_stage_larvae.Rep_2
L3_stage_larvae_12_hr_post.molt.R1
L3_stage_larvae_12_hr_post.molt.R2
b
boundary genes
2
1
0
−1
−2
−3
Kc167_cell_line
embryos_6.8_hr
embryos_8.10_hr
embryos_10.12_hr
embryos_12.14_hr
embryos_14.16_hr
embryos_18.20_hr
embryos_22.24_hr
L1_stage_larvae
L2_stage_larvae
L3_stage_larvae_12_hr_post.molt
pupae_12_hr_after_WPP
pupae_2_days_after_WPP
pupae_3_days_after_WPP
adult_female_1_day_after_eclosion
c
coordinated expression
coordinated expression (shuffled)
No. of Pairs
0
5
15
0.0
0.2
0.4
0.6
0.8
1.0
Pvalue
non-boundary genes
d
with boundaries : R = 0.138
without boundaries : R = 0.649
with boundaries : R = 0.135
without boundaries : R = 0.282
with boundaries : R = −0.014
without boundaries : R = 0.498
log2(CV) Gene 1
log2(CV) Gene 2

Supplementary Figure 2. Gene expression is coordinated inside TADs. a. Euclidean distances between RNA-Seq samples from modENCODE used in this study. Replicates were later merged (mean) for the analysis. **b.** Clustering of genes by expression in Kc167 cells and at different developmental stages. Genes lying on either side of TAD boundaries tend to show consistent expression (top), while genes within TADs show variable expression (bottom) during development (color bar : row-wise z-score). Genes without boundaries were sampled randomly to the same number as genes with boundaries. **c.** P-values from ANOVA between genes within pairs of adjacent TADs (see methods). Expression within TADs is more coordinated (left) compared to genes randomly assigned to TADs (right). **d.** Same as Fig. 2d, here the adjacent gene-pairs are separated by their relative orientation: divergent (top), convergent (middle), and tandem (below) pairs. Gene-pairs without boundaries were sampled randomly to the same number as genes with boundaries. Line shows the linear model fit (shaded region: std. error).

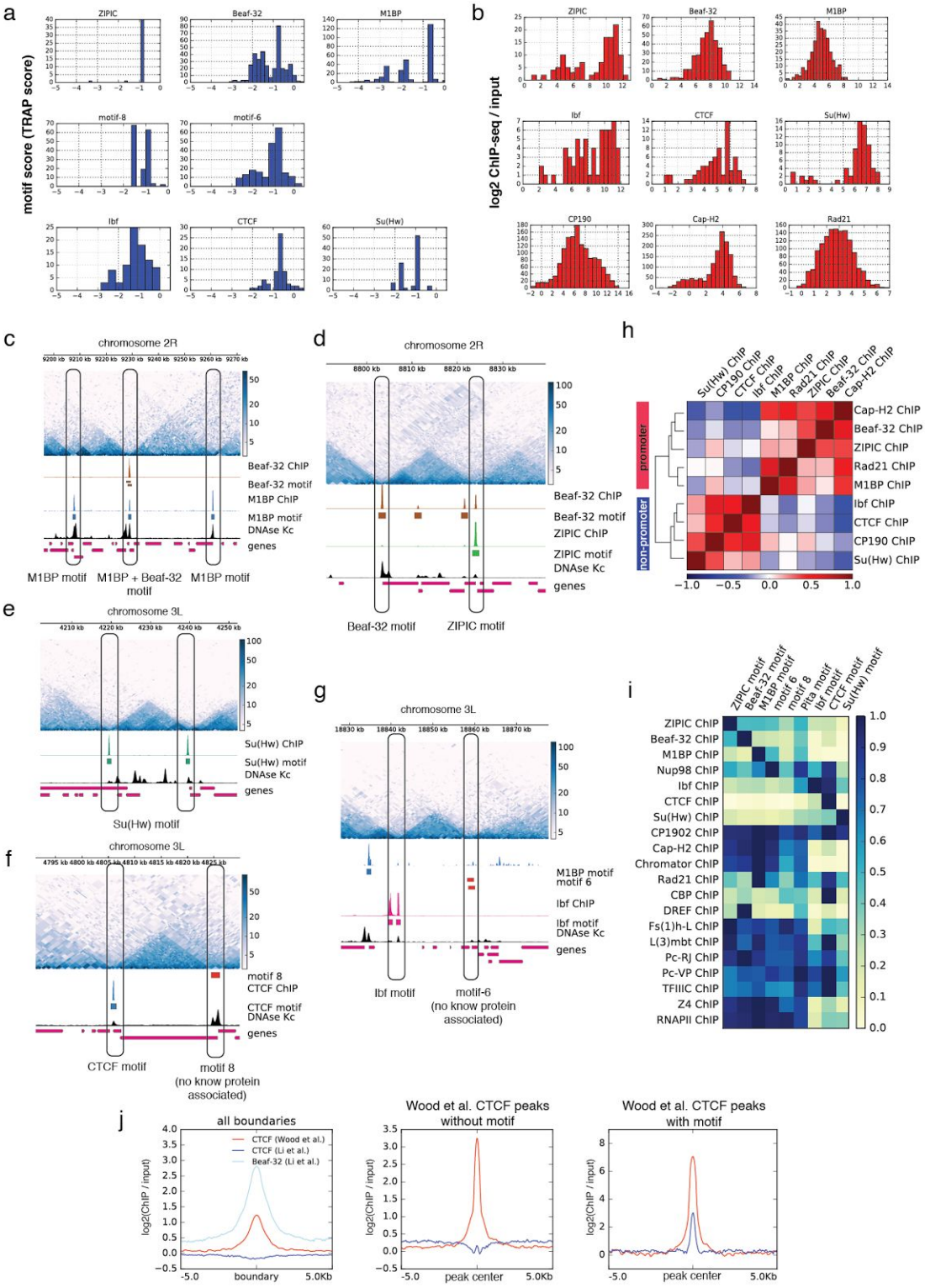
a
motif score (TRAP score)
ZIPIC
Beaf-32
M1BP
motif-8
motif-6
Ibf
CTCF
Su(Hw)
b
log2 ChIP-seq / input
ZIPIC
Beaf-32
M1BP
Ibf
CTCF
Su(Hw)
CP190
Cap-H2
Rad21
c
chromosome 2R
Beaf-32 ChIP
Beaf-32 motif
M1BP ChIP
M1BP motif
DNAse Kc
genes
M1BP motif
M1BP + Beaf-32 motif
M1BP motif
d
chromosome 2R
Beaf-32 ChIP
Beaf-32 motif
ZIPIC ChIP
ZIPIC motif
DNAse Kc
genes
Beaf-32 motif
ZIPIC motif
h
Su(Hw) ChIP
CP190 ChIP
CTCF ChIP
Ibf ChIP
M1BP ChIP
Rad21 ChIP
ZIPIC ChIP
Beaf-32 ChIP
Cap-H2 ChIP
promoter
non-promoter
Cap-H2 ChIP
Beaf-32 ChIP
ZIPIC ChIP
Rad21 ChIP
M1BP ChIP
Ibf ChIP
CTCF ChIP
CP190 ChIP
Su(Hw) ChIP
−1.0 −0.5 0.0 0.5 1.0
e
chromosome 3L
Su(Hw) ChIP
Su(Hw) motif
DNAse Kc
genes
Su(Hw) motif
g
chromosome 3L
M1BP motif
motif 6
Ibf ChIP
Ibf motif
DNAse Kc
genes
Ibf motif
motif-6
(no know protein associated)
i
ZIPIC motif
Beaf-32 motif
M1BP motif
motif 6
motif 8
Pita motif
Ibf motif
CTCF motif
Su(Hw) motif
ZIPIC ChIP
Beaf-32 ChIP
M1BP ChIP
Nup98 ChIP
Ibf ChIP
CTCF ChIP
Su(Hw) ChIP
CP1902 ChIP
Cap-H2 ChIP
Chromator ChIP
Rad21 ChIP
CBP ChIP
DREF ChIP
Fs(1)h-L ChIP
L(3)mbt ChIP
Pc-RJ ChIP
Pc-VP ChIP
TFIIIC ChIP
Z4 ChIP
RNAPII ChIP
f
chromosome 3L
motif 8
CTCF ChIP
CTCF motif
DNAse Kc
genes
CTCF motif
motif 8
(no know protein associated)
j
all boundaries
CTCF (Wood et al.)
CTCF (Li et al.)
Beaf-32 (Li et al.)
log2(ChIP / input)
-5.0 boundary 5.0Kb
Wood et al. CTCF peaks without motif
log2(ChIP / input)
-5.0 peak center 5.0Kb
Wood et al. CTCF peaks with motif
log2(ChIP / input)
-5.0 peak center 5.0Kb

Supplementary Figure 3. Boundary motifs and their relationship to the ChIP-Seq profiles. **a.** TRAP scores for each of the TAD boundary motifs within their cluster. **b**. ChIP-seq log2 ratio (ChIP/input) for the insulator proteins within their cluster. In the case of CP190, Cap-H2 and Rad21 the histogram contains the values over all boundaries. **c-g.** Examples of distinct insulators at boundaries**.** As in Fig. 1a, the top track shows Hi-C corrected counts. **h.** Heatmap showing Pearson correlations of ChIP-seq log2 ratios (IP / input) measured at TAD boundaries. The *complete* linkage method (also known as furthest neighbour clustering) was used for the hierarchical clustering. **i.** As in Fig. 3d. Each cell in the matrix contains the mean fold change of all respective ChIP-seq peaks having the motif. For each row, the maximum fold change was scaled to 1. **j.** Comparison of CTCF ChIP-seq experiments from Wood et. al.[4] and Li et. al.[5]. The first panel contains the mean values over all boundaries, the middle panel contains mean values for all CTCF peaks from Wood et. al.[4] that do not have the CTCF motif, and the last panel contains CTCF peaks from Wood et. al.[4] that have the CTCF motif. The CTCF ChIP-seq from Li et. al.[5] only shows enrichment when the CTCF motif is present while the CTCF ChIP-seq from Wood et al.[6] has unspecific bindings.

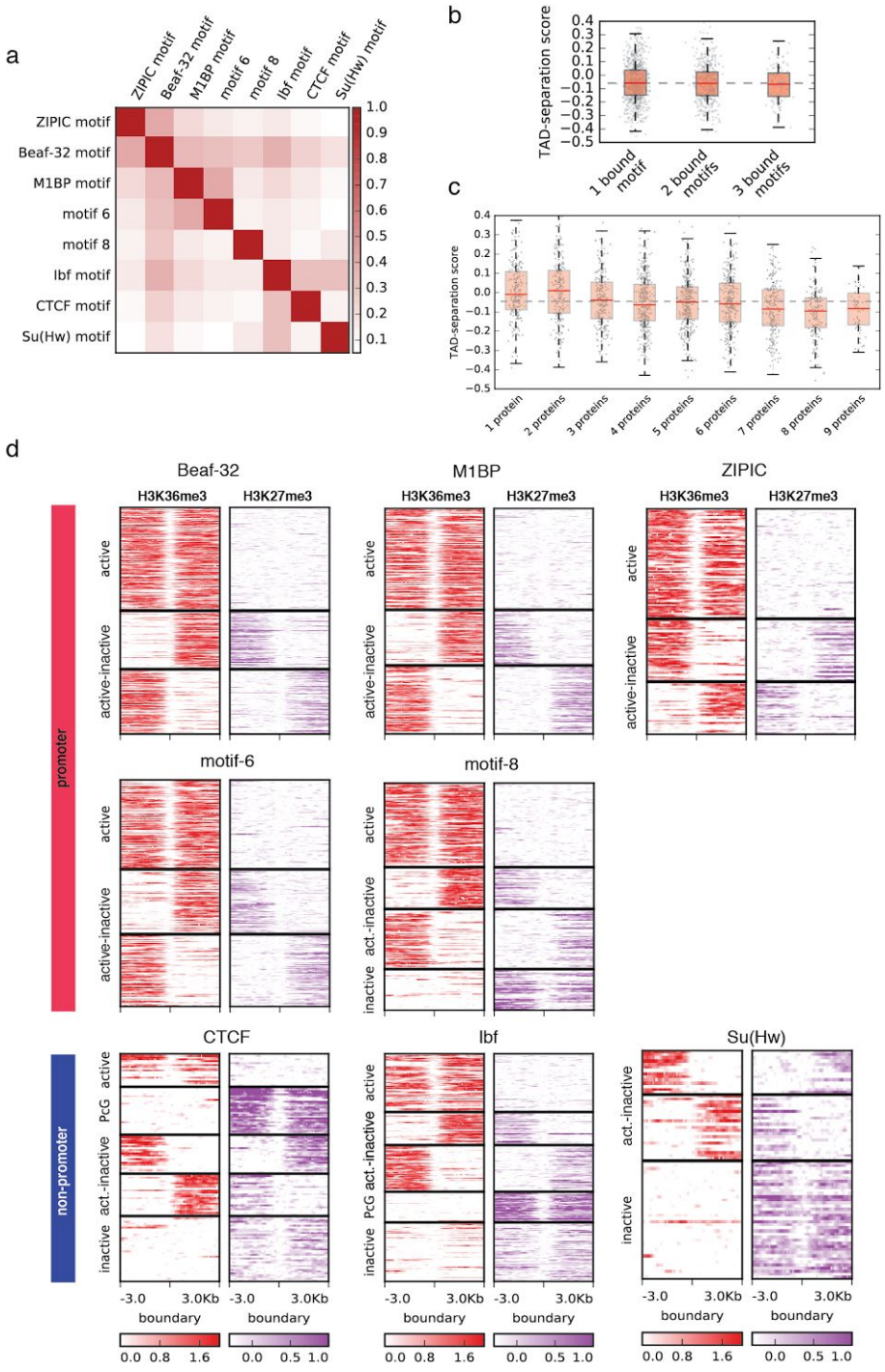
a
ZIPIC motif
Beaf-32 motif
M1BP motif
motif 6
motif 8
Ibf motif
CTCF motif
Su(Hw) motif
b
TAD-separation score
1 bound motif
2 bound motifs
3 bound motifs
c
TAD-separation score
1 protein
2 proteins
3 proteins
4 proteins
5 proteins
6 proteins
7 proteins
8 proteins
9 proteins
d
Beaf-32
M1BP
ZIPIC
H3K36me3
H3K27me3
promoter
active
active-inactive
motif-6
motif-8
act.-inactive
inactive
CTCF
Ibf
Su(Hw)
non-promoter
PcG
boundary
-3.0
3.0Kb

Supplementary Figure 4. **Effect of motif combinations on boundary strength and chromatin marks. a**. Heatmap of the overlap coefficient between boundary motifs. For each pair of motifs, the overlap coefficient is defined as Overlap-coefficient$(A, B) = A \cap B / \min(|A|, |B|)$ where A, B are the sets of all boundaries containing either motif A or B. **b**. TAD separation at boundaries containing one, two or three insulator motifs. Virtually no difference in boundary strength is observed with the number of insulator motifs present at boundaries. **c.** TAD separation score at boundaries bound by 1 up to 10 proteins known to be associated with boundaries (discarding information about motif enrichment). If we do not consider motif information, some variation can be seen in boundary strength associated to the number of bound proteins, especially between 2 to 3 boundary proteins and between 6 and 7 proteins (*p*-value <= 0.01 Wilcoxon rank sum test). **d.** Normalized log2 ChIP/input at transitions from different histone marks at boundaries for the active chromatin H3K36me3 and the repressive chromatin mark H3K27me3 on a 6 kb region centered at the boundaries. We performed *k*-means clustering using deepTools [6]. For CTCF and Ibf five clusters were used to distinguish boundaries between Polycomb group TADs. The low histone mark values at the boundaries (white color running at the center of the heatmaps) are indicative of nucleosome free regions. The polycomb group repressed chromatin (PcG) is characterized by higher intensities of H3K27me3 compared to the inactive chromatin.

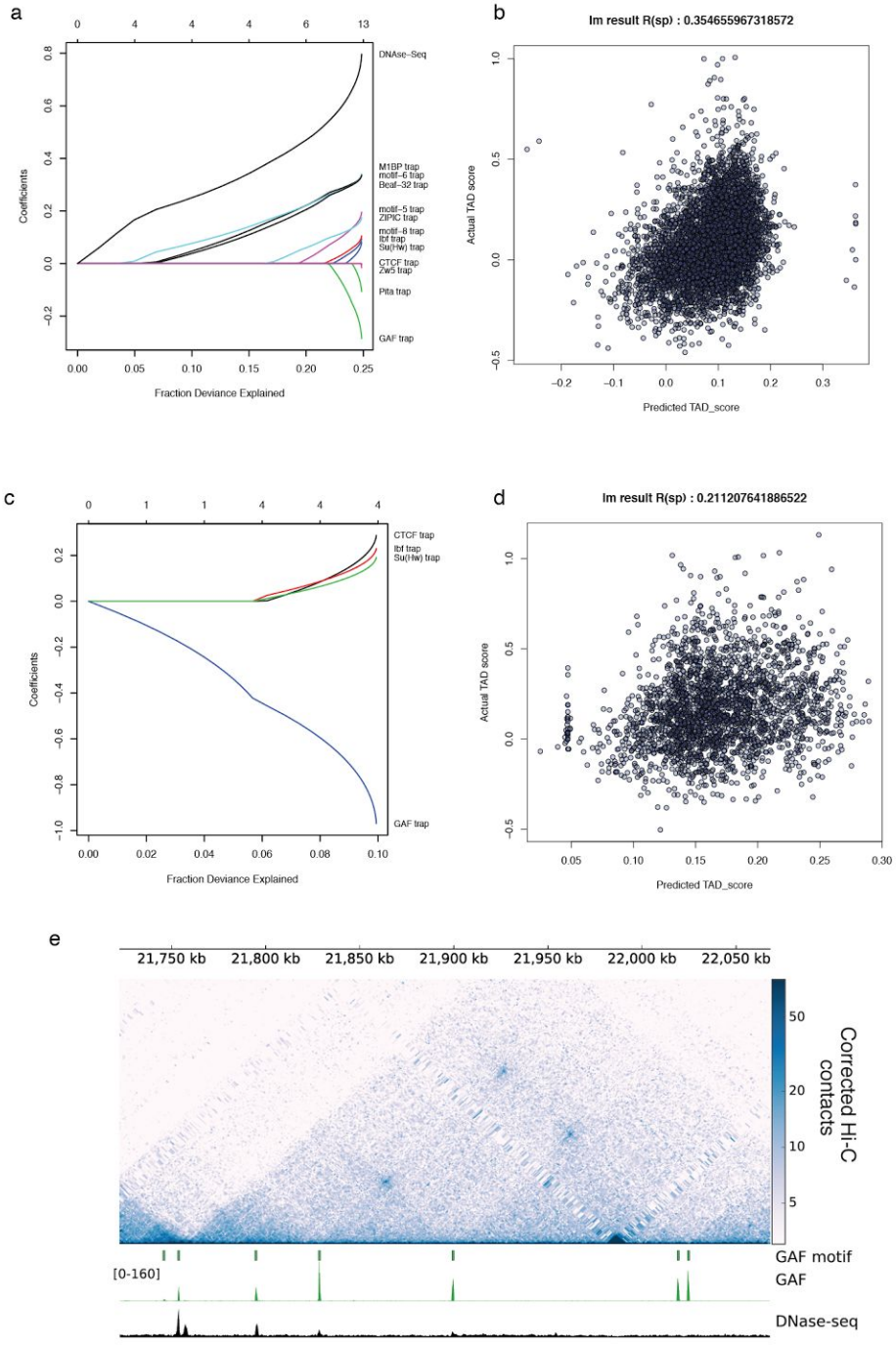
a
Coefficients
Fraction Deviance Explained
DNAse-Seq
M1BP trap
motif-6 trap
Beaf-32 trap
motif-5 trap
ZIPIC trap
motif-8 trap
Ibf trap
Su(Hw) trap
CTCF trap
Zw5 trap
Pita trap
GAF trap
b
lm result R(sp) : 0.354655967318572
Actual TAD score
Predicted TAD_score
c
Coefficients
Fraction Deviance Explained
CTCF trap
Ibf trap
Su(Hw) trap
GAF trap
d
lm result R(sp) : 0.211207641886522
Actual TAD score
Predicted TAD_score
e
21,750 kb
21,800 kb
21,850 kb
21,900 kb
21,950 kb
22,000 kb
22,050 kb
Corrected Hi-C contacts
GAF motif
[0-160]
GAF
DNase-seq

Supplementary Figure 5. Results from lasso and linear model predictions. a. Lasso penalized coefficients for promoters. Open chromatin (DNAse-seq), followed by Beaf-32, M1BP and motif-6 are the three top predictors to classify promoters as TAD boundaries, while GAF and Pita are negatively associated. **b**. At promoters: TAD score predictions using linear model on an independent test dataset. The predicted scores correlate with the actual TAD-separation scores on promoters. **c**. Lasso penalized coefficients for non-promoter open sites. TRAP score signal for CTCF, Ibf1 and Su(Hw) are positively correlated with boundaries, while GAF shows negative correlation. **d**. At non-promoter open sites : predicted TAD scores from linear model on an independent test dataset. **e**. GAF motif, which is negatively associated with promoter and non-promoter boundaries, can be found alone along with the protein at loop domains.

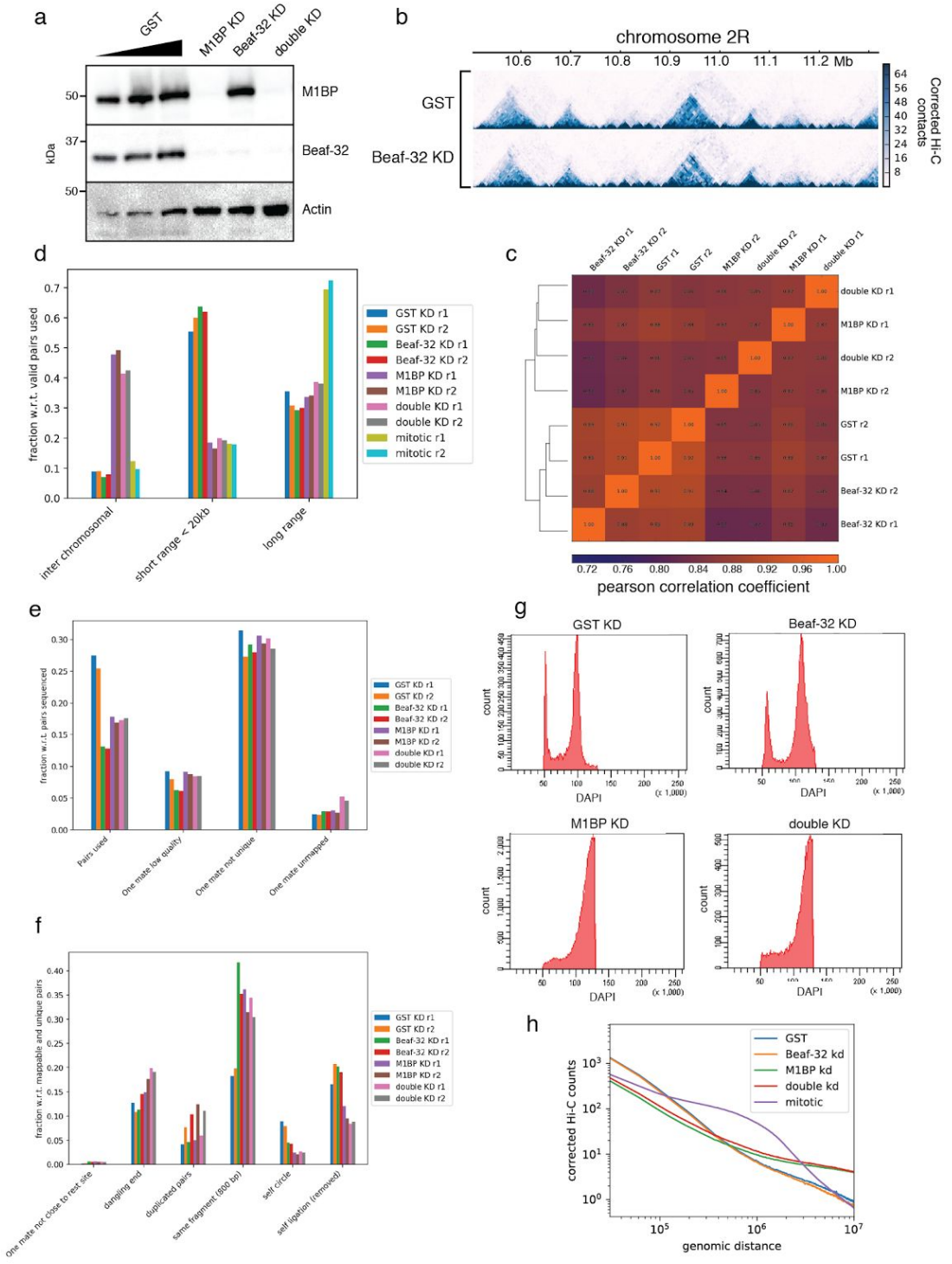
a
GST
M1BP KD
Beaf-32 KD
double KD
M1BP
Beaf-32
Actin
kDa
50
37
50
b
chromosome 2R
10.6
10.7
10.8
10.9
11.0
11.1
11.2 Mb
GST
Beaf-32 KD
Corrected Hi-C contacts
c
pearson correlation coefficient
d
fraction w.r.t. valid pairs used
inter chromosomal
short range < 20kb
long range
GST KD r1
GST KD r2
Beaf-32 KD r1
Beaf-32 KD r2
M1BP KD r1
M1BP KD r2
double KD r1
double KD r2
mitotic r1
mitotic r2
e
fraction w.r.t. pairs sequenced
Pairs used
One mate low quality
One mate not unique
One mate unmapped
f
fraction w.r.t. mappable and unique pairs
One mate not close to rest site
dangling end
duplicated pairs
same fragment (800 bp)
self circle
self ligation (removed)
g
GST KD
Beaf-32 KD
M1BP KD
double KD
count
DAPI
(x 1,000)
h
corrected Hi-C counts
genomic distance
GST
Beaf-32 kd
M1BP kd
double kd
mitotic

Supplementary Figure 6. Beaf-32 and M1BP knockdowns Hi-C. a. Western blots showing protein levels of M1BP and Beaf-32 (compared to GST control) after RNAi treatment in S2 cells. **b**. Example region showing contacts for all GST and Beaf-32 KD. All matrices were normalized to match the total number of contacts of the smaller matrix. The bin size used was 3kb. **c**. Pearson correlation of corrected Hi-C matrices. The correlation was done between Hi-C bins within 50 kbp. **d.** Fraction of Hi-C pairs classified as inter-chromosomal by *cis* distancer. Mitotic data values were added for comparison from Hug et al.[7] The total number of reads sequenced are listed in Supplementary Table 5. **e.** Fraction of valid Hi-C pairs used compared to low quality, unmapped and non-unique. **f**. Fraction of Hi-C pairs that are filtered by various reasons. These plots is part of the QC module of HiCExplorer. **g**. FACS analysis using DAPI for GST, Beaf-32, M1BP and M1BP + Beaf-32 knockdowns. M1BP knockdown affects cell growth and causes an arrest in cell-cycle not seen in GST or Beaf-32 KD. **h**. Genomic distance vs. Hi-C counts. Larger matrices were scaled down to match the sum of the smallest matrix. Only replicate 1 of all experiments was used. The 'mitotic' data is based on the Hi-C data on mitotic fly cells from Hug et. al. [7].

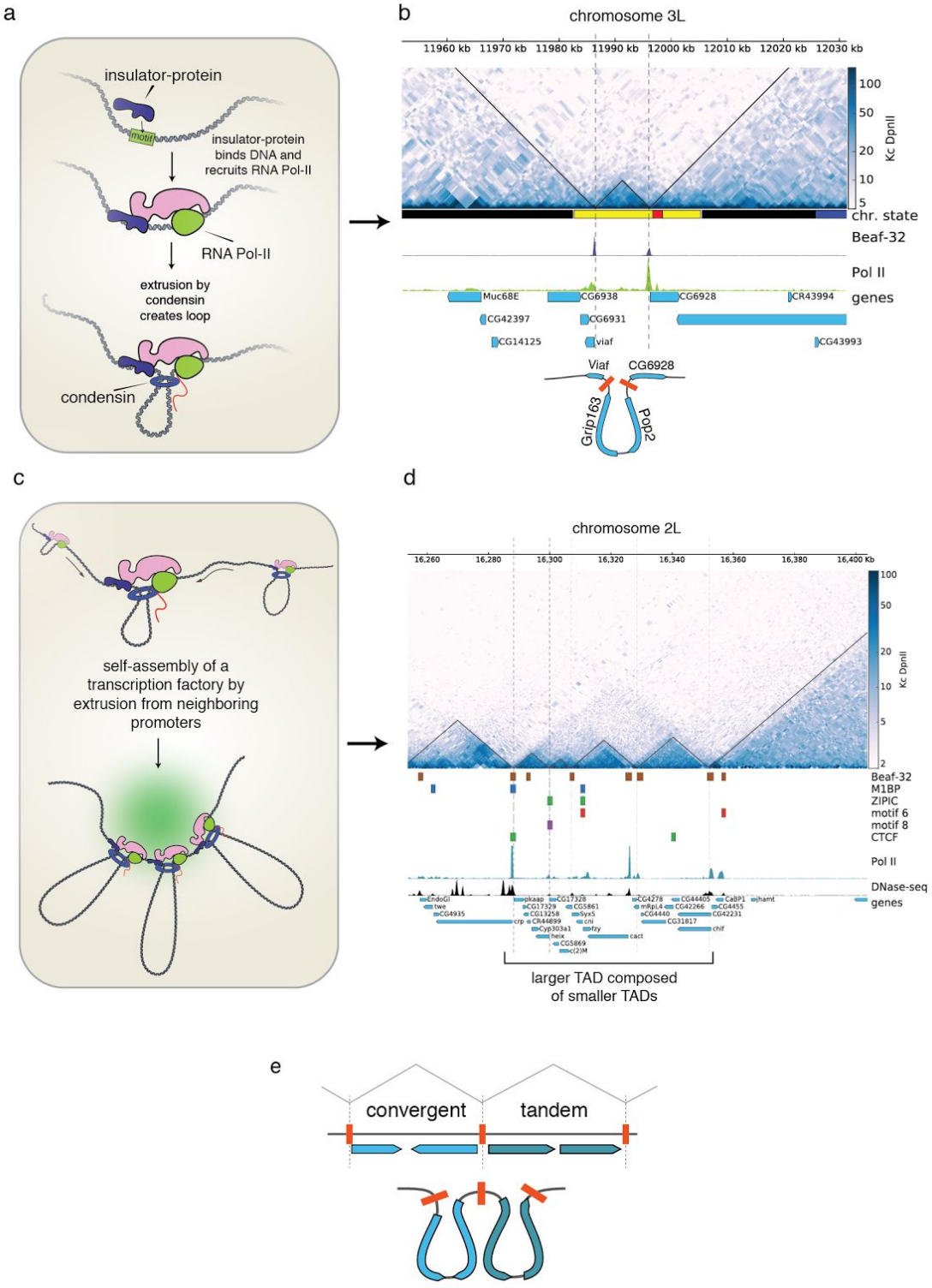
a
insulator-protein
motif
insulator-protein binds DNA and recruits RNA Pol-II
RNA Pol-II
extrusion by condensin creates loop
condensin
b
chromosome 3L
11960 kb 11970 kb 11980 kb 11990 kb 12000 kb 12010 kb 12020 kb 12030 kb
100
50
20
10
5
Kc DpnII
chr. state
Beaf-32
Pol II
genes
Muc68E
CG6938
CG6928
CR43994
CG42397
CG6931
CG14125
viaf
CG43993
Viaf
CG6928
Grip163
Pop2
c
self-assembly of a transcription factory by extrusion from neighboring promoters
d
chromosome 2L
16,260 16,280 16,300 16,320 16,340 16,360 16,380 16,400 Kb
100
50
20
10
5
2
Kc DpnII
Beaf-32
M1BP
ZIPIC
motif 6
motif 8
CTCF
Pol II
DNase-seq
genes
larger TAD composed of smaller TADs
e
convergent
tandem

Supplementary Figure 7. Model for the formation of TADs. a. Top: Binding of an insulator protein to its cognate motif at at core promoter facilitates RNA Pol-II initiation which in turn recruits condensin complex which initiates extrusion [8]. **b.** As shown by simulations [9,10] TADs in Hi-C contact maps are consistent with loop extrusion. Here we show a small active region between two large inactive TADs. The active region contains two genes and is flanked by the Beaf-32 insulator. The expected loop from this region is shown below. **c.** Neighboring promoters, each extruding a loop, end up meeting each other to form a rosette reminiscent of proposed transcription factories [11,12]. Such clusters, are also observed in a recent single-nucleus HiC study [13]. **d.** The TADs demarcated by the insulators motif and RNA Pol-II form a larger TAD. This implies that the smaller TADs remain in closer contact to each other compared to the surrounding inactive chromatin. This hierarchical TAD structure resembles the proposed structure of transcription factories. **e.** Insulators at divergent gene promoters serve as good anchors, by recruiting two Pol-II/Condensin machines in both directions. Red bars represent insulator motifs at promoters and dotted lines show the location of boundaries. The expected loops from this region are shown below.

Supplementary Table 1. Enriched motifs found at ChIP-seq peaks.

MOTIF Protein	Beaf-32	M1BP	Pita	CTCF	Ibf1/2	ZIPIC	Zw5	Su(Hw)	GAF	CP190	Mod (mdg4)	Cap-H2	Chro-mator	Rad21
Beaf-32 motif	285(600) 3.3e-230	95(600) 4.2e-18	85(600) 1.2e-014			119(600) 5.2e-72				51(300) 2.8e-5		219(600) 3.0e-187	102(300) 5.5e-52	28(300) 9.9e-8
M1BP motif	30(600) 9.5e-7	519(600) 6.0e-1012	73(600) 8.4e-054			47(600) 2.3e-6	28(300) 2.1e-10			88(300) 3.3e-42		102(600) 3.4e-98	88(300) 1.2e-074	84(300) 4.2e-97
Pita motif			114(600) 1.1e-093		56 (300) 3.8e-21									
CTCF motif	24(600) 1.1e+3		74(600) 1.1e-53	272(600) 5.0e-562	75(300) 9.3e-92	73(600) 1.2e-22				32(300) 1.0e-20	42(300) 9.4e-44			
Ibf1/2 motif				3.5e-008 (dreme)	195(300) 2.6e-49					2.5e-9 (dreme)				
ZIPIC motif	168(600) 7.6e-55	19(600) 1.4	108(600) 3.3e-108			356(600) 6.1e-256				28(300) 3.6e-4		120(600) 1.2e-61		
Zw5 motif							87(300) 3.1e-98							
Su(Hw) motif								175(300) 3.8e-208		66(300) 7.1e-60	27(300) 9.4e-13		24(300) 5.4e-9	
GAF motif									67(300) 1.8e-152		27(300) 9.4e-13			
Ohler motif 5 motif	40(600) 3.5e+6	27(600) 5.5e-1	48(600) 1.8e-21			71(600) 2.7e-23	27(300) 8.9e-12			26(300) 5.3e-6				
Ohler motif 6 motif		138(600) 9.6e-94				40(600) 3.0e-11				67(300) 4.0e-10		67(600) 4.8e-14		
Ohler motif 8 motif	30(600) 9.5e-7	12(600) 6.1e+8			54(300) 1.0e-7	30(600) 4.7e+3				49(300) 1.6e-2	42(300) 3.4e-9	18(600) 2.4e-12		98(300) 3.0e-7
A-rich repeat									128(300) 6.4e-15				118(300) 2.8e-105	
(CA)n repeat						40(600) 1.0e-11		43(300) 1.7e-42	77(300) 2.5e-276					35(300) 2.0e-22

The table shows number of sites with motifs (total number of sites) and MEME[14] E-value. In some cases the DREME[15] E-value is shown.

Supplementary Table 2. Comparison of motif enrichment using different sets of boundaries.

	DE-NOVO						KNOWN			
MOTIF	**AME all**	**TRAP all**	**AME Non promoters**	**TRAP Non promoters**	**Meme Non promoters**	**Dreme Non promoters**	**AME all**	**TRAP all**	**AME Non promoters**	**TRAP Non promoters**
Sexton et al.										
M1BP	6.36E-29	1.49E-22					9.11E-36	2.67E-27		
Beaf-32	1.72E-21	1.87E-23					6.02E-22	4.07E-22		
Motif-6	1.39E-11	5.73E-17					6.50E-16	9.86E-18		
ZIPIC	NA	NA					6.71E-15	1.87E-10		
Motif-8	NA	NA					3.34E-04	2.9E-5		
CTCF	NA	NA	NA		4.00E+10		NA	0.96	5.04E-09	1.4E-4
Su(Hw)	NA	NA	2.91E-01	0.0313	6.20E+14		NA	0.082	2.49E-02	0.0381
Ibf1/2	NA	NA	NA				2.22E-04	1.3E-3	NA	6.6E-4
Cubeñas-Potts et al.										
M1BP	1.17E-50	5.90E-34					8.65E-53	6.38E-40		
Beaf-32	1.25E-52	1.04E-50					1.45E-46	1.16E-48		
Motif-6	9.64E-38	1.52E-45					2.23E-38	3.91E-43		
ZIPIC	NA	NA					8.10E-27	1.07E-19		
Motif-8	NA	NA					1.47E-10	9.12E-11		
CTCF	NA	NA	8.10E-11	0.00129	9.17E-06		NA	0.117	7.53E-06	0.0633
Su(Hw)	NA	NA	NA	6.79E-06			3.69E-02	3.5E-4	1.52E-06	0.03481
Ibf1/2	NA	NA	NA				1.08E-11	2.75E-09	9.03E-02	6.53E-05
This study										
M1BP	4.24E-72	9.96E-72					7.84E-85	5.20E-87		
Beaf-32	2.10E-64	1.27E-74					1.63E-64	3.27E-70		
Motif-6	4.83E-45	5.26E-64					1.47E-48	8.65E-66		
ZIPIC	NA	NA					5.09E-37	1.07E-30		
Motif-8	1.58E-04	0.721					8.86E-08	7.27E-16		
CTCF	NA	NA	1.83E-04	0.0511	1.10E-02	1.10E-06	NA	0.095184	7.53E-06	0.0636
Su(Hw)	NA	0.0987	2.09E-03	3.89E-23	NA	2.10E-04	3.78E-03	4.30E-07	1.52E-06	3.87E-10
Ibf	NA	NA	NA	0.00137	NA		3.16E-07	6.22E-10	9.03E-02	2.03E-05

Supplementary Table 3. Hi-C data sources

Source	Restriction enzyme	No. of usable reads	GEO accession	Reference
Whole embryos	DpnII	133.483.965	GSE34453	[2]
Kc167	DpnII	135.274.348	GSE63515	[16]
Kc167	DpnII	110.807.526	GSE80701	[3]
Kc167	HindIII	71.278.991	GSE38468	[17]
S2	HindIII	680.121.887	GSE58821	[18]
Clone-8	HindIII	131.426.003	GSE58821	[18]
third instar larvae salivary glands	HindIII	9.404.794	GSE72512	[19]

Supplementary Table 4. ChIP-seq data sources.

Source	GEO accession	Reference
Kc167 Beaf-32	GSM762845	4
Kc167 CP190	GSM762836	4
Kc167 CTCF	GSM1535983	16
Kc167 Su(Hw)	GSM762839	4
Kc167 Cap-H2	GSM1318356	20
Kc167 Chromator	GSM1318357	20
Kc167 Rad21	GSM1318352	20
Kc167 Pita	GSM2133768	3
Kc167 ZIPIC	GSM2133769	3
Kc167 GAF	GSM2133762	3
Kc167 Ibf 1	GSM2133766	3
Kc167 Ibf 2	GSM2133767	3
Embryo Zw5	GSM2042227	21
S2 M1BP	GSM1208162	22
Kc167 RNA Pol-II	GSM1536014	16
S2 DNase-seq	GSM1000406	23

Supplementary Table 5. Number of sequencing reads for Hi-C control and knockdowns.

	GST rep. A	GST rep. B	Beaf-32 KD rep. A	Beaf-32 KD rep. B	M1BP KD rep. A	M1BP KD rep. B	double KD rep. A	double KD rep. B
Pairs considered	107.8M	118.5M	102.4M	151.0M	298.1M	213.8M	217.3M	180.5M
Pairs used	32.1M	32.5M	14,5M	22.0M	58.7M	40.8M	42.9M	36.6M

References

1. Lex, A., Gehlenborg, N., Strobelt, H., Vuillemot, R. & Pfister, H. UpSet: Visualization of Intersecting Sets. *IEEE Trans. Vis. Comput. Graph.* **20,** 1983–1992 (2014).
2. Sexton, T. *et al.* Three-dimensional folding and functional organization principles of the Drosophila genome. *Cell* **148,** 458–472 (2012).
3. Cubeñas-Potts, C. *et al.* Different enhancer classes in Drosophila bind distinct architectural proteins and mediate unique chromatin interactions and 3D architecture. *Nucleic Acids Res.* **45,** 1714–1730 (2017).
4. Wood, A. M. *et al.* Regulation of Chromatin Organization and Inducible Gene Expression by a Drosophila Insulator. *Mol. Cell* **44,** 29–38 (2011).
5. Li, L. *et al.* Widespread rearrangement of 3D chromatin organization underlies polycomb-mediated stress-induced silencing. *Mol. Cell* **58,** 216–231 (2015).
6. Ramírez, F. *et al.* deepTools2: a next generation web server for deep-sequencing data analysis. *Nucleic Acids Res.* **44,** W160–5 (2016).
7. Hug, C. B., Grimaldi, A. G., Kruse, K. & Vaquerizas, J. M. Chromatin Architecture Emerges during Zygotic Genome Activation Independent of Transcription. *Cell* **169,** 216–228.e19 (2017).
8. Iwasaki, O. *et al.* Interaction between TBP and Condensin Drives the Organization and Faithful Segregation of Mitotic Chromosomes. *Mol. Cell* **59,** 755–767 (2015).
9. Sanborn, A. L. *et al.* Chromatin extrusion explains key features of loop and domain formation in wild-type and engineered genomes. *Proc. Natl. Acad. Sci. U. S. A.* **112,**

E6456–65 (2015).

10. Goloborodko, A., Imakaev, M. V., Marko, J. F. & Mirny, L. Compaction and segregation of sister chromatids via active loop extrusion. *Elife* **5,** (2016).
11. Cook, P. R. A model for all genomes: the role of transcription factories. *J. Mol. Biol.* **395,** 1–10 (2010).
12. Sutherland, H. & Bickmore, W. A. Transcription factories: gene expression in unions? *Nat. Rev. Genet.* **10,** 457–466 (2009).
13. Stevens, T. J. *et al.* 3D structures of individual mammalian genomes studied by single-cell Hi-C. *Nature* **544,** 59–64 (2017).
14. Bailey, T. L. & Elkan, C. Fitting a mixture model by expectation maximization to discover motifs in biopolymers. *Proc. Int. Conf. Intell. Syst. Mol. Biol.* **2,** 28–36 (1994).
15. Bailey, T. L. DREME: motif discovery in transcription factor ChIP-seq data. *Bioinformatics* **27,** 1653–1659 (2011).
16. Li, L. *et al.* Widespread Rearrangement of 3D Chromatin Organization Underlies Polycomb-Mediated Stress-Induced Silencing. *Mol. Cell* **58,** 216–231 (2015).
17. Hou, C., Li, L., Qin, Z. S. & Corces, V. G. Gene density, transcription, and insulators contribute to the partition of the Drosophila genome into physical domains. *Mol. Cell* **48,** 471–484 (2012).
18. Ramírez, F. *et al.* High-Affinity Sites Form an Interaction Network to Facilitate Spreading of the MSL Complex across the X Chromosome in Drosophila. *Mol. Cell* **60,** 146–162 (2015).
19. Eagen, K. P., Hartl, T. A. & Kornberg, R. D. Stable Chromosome Condensation Revealed by Chromosome Conformation Capture. *Cell* **163,** 934–946 (2015).
20. Van Bortle, K. *et al.* Insulator function and topological domain border strength scale with architectural protein occupancy. *Genome Biol.* **15,** R82 (2014).

21. Zolotarev, N. *et al.* Architectural proteins Pita, Zw5,and ZIPIC contain homodimerization domain and support specific long-range interactions in Drosophila. *Nucleic Acids Res.* **44,** 7228–7241 (2016).

22. Li, J. & Gilmour, D. S. Distinct mechanisms of transcriptional pausing orchestrated by GAGA factor and M1BP, a novel transcription factor. *EMBO J.* **32,** 1829–1841 (2013).

23. Arnold, C. D. *et al.* Genome-wide quantitative enhancer activity maps identified by STARR-seq. *Science* **339,** 1074–1077 (2013).

A.2 Galaxy HiCExplorer

I contributed to the development of HiCExplorer and designed the template workflow for the galaxy web server. I contributed to the writing and revision of the manuscript along with Joachim Wolff and other authors.

Published online 13 June 2018 *Nucleic Acids Research, 2018, Vol. 46, Web Server issue* ***W11–W16***
doi: 10.1093/nar/gky504

Galaxy HiCExplorer: a web server for reproducible Hi-C data analysis, quality control and visualization

Joachim Wolff[1], Vivek Bhardwaj[2,6], Stephan Nothjunge[5,8], Gautier Richard[2,7], Gina Renschler[2,6], Ralf Gilsbach[5], Thomas Manke[2], Rolf Backofen[1,3,4], Fidel Ramírez[2,*] and Björn A. Grüning[1,3,*]

[1]Bioinformatics Group, Department of Computer Science, University of Freiburg, Georges-Köhler-Allee 106, 79110 Freiburg, Germany, [2]Max Planck Institute of Immunobiology and Epigenetics, Stübeweg 51, 79108 Freiburg im Breisgau, [3]Center for Biological Systems Analysis (ZBSA), University of Freiburg, Habsburgerstr. 49, 79104 Freiburg, Germany, [4]BIOSS Centre for Biological Signaling Studies, University of Freiburg, Schänzlestr. 18, 79104 Freiburg, Germany, [5]Institute of Experimental and Clinical Pharmacology and Toxicology, Faculty of Medicine, University of Freiburg, Albertstr. 25, 79104 Freiburg, Germany, [6]Faculty of Biology, University of Freiburg, Schänzlestr. 1, 79104 Freiburg, Germany, [7]IGEPP, INRA, Agrocampus Ouest, Univ Rennes, 35600 Le Rheu, France and [8]Hermann Staudinger Graduate School, University of Freiburg, Hebelstrasse 27, 79104 Freiburg, Germany

Received February 23, 2018; Revised April 27, 2018; Editorial Decision May 10, 2018; Accepted May 22, 2018

ABSTRACT

Galaxy HiCExplorer is a web server that facilitates the study of the 3D conformation of chromatin by allowing Hi-C data processing, analysis and visualization. With the Galaxy HiCExplorer web server, users with little bioinformatic background can perform every step of the analysis in one workflow: mapping of the raw sequence data, creation of Hi-C contact matrices, quality assessment, correction of contact matrices and identification of topological associated domains (TADs) and A/B compartments. Users can create publication ready plots of the contact matrix, A/B compartments, and TADs on a selected genomic locus, along with additional information like gene tracks or ChIP-seq signals. Galaxy HiCExplorer is freely usable at: https://hicexplorer.usegalaxy.eu and is available as a Docker container: https://github.com/deeptools/docker-galaxy-hicexplorer.

INTRODUCTION

Chromosome conformation capture techniques are now widely used to analyse the 3D conformation of chromatin inside the nucleus across a rising number of species, tissues and experimental conditions. In particular, the Hi-C protocol (1) has helped to uncover folding principles of chromatin, demonstrating that the genome is partitioned into active and inactive compartments (called A and B) (1) and that these compartments are further subdivided into topological associated domains (TADs) (2,3). Furthermore, Hi-C has allowed identification of chromatin loops (4,5), as well as enhancer–promoter interactions (6,7) and their influence on gene expression (8,9).

However, Hi-C data processing requires tabulating hundreds of millions to billions of paired-end reads into large matrices. This poses bioinformatic challenges for efficient processing of the data and subsequent analyses. Here, we introduce Galaxy HiCExplorer, a package that aims to make Hi-C data processing, analysis and visualization available to non-bioinformaticians. Our goal is to provide a software environment able to automate the whole workflow of Hi-C data analyses from raw read mapping, filtering and correction, to the computation of topological associated domains and A/B compartments, and finally to the visualization of contact matrices, along with various other genomic features and omics data. Moreover, Galaxy HiCExplorer is easy to install, maintainable, stable and well documented. The availability of a docker container in conjunction with Bioconda (http://dx.doi.org/10.1101/207092), eliminates the need for complex software and dependency installations. Finally, HiCExplorer is transparently developed by a community of collaborators based on best practices (10) for version control, code revisions, manual and automated testing and comprehensive documentation.

COMPREHENSIVE SERVER FOR HI-C ANALYSES

Galaxy HiCExplorer is freely available at https://hicexplorer.usegalaxy.eu as well as a Docker container: https://github.com/deeptools/docker-galaxy-hicexplorer. Galaxy HiCExplorer was designed to provide an easily accessible data-analysis environment such that

*To whom correspondence should be addressed. Tel: +49 761 2037460; Fax: +49 761 2037462; Email: gruening@informatik.uni-freiburg.de
Correspondence may also be addressed to Fidel Ramírez. Email: ramirez@ie-freiburg.mpg.de

W12 Nucleic Acids Research, 2018, Vol. 46, Web Server issue

biomedical researchers can focus on critical research aspects instead of dealing with terminal-based applications that are not user-friendly. It smoothly integrates the HiCExplorer analysis toolset (8) into the Galaxy scientific analysis platform to provide web-based, easy-to-use and thoroughly tested workflows that provide pipelines for the most common Hi-C data processing steps.

In contrast to other available Hi-C analysis software like HiCUP (14), HOMER (15) and TADbit (16) among others (see (17,18) for a comprehensive list of tools), Galaxy HiCExplorer provides a fully comprehensive analysis pipeline available to much broader community of researchers and is not restricted to a subset of important features. HiC-Pro (19) is one of the few packages that offers a complete pipeline; however, its visualization tools are limited and it is only available as a command line tool. Similarly, Juicer (20) offers a command line tool processing pipeline while Juicebox (21) only provides visualizations. Moreover, the integration of HiCExplorer into Galaxy offers the possibility to process and integrate other data types like ChIP-Seq or RNA-Seq into the analysis using the same interface. None of the aforementioned tools offer web server access except HiFive (22).

A strong advantage of HiCExplorer is that it can take multiple matrix data formats developed by different research groups as input. Thus, it is well integrated in the landscape of Hi-C data analysis algorithms, as Hi-C matrices can be produced by other tools and visualized with HiCExplorer. Conversely, matrices can be created with HiCExplorer and then exported to be used by other software. Currently, the Galaxy HiCExplorer supports two major formats: The HiCExplorer specific h5 format and to promote standardization of Hi-C contact matrices the cooler format (23) developed within the 4D nucleome project (24).

GALAXY HiCExplorer TOOLS AND WORKFLOWS

Galaxy HiCExplorer provides a plethora of tools for processing, normalization, analysis, and visualization of Hi-C data (Figure 1A). Apart from HiCExplorer, the https://hicexplorer.usegalaxy.eu website and the Docker container also include the genome alignment tools BWA-MEM (25) and Bowtie2 (26), as well as additional tools for text manipulation, data import and quality control. The inclusion of deepTools (27) further facilitates the integration of ChIP-seq, RNA-seq, MNase-seq as well as other kind of datasets with Hi-C data.

The analysis of Hi-C data can be divided into three steps: pre-processing (including quality control), analysis and visualization.

Pre-processing and quality control

hicBuildMatrix. A contact matrix is the main data structure of Hi-C data analysis which is generated from the individual alignment of valid Hi-C paired-end reads. This tool filters out potentially erroneous reads, such as unmappable reads, self-ligated reads, dangling-ends, PCR duplicates or incomplete digestions (4,14) and tabulates the results based on user defined bins (either based on restriction sites or on fixed size bins). Because building the Hi-C matrix is one of the most time consuming steps in the Hi-C workflow, we developed *hicBuildMatrix* to be multi-processing to significantly reduce running time. A comprehensive quality report is generated as an HTML file. This report includes a number of useful quality measures including: number of valid Hi-C read pairs and the number of filtered reads per category (unmappable and non-unique pairs, duplicates, dangling ends, self-circles, etc.), number of intra-chromosomal, short-range (<20 kb) and long-range contacts, and read pair orientation. Reports from multiple samples can be integrated using MultiQC (28) or using the HiCExplorer tool *hicQC*. Inspection of the *hicBuildMatrix* quality reports helps to identify potential biases or errors in the Hi-C library preparation. For example, a high number of dangling ends is indicative of a problem with the re-ligation step or inefficient removal of dangling ends. The quality report can also be useful to identify differences (long-range versus short-range contacts enrichment for instance) between samples obtained in different conditions.

hicMergeMatrixBins. After a Hi-C contact matrix has been created, lower resolution matrices can be obtained by merging neighboring bins. This is mostly useful for visualization at different zoom levels or to create matrices of lower resolution (larger bin size) in the event of a Hi-C matrix being too poor due to low sequencing depth.

hicCorrelate. This tool computes the correlation between several Hi-C matrices (Figure 1B). *hicCorrelate* can produce a scatter plot or a heatmap using either Pearson or Spearman correlations. The computation of the correlation can be restricted to a range of genomic distances to avoid biasing the correlation results with background contacts. These correlations are useful as a quality control step to compare replicates and to test for differences between various treatments.

hicPlotDistVsCounts. This tool plots the average number of Hi-C contacts at different genomic distances (Figure 1C). It allows the estimation of long-range and short-range contacts from multiple samples at once, and is a useful tool for both quality control and comparison of, for example, treated versus untreated samples that alter chromosome conformation.

hicSumMatrices. After different replicates or similarly obtained Hi-C matrices have been compared using *hicCorrelate*, they can be added up into one single contact matrix with this tool.

hicCorrectMatrix. Allows the removal of biases from the Hi-C matrix using a very fast version of the iterative correction algorithm from Imakaev *et al.* (29). Before the contact matrix is corrected, the right thresholds to prune values need to be selected. The *diagnostic plot* helps users in determining these thresholds.

Analysis

hicFindTADs. This utility can identify TADs from a given corrected contact matrix by first computing a TAD-

Nucleic Acids Research, 2018, Vol. 46, Web Server issue **W13**

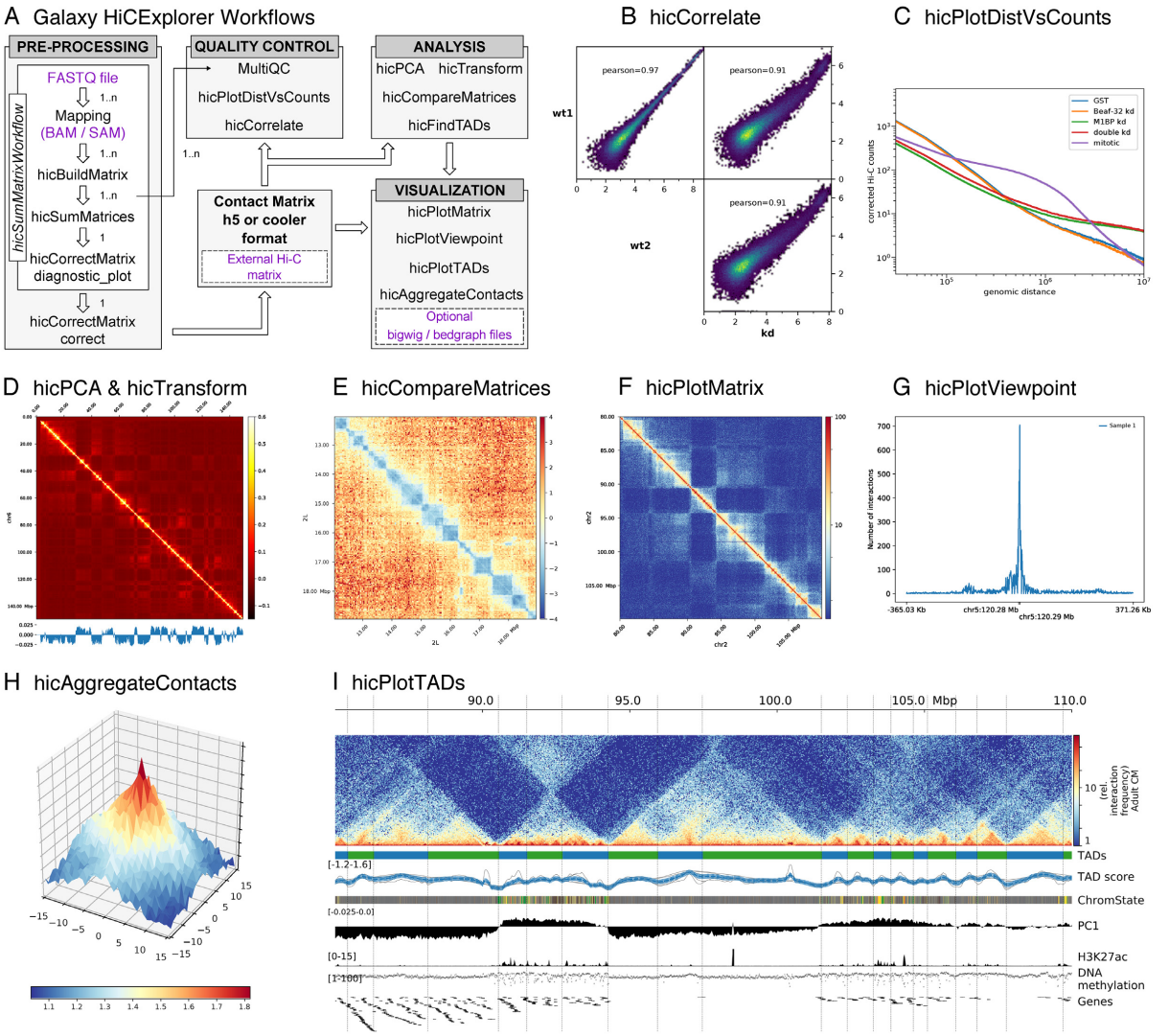

Figure 1. (**A**) Galaxy HiCExplorer workflows and tools. Entry points for external data are highlighted in purple. **Quality control tools:** (**B**) Output of *hicCorrelate* comparing two wild types and one knockdown samples. (**C**) Output of *hicPlotDistVsCounts* that shows changes of the number of contacts for different conditions. **Analysis tools:** (**D**) *hicPlotMatrix* of the Pearson correlation matrix derived from a contact matrix for chromosome 6 in mouse computed with hicTransform. The optional data track at the bottom shows the first eigenvector for A/B compartment obtained using *hicPCA*. (**E**) The pixel difference between a Hi-C corrected matrix for wild type condition and a knock down was computed using *hicCompareMatrices* and a 7Mb region is visualized using *hicPlotMatrix*. **Visualization tools:** (**F**) Contact matrix plot of a 80 to 105 Mb region of chromosome 2 in log scale. (**G**) Example output of *hicPlotViewpoint* showing the corrected number of Hi-C contacts for a single bin in chromosome 5 (output similar to 4C-seq) (11). (**H**) A Hi-C matrix was converted into an observed vs. expected matrix using *hicTransform* and this matrix, together with the location of high-affinity sites from (12) were used to run *hicAggregateContacts*. (**I**) 85 Mb to 110 Mb region from human chromosome 2 visualized using *hicPlotTADs*. TADs were computed by *hicFindTADs*. The additional tracks added correspond to: TAD- separation score (as reported by *hicFindTADs*), chromatin state , principal component 1 (A/B compartment) computed using *hicPCA*, ChIP-seq coverage for the H3K27ac mark, DNA methylation, and a gene track. Hi-C data for B, C, E and H from *Drosophila melanogaster* S2 cells from (8). Hi-C data for D, F and I from mouse cardiac myocytes (13). Additional tracks in I from (13).

separation score and then identifying local minima indicative of TAD boundaries (8). In contrast to other TAD identification methods, this tool also returns the TAD-separation score, which can be visualized in a genome browser or using *hicPlotTADs*. The TAD-separation score contains useful information to identify strong and weak boundaries and the density of contacts within TAD and can be visualized along with the Hi-C matrix (see *hicPlotTADs* tool).

hicPCA. A/B compartments (1) refer to open and closed chromatin that is spatially separated in the cell nucleus (30,31). We compute this using eigenvector decomposition as described by Lieberman-Aiden (1) and using the first

W14 Nucleic Acids Research, 2018, Vol. 46, Web Server issue

and second eigenvector. The positive/negative values correspond to open/closed chromatin. A visualization of A/B compartments is shown in Figure 1D.

hicTransform. The three matrices used to compute the A/B compartments (observed/expected, Pearson correlation and covariance matrices) are useful during visualization to achieve a better understanding of the Hi-C data. To enable this, *hicTransform* can compute these three matrices independently of *hicPCA*, and the matrices can then be plotted using the visualization tools.

hicCompareMatrices. hicCompareMatrices allows the computation of difference, ratio or log2ratio between two matrices. This is useful to compare replicates or samples from different conditions. It can, for example, help to characterize TAD structure modifications when followed by *hicPlotMatrix* (Figure 1E).

Visualization

hicPlotMatrix. This tool is used to plot contact matrices for a collection of individual chromosomes. It has multiple options to select the matrix colors and the values range. Additionally, *bigwig* tracks can be attached to plot additional features such as A/B compartments or ChIP-seq data. It is possible to plot a multitude of domains; the entire interaction matrix, individual chromosomes, multiple chromosomes, and various regions of interest (see Figure 1D–F).

hicPlotViewpoint. The viewpoint plot supports a visualization of the number of interactions around a specific reference point or region in the genome, and makes the long-range interactions visible as shown in Figure 1G. The output is comparable to what is obtained using the 4C-seq protocol.

hicAggreateContacts. Facilitates the analysis of long range-contacts by visualizing the average contacts over multiple smaller matrices around a given set of regions (Figure 1H).

hicPlotTADs. To visualize the computed TADs this tool flips the main diagonal of the Hi-C contact matrix by 45° and marks the TADs with triangles. It is possible to plot multiple matrices and add additional data like genes, chromatin states, long-range interactions and any other feature that can be represented as a bigwig or bedgraph file like methylation data, ChIP-seq, or RNA-seq to visually correlate them with TADs and their boundaries. There are multiple options to select the Hi-C matrix layout and colormap, different ways to visualize genes and regions files and also multiple configurations to plot coverage tracks like color, line width, line type, as dots, filled etc. (Figure 1I).

Workflows

Galaxy HiCExplorer provides pre-defined workflows to reduce intermediate steps and to guide a researcher through the different stages. The Galaxy framework offers the possibility to connect tools into workflows called Galaxy workflows. The provided workflows are subdivided into categories depending on the start of the analysis: First, raw FASTQ files are mapped to generate a contact matrix and its corrected equivalent. Different workflows are provided to cover the case of running many analyses in parallel or whether replicates should be merged to one contact matrix. Second, said contact matrix (or other) is used to compute TADs, A/B compartments and/or to plot them using the provided workflows. All workflows are linked on the homepage of the Galaxy HiCExplorer.

All Galaxy Workflows share a common notion that they should guide the researcher through the analysis, i.e. most parameters in the workflows do not need to be changed. The reference genome needs to be set for the mappers, and a desired bin size as well as the used restriction sites needs to be selected in order to build the contact matrix. Every workflow containing a plotting step needs the region to plot as input.

IMPLEMENTATION

Galaxy HiCExplorer is implemented as a Docker container based on the web-based Galaxy scientific workflow platform (32). HiCExplorer itself is implemented in Python, supporting version 2.7, 3.5 and 3.6, and available as a Bioconda package (http://dx.doi.org/10.1101/207092) and as BioContainer (33). This guarantees a fixation of versions and therefore reproducibility of analysis. Galaxy wrappers for HiCExplorer are available at the Galaxy tool shed.

USING HiCExplorer

Installation and usage

The Galaxy HiCExplorer web server can be used by visiting http://hicexplorer.usegalaxy.eu, or by installing it on a personal computer or locally (e.g. an institute intranet). For this, pre-configured Docker containers and conda packages are available.

Galaxy HiCExplorer:

Docker :

docker run -p 8080:80 quay.io/bgruening/galaxy-hicexplorer

hicexplorer.usegalaxy.eu : On https://hicexplorer.usegalaxy.eu all HiCExplorer tools and workflows are installed. Use this option if you require high computational resources (e.g. large memory requirements).

HiCExplorer:

The HiCExplorer as a command line tool is available via *conda* or *BioContainers*.

Conda : *conda install hicexplorer -c bioconda*

BioContainer :

docker run quay.io/biocontainers/hicexplorer:latest

Training

Training and a documentation are crucial to enable as many scientists as possible to use and understand the Galaxy HiCExplorer. To introduce scientists who are new to Galaxy a guided tour through the Galaxy interface is provided as well as a tour to learn Hi-C data analysis. The tour content is available on the Galaxy Training Network (http://dx.doi.org/10.1101/225680) as well and includes example

Nucleic Acids Research, 2018, Vol. 46, Web Server issue ***W15***

data hosted on Zenodo. All intermediate files are available in the shared data library of the Galaxy HiCExplorer.

For advanced users a detailed step-by-step tutorial for the analysis of Hi-C data from mouse embryonic stem-cells, as well as a comprehensive API documentation, is hosted at https://hicexplorer.readthedocs.org. The how-to describes how to set up the mapping of the reads. It suggests parameter settings for the creation of Hi-C contact matrices and describes the process of merging and threshold determination to remove poor bins prior to correction. The determination of TADs using the separation score is described in detail, including examples on visualization.

DISCUSSION

Galaxy HiCExplorer gives researchers the opportunity to run their Hi-C data analysis in a user-friendly, web browser based environment. The highly configurable framework provided by Galaxy makes this web server extendable to the various needs of researchers. Especially in conjunction with software for other high-throughput analysis protocols like RNA-seq or ChIP-seq, Galaxy HiCExplorer serves as a powerful basis for flexible explorative biomedical research in a high-throughput sequencing data analysis environment.

By combining all the necessary stages of pre-processing and visualization into a single tool, analysis not only becomes easier, but faster, highly reproducible, and more readily exchangeable. Biomedical researchers can focus their efforts on their data analysis without having to concern themselves with the particulars of managing various different software setups and configurations or learning to use command-line tools in an UNIX environment.

ACKNOWLEDGEMENTS

We thank the bioinformatics group at the University of Freiburg and the bioinformatics unit at the Max Planck Institute of Immunobiology and Epigenetics Freiburg.

FUNDING

German Research Foundation for the Collaborative Research Centre 992 Medical Epigenetics [SFB 992/1 2012 and SFB 992/2 2016 awarded to T.M. and R.B. and to Lutz Hein (in support of S.N. and R.G.) and for the DFG project GI 747/2-1 to R.G]; Federal Ministry of Education and Research through the German Epigenome Programme DEEP [01KU1216G awarded to T.M.]; German Federal Ministry of Education and Research [031 A538A de.NBI-RBC awarded to R.B.]; German Federal Ministry of Education and Research [031 L0101C de.NBI-epi awarded to B.G.]. Funding for open access charge: German Federal Ministry of Education and Research.
Conflict of interest statement. None declared.

REFERENCES

1. Lieberman-Aiden,E., Van Berkum,N.L., Williams,L., Imakaev,M., Ragoczy,T., Telling,A., Amit,I., Lajoie,B.R., Sabo,P.J., Dorschner,M.O. *et al.* (2009) Comprehensive mapping of long-range interactions reveals folding principles of the human genome. *Science*, **326**, 289–293.
2. Dixon,J.R., Selvaraj,S., Yue,F., Kim,A., Li,Y., Shen,Y., Hu,M., Liu,J.S. and Ren,B. (2012) Topological domains in mammalian genomes identified by analysis of chromatin interactions. *Nature*, **485**, 376–380.
3. Nora,E.P., Lajoie,B.R., Schulz,E.G., Giorgetti,L., Okamoto,I., Servant,N., Piolot,T., Van Berkum,N.L., Meisig,J., Sedat,J. *et al.* (2012) Spatial partitioning of the regulatory landscape of the X-inactivation centre. *Nature*, **485**, 381–385.
4. Rao,S.S.P., Huntley,M.H., Durand,N.C. and Stamenova,E.K. (2014) A 3D map of the human genome at kilobase resolution reveals principles of chromatin looping. *Cell*, **159**, 1665–1680.
5. Sanborn,A.L., Rao,S.S.P., Huang,S.-C., Durand,N.C., Huntley,M.H., Jewett,A.I., Bochkov,I.D., Chinnappan,D., Cutkosky,A., Li,J. *et al.* (2015) Chromatin extrusion explains key features of loop and domain formation in wild-type and engineered genomes. *Proc. Natl. Acad. Sci. U.S.A.*, **112**, E6456–E6465.
6. Bonev,B., Mendelson Cohen,N., Szabo,Q., Fritsch,L., Papadopoulos,G.L., Lubling,Y., Xu,X., Lv,X., Hugnot,J.P., Tanay,A. *et al.* (2017) Multiscale 3D genome rewiring during mouse neural development. *Cell*, **171**, 557–572.
7. Ron,G., Globerson,Y., Moran,D. and Kaplan,T. (2017) Promoter-enhancer interactions identified from Hi-C data using probabilistic models and hierarchical topological domains. *Nat. Commun.*, **8**, 2237.
8. Ramírez,F., Bhardwaj,V., Arrigoni,L., Lam,K.C., Grüning,B.A., Villaveces,J., Habermann,B., Akhtar,A. and Manke,T. (2018) High-resolution TADs reveal DNA sequences underlying genome organization in flies. *Nat. Commun.*, **9**, 189.
9. Babaei,S., Mahfouz,A., Hulsman,M., Lelieveldt,B.P., de Ridder,J. and Reinders,M. (2015) Hi-C chromatin interaction networks predict Co-expression in the mouse cortex. *PLoS Comput. Biol.*, **11**, e1004221.
10. Jiménez,R.C., Kuzak,M., Alhamdoosh,M., Barker,M., Batut,B., Borg,M., Capella-Gutierrez,S., Chue Hong,N., Cook,M., Corpas,M. *et al.* (2017) Four simple recommendations to encourage best practices in research software. *F1000Research*, **6**, 876.
11. Andrey,G., Schöpflin,R., Jerković,I., Heinrich,V., Ibrahim,D.M., Paliou,C., Hochradel,M., Timmermann,B., Haas,S., Vingron,M. *et al.* (2017) Characterization of hundreds of regulatory landscapes in developing limbs reveals two regimes of chromatin folding. *Genome Res.*, **27**, 223–233.
12. Ramírez,F., Lingg,T., Toscano,S., Lam,K.C., Georgiev,P., Chung,H.R., Lajoie,B.R., de Wit,E., Zhan,Y., de Laat,W. *et al.* (2015) High-affinity sites form an interaction network to facilitate spreading of the MSL complex across the X chromosome in Drosophila. *Mol. Cell*, **60**, 146–162.
13. Nothjunge,S., Nührenberg,T.G., Grüning,B.A., Doppler,S.A., Preissl,S., Schwaderer,M., Rommel,C., Krane,M., Hein,L. and Gilsbach,R. (2017) DNA methylation signatures follow preformed chromatin compartments in cardiac myocytes. *Nat. Commun.*, **8**, 1667.
14. Wingett,S., Ewels,P., Furlan-Magaril,M., Nagano,T., Schoenfelder,S., Fraser,P. and Andrews,S. (2015) HiCUP: pipeline for mapping and processing Hi-C data. *F1000Research*, **1310**, 1–12.
15. Heinz,S., Benner,C., Spann,N., Bertolino,E., Lin,Y.C., Laslo,P., Cheng,J.X., Murre,C., Singh,H. and Glass,C.K. (2010) Simple combinations of lineage-determining transcription factors prime cis-regulatory elements required for macrophage and B cell identities. *Mol. Cell*, **38**, 576–589.
16. Serra,F., Baù,D., Goodstadt,M., Castillo,D., Filion,G. and Marti-Renom,M.A. (2017) Automatic analysis and 3D-modelling of Hi-C data using TADbit reveals structural features of the fly chromatin colors. *PLoS Comput. Biol.*, **13**, e1005665.
17. Schmid,M.W., Grob,S. and Grossniklaus,U. (2015) HiCdat: A fast and easy-to-use Hi-C data analysis tool. *BMC Bioinformatics*, **16**, 277.
18. Forcato,M., Nicoletti,C., Pal,K., Livi,C.M., Ferrari,F. and Bicciato,S. (2017) Comparison of computational methods for Hi-C data analysis. *Nat. Methods*, **14**, 679–685.
19. Servant,N., Varoquaux,N., Lajoie,B.R., Viara,E., Chen,C.J., Vert,J.P., Heard,E., Dekker,J. and Barillot,E. (2015) HiC-Pro: An optimized and flexible pipeline for Hi-C data processing. *Genome Biology*, **16**, 259.

W16 Nucleic Acids Research, 2018, Vol. 46, Web Server issue

20. Durand,N.C., Shamim,M.S., Machol,I., Rao,S.S., Huntley,M.H., Lander,E.S. and Aiden,E.L. (2016) Juicer provides a One-Click system for analyzing Loop-Resolution Hi-C experiments. *Cell Syst.*, **3**, 95–98.
21. Durand,N.C., Robinson,J.T., Shamim,M.S., Machol,I., Mesirov,J.P., Lander,E.S. and Aiden,E.L. (2016) Juicebox provides a visualization system for Hi-C contact maps with unlimited zoom. *Cell Syst.*, **3**, 99–101.
22. Sauria,M.E., Phillips-Cremins,J.E., Corces,V.G. and Taylor,J. (2015) HiFive: A tool suite for easy and efficient HiC and 5C data analysis. *Genome Biol.*, **16**, 237.
23. Abdennur,N., Goloborodko,A., Imakaev,M. and Mirny,L. (2017) *mirnylab/cooler v0.7.6*. zenodo.org.
24. Dekker,J., Belmont,A.S., Guttman,M., Leshyk,V.O., Lis,J.T., Lomvardas,S., Mirny,L.A., O'Shea,C.C., Park,P.J., Ren,B. *et al.* (2017) The 4D nucleome project. *Nature*, **549**, 219–226.
25. Li,H. (2013) Aligning sequence reads, clone sequences and assembly contigs with BWA-MEM. *arxiv.org*, [arXiv:1303.3997].
26. Langmead,B. and Salzberg,S.L. (2012) Fast gapped-read alignment with Bowtie 2. *Nat. Methods*, **9**, 357–359.
27. Ramírez,F., Ryan,D.P., Grüning,B., Bhardwaj,V., Kilpert,F., Richter,A.S., Heyne,S., Dündar,F. and Manke,T. (2016) deepTools2: a next generation web server for deep-sequencing data analysis. *Nucleic Acids Res.*, **44**, W160–W165.
28. Ewels,P., Magnusson,M., Lundin,S. and Käller,M. (2016) MultiQC: summarize analysis results for multiple tools and samples in a single report. *Bioinformatics*, **32**, 3047–3048.
29. Imakaev,M., Fudenberg,G., McCord,R.P., Naumova,N., Goloborodko,A., Lajoie,B.R., Dekker,J. and Mirny,L.A. (2012) Iterative correction of Hi-C data reveals hallmarks of chromosome organization. *Nat. Methods*, **9**, 999–1003.
30. Stevens,T.J., Lando,D., Basu,S., Atkinson,L.P., Cao,Y., Lee,S.F., Leeb,M., Wohlfahrt,K.J., Boucher,W., O'Shaughnessy-Kirwan,A. *et al.* (2017) 3D structures of individual mammalian genomes studied by single-cell Hi-C. *Nature*, **544**, 59–64.
31. Dixon,J.R., Jung,I., Selvaraj,S., Shen,Y., Antosiewicz-Bourget,J.E., Lee,A.Y., Ye,Z., Kim,A., Rajagopal,N., Xie,W. *et al.* (2015) Chromatin architecture reorganization during stem cell differentiation. *Nature*, **518**, 331–336.
32. Afgan,E., Baker,D., van den Beek,M., Blankenberg,D., Bouvier,D., Čech,M., Chilton,J., Clements,D., Coraor,N., Eberhard,C. *et al.* (2016) The Galaxy platform for accessible, reproducible and collaborative biomedical analyses: 2016 update. *Nucleic Acids Res.*, **44**, W3–W10.
33. da Veiga Leprevost,F., Grüning,B.A., Alves Aflitos,S., Röst,H.L., Uszkoreit,J., Barsnes,H., Vaudel,M., Moreno,P., Gatto,L., Weber,J. *et al.* (2017) BioContainers: an open-source and community-driven framework for software standardization. *Bioinformatics*, **33**, 2580–2582.

A.3 Analysis of dosage compensation in flies via promoter-profiling

I contributed to the development of the MAPCap protocol by providing the analysis input, where all the experiments were performed by Giuseppe Semplicio. I developed the icetea bioconductor package and performed all the analysis presented in the paper, made the figures and wrote the manuscript with input from Giuseppe Semplicio.

Quantitative analysis of dosage compensation in flies using promoter profiling

Vivek Bhardwaj[1,2*], Giuseppe Semplicio[1,2*], Thomas Manke[1], Asifa Akhtar[1#]

[1]Max Planck Institute for Immunobiology and Epigenetics, 79108, Freiburg, Germany

[2]Faculty of Biology, University of Freiburg, 79104, Freiburg, Germany

*equal contribution

#corresponding author

akhtar@ie-freiburg.mpg.de

Phone: +49 (0)7615108565

Fax: +49 (0)7615108566

Abstract

Promoter architecture, shape and position of transcription start sites (TSS) play an important role in the regulation of eukaryotic gene expression. Promoter profiling methods like CAGE (Cap Analysis of Gene Expression) are widely used to detect transcription start sites and alternative promoter usage between tissues or during development. However, these methods are rarely used for differential expression analysis. In this study, we describe an approach to combine promoter profiling and differential expression analysis in a single setup, using a fast and simple protocol, MAPCap (Multiplexed Affinity Purification of Capped RNA) along with a new tool "icetea" (https://bioconductor.org/packages/icetea). icetea enables detection of TSS at high-resolution after UMI-based removal of PCR duplicates and detects differential gene expression and promoter usage using both internal and external normalization controls. Using MAPCap and icetea, we analyzed TSS expression in the brains of *Drosophila melanogaster* larvae, and observed the effects of knockout of MLE (male-less) helicase on X chromosome dosage compensation at promoters. Our results expand the scope of TSS profiling methods to differential expression analysis.

Introduction

Most genes in eukaryotes express multiple isoforms and transcript isoform expression is a major mechanism behind tissue-specific regulation of gene expression. Isoform diversity could be achieved by the usage of alternative exons, UTRs, transcript start and end sites. Recent analysis of Flies and Human genome has suggested that transcript start and end site selection is a major driver of alternative isoform usage across tissues [1]. Promoter profiling methods, such as CAGE [2], RAMPAGE [3], NanoCAGE [4] and GRO-cap [5] are widely to identify transcription start sites (TSSs), therefore making them useful for the detection of alternative isoform usage across tissues or developmental stages. A recent comparative analysis of six

such methods identifies CAGE as the overall best method [6] while RAMPAGE [3] comes close second. The amount of time and number of steps required per library was found to be highest for CAGE. RAMPAGE reduces the processing time (to 2 days) and the required input material (up to 5uG) therefore providing a suitable alternative. Despite this improvement, the CAGE methods have not gained wide usage besides the detection of new TSS and analysis of promoter architecture.

In this study, we developed a short and easy to perform 5' profiling method, termed as MAPCap (Multiplexed Affinity Purification of Capped RNA), which allows multiplexing of samples and produces paired-end reads. Synthetically designed random barcodes allow removal of PCR duplicates, and external spike-in controls allow accurate relative quantification of TSS expression changes. Further we developed an R/Bioconductor package **icetea** (Integrating Cap Enrichment and Transcript Expression Analysis) (https://bioconductor.org/packages/icetea), which allows easy processing and analysis of data obtained from protocols such as MAPCap and RAMPAGE. We performed MAPCap on brains isolated from 3rd instar Fly larvae and quantified the defect of dosage compensation upon knockout of male-less (MLE) gene on X chromosome at transcription start site resolution.

Results

MAPCap enriches Capped RNA from multiplexed samples

A new type of adapter oligo developed previously by our group (called the s-oligo) has dramatically increased the speed to perform transcriptome-wide RNA-protein interaction assays [7] . One main reason is the suppression of so-called "adapter-dimers" which can frequently occur in ligation-mediated clonings of RNA, a widely used approach in RNA library preparation, including promoter-profiling methods. The successful application of the s-oligo in CLIP experiments prompted us to develop a similar approach for promoter-profiling. MAPCap is a method that combines the power of the s-oligo with the easy handling of bead-based affinity purifications (Fig. 1A, see methods). This allows a for a fast and reproducible processing of even low RNA input amounts. Abundant RNA species such as sn- and snoRNAs are selectively

degraded by targeted antisense oligos and RNase H increasing the recovery of other capped RNA species. The s-oligo incorporates the sequences of both standard sequencing adapters which omits the usage of an RT-primer and allows for a highly efficient intramolecular ligation. The linear PCR amplification product creates a uniform library with ideal insert sizes of around 150 nt (Fig. S1A).

We performed MAPCap on stage 15 *Drosophila* embryos, in four replicates, and obtained ~10 Million reads per sample after de-multiplexing (Fig. S1B, see methods). For comparison, we analysed the CAGE data downloaded from modENCODE [8] and the RAMPAGE data [3] from embryos corresponding to the same stage. Reads obtained from both CAGE and RAMPAGE protocols show a high 'G' nucleotide bias due to the template-free activity of the reverse-transcriptase during cDNA preparation in RAMPAGE [9], and the design of the attached linkers in CAGE [10] . This demands post-mapping correction and sometimes affects the accuracy of TSS detection [11] . MAPCap, on the other hand, shows no such bias due to the use of s-oligo (Fig. 1B).

In order to evaluate the performance of MAPCap for TSS detection, we first performed TSS calling from MAPCap data using the paraclu method, and compared them to the TSS detected from CAGE and RAMPAGE data using the same method and filtering parameters (see methods). We then evaluated the TSS detection sensitivity, specificity, precision and F1-score between the methods, by comparing them to all annotated TSS present in the *Drosophila* ensembl annotation (release 76) as well as the RNA-Seq data obtained from modENCODE (see methods). CAGE performed the best amongst the three methods, as observed before [6], followed by RAMPAGE and MAPCap (Fig S1C).

We then correlated the depth-normalized counts on 5'-UTRs of known genes between MAPCap, CAGE, RAMPAGE and total RNA-Seq data from the same stage obtained from modENCODE project (see methods). We find that although MAPCap signal shows good correlation with other protocols, CAGE and RAMPAGE show better correlation with each other while MAPCap showed better correlation with RNA-Seq (Fig 1B-C, S1D). An independently performed MAPCap experiment with S2 cells shows the same relationship between the protocols, suggesting that MAPCap produces gene expression estimates closer to RNA-Seq compared to these protocols.

Figure 1

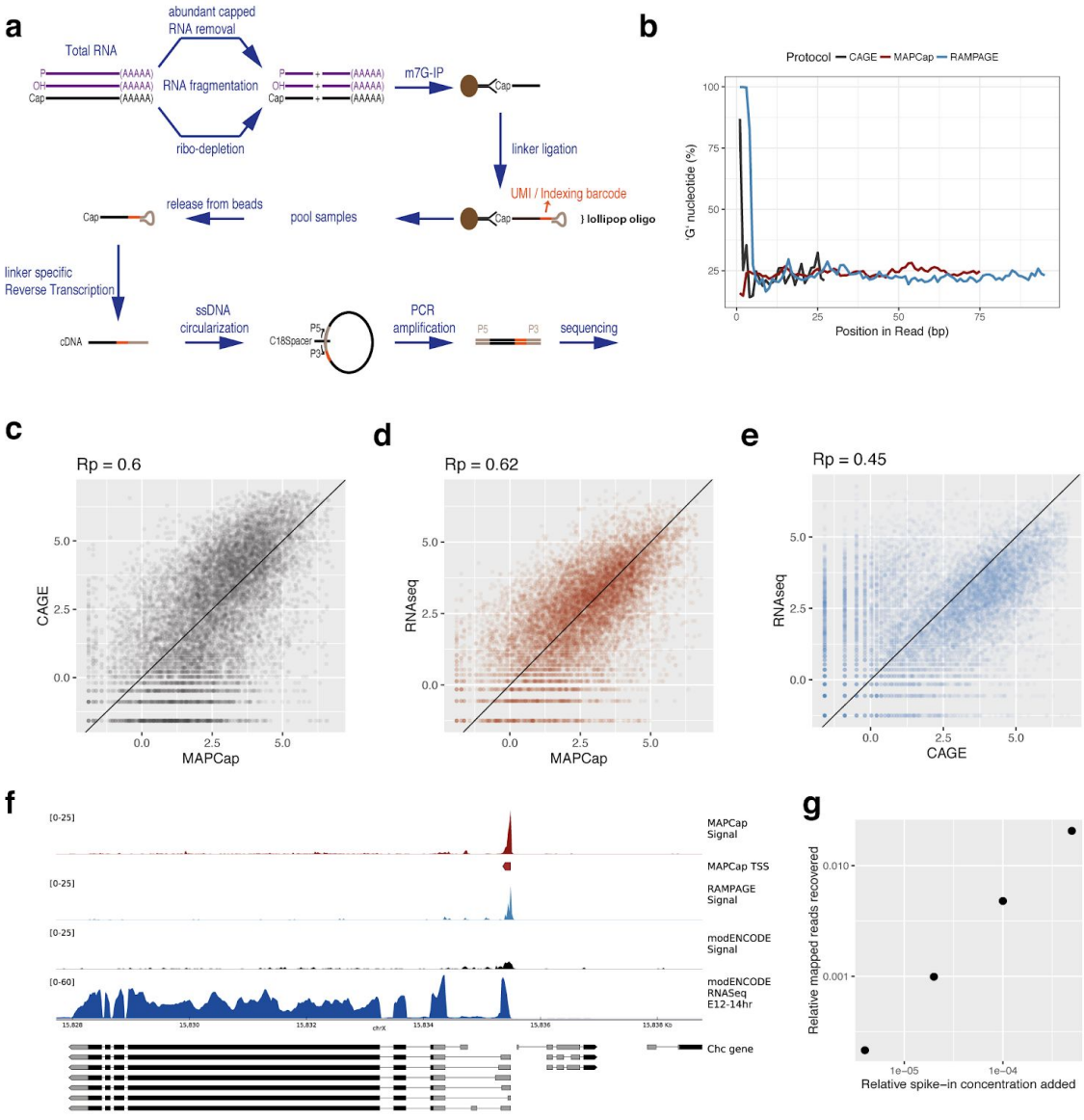

Fig 1. MAPCap protocol and its data quality. A. *Overview of the MAPCap protocol. After fragmentation and ribo-depletion, the Capped RNA is immunoprecipitated using an antibody, and the s-oligos are attached, afterwards the samples are pooled for PCR and library preparation steps.* ***B.*** *Nucleotide content in read positions. CAGE and RAMPAGE show a high*

artificial G-bias, due to their cloning steps, while MAPCap shows low bias for any specific nucleotide. ***C-E.*** *Correlation of MAPCap counts with CAGE, RNA-seq and the correlation of counts between CAGE and RNA-seq, on 3'UTR of genes. MAPCap shows better correlation with RNA-seq than CAGE.* ***F.*** *Genome track of the de-duplicated counts from MAPCap, RAMPAGE and CAGE on TSS. For MAPCap and RAMPAGE, the de-duplication was performed using 5'-position of the reads and the UMIs, while for CAGE it was performed using only 5'-position. RNA-seq track is shown for comparison.* ***G.*** *Added relative concentration (w.r.t. total RNA concentration) vs recovered relative counts (w.r.t total read counts) for the embryos. The samples were added with increasing relative concentration of ERCCs.*

The random barcodes present in lollipop oligos allow us to remove PCR duplicates, while preserving the transcript expression signal. Similar de-duplication can be performed for data obtained from the RAMPAGE protocol, where the oligos used as RT-PCR primers also serve as 'pseudo-random' barcodes [3]. A comparison of PCR duplicate removed signal from the three protocols show that both MAPCap and RAMPAGE protocols preserve the signal on the TSS, while de-duplication in absence of UMIs lead to near-complete loss of signal from the CAGE protocol (Fig. 1E).

Finally, we tested the sensitivity and relative quantification accuracy of MAPCap protocol for RNAs at different concentration by using external ERCC controls. We prepared spike-in mix containing 10 in-vitro capped ERCC spikes (see methods) in a 2-fold relative concentration ranging from 15.6 pM to 8 nM. We then mixed each replicate of the embryo sample with different concentrations of this spike-in mix (from 0.0004% to 0.05% of isolated RNA), before the beginning of the protocol. Processing of data shows that the relative concentration of spike-ins betweens sample can be faithfully recovered after sequencing (Fig. 1G). Relative ratio between individual spike-ins within each mix could also be accurately recovered (Fig. S1F), suggesting that MAPCap provides good sensitivity and accuracy to detect original transcript concentrations.

High resolution TSS detection and differential expression analysis using biological replicates

The ease of use and multiplexing ability of MAPCap protocol allows performing biological replicates without adding additional time and effort. We therefore sought to develop analysis methods which could benefit from biological replicates. Popularly used methods for TSS detection (parclu and distclu) are performed on within sample clustering of tags, and don't incorporate biological replicates to improve the performance of TSS detection. We developed a window-based TSS detection method that borrows ideas from window based peak calling methods developed for ChIP-Seq [12,13]. Reads counts are modelled using negative binomial distribution and the TSSs are detected as windows of enrichment in the genome, with respect to a local background (Fig. S2A, see methods). Consecutively enriched windows are then merged to detect both short and long TSSs. We compared peaks obtained from our method with those from paraclu method on the embryos to evaluate sensitivity and specificity. TSSs detected from the new method show higher sensitivity as well as specificity (Fig. 2a).

Apart from the accuracy of TSS detection, the shape of TSSs have also been shown to reflect biologically meaningful signal. Genes with sharp, focussed TSSs are mostly tissue specific and developmentally regulated, while the genes with long TSSs are shown to have housekeeping functions [14]. GO term enrichment analysis of the sharp and broad TSSs obtained from our method confirms previous results (see methods). Genes with sharp TSSs are enriched for processes like morphogenesis and development (Fig. 2B) while genes with broad TSSs are enriched for processes such as protein localization, metabolism and membrane organization (Fig. S2B), suggesting that the new method successfully detects biologically meaningful TSS shapes. Motif enrichment analysis of sharp and broad TSSs further confirm these results, with sharp TSSs being enriched for the Inr element, while broad TSS being enriched for core promoter motif M1BP and others (Fig. 2C, see methods).

Figure 2

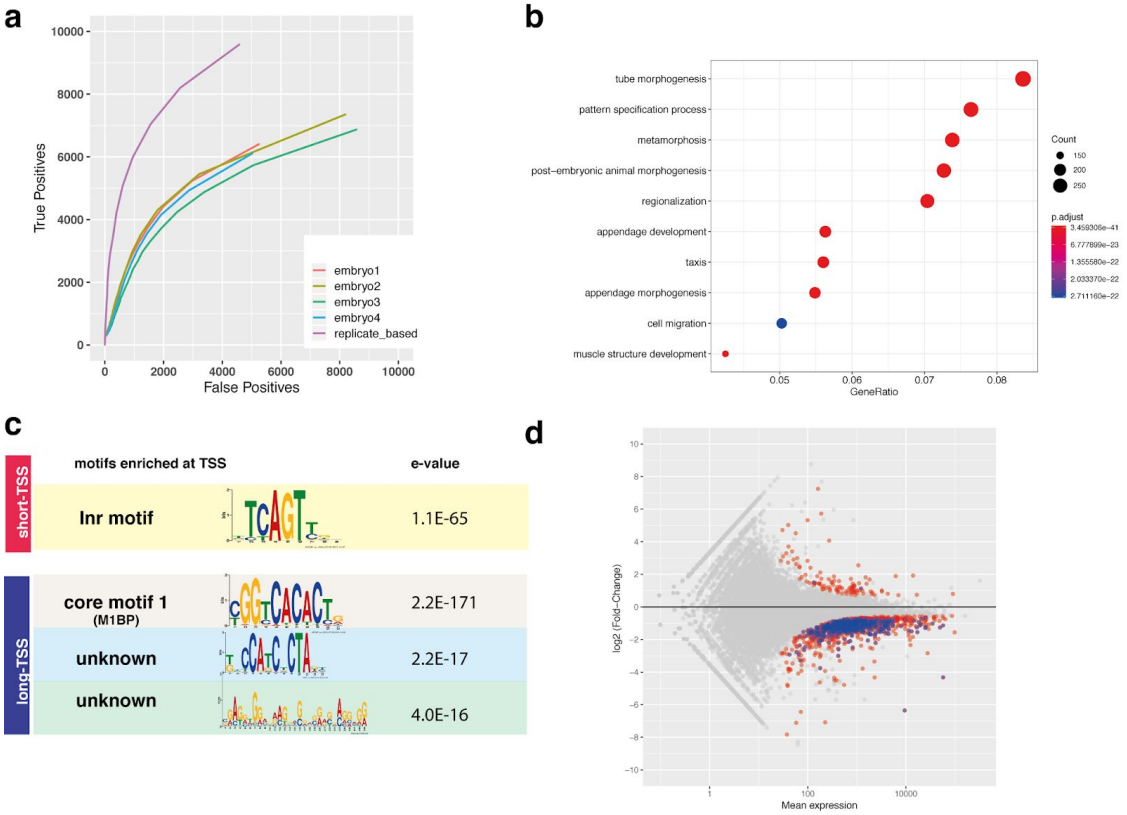

Fig 2. A replicate-based method of TSS detection. A. *ROC curve of MAPCap data on embryos, samples labelled embryo1 to 4 were processed using paraclu method and compared with the new method (replicate based) that uses all 4 samples as replicated for TSS detection. The detection accuracy improves using the new method.* ***B.*** *GO enrichment of "sharp" TSSs (<20bp) detected by the new method.* ***C.*** *Motif enrichment of the "sharp" (<20bp) and "broad" (>100bp) TSS detected by the method.* ***D.*** *Gene-level differential expression estimates obtained from MAPCap data in brains of MLE KO males. Differentially expressed TSSs on X-chromosome are highlighted in blue.*

Finally, we also sought to utilize the capped ERCC controls added to the protocol for the analysis of differential TSS usage between groups of samples. To this end, we performed MAPCap on RNA isolated from flies which are knock-outs of *maleless* (MLE) RNA helicase, and compared them with RNA from wild-type flies. The MLE helicase is an important component of the MSL complex which recognizes roX RNAs on the X-chromosome and helps guide the MSL complex to the X, leading to 2-fold upregulation of the male X-chromosome. In absence of MLE,

we therefore expected X chromosome to be downregulated due to failure of dosage compensation. We adopted popularly used method of gene-level differential expression analysis to the MAPCap data and utilized the spike-ins for normalization (see methods). Results show that most genes in MLE KO were downregulated, and most of the downregulated genes were on X chromosome (Fig. 2D). In absence of spike-in normalization, however, we saw more balanced number of up and down-regulated genes, where a bias towards the X-chromosome was not clearly visible (Fig. S2C), suggesting that spike-in normalization provides more useful biological insights.

Effect of MLE KO on dosage compensation of male promoters

After confirming the validity of our experimental and analysis method, we applied MAPCap on total RNA isolated from brains of male and female *Drosophila melanogaster* larvae of both wild-type and MLE KO background (see methods). We then deployed a pipeline that performs de-multiplexing, mapping, de-duplication, TSS detection and annotation of the TSS (Fig. S3A-B). We detected TSSs using our new method, using a fold-change threshold of 4x over the background, followed by comprehensive functional annotation of the detected TSS (see methods). While most of the detected TSS originated from previously annotated TSSs, X% of detected TSS in all samples came from promoter-proximal or intergenic enhancers (Fig 3A).

We then compared the MLE KO and wild-type genotypes in both male and female brains in order to detect differential promoter usage after spike-in normalization. Comparison of wild-type male and female brains showed that most promoters are equally utilized between sexes (Fig. S3C). Similar to our gene-level differential expression analysis, our differential promoter usage analysis revealed a significant downregulation of TSS from X-chromosome in KO males (Fig. 3B), while the females showed almost no effect in promoter usage (Fig. S3D).

Figure 3

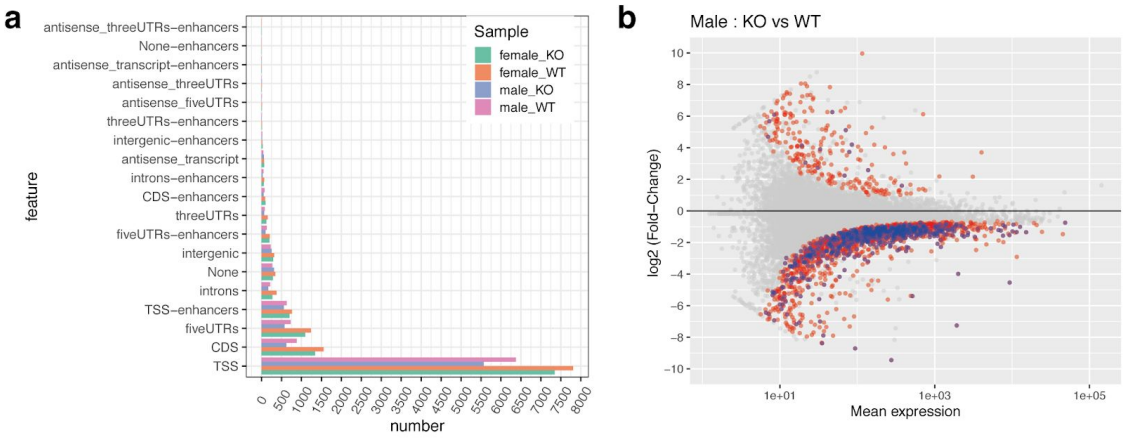

Fig 3. Assessment of promoter usage in the male and female fly brains. A. *Annotation of detected TSS into different functional categories. Both wild-type and KO samples show similar enrichment of TSS in each category.* ***B.*** *Differential TSS (promoter usage) in male KO, compared to wild-type. Differentially expressed TSSs from X-chromosome are highlighted in blue.*

icetea simplifies TSS detection and expression analysis from promoter profiling data

We implemented the processing and analysis methods described in this manuscript in an easy to use R package **icetea** (Integrating Cap Enrichment with Transcript Expression Analysis). **Icetea** performs sample de-multiplexing, PCR de-duplication as well as employs the new TSS detection approach described previously that takes advantage of biological replicates (Fig. 4A) . Further functions for quality control (Fig. 4B-C) and quick annotation of detected TSS (Fig. 4D) are also implemented. Differential TSS expression analysis can be performed between group of samples, using either internal or external (spike-in) normalization, allowing accurate quantification of relative gene and isoform expression changes (Fig. 4E). **Icetea** is especially suitable for end-to-end analysis of paired-end 5' profiling techniques such as MAPCap and RAMPAGE, however it can easily be used for analysis of CAGE, GRO-Cap and other promoter profiling protocols. **icetea** is open source and available for use via Bioconductor (https://bioconductor.org/packages/icetea) and the source code is available on GitHub (https://github.com/vivekbhr/icetea).

Figure 4

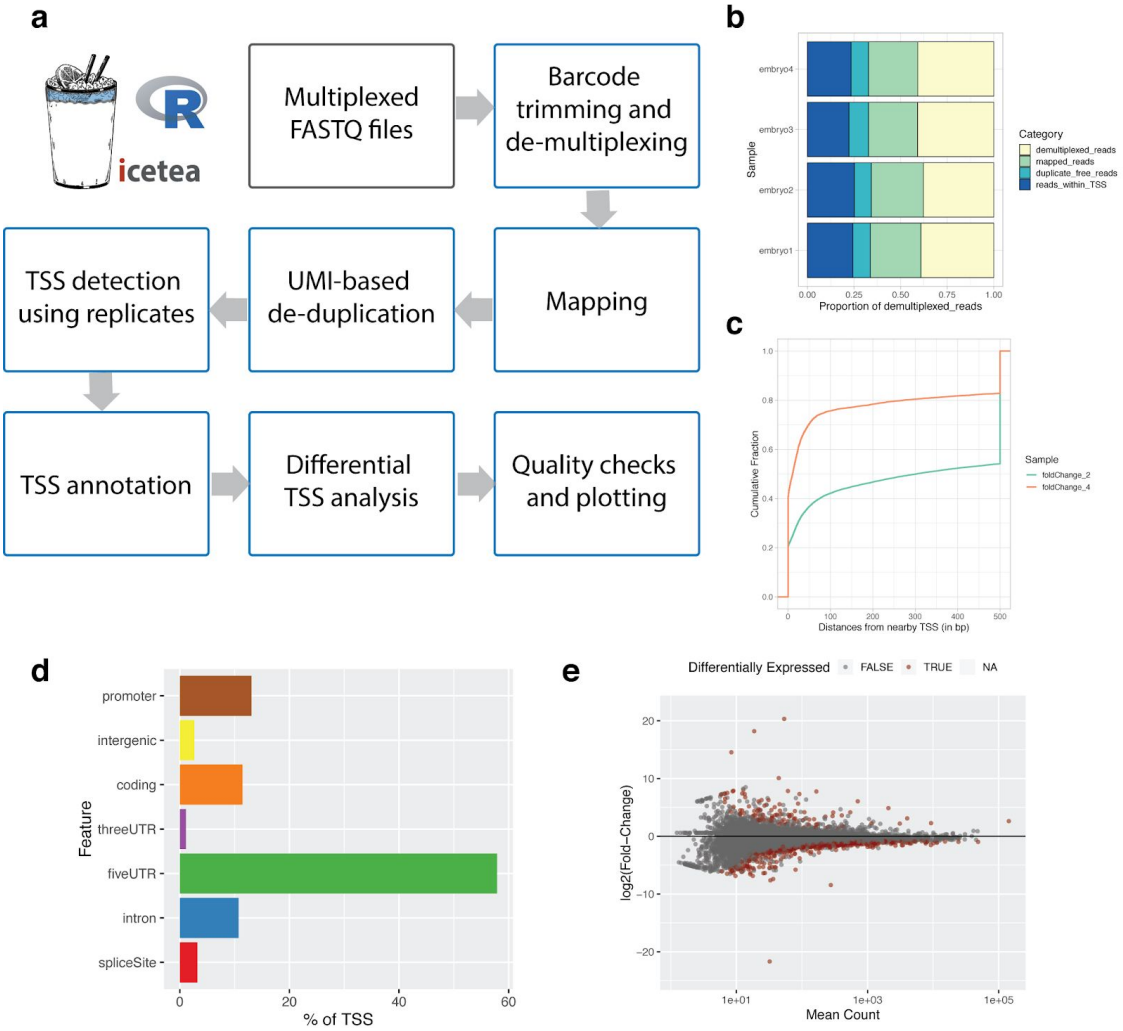

Fig 4. ***Description of the icetea bioconductor package for analysis of promoter-profiling data. A.*** *Steps of data analysis implemented in icetea. Read de-multiplexing and de-duplication based on UMI is supported for MAPCap and RAMPAGE data.* ***B-E.*** *Some examples of results obtained from icetea. B) Read mapping statstistics for embryo data (plotReadStats) C) TSS distance precision (distance of detected TSS to nearby annotated TSS) at different fold-change cutoffs on embryo data (plotTSSprecision) D) Annotation of detected TSS for male WT brains (annotateTSS). E) Differentially expressed TSS between male and female KO samples (detectDiffTSS).*

Discussion

In this study we introduce an easy to perform promoter profiling technique, along with a new analysis approach which simplifies the integration of TSS discovery and transcript expression analysis. The use of MAPCap protocol along with icetea analysis provides most benefits of CAGE and RNA-seq, at a fraction of total cost and time of performing both the protocols. Unlike CAGE or RAMPAGE which utilize protocol-specific optimization, MAPCap utilizes protocol-agnostic s-oligos, which, apart from promoter profiling, could also be used for iCLIP experiments [7], as well as for RNA-Seq, allowing for wider scope of integrative analysis. We propose that this approach would prove optimal for pilot projects of transcript discovery and gene expression analysis of newly assembled as well as annotated genomes.

Methods

Cells

S2 cells (gift from the butros lab, Heidelberg) were cultured in Express Five SFM media (Thermo Fisher) supplemented with 10% (v/v) Glutamax (Thermo Fisher). Cultures were maintained adherent or in shaking incubators at 27ºC at a speed of 80 rpm. Cells were kept at a density of 1-16 million/ml.

Generation of capped ERCC spikes

Ten spikes sequences were chosen from the ERCC spike mix, trimmed to ~500 bp length and ordered as gBlocks from IDT. At the 5' end we inserted a T7 class II promoter ϕ2.5, which has been shown to create more homogenous 5' ends transcription promoter sequence [15]. Spikes were in vitro transcribed using T7-FLASHScribe Transcription kit (CellScript) according to manufacturer's instructions and purified using MegaClear kit. In vitro capping was performed with Vaccinia capping system. Potentially uncapped RNAs were degraded by treatment of spikes with polyphosphatase and terminator. Samples were cleaned using OCC, concentrations

measured on Qubit. A master mix was created where each subsequent spike was added at half the concentration of the previous spike, starting from 8 fmol/ul.

MAPCap library preparation

RNA from S2 cells was extracted using the Quick RNA Kit (Zymo Research). RNA from dissected brains of embryos was isolated using the DirectZol Kit (Zymo Research). RNA was eluted in 25 ul of RNase-free water. The concentrations are adjusted and capped ERCC spikes and HEK polyA RNA were added at 0.05% of input amount. To remove abundant capped RNAs (snRNA, snoRNAs) as well as rRNA contamination, we added antisense DNA oligos (see table) targeting the RNA species detected from a preliminary MAPCap run. 8ul of oligo mix were added together with 4ul of 10x terminator buffer A (Epicentre). The RNA was heated to 70 ºC for 2min followed by an active cooling in the Thermomixer (Eppendorf) to 37 ºC. Upon reaching this temperature, 1ul of RNaseH (Life/Invitrogen) was added and incubated at 37 ºC for 30 min. The samples were then heated to 70 ºC for 2 min, put immediately on ice for 1 min and 1 ul of Terminator exonuclease was added for 1 hr at 30 ºC. RNA was purified using RNA clean and concentrator (Zymo Research) and eluted with 100ul TE buffer. The samples were fragmented using a Covaris E220 Ultrasonicator (200 cycles/burst, Duty cycle 5, 175 W, 10%) for 180 s per sample. Fragmented RNA was incubated with 2.5-5 ug of anti-m7G antibody (SYSY, cat no. 201001) pre-coupled to Protein G magnetic beads for 1 hour in IPP buffer (50 mM Tris-HCl pH 7.4, 150 mM NaCl, 0.1% NP-40) rotating at 4 ºC. Beads were washed three times with IPP and RNA 3' ends were dephosphorylated using PNK for 30 min at 37 ºC. Beads were washed and the s-oligo was ligated using T4 RNA Ligase 1 for 1 hr at 25 ºC. S-oligos contain barcode and random nucleotides in the following pattern NNNNNTTTTTTNN (N=random nucleotide; T=barcode nucleotide). Excess s-oligos were washed away with IPP buffer and samples were pooled together. After 30 min of treatment with rSAP at 30 ºC to dephosphorylate the s-oligo, the RNA was released from the beads using Proteinase K treatment and column purification (Oligo Clean and Concentrator (OCC), Zymo Research). Isolated RNA was reverse-transcribed using SuperScript III (Invitrogen) for 10 consecutive minutes at 42, 50, 55 and 65 ºC. After 30 min treatment with RNaseH the cDNA was column-purified using OCC and circularized with CircLigase2 for 2-16 hr. 1 ul of circularized cDNA was taken to determine the amplifications

cycles using qPCR. After PCR amplification the libraries were cleaned up twice using 1x Ampure beads (Beckman Coulter), quantified with Qubit (Thermo Fisher Scientific) and the quality was assessed on Bioanalyzer (Agilent). MAPCap libraries were sequenced on Illumina NextSeq 500, 3000 or HiSeq 2000.

Processing of MAPCap data

Paired-end FASTQ files were trimmed for adaptors using Trimmomatic [16] (v 0.3.7). Samples were de-multiplexed by icetea (v0.99, demultiplexFastq) using provided barcode information, and mapped to the dm6 genome using Rsubread [17] (v 1.22.3, mapping wrapper provided in icetea). For de-duplication, we consider all reads mapping to the same 5'-position and having the same random barcode as duplicates and only keep the first instance of each such alignment (using icetea - filterDuplicates). BigWigs were created using deepTools [18] (v3.0.2) bamCoverage and bamCompare, with the option `*--offSet 1 --binSize 1*`. Quality control was performed using deepTools and multiQC [19] (v1.3). Genomic regions were plotted using pyGenomeTracks [20] (v2.0). The full MAPCap data processing workflow (described in Fig. S3A) is available at : https://github.com/vivekbhr/cage_pipeline

Comparison with external methods

For evaluation of TSS detection accuracy, we used the *paraclu* method [21] to cluster CAGE tags from CAGE, RAMPAGE and MAPCap data. We used the 12-14hr Sample from modENCODE, and merged the 12, 13 and 14hr samples from RAMPAGE to compare with merged (embryo 1-4) samples from MAPCap data. All samples were then downsampled to 10 million reads and paraclu was run with the parameters : *min_value = 1, min_density_rise = 1, min_pos_with_data = 1, min_sum = 1, min_width = 3, max_width = 300* (i.e. all criteria such as minimum reads used for clustering and minimum density of reads per cluster etc. were kept to the lowest, and tag clusters of length 3 to 300 bp were considered for analysis).

The "density score" provided by paraclu for each tag cluster was used to calculate precision and sensitivity. Scores between 10 and 500 were plotted for ROC curve. For the evaluation of true and false positives, we used the RNA-seq data of 12-14 hr embryo from modENCODE and

calculated transcript-level TPMs using Salmon [22]. Transcripts with TPM > 1.0 were considered "expressed" and the TSSs of expressed transcripts which were not detected by the promoter-profiling methods considered "false negatives". TSSs detected by the methods which did not overlap with a known TSS in dm6 (ensembl-79) annotation were considered "false positives".

For comparison between replicate-based and paraclu method, we ran paraclu on samples with same criteria, while for our new method we obtained TSSs using a 2-fold local background cutoff. The score per TSS (mean fold-change across enriched windows) was used to evaluate the true and false positives for the analysis. Since the range of scores obtained per TSS is very different between paraclu and our method, there is no comparable cutoff for comparison of precision and sensitivity.

TSS detection and differential TSS usage analysis using replicates

For the detection of transcription start sites using replicates, we first count the 5'-end of reads in 10 bp sliding windows (w) across the genome for all samples (with a slide of 5 bp). For each window, we also calculate all 5'-ends of the reads falling into the corresponding 2 kb background region (b) centered at the window. Counting is done in a strand-specific way, using the *intersectionStrict* mode. We then calculate the fold change (delta) of each window with respect to the background as :

$$\delta = Avg(\hat{\omega}) / Avg(\hat{b})$$

Where $Avg(\hat{\omega})$ and $Avg(\hat{b})$ are average logCPM values across replicates, obtained by a fitting single group negative binomial glm :

$$\hat{Y}wi \sim NB(Mi\rho wj, \phi w)$$

implemented in *mglmOnegroup* function of the edgeR package [23].

For differential TSS usage analysis, strand-specific counting is performed in the same way, on the union of TSSs detected across samples. Library sizes were normalized using the size factors obtained from ERCC counts using median of ratios method from DESeq2. The differential expression analysis was then performed in DESeq2 using *nbinomWaldTest* function.

TSSs with and adjusted p < 0.05 were considered significantly different between tissues and sexes.

To perform differential gene expression analysis from MAPCap data, we summed the counts obtained from all 3'UTRs of a gene into one, and performed the normalization and differential expression using DESeq2. Spike-in normalization was performed the same way as above.

TSS annotation

For a comprehensive annotation of our detected TSSs, we first created a mutually exclusive set of annotations from dm6 (ensembl-79) GTF file, by first separating genic from intergenic regions , followed by ranking them in this order (5'UTR > CDS > 3'UTR > Introns; and sense > antisense). Further the features were re-annotated by overlapping them with enhancers [24] and repeats (RepBase release 20140131). The annotation pipeline is available as part of the full MAPCap data processing pipeline at : https://github.com/maxplanck-ie/cage_pipeline

Evaluation of promoter width

To evaluate the promoter width distribution obtained from icetea analysis, we divided our 12921 detected TSS into "broad" and "sharp" categories, by taking arbitrary cutoffs : >50 bp (8.1%) and <20 bp (36%), respectively. We performed GO enrichment analysis of the two categories for biological processes (BP) terms and plotted them using the *clusterProfiler* bioconductor package [25] (p < 0.01, q < 0.05). Further we, extracted the FASTA sequences associated with the two categories from the dm6 genome using the *BSgenome* package and performed de-novo motif enrichment via *meme* [26]. We sampled 10000 3'UTR sequences (100 bp regions) and used them as control for the motif enrichment. *Meme* was then run with the parameters: *-mod zoops -nmotifs 3 -minw 6 -maxw 30 -dna -revcomp*

Acknowledgements

The authors acknowledge the deep-sequencing unit at MPI-IE for data production. AA and TM acknowledge funding from the German Science Foundation (CRC992 "Medical Epigenetics").

Author Contributions

VB performed the analysis of data with input from GS, developed the icetea bioconductor package, and wrote the manuscript with input from all authors. GS developed the MAPCap protocol with analysis input from VB and performed all the experiments. GS and VB conceived the project with input from AA. TM and AA supervised VB and GS during the project.

Code availability

Icetea is available open source at https://github.com/vivekbhr/icetea. All the data presented in the manuscript has been processed via the cage analysis pipeline available at https://github.com/vivekbhr/cage_pipeline .

Conflict of interest

The authors declare no conflict of interest.

References

1. Reyes A, Huber W. Alternative start and termination sites of transcription drive most transcript isoform differences across human tissues. Nucleic Acids Res. 2018;46:582–92.

2. Kodzius R, Kojima M, Nishiyori H, Nakamura M, Fukuda S, Tagami M, et al. CAGE: cap analysis of gene expression. Nat Methods. 2006;3:211–22.

3. Batut P, Dobin A, Plessy C, Carninci P, Gingeras TR. High-fidelity promoter profiling reveals widespread alternative promoter usage and transposon-driven developmental gene expression. Genome Res. 2013;23:169–80.

4. Salimullah, Sakai M, Plessy C, Carninci P. NanoCAGE: A High-Resolution Technique to Discover and Interrogate Cell Transcriptomes. Cold Spring Harb Protoc. 2011;2011:db.erratum2011_01.

5. Core LJ, Martins AL, Danko CG, Waters CT, Siepel A, Lis JT. Analysis of nascent RNA identifies a unified architecture of initiation regions at mammalian promoters and enhancers. Nat Genet. 2014;46:1311–20.

6. Adiconis X, Haber AL, Simmons SK, Levy Moonshine A, Ji Z, Busby MA, et al. Comprehensive comparative analysis of 5'-end RNA-sequencing methods. Nat Methods [Internet]. 2018; Available from: http://dx.doi.org/10.1038/s41592-018-0014-2

7. Aktaş T, Avşar Ilık İ, Maticzka D, Bhardwaj V, Pessoa Rodrigues C, Mittler G, et al. DHX9 suppresses RNA processing defects originating from the Alu invasion of the human genome. Nature. 2017;544:115–9.

8. The modENCODE Consortium, Roy S, Ernst J, Kharchenko PV, Kheradpour P, Negre N, et al. Identification of Functional Elements and Regulatory Circuits by Drosophila modENCODE. Science. American Association for the Advancement of Science; 2010;330:1787–97.

9. Batut P, Gingeras TR. RAMPAGE: Promoter Activity Profiling by Paired-End Sequencing of 5′-Complete cDNAs. Current Protocols in Molecular Biology. John Wiley & Sons, Inc.; 2001.

10. Carninci P, Sandelin A, Lenhard B, Katayama S, Shimokawa K, Ponjavic J, et al. Genome-wide analysis of mammalian promoter architecture and evolution. Nat Genet. 2006;38:626–35.

11. Kawaji H, Lizio M, Itoh M, Kanamori-Katayama M, Kaiho A, Nishiyori-Sueki H, et al. Comparison of CAGE and RNA-seq transcriptome profiling using clonally amplified and single-molecule next-generation sequencing. Genome Res. 2014;24:708–17.

12. Zhang Y, Liu T, Meyer CA, Eeckhoute J, Johnson DS, Bernstein BE, et al. Model-based

analysis of ChIP-Seq (MACS). Genome Biol. 2008;9:R137.

13. Lun ATL, Smyth GK. csaw: a Bioconductor package for differential binding analysis of ChIP-seq data using sliding windows. Nucleic Acids Res. 2016;44:e45.

14. Lenhard B, Sandelin A, Carninci P. Metazoan promoters: emerging characteristics and insights into transcriptional regulation. Nat Rev Genet. 2012;13:233–45.

15. Huang F, He J, Zhang Y, Guo Y. Synthesis of biotin-AMP conjugate for 5' biotin labeling of RNA through one-step in vitro transcription. Nat Protoc. 2008;3:1848–61.

16. Bolger AM, Lohse M, Usadel B. Trimmomatic: a flexible trimmer for Illumina sequence data. Bioinformatics. 2014;30:2114–20.

17. Liao Y, Smyth GK, Shi W. The Subread aligner: fast, accurate and scalable read mapping by seed-and-vote. Nucleic Acids Res. 2013;41:e108.

18. Ramírez F, Ryan DP, Grüning B, Bhardwaj V, Kilpert F, Richter AS, et al. deepTools2: a next generation web server for deep-sequencing data analysis. Nucleic Acids Res. 2016;44:W160–5.

19. Ewels P, Magnusson M, Lundin S, Käller M. MultiQC: summarize analysis results for multiple tools and samples in a single report. Bioinformatics. 2016;32:3047–8.

20. Ramírez F, Bhardwaj V, Arrigoni L, Lam KC, Grüning BA, Villaveces J, et al. High-resolution TADs reveal DNA sequences underlying genome organization in flies. Nat Commun. 2018;9:189.

21. Frith MC, Valen E, Krogh A, Hayashizaki Y, Carninci P, Sandelin A. A code for transcription initiation in mammalian genomes. Genome Res. 2008;18:1–12.

22. Patro R, Duggal G, Love MI, Irizarry RA, Kingsford C. Salmon provides fast and bias-aware quantification of transcript expression. Nat Methods. 2017;14:417–9.

23. Robinson MD, McCarthy DJ, Smyth GK. edgeR: a Bioconductor package for differential expression analysis of digital gene expression data. Bioinformatics. 2010;26:139–40.

24. Kvon EZ, Kazmar T, Stampfel G, Yáñez-Cuna JO, Pagani M, Schernhuber K, et al. Genome-scale functional characterization of Drosophila developmental enhancers in vivo. Nature. 2014;512:91–5.

25. Yu G, Wang L-G, Han Y, He Q-Y. clusterProfiler: an R package for comparing biological themes among gene clusters. OMICS. 2012;16:284–7.

26. Bailey TL, Elkan C, Others. Fitting a mixture model by expectation maximization to discover motifs in bipolymers. Department of Computer Science and Engineering, University of California, San Diego; 1994; Available from: http://www.cs.toronto.edu/~brudno/csc2417_15/10.1.1.121.7056.pdf

Supplementary Figures

Figure S1

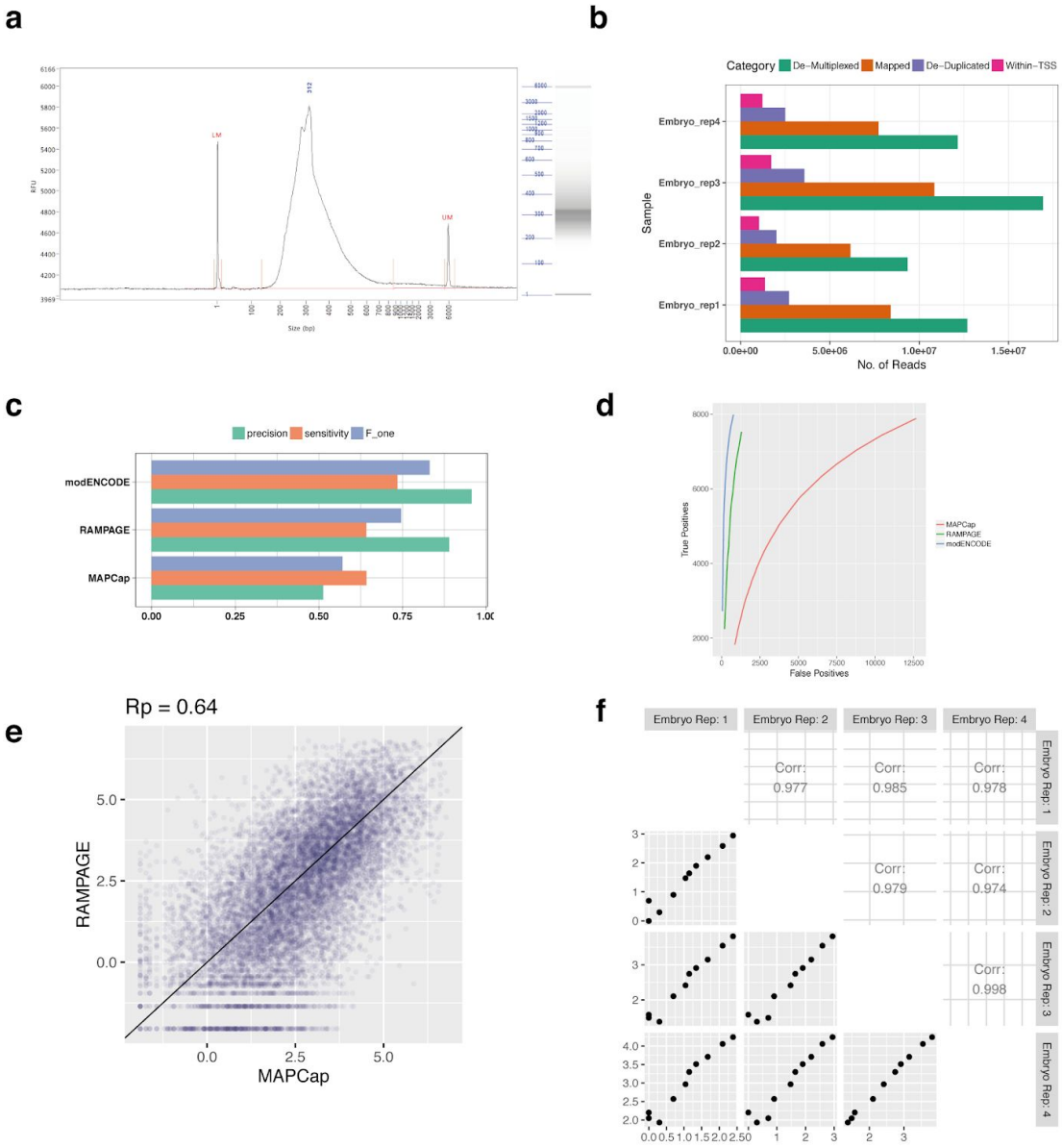

Fig. S1. Assessment of the MAPCap data quality. A. *BioAnalyzer profile of the MAPCap library.* ***B.*** *Number of reads kept at each step of MAPCap analysis, for the embryo samples.* ***C.***

Precision, Sensitivity and F1-score analysis of MAPCap and other protocols. ***D.*** *ROC curve of the MAPCap protocol compared to other protocols. TSS overlapping with those present in dm6 annotation and also expressed in modENCODE RNAseq data were considered true positives for these analysis.* ***E.*** *Same as Fig. 1C; correlation of depth-normalized read counts for MAPCap and RAMPAGE.* ***F.*** *Correlation of recovered counts of individual ERCC oligos between samples. Oligo mix was created after 2-fold serial dilution of individual oligos, which is also reflected in the data.*

Figure S2

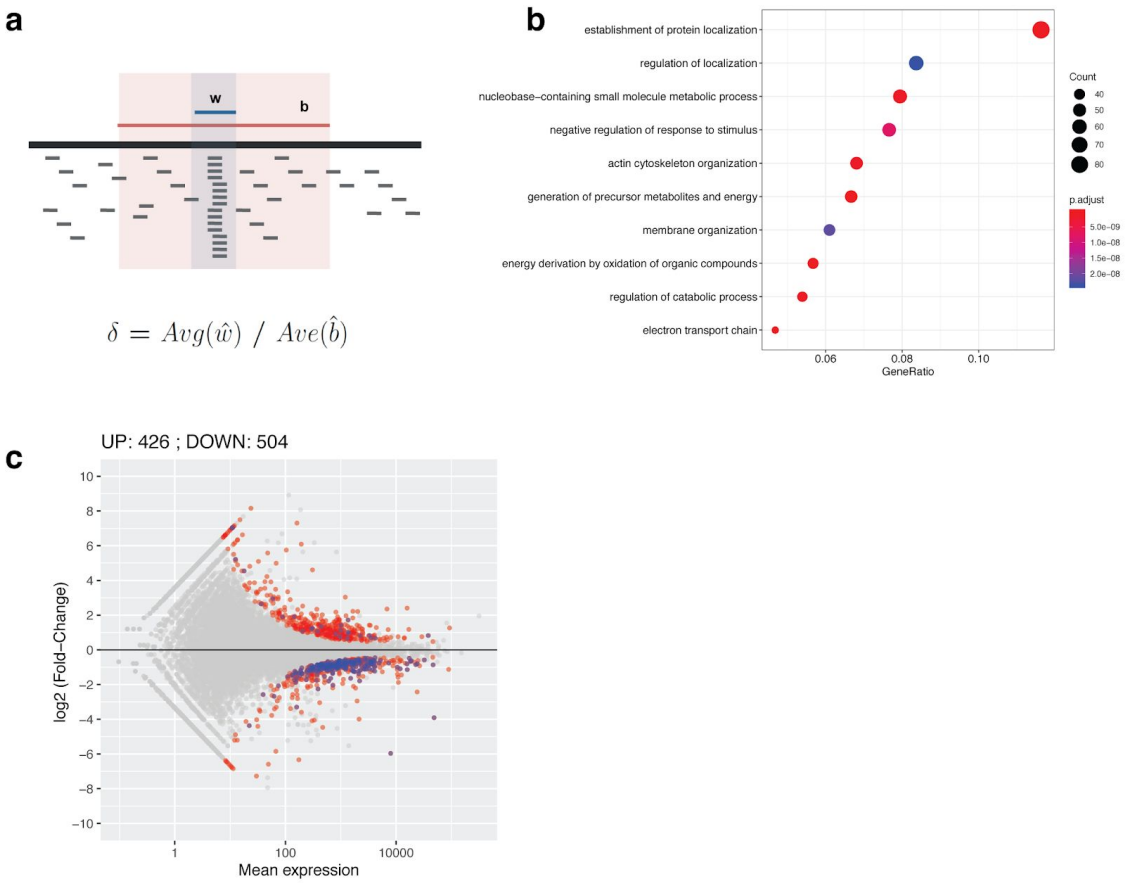

Fig S2. Evaluation of the new TSS detection and differential expression approach. A. *Schematic diagram of "local enrichment" method, the fold-change (**δ**) for windows (w) over background (b) is calculated as average fold change of replicates after depth-normalization.* ***B.*** *GO enrichment of "broad" (>100bp) TSS detected using our method shows enrichment of basic cellular functions.* ***C.*** *MA plot of gene-level differential expression estimates from MAPCap data using internal normalization.*

Figure S3

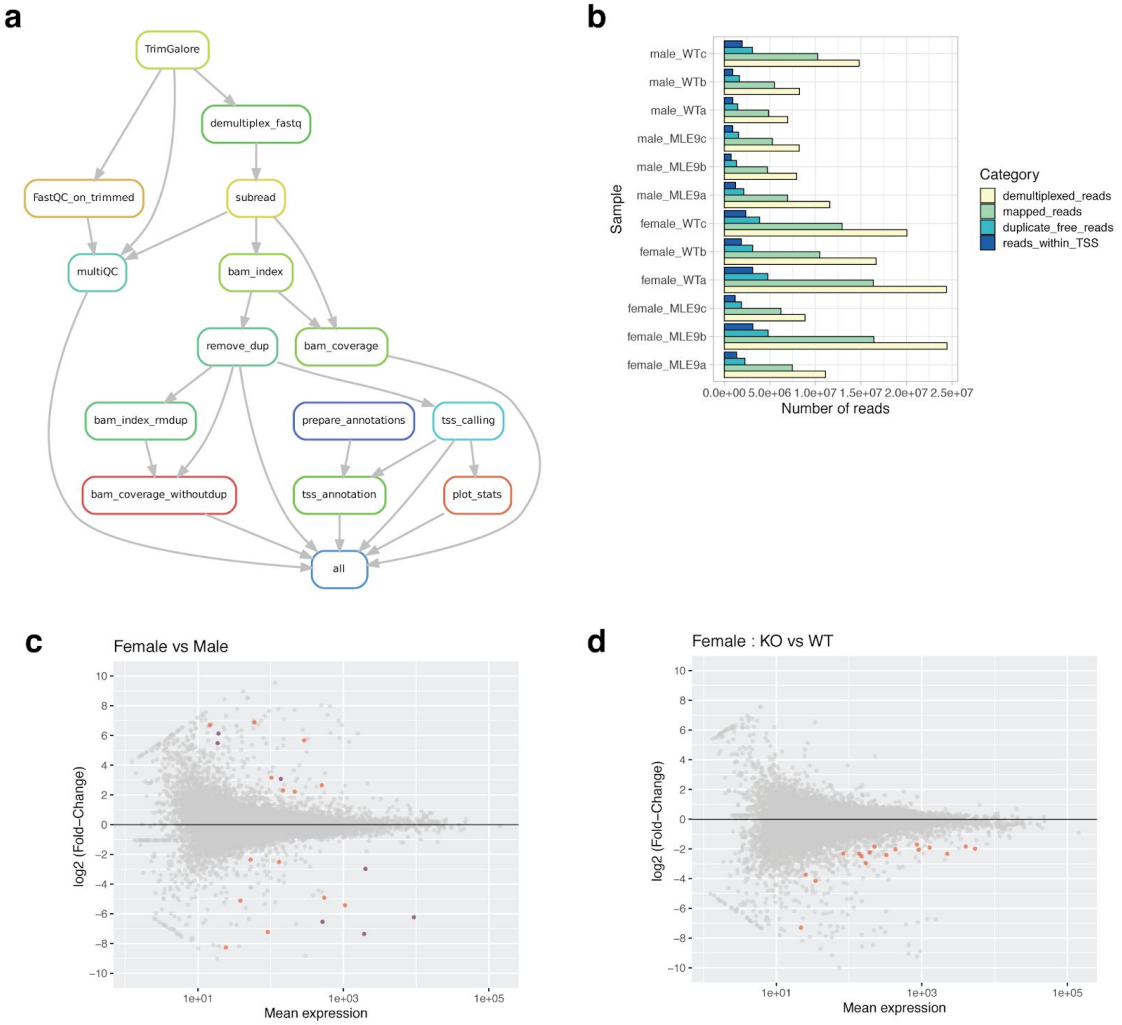

Fig S3. Analysis of dosage compensation defects in MLE KO flies. A. *Workflow used for the analysis of data. It involves read trimming, demultiplexing using sample barcodes, mapping, duplicate removal (using random barcodes), TSS detection, TSS annotation and generation of coverage files and plots (see methods).* ***B.*** *Number of reads kept at each step of the analysis.* ***C-D.*** *MA plot of differentially used promoters between wild-type male and female brains, and between MLE KO female brain over wild-type.*

Supplementary table 1. List of oligos used for abundant RNA depletion :

CCATAAGGCCGAGAAGCGAT
CCTCTACGCCAGGTAAGTAT
TATCGCCTCTGCGCAAAGAT
TATTGCCACTGCGCAAAGAT
TGATGATCCCCGACACTCGA
CAGTCTACCTCTACTAATGA
TGAAGCGGCGATCGAGACAT
ATCCTGTGAAGTATAGTCTT
AATTGAAGAGAAACCAGAGT
AGAGAATAAAAATTTTCAAT
ACCCAATCGTCACCTCTCGCA
CCAGGACGAGCACCCTTTTT
CTCCCCAAGACAAGGAAGGT
TACTCATTAGTTTGAGGCAC
TTCATCATATCATCTAGAGA
TGTTCTGCCGAAGCAAGAAC
GCTCTCCTTCCAAACAACAC
ATGTAATGTTCATCATGTCG

A.4 Interaction of MLE ortholog DHX9 with Alu elements in the human genome

I performed the analysis of UV-CLAP data for estimation of Alu enrichment (Extended data Fig. 2 and 3) and performed the RNA-seq analysis for detection of differential expression, splicing, circular RNAs and RNA editing (Fig. 2a, 2b, 3a, Extended Data Figure 6, 7, 10). I contributed to the writing and revision of the manuscript along with Tugce Aktas, Ibrahim Ilik, Asifa Akhtar and other authors.

LETTER

doi:10.1038/nature21715

DHX9 suppresses RNA processing defects originating from the *Alu* invasion of the human genome

Tuğçe Aktaş[1]*, İbrahim Avşar Ilık[1]*, Daniel Maticzka[2], Vivek Bhardwaj[1,3], Cecilia Pessoa Rodrigues[1,3], Gerhard Mittler[1], Thomas Manke[1], Rolf Backofen[2] & Asifa Akhtar[1]

Transposable elements are viewed as 'selfish genetic elements', yet they contribute to gene regulation and genome evolution in diverse ways[1]. More than half of the human genome consists of transposable elements[2]. *Alu* elements belong to the short interspersed nuclear element (SINE) family of repetitive elements, and with over 1 million insertions they make up more than 10% of the human genome[2]. Despite their abundance and the potential evolutionary advantages they confer, *Alu* elements can be mutagenic to the host as they can act as splice acceptors, inhibit translation of mRNAs and cause genomic instability[3]. *Alu* elements are the main targets of the RNA-editing enzyme ADAR[4] and the formation of *Alu* exons is suppressed by the nuclear ribonucleoprotein HNRNPC[5], but the broad effect of massive secondary structures formed by inverted-repeat *Alu* elements on RNA processing in the nucleus remains unknown. Here we show that DHX9, an abundant[6] nuclear RNA helicase[7], binds specifically to inverted-repeat *Alu* elements that are transcribed as parts of genes. Loss of DHX9 leads to an increase in the number of circular-RNA-producing genes and amount of circular RNAs, translational repression of reporters containing inverted-repeat *Alu* elements, and transcriptional rewiring (the creation of mostly nonsensical novel connections between exons) of susceptible loci. Biochemical purifications of DHX9 identify the interferon-inducible isoform of ADAR (p150), but not the constitutively expressed ADAR isoform (p110), as an RNA-independent interaction partner. Co-depletion of ADAR and DHX9 augments the double-stranded RNA accumulation defects, leading to increased circular RNA production, revealing a functional link between these two enzymes. Our work uncovers an evolutionarily conserved function of DHX9. We propose that it acts as a nuclear RNA resolvase that neutralizes the immediate threat posed by transposon insertions and allows these elements to evolve as tools for the post-transcriptional regulation of gene expression.

Mammalian cells react to excessive double-stranded RNA (dsRNA) as a sign of viral infection with an intricate system collectively called the dsRNA response[8]. ADAR[3], PKR[9], Staufen[10], as well as cytoplasmic RNA helicases MDA-5 and RIG-I[11], are known to be involved in suppression or activation of the dsRNA response. DHX9 has a unique domain organization that resembles ADAR and PKR (Extended Data Fig. 1a). Surprisingly, despite its essential nature in mouse and human cells[12,13] and abundance (>1 million copies per cell[6]), little is known about the role of DHX9 in cellular homeostasis. Thus, in order to shed light on the cellular function of DHX9, we first identified its *in vivo* targets by using a UV-crosslinking-based method (uvCLAP: UV crosslinking and affinity purification, Extended Data Fig. 1b, see Methods). Generation of a cell line that expresses DHX9 with a 3×Flag and HBH tag at its C terminus[14] allowed direct comparison with other RNA-binding proteins including QKI-5, QKI-6, KHDRBS1-3, HNRNPK and EIF4A1 (Fig. 1a and Extended Data Figs 1, 2). We observed that human/mouse DHX9 and its fly orthologue Maleless (Mle) interacts mainly with intronic RNA (Extended Data Fig. 2i). Closer inspection revealed that DHX9 peaks are significantly enriched on *Alu* SINEs (Fig. 1a): 60% of DHX9 peaks are on or within 100 nucleotides (nt) of *Alu* repeats; compared to 3–10% for controls (Fig. 1b, all P values $<2.2\times10^{-16}$, Fisher's exact test). Using another UV-crosslinking method (FLASH: fast ligation of RNA after some sort of affinity purification for high-throughput sequencing, see Methods) that can utilize antibodies against endogenously expressed proteins in addition to tagged constructs, we obtained virtually identical DHX9 profiles to those derived with the tagged protein using uvCLAP, confirming the robustness of our observations (Fig. 1a, also see Extended Data Fig. 2a–d). DHX9 peaks obtained by FLASH fall predominantly on *Alu* repeats (Fig. 1b and Extended Data Fig. 1d) and shuffling DHX9 FLASH peaks within introns significantly reduces the percentage of peaks that fall on *Alu* elements (Fig. 1b). Analysis of uvCLAP/FLASH peaks that do not fall directly on *Alu* elements shows that DHX9 peaks tend to be closer to *Alu* elements compared to peaks of other RNA-binding proteins (Fig. 1c and Extended Data Fig. 1c). Shuffling the DHX9 peaks randomly within introns abrogates this closeness to *Alu* elements (Fig. 1c and Extended Data Fig. 1c). Using two genome-mapping-free approaches we further verified that the *Alu* enrichment we score is specific to DHX9 (see Methods and Extended Data Fig. 2e–g).

As *Alu* elements are strictly primate specific-retrotransposons[15], we next tagged endogenous DHX9 with 3×Flag–Avitag[16] in mouse embryonic stem cells and carried out uvCLAP/FLASH experiments (Extended Data Figs 2h and 3a–c). In mice, DHX9 peaks fall predominantly on B1 SINEs (Extended Data Fig. 1f and 3d–f). DHX9 peaks that do not directly fall on B1 elements are close to them compared to shuffled controls (Extended Data Fig. 1g, h). Notably, both *Alu* elements and B1 elements evolved independently from the ancestral 7SL RNA[17] (Extended Data Fig. 1e). Similar to the human data, we used genome-mapping-free methods to verify the specificity of B1 enrichment in DHX9 data (Extended Data Fig. 3d, e).

The common denominator between *Alu*, B1 and roX RNAs (main targets of human, mouse and *Drosophila* DHX9) is their propensity to form structured RNAs[18,19] that can directly attract DHX9 activity. Notably, however, even a visual inspection of DHX9 binding reveals that not all *Alu* elements are DHX9 targets (Fig. 1a). In order to determine the rules of DHX9 binding, we used a genomic similarity search tool (YASS[20]) to look for *Alu* elements that can base pair with each other to form exceptionally long dsRNA (Extended Data Fig. 4a, b). We observed that *Alu* elements that are not targeted by DHX9 have a median distance of 1,482 nt ($n=173{,}653$) to their closest potential binding partner, whereas *Alu* elements that are targeted by DHX9 have a much shorter median distance of 458 nt ($n=13{,}663$) indicating that DHX9 specifically targets long dsRNA formed by base pairing *Alu* elements (Fig. 1d, two-tailed Mann–Whitney U-test, $P<2.2\times10^{-16}$;

[1]Max Planck Institute of Immunobiology and Epigenetics, Freiburg, Germany. [2]Institute for Informatics, Albert-Ludwigs-University, Freiburg, Germany. [3]Faculty of Biology, University of Freiburg, 79104 Freiburg, Germany.
*These authors contributed equally to this work.

RESEARCH LETTER

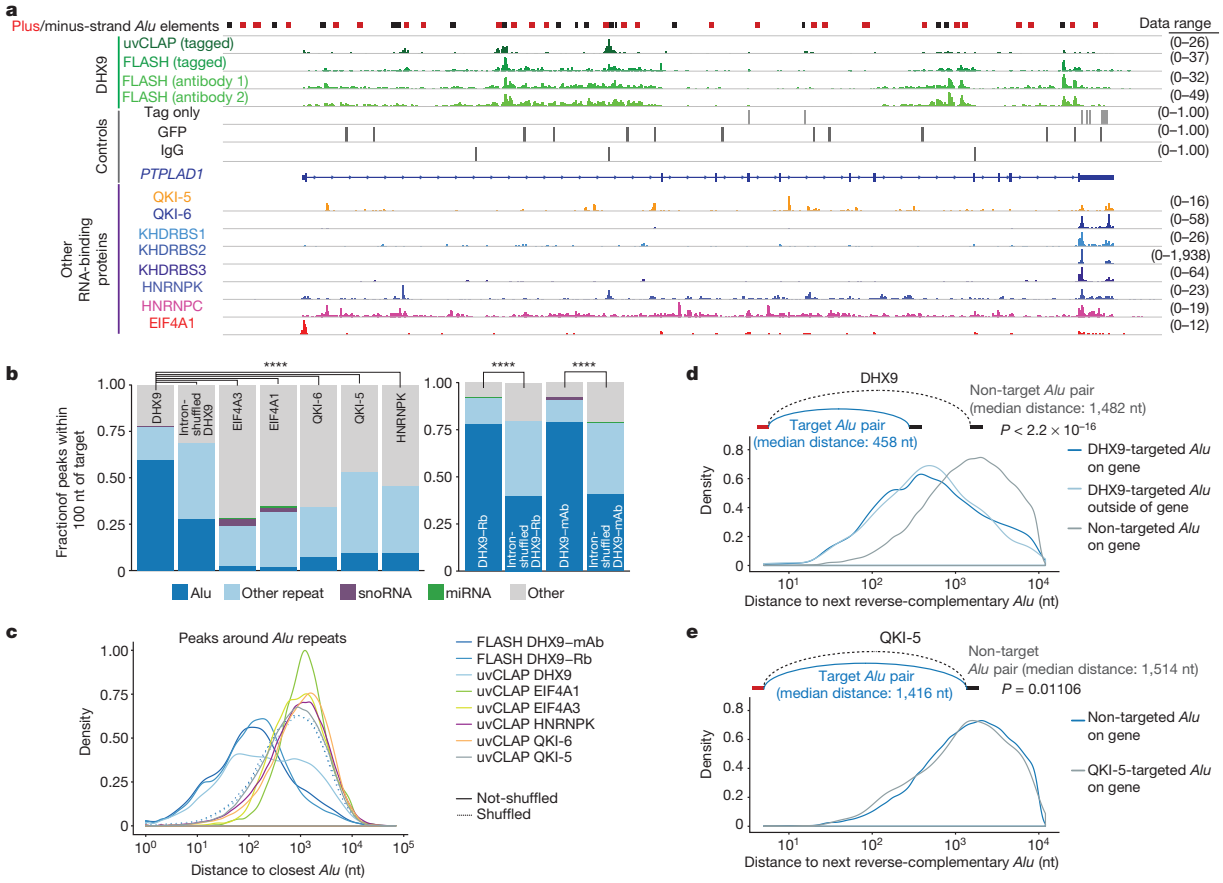

Figure 1 | uvCLAP and FLASH reveal DHX9 binding on *Alu* elements. **a**, IGV (Integrative Genomics Viewer) snapshot showing tagged (uvCLAP) and endogenous (FLASH) DHX9 binding on *Alu* elements of PTPLAD1. Additional tracks include control experiments and other RNA-binding proteins (tracks show merged biological duplicates). 'Data range' shows the coverage of uniquely mapped alignments for each profile. **b**, Enrichment of uvCLAP (left) and FLASH (right) peaks on *Alu* (all *P* values $<2.2 \times 10^{-16}$, Fisher's exact test) or other elements in humans. miRNA, microRNA; snoRNA, small nucleolar RNA. **c**, Distance of uvCLAP/FLASH peaks to the nearest *Alu* element. DHX9 peaks are closer to *Alu* elements, compared to shuffled peaks and other RNA-binding proteins (all *P* values $<2.2 \times 10^{-16}$, one-tailed Mann–Whitney *U*-test). **d**, **e**, Distance distributions of target, or non-target *Alu* pairs in DHX9 (**d**) or QKI-5 (**e**) uvCLAP peaks (*P* values calculated with two-tailed Mann–Whitney *U*-test, see Supplementary Table 3).

Extended Data Fig. 4c–h). DHX9 FLASH yields virtually identical results while other RNA-binding proteins appear to be agnostic to the positioning of *Alu* elements in and around their binding sites (Fig. 1e, Extended Data Fig. 4c–h and Supplementary Table 3).

Presence of *Alu* repeats and complementary sequences around exons correlate with circular RNA (circRNA) formation[21,22]. To determine whether DHX9 plays a role in this process, we first checked the abundance of previously reported circRNAs[23] using quantitative reverse-transcription PCR (RT–qPCR) in DHX9-depleted cells and observed a robust increase in circRNA levels (Extended Data Fig. 5a). Next, we generated sequencing libraries from poly(A)$^+$-depleted total RNA and indeed observed a clear, reproducible and global increase in the number of unique circRNAs in DHX9-depleted cells (Fig. 2a). In total, we detected 25,658 unique circRNAs in control short interfering RNA (siRNA)-treated samples and 50,355 in DHX9-siRNA-treated samples. DHX9-specific circRNAs contain significantly more *Alu* elements in flanking introns compared to control-specific circRNAs (90.65% in at least one flanking intron, 71.78% in both, $P < 2.2 \times 10^{-16}$, Fisher's exact test). Moreover, DHX9-depleted cells showed more than a fourfold increase in circRNA-producing genes compared to controls (Fig. 2b). We independently verified the upregulation and RNaseR insensitivity of the ten most upregulated circRNAs by RT–qPCR (Fig. 2c and Extended Data Fig. 5b).

In order to determine whether DHX9 has any effect on mRNAs that contain inverted-repeat *Alu* elements in their 3′ UTRs, we used a luciferase reporter system comparing constructs that have inverted-repeat-*Alu*-containing 3′ UTRs to *Alu*-free 3′ UTR constructs (Extended Data Fig. 5c, d). We observed a significant downregulation of luciferase activity for constructs that contain 3′ UTR inverted-repeat *Alu* elements upon *DHX9* depletion (Fig. 2d, Extended Data Fig. 5e–g). This effect could be rescued by overexpressing a wild-type DHX9 transgene but not a 'helicase-dead' mutant[24] (DHX9(GET)), suggesting that DHX9 resolves rather than passively coats inverted-repeat *Alu* elements, as previously suggested for Staufen proteins[25], in order to de-repress translation of mRNAs with inverted-repeat *Alu* elements in their 3′ UTRs (Fig. 2d, Extended Data Fig. 5c–g).

In addition to increasing circRNA formation, *Alu* elements can potentially disrupt normal RNA biogenesis by masking primary RNA sequences for splicing and transcript termination. Analysis of sequencing libraries prepared with poly(A)$^+$ RNA from DHX9-depleted cells revealed significant changes in the expression of 5,890 genes (Extended Data Fig. 6a–g). Further analysis showed 9,146 differentially spliced exons (at FDR-adjusted $P < 0.01$) affecting more than 4,400 genes in total (Extended Data Fig. 6e, f). Notably, CCL25, a cytokine that is almost exclusively expressed in the intestines and tissues involved in T-cell development[26] was among the most highly upregulated genes

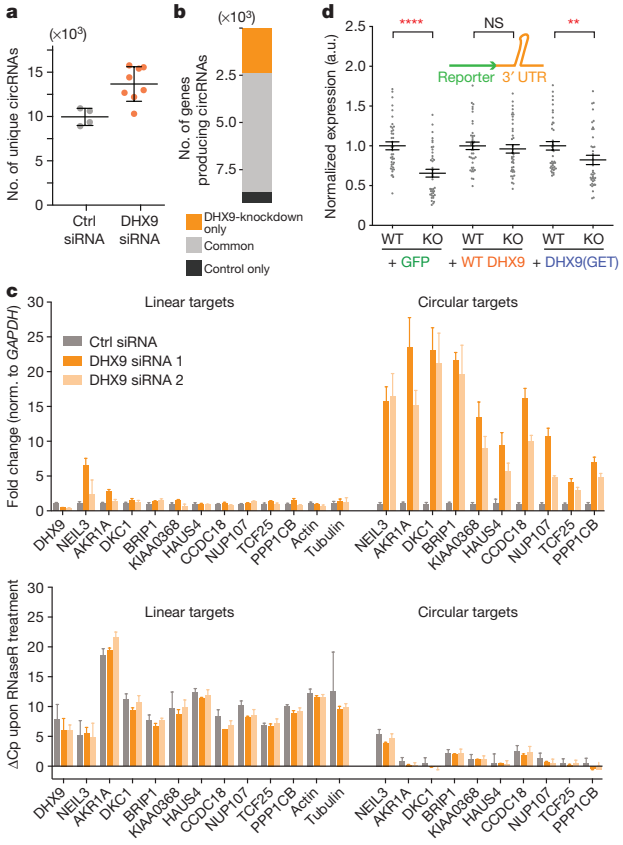

Figure 2 | Loss of DHX9 protein causes increased circular RNA generation and impaired translation. a, Number of unique circRNAs detected in control (grey) or DHX9-siRNA-treated samples (orange). Error bars represent s.d. of biological quadruplicates. **b**, Number of genes producing circRNA species. Orange, DHX9-knockdown-specific; black, control-specific; grey, common. **c**, Top, RT–qPCR assays quantifying changes in linear RNAs versus circRNAs. Bottom, sensitivity of linear/circRNA to RNaseR represented as the change in the value of crossing points (ΔCp). Error bars represent s.e.m. of four biological replicates. **d**, Luciferase assays show that DHX9 depletion significantly reduces expression of inverted-repeat-*Alu*-containing 3′ UTR elements, which can be alleviated with wild-type (WT) DHX9 overexpression and only partially with DHX9(GET). Mann–Whitney *U*-test was used to calculate *P* values. ****$P < 0.0001$; **$P = 0.0032$; wild-type DHX9, $P = 0.4278$. Error bars represent s.d. of two biological replicates.

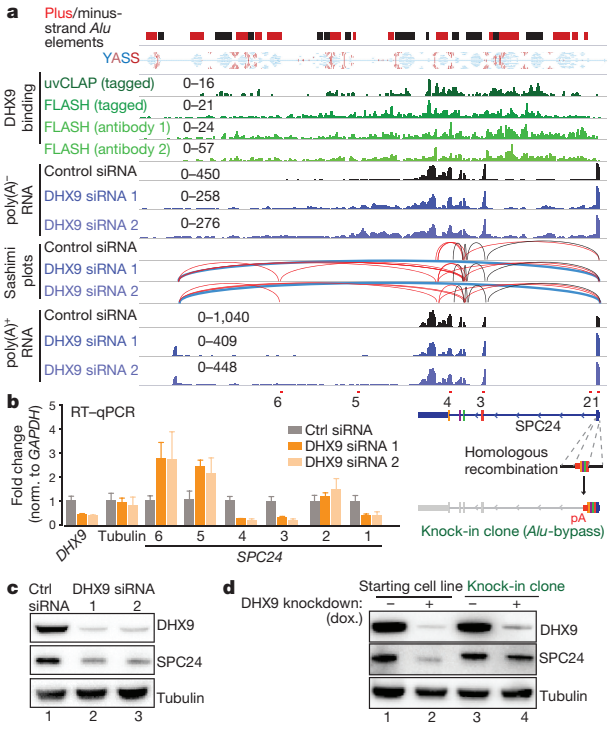

Figure 3 | Loss of DHX9 leads to RNA processing defects. a, IGV plots of DHX9-binding (green) and poly(A)$^+$/poly(A)$^-$ RNA sequencing (blue) data and Sashimi plots depicting exon–exon connectivities (red, non-canonical splicing events; blue, connection between the first and the newly emerging terminal exon of *SPC24*). For visual clarity, only the reads on the same strand as *SPC24* are depicted. Data range shows the coverage of uniquely mapped alignments for each profile. **b**, Left, RT–qPCR validation of *SPC24* reduction following DHX9 depletion (qPCR amplicons (1–6) are depicted in **a**, bottom). Error bars represent s.e.m. of biological quadruplicates. Right, schematic representation of the Alu-bypass allele. **c**, SPC24 levels in HeLa cells upon DHX9 knockdown with two independent siRNAs compared to control siRNA. **d**, SPC24 levels are shown before (lanes 1, 3) or after (lanes 2, 4) DHX9 depletion, in parental (left) or *Alu*-bypass (right) cell line. Representative of three experiments.

(Extended Data Fig. 6h). Closer inspection of this locus revealed that upregulation of *CCL25* is probably caused by a splicing/termination failure during the processing of an *ELAVL1* anti-sense transcript (*ELAVL1*^{AS}) that is bound by DHX9 *in vivo* (Extended Data Fig. 6i). Sashimi plots show that upon DHX9 depletion, the first exon of *ELAVL1*^{AS} is spliced to a cryptic splice-acceptor site in the first exon of *CCL25* (approximately 40 kb downstream of *ELAVL1*^{AS}), leading to around a 60-fold upregulation of *CCL25*. Similar defects were observed in other highly upregulated genes (see Extended Data Fig. 7a–d).

We next investigated the consequences of DHX9 depletion on cell morphology and observed the formation of giant cells containing numerous small, pleomorphic nuclei (Extended Data Fig. 8a–c, Supplementary Videos 1–7). Live cell imaging revealed that cells lose the ability to align their chromosomes at the metaphase plate and eventually disintegrate into small and large spherical pieces that rapidly fuse to form a large cell containing a variable number of small nuclei (as many as 23 nuclei per cell, Extended Data Fig. 8c; also compare Supplementary Video 2 with Supplementary Video 7). A similar phenotype has been reported by the MitoCheck consortium[27] under the 'Grape' category. Among the 153 Grape-phenotype-causing genes that were expressed in cells in our study, *SPC24* stands out as the most downregulated, and is one of four genes that has inverted *Alu* repeats at its 3′ UTR (Fig. 3a, b, left, and Extended Data Fig. 8d, left). Consistent with the chromosomal alignment defects, SPC24 is part of the Ndc80 complex, which acts as a tether between microtubules and chromosomes, forming an essential part of the kinetochore[28] (Extended Data Fig. 8d, right). Transcriptional reduction of *SPC24* also coincides with a reduction in its protein levels (Fig. 3c). Notably, both the 3′ UTR of *SPC24* and a downstream, *Alu*-rich intergenic domain are bound almost end-to-end by DHX9 (Fig. 3a). Similar to *CCL25*, Sashimi plots reveal that the first exon of *SPC24* is frequently spliced to a newly emerging exon around 15 kb downstream of the original terminal exon (blue lines in Fig. 3a). To rescue this defect, we created an '*Alu*-bypass allele' of *SPC24* by knocking-in a construct that contains the coding region of *SPC24* (amino acids 54–197), together with a polyadenylation site, immediately downstream of the first exon of *SCP24* that codes for the first 53 amino acids (Fig. 3b, right, and Extended Data Fig. 8e). Unlike the wild-type allele, the *Alu*-bypass allele is expressed independently of DHX9, indicating that the presence of *Alu* elements interferes with *SPC24* expression in the absence of DHX9 (Fig. 3d).

RESEARCH LETTER

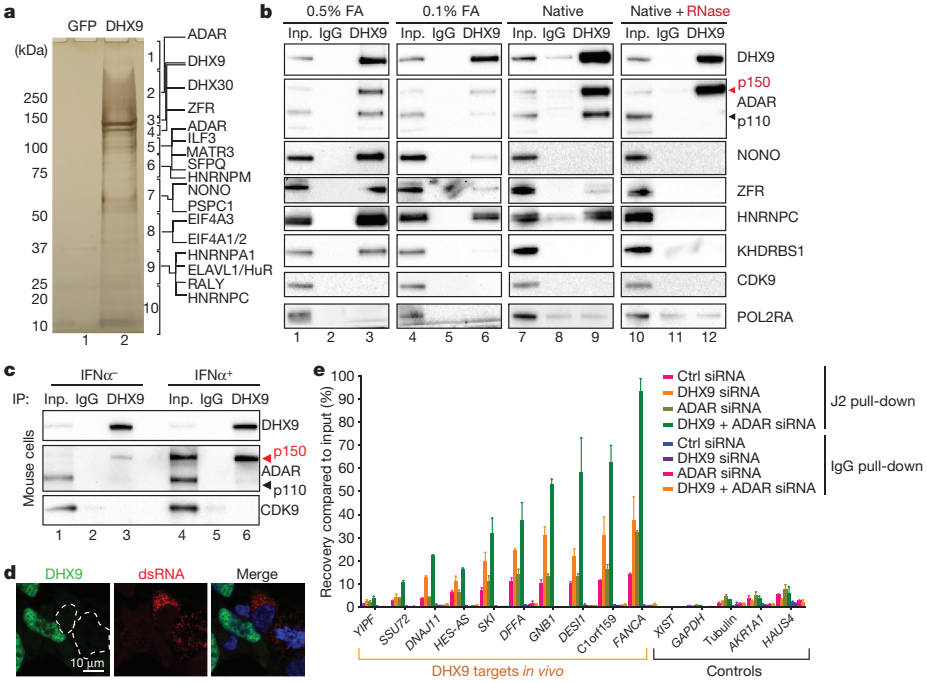

Figure 4 | RNA-independent interaction of ADAR^{p150} with DHX9 is conserved between mouse and human. a, Silver-stained gel image for the tandem-affinity purification experiment (see Extended Data Fig. 9a–c). **b**, Immunoprecipitation of the endogenous DHX9 protein using formaldehyde-crosslinked nuclei or native whole-cell lysates. Lanes 1, 4: inputs for 0.5%, 0.1% formaldehyde-crosslinked nuclei, respectively; lanes 7, 10: inputs for the native lysates without and with RNaseA treatment, respectively; lanes 2, 5, 8, and 11: IgG controls; lanes 3, 6, 9, 12: DHX9 immunoprecipitations. For gel source data, see Supplementary Fig. 1. **c**, Mouse DHX9 interacts with nuclear ADAR(p150) (lanes 3 and 6) (Also see Extended Data Fig. 9h–l). **d**, DHX9 depletion leads to accumulation of dsRNA (green, DHX9; red, dsRNA (J2); blue, DNA (Hoechst). Representative of two independent experiments. **e**, RIP–qPCR (RNA immunoprecipitation quantitative PCR) with J2 antibody. Error bars show s.d. of two independent experiments.

Next, we used a stringent, SILAC (stable isotope labelling with amino acids in cell culture)-based purification strategy to determine the DHX9 interactome in human cells (Fig. 4a, Extended Data Fig. 9a–f and Methods). We identified 80 reproducible DHX9 interactors showing at least tenfold enrichment over background, (Supplementary Table 1) of which approximately 94% (75/80) are classified as 'RNA-binding' (UniProt[29]). Purifications performed under native conditions with or without RNase treatment revealed that the majority of these interactions are RNA-bridged (Extended Data Fig. 9d–f and Fig. 4b). Notably, while we detected two major isoforms of ADAR (ADAR(p150) and ADAR(p110); interferon-inducible and constitutive isoforms of ADAR, respectively) co-immunoprecipitating with DHX9 under cross-linked and native conditions, only ADAR(p150)-interaction resisted RNase-treatment (Fig. 4b, lanes 9 and 12). We further verified this interaction by expressing Flag-tagged ADAR(p150) in HEK293 cells (Extended Data Fig. 9g). Despite the evolutionary divergence of SINEs, the DHX9–ADAR(p150) interaction is conserved in mice (Fig. 4c) and is most pronounced in the nucleus, even though ADAR(p150) is equally distributed between the nucleus and cytoplasm (Extended Data Fig. 9h–l).

Finally, we observed that DHX9-depletion leads to appearance of J2 mAb-positive speckles, indicative of accumulating dsRNA in cells (Fig. 4d and Extended Data Fig. 10a). RNA immunoprecipitation–qPCR experiments using the same antibody revealed that DHX9 depletion leads to a two- to threefold increase in J2-recovered DHX9 targets, while ADAR depletion has little effect (Fig. 4e). Surprisingly, although we did not observe major changes in RNA-editing upon DHX9 depletion (Extended Data Fig. 10c), co-depletion of DHX9 and ADAR led to an augmented phenotype in all target regions both in immunoprecipitated dsRNA (Fig. 4e) and circRNA production (Extended Data Figs 10b, d), suggesting a synergistic interaction.

In summary, DHX9 binds to independently evolved SINEs in humans and mice and interacts specifically with ADAR(p150), underscoring its role as a nuclear dsRNA resolvase both under normal conditions and probably during viral invasion. We propose that elevated levels of DHX9 as a potential pre-emptive measure against viral invasions can increase the tolerance of the host genome for a higher number of SINE insertions over the course of evolution which may enhance SINE/LINE-mediated genomic or transcriptomic innovation in evolutionarily complex organisms (Extended Data Fig. 10e).

Online Content Methods, along with any additional Extended Data display items and Source Data, are available in the online version of the paper; references unique to these sections appear only in the online paper.

Received 5 August 2016; accepted 23 February 2017.
Published online 29 March 2017.

1. Kazazian, H. H., Jr. Mobile elements: drivers of genome evolution. *Science* **303,** 1626–1632 (2004).
2. de Koning, A. P. J., Gu, W., Castoe, T. A., Batzer, M. A. & Pollock, D. D. Repetitive elements may comprise over two-thirds of the human genome. *PLoS Genet.* **7,** e1002384 (2011).
3. Elbarbary, R. A., Lucas, B. A. & Maquat, L. E. Retrotransposons as regulators of gene expression. *Science* **351,** aac7247 (2016).
4. Kim, D. D. Y. *et al.* Widespread RNA editing of embedded alu elements in the human transcriptome. *Genome Res.* **14,** 1719–1725 (2004).
5. Zarnack, K. *et al.* Direct competition between hnRNP C and U2AF65 protects the transcriptome from the exonization of Alu elements. *Cell* **152,** 453–466 (2013).
6. Hein, M. Y. *et al.* A human interactome in three quantitative dimensions organized by stoichiometries and abundances. *Cell* **163,** 712–723 (2015).

7. Koh, H. R., Xing, L., Kleiman, L. & Myong, S. Repetitive RNA unwinding by RNA helicase A facilitates RNA annealing. *Nucleic Acids Res.* **42,** 8556–8564 (2014).
8. Gantier, M. P. & Williams, B. R. G. The response of mammalian cells to double-stranded RNA. *Cytokine Growth Factor Rev.* **18,** 363–371 (2007).
9. Lemaire, P. A., Anderson, E., Lary, J. & Cole, J. L. Mechanism of PKR Activation by dsRNA. *J. Mol. Biol.* **381,** 351–360 (2008).
10. Elbarbary, R. A., Li, W., Tian, B. & Maquat, L. E. STAU1 binding 3′ UTR IR*Alu*s complements nuclear retention to protect cells from PKR-mediated translational shutdown. *Genes Dev.* **27,** 1495–1510 (2013).
11. Oshiumi, H., Kouwaki, T. & Seya, T. Accessory factors of cytoplasmic viral RNA sensors required for antiviral innate immune response. *Front. Immunol.* **7,** 200 (2016).
12. Lee, C. G. *et al.* RNA helicase A is essential for normal gastrulation. *Proc. Natl Acad. Sci. USA* **95,** 13709–13713 (1998).
13. Wang, T. *et al.* Identification and characterization of essential genes in the human genome. *Science* **350,** 1096–1101 (2015).
14. Tagwerker, C. *et al.* A tandem affinity tag for two-step purification under fully denaturing conditions: application in ubiquitin profiling and protein complex identification combined with *in vivo*cross-linking. *Mol. Cell. Proteomics* **5,** 737–748 (2006).
15. Batzer, M. A. & Deininger, P. L. Alu repeats and human genomic diversity. *Nat. Rev. Genet.* **3,** 370–379 (2002).
16. Kim, J., Cantor, A. B., Orkin, S. H. & Wang, J. Use of *in vivo* biotinylation to study protein-protein and protein-DNA interactions in mouse embryonic stem cells. *Nat. Protocols* **4,** 506–517 (2009).
17. Kramerov, D. A. & Vassetzky, N. S. Origin and evolution of SINEs in eukaryotic genomes. *Heredity* **107,** 487–495 (2011).
18. Ilik, I. A. *et al.* Tandem stem-loops in roX RNAs act together to mediate X chromosome dosage compensation in *Drosophila*. *Mol. Cell* **51,** 156–173 (2013).
19. Quinn, J. J. *et al.* Revealing long noncoding RNA architecture and functions using domain-specific chromatin isolation by RNA purification. *Nat. Biotechnol.* **32,** 933–940 (2014).
20. Noé, L. & Kucherov, G. YASS: enhancing the sensitivity of DNA similarity search. *Nucleic Acids Res.* **33,** W540–W543 (2005).
21. Jeck, W. R. *et al.* Circular RNAs are abundant, conserved, and associated with ALU repeats. *RNA* **19,** 141–157 (2013).
22. Zhang, X.-O. *et al.* Complementary sequence-mediated exon circularization. *Cell* **159,** 134–147 (2014).
23. Memczak, S. *et al.* Circular RNAs are a large class of animal RNAs with regulatory potency. *Nature* **495,** 333–338 (2013).
24. Lee, C. G., Chang, K. A., Kuroda, M. I. & Hurwitz, J. The NTPase/helicase activities of *Drosophila* maleless, an essential factor in dosage compensation. *EMBO J.* **16,** 2671–2681 (1997).
25. Ricci, E. P. *et al.* Staufen1 senses overall transcript secondary structure to regulate translation. *Nat. Struct. Mol. Biol.* **21,** 26–35 (2014).
26. Svensson, M. & Agace, W. W. Role of CCL25/CCR9 in immune homeostasis and disease. *Expert Rev. Clin. Immunol.* **2,** 759–773 (2006).
27. Neumann, B. *et al.* Phenotypic profiling of the human genome by time-lapse microscopy reveals cell division genes. *Nature* **464,** 721–727 (2010).
28. McCleland, M. L. *et al.* The highly conserved Ndc80 complex is required for kinetochore assembly, chromosome congression, and spindle checkpoint activity. *Genes Dev.* **17,** 101–114 (2003).
29. UniProt Consortium. UniProt: a hub for protein information. *Nucleic Acids Res.* **43,** D204–D212 (2015).

Supplementary Information is available in the online version of the paper.

Acknowledgements We thank members of the Akhtar laboratory especially B. Sheikh, C. Keller and K. Lam for critical reading of the manuscript and helpful discussions. We also thank N. Iovino and R. Sawarkar for critical reading of the manuscript. We also thank the members of the Deep Sequencing, Imaging, FACS and the Proteomics Facilities for their support. We acknowledge the support of the Freiburg Galaxy Team: B. Grüning and T. Houwaart, Bioinformatics, University of Freiburg. This work was supported by CRC 992/2 2016 awarded to A.A., T.M. and R.B., and CRC 746 and CRC 1140 awarded to A.A. R.B. is also funded by BA2168/11-1, SPP 1738 and CRC TRR 167.

Author Contributions T.A., I.A.I. and A.A. designed the experiments, T.A. and I.A.I. performed most of the experiments except live-cell imaging and mass-spectrometry, which were carried out by C.P.R. and G.M., respectively; I.A.I. and T.A. developed uvCLAP and FLASH methods with input from D.M., R.B. and A.A.; D.M. analysed uvCLAP and FLASH data and was supervised by R.B.; V.B. analysed the RNA-seq data, carried out repeat-enrichment and circRNA analysis and was supervised by T.M. and A.A.; I.A.I., T.A. and A.A. wrote the manuscript with input from D.M. and V.B.; R.B. and A.A. acquired funding; A.A. supervised all aspects of the study. All authors reviewed, edited and approved the paper.

Author Information Reprints and permissions information is available at www.nature.com/reprints. The authors declare competing financial interests: details are available in the online version of the paper. Readers are welcome to comment on the online version of the paper. Publisher's note: Springer Nature remains neutral with regard to jurisdictional claims in published maps and institutional affiliations. Correspondence and requests for materials should be addressed to A.A. (akhtar@ie-freiburg.mpg.de).

RESEARCH LETTER

METHODS

No statistical methods were used to predetermine sample size. $P < 0.01$ was considered statistically significant. The experiments were not randomized and the investigators were not blinded to allocation during experiments and outcome assessment.

Cell culture and generation of stable cell lines. HEK293FT (gift from the Jenuwein laboratory), HeLa (gift from the Ellenberg laboratory) and FLPin Trex HEK293 (Thermo Fisher Scientific, R78007) cells are maintained with DMEM-Glutamax supplemented with sodium pyruvate, glucose and 10% FBS. In addition to those supplements, FLPin Trex HEK293 cells were maintained in zeocin- and blasticidin-containing medium according to manufacturer's protocol and the zeocin selection is exchanged with hygromycin upon transgene transfection. All the transgenes were cloned into pCDNA5-FRT/To (Thermo Fisher Scientific catalogue no. V6520-20) with a C-terminal 3×Flag–HBH tag and were co-transfected with pOG44 plasmid with a 1:9 DNA concentration ratio. Cells were re-plated in different dilutions 24 h after transfection and 150 μg ml^{-1} hygromycin selection was initiated 48 h after transfection. Cell lines were maintained with blasticidin and hygromycin at all times and the transgenes were induced with either with 0.1 μg ml^{-1} (for uvCLAP) or 1.0 μg ml^{-1} (for purifications) doxycyclin.

CRISPR–Cas9 facilitated endogenous GFP tagging of the human DHX9 was performed in FLPinTrex HEK293 cell line carrying the inducible SPOP-GFP-nanobody[30]. The repair template was co-transfected in a 3:1 ratio with SpCas9 (pX459, Addgene no. 62988) vector carrying the guide RNA #1 (Extended Data Fig. 5d). Cells were selected 48 h after the initial selection with 1 μg ml^{-1} puromycin for 4 days total. Single-cell sorting into 96-well plates was carried out by gating for the cells with the strongest GFP signals (9.42% of all events). Colonies were expanded and screened for homozygously tagged DHX9 alleles using western blots. The knock-in of resistant allele at the *SPC24* locus was performed in a homozygously GFP-tagged DHX9 clone using same conditions as described above (see Supplementary Table 2 for the sequences of guide RNAs, repair templates and screening oligos).

Mouse ES cells were maintained with 15% FBS, 2,000 U ml^{-1} LIF, sodium pyruvate, NEAA, Glutamax and 0.1 nM β-mercaptoethanol supplemented into DMEM. CRISPR–Cas9 facilitated endogenous tagging of the mouse DHX9 was performed in a mouse ES cell line (WT26 male ES cell line was a gift from the Jenuwein laboratory) that we modified by adding a BirA ligase (plasmid provided by the Orkin laboratory[16]). Endogenous tagging was achieved by a co-transfection of ssODN (sequences of ssODN and screening oligos are listed in Supplementary Table 2) that provided the repair template with a 3×Flag–Avitag tag and the Cas9 plasmid that provided the guide RNA (based on pX459; Zhang laboratory) according to an earlier published protocol[31]. Initial screening of the clones was performed by PCR amplification flanking the tagged locus and scoring a size shift in PCR product. Positive clones from the first screen are then validated for the expression of Flag-tagged DHX9 protein (see Supplementary Table 2 for the sequences of guide RNAs, repair templates and screening oligos). ES cells were differentiated into NPCs as described previously[32]. FLP-in-3T3 cells were purchased from Thermo Fisher (R76107) and maintained in DMEM-Glutamax supplemented with sodium pyruvate, glucose and 10% FBS and zeocin according to the manufacturer's protocol. All cell lines are regularly checked for the absence of mycoplasma by PCR detection kit (Jena Bioscience PP-401).

uvCLAP. Stable cell line derived from FLPin Trex HEK293 cells are induced with 0.1 μg ml^{-1} doxycycline for ~16 h; as controls, cell lines expressing either the tag alone or eGFP with the same tag were used. Cells are rinsed with PBS and crosslinked with 0.15 mJ cm^{-2} UVC light. After crosslinking, cells are pelleted by centrifugation, snap-frozen in liquid nitrogen and kept at −80 °C until use. Cells are lysed with 0.5 ml of lysis buffer (50 mM Tris-Cl, pH 7.4; 140 mM NaCl, 1 mM EDTA, 1% Igepal CA-630, 0.1% SDS, 0.1% DOC), mildly sonicated and immunoprecipitated with anti-Flag beads for 1 h at 4 °C. Beads are washed with lysis buffer and bound material is eluted with 3×Flag peptide (250 μg ml^{-1}). The eluate is then incubated with MyONEC1 beads to collect biotinylated target protein, after which the beads are washed with high-stringency buffers (0.1% SDS, 1 M NaCl, 0.5% LiDS, 0.5 M LiCl and 1% SDS, 0.5 M LiCl) to remove non-specific interactors. 3′ linkers are ligated with T4 RNA Ligase 1, excess adapters are washed away and 3′-tagged, cross-linked RNA is released with proteinase K digestion and column purification (Zymo DNA Clean & Concentrator). Reverse transcription is carried out with SuperScript III and barcoded reverse-transcription primers. After reverse transcription, relevant samples are mixed and the cDNA is separated on a 6% 6M Urea PAA gel. Size-fractionated cDNA is then processed essentially as described in the iCLIP protocol to generate sequencing libraries[33].

uvCLAP employs a tri-barcode approach that combines barcoded ScriptSeq Index PCR Primers and two custom barcodes located adjacent to the 5′ and 3′ adapters. Barcodes located at the 5′ end of the inserts were designed using edittag[34]. Barcodes located at the 3′ end of the inserts were created according to the semi-random patterns DRYYR and DYRRY (where D = not C; R = purine; Y = pyrimidine) and allowed to encode two mutually exclusive experimental conditions. uvCLAP uses a random tag strategy[35] to determine individual crosslinking events. uvCLAP primers contain 5 random nucleotides that are interleaved with the 5′ barcodes according to the pattern $NNNT_1T_2T_3T_4T_5NN$ (N = random nucleotide; T = barcode nucleotide). In combination with the semi-random 3′ barcodes, this allows us to distinguish at least 49,152 ($4^5 \cdot 3 \cdot 2^4$) crosslinking events per nucleotide.

Size fractions were tagged via indexed PCR primers, pull-down conditions and biological replicates were tagged via 5′ and 3′ barcodes. Barcodes and random tags were extracted using custom scripts. Adapters were trimmed and the library was demultiplexed using Flexbar (v2.32)[36]. Possible readthroughs into the barcoded regions were removed by clipping 10 and 5 nt from the 3′ ends of first and second mate reads. Reads were mapped to the reference genomes (hg19, mm10, dm3) using bowtie2 (v2.2.0)[37] with parameters: –very-sensitive –end-to-end –no-mixed –no-discordant –maxins 200. We excluded all reads for which bowtie2 could identify multiple distinct alignments as indicated by the 'XS:i' flag and used the alignments of the remaining uniquely mapped reads to determine crosslinking events and crosslinked nucleotides as previously described[18]. Crosslinking events of the size fractions and biological replicates were combined.

uvCLAP peaks were called on crosslinked nucleotides with JAMM (version 1.0.7rev1, parameters: -d y -t paired -b 50 -w 1 -m normal)[38] using the two replicates of the respective pull-down condition as foreground and the two replicates of the corresponding control pull-down condition as background (Extended Data Fig. 2a–d, h). The peaks of all experiments were merged and used to calculate pairwise Spearman correlations among all replicates based on the number of events falling on each peak region, showing increased pairwise correlations between biological replicates within each condition over replicates of differing experimental conditions (deeptools version 2.3.5)[39] (see Extended Data Fig. 2a–d).

FLASH. Cells were crosslinked with 0.15 mJ cm^{-2} UVC irradiation, lysed with 1× NLB buffer (1× PBS, 0.3 M NaCl, 1% Triton-X, 0.1% Tween-20) and homogenized by water-bath sonication. The target protein of interest was pulled-down with paramagnetic beads pre-coupled to antibodies against the protein of interest. After a brief RNase I-digestion, RNA 3′ ends were healed with T4 PNK. Custom-made, barcoded adapters were ligated using T4 RNA Ligase 1 or T4 RNA Ligase 2KQ (if pre-adenylated adapters are used) for 1 h at 25 °C. Custom FLASH adapters contained two barcodes and random nucleotides adjacent to the 3′-adapters according to the pattern $NNB_1B_2NT_1T_2T_3T_4T_5T_6NN$ (N = random tag nucleotide; T = tag nucleotide; B = RY-space tag nucleotide). Random tags were used to merge PCR-duplicates, regular tags were used to specify the pull-down condition, and semi-random RY-space tags were used to distinguish the biological replicates. Excess adapters were washed away, negative controls were mixed with experimental controls and RNA was isolated with Proteinase K treatment and column purification. Isolated RNA was reverse-transcribed and treated with RNase H. cDNA was column-purified and circularized with CircLigase for 2–16 h. Circularized cDNA was directly PCR amplified, quantified with Qubit/Bioanalyzer and sequenced on Illumina NextSeq 500 in paired-end mode.

FLASH read processing and mapping was performed using the Galaxy platform[40]. Adapters were trimmed using Flexbar (v2.5). Libraries were demultiplexed using bctools (https://github.com/dmaticzka/bctools, v0.2.0) and Flexbar (v2.5). Possible readthroughs into the barcoded regions were removed by clipping 13 nt from the 3′ ends of first mate reads. Reads were mapped to the reference genomes (hg19, mm10) using bowtie2 (v2.2.6) with parameters: –very-sensitive –end-to-end –no-mixed –no-discordant –maxins 500. We excluded all reads for which bowtie2 could identify multiple distinct alignments as indicated by the XS:i flag and used the alignments of the remaining uniquely mapped reads to determine crosslinking events as previously described[18].

FLASH peaks were called on alignments of crosslinking events with PEAKachu (https://github.com/tbischler/PEAKachu/releases/tag/0.0.1alpha2, version 0.0.1alpha2, parameters: –pairwise_replicates -m 0 -n manual –size_factors 1 1 0.75 0.75)[41], using the two replicates of the respective pulldown condition as foreground and the two replicates of the corresponding control pull-down condition as background (Supplementary Table 3). Pairwise Spearman correlations were calculated as for uvCLAP (Extended Data Fig. 2a–d, h).

Graph based clustering and repeat enrichment of uvCLAP data. We followed a strategy described before to assess the enrichment of different repeat families in uvCLAP samples[42]. Briefly, we created a library of canonical repeat sequences and repeat instances from the corresponding human (hg38) and mouse (mm10) genome, from repeatmasker (RepeatMasker open-4.0.5). We then mapped the sequencing reads to this library, and the uniquely mapping reads were used to calculate the maximum likelihood estimate of enrichment (MLE) for each repeat family, for the test (eg. DHX9) samples over the corresponding control (empty vector)

sample. We then performed hierarchical clustering using the MLE scores to visualize uniquely enriched repeat families for each sample.

As an alternative approach, we followed a mapping-free, graph-based sequence clustering approach described previously for plant genomes[43]. In brief, we first sampled 100,000 reads from DHX9, EIF4A3, QKI-6 and QKI-5 datasets, followed by a clustering pipeline[44] which performs an all-to-all pairwise comparison between the reads in order to construct a graph, containing reads as nodes and the overlap between reads as edges. The vertices in the graph correspond to the reads and the edge weights represent the similarity score between the reads. The graph is then divided into clusters representing different connected communities. We then annotated the reads belonging to each cluster using RepeatMasker for the presence of different repeat families. Top clusters (with highest number of reads) for each sample are then visualized to assess the composition of major *Alu* families and other repeats. Increasing the sample size or multiple rounds of sampling had no effect on the composition of top clusters. Analysis code is publicly available at: https://github.com/vivekbhr/dhx-alu.

Detection of paired *Alu* elements. We performed a similarity search (YASS[20] v1.4) to determine pairs of sequences reverse-complementary to each other within each gene (Ensembl 75). For each experiment, we selected all genes containing at least one peak and three annotated *Alu* elements (UCSC RepeatMasker track). Within the selected genes we determined *Alu* pairs based on all reverse-complementary YASS pairs with distances below 10,000 nt. Two *Alu* elements were considered paired if at least 75% of the first *Alu* was overlapped by one part of the YASS alignment and at least 75% of the second *Alu* was overlapped by the corresponding reverse-complementary part of the YASS alignment. For each paired *Alu* we then determined the distance to its nearest partner. *Alu* elements were categorized as targeted if a peak was located within 100 nt, otherwise as untargeted. For DHX9 we repeated this analysis for targeted *Alu* elements in extragenic regions.

Sample preparation for qPCR detection of circular RNAs and RNA-seq libraries. The siRNA knockdowns (5 nM of Silencer Select (Ambion) control siRNA 4390846 or s4019 and s4020 siRNA for DHX9 and s1009 for ADAR) were performed on FLPinTrex HEK293 cells for 3 days in quadruplicates using RNAiMAX (Thermo Fisher Scientific). Total RNA extracts from siRNA transfected cells was prepared by Zymo Quick-RNA Kit and first-strand cDNA synthesis was carried out with SuperScriptIII. Quantitative real-time PCR is performed using the oligos listed in Supplementary Table 2 with FastStart SYBR Green Master (Roche 04 913 914 001). For RNase R treated samples: 500 ng of total RNA was incubated with 20 U of RNase R (Epicentre/Illumina) for 30 min at 30 °C after which the reactions were cleaned up with RNA Clean and Concentrator columns (Zymo) before proceeding with reverse transcription. For the poly(A)$^+$ libraries, TruSeq Stranded mRNA Library Prep Kit (Illumina) was used as per manufacturer's instructions. For the poly(A)$^-$ libraries, poly(A)$^+$ RNA was depleted using paramagnetic oligo-d(T) beads (Thermo Fisher Scientific) twice. The remaining, poly(A)$^+$-depleted RNA is processed with the TruSeq Stranded Total RNA Library Prep Kit (Illumina).

RNA sequencing and analysis. Both poly(A)$^+$ and poly(A)$^-$ reads were trimmed using Trim Galore to remove adaptors and mapped to GRCh38 (hg38) genome sequence using TopHat2 (v2.0.13)[45]. Poly(A) reads were assigned to features (Gencode 21) using featurecounts (v1.5.1) (counting properly paired primary alignments above mapping quality of 10)[46], and differential expression analysis was performed using edgeR (v3.12.0)[47]. We identified genes as differentially expressed if they are called significant in two independent comparisons (control vs siRNA1-s4019 and control vs siRNA2-s4020, FDR < 0.05), with expression fold change in same direction, in both comparisons. For analysis of differentially spliced exons, the gene models were flattened and differential expression was performed at exon level using DEXSeq (v1.18)[48]. Exons were called differentially spliced at FDR adjusted $P < 0.01$. For the poly(A)$^-$ library, the reads were mapped to the genome using STAR (v2.4.2)[49] (using option –chimSegmentMin 20) and the circular RNAs were annotated using circExplorer (v2.1)[22]. Depth of sequencing was not significantly different between samples, $P = 0.9482$, Welch *t*-test.

Luciferase assays. The siRNA knock-downs (5 nM of Silencer Select (Ambion) control siRNA 4390846 or s4019 siRNA for DHX9) were performed on HEK293FT or HeLa cells and the reporter constructs (50 ng of pmirGlo with 3′ UTR inserts) were transfected on the 48th hour of knockdown. All luciferase assays were performed on the 72nd hour of knockdown. The knockout clone was generated by co-transfecting the two guide RNAs; 1 and 2 (Extended Data Fig. 5d) co-expressing wild-type SpCas9 (pX459, Addgene no. 62988) and selected with 1 μg ml^{-1} puromycin for 4 days. Colonies were picked, screened and expanded. Rescue constructs (GFP, wild-type DHX9, and DHX9(GET)) were transfected into wild-type (only Cas9-expressing) and knockout clones and the transfection of the luciferase constructs was performed 24 h after the rescue construct transfection in technical quadruplicates (see Extended Data Fig. 5e for the expression validation of the rescue constructs). All luciferase reads were performed on the 48th hour of the primary transfection. The data points in Fig. 2d (and in Extended Data Fig. 5f) show all technical quadruplicates of the two biological replicates (that is, eight data points per 3′ UTR construct).

Live cell imaging. All live cell imaging experiments were performed using monoclonal reporter cell lines that were generated as previously described[50]. In brief, HeLa 'Kyoto' cell line was transfected with pH2V-mpH2B-mCherry-IRES-neo3 and pmEGFP-α-tubulin-IRES-puro2b plasmids. Thus, in the presence of neomycin and puromycin cells are H2B-mCherry-tubulin-EGFP stable reporter cells. Cells were cultured in Dulbecco's modified eagle medium (DMEM; GIBCO) supplemented with 10% (v/v) and treated either with siRNA control or siRNA against DHX9 in eight-well coverslip-bottomed dishes (ibidi GmbH cat. no. 80826). Six hours following transfection, medium was changed and supplemented with 1% penicillin/streptomycin, puromycin (1 μg μl^{-1}) and geneticin/neomycin (200 μg ml^{-1}) (Invitrogen, Life Technologies, cat. no. 21810031). 24, 48 or 72 h post transfection, dishes were transferred to a Tokai Hit stage incubation unit, wherein cells were maintained at 37 °C and humidified atmosphere of 5% CO_2 throughout the experiment. Cells were imaged using a Zeiss Observer.Z1 with the CSU-X1 spinning disk head (Yokogawa) and the QuantEM:512SC camera (Photometrics) and were visualized using an air 40× objective. *Z*-stack parameters were taken every 5 min for at least 16 h and a maximum of 24 h. Laser power and exposure times were kept to a minimum condition (<9%). For analysis cells were manually counted and evaluated at the latest time point using Zen lite-Blue software (ZEISS). Nuclei numbers (Extended Data Fig. 8c) come from 15 fields of each condition at 24 h knockdown (in total 21 cells for wild type, 21 cells for DHX9 knockdown are included in the plot), from 5 fields for wild type and 15 fields for knockdown at 48 h knock-down (in total 28 cells for wild type and 40 cells for DHX9 knockdown are included in the plot), and from 10 fields for wild type and 15 fields for DHX9 knockdown at 72 h knockdown (in total 30 cells for wild type, 32 cells for DHX9 knockdown are included in the plot).

SILAC labelling of the cells and the biochemical purification of DHX9. Cells were adapted to SILAC medium (with K8R10 (1:1500 each) for Heavy or with K0R0 for Light) for 7 days and then were expanded to larger cell culture plates for another 7–10 days. Crosslinked purification was performed on 5–10 mg of 0.5% formaldehyde crosslinked nuclear extracts that were solubilized by mechanical shearing using sonication. Flag IP (Flag-M2 Agarose resin) was performed overnight at 4 °C and the proteins were eluted by 6 M urea-containing buffer (6M Urea, 0.5 M NaCl, 0.5% NP-40, 50 mM Na_2HPO_4, 50 mM Tris pH 8.0, 0.05% Tween-20). Streptavidin (using MyOneC1 magnetic beads) pull-down was performed on the diluted (down to 1 M urea) eluate for 3 h at 4 °C. Streptavidin-bound proteins were sequentially washed with buffers containing 1 M and 6 M Urea. For the in-gel analysis proteins were eluted from beads by boiling and for the in-solution analysis beads were rinsed three times in *N*-octyl-β-glucopyranoside containing Tris (pH 7.4) buffer before trypsinization. Native purifications were performed on whole-cell extracts that were prepared in 450 mM NaCl and 1% Triton-X containing buffer. Silver Gel staining was performed using the Silver Quest Silver Staining Kit (Thermo Fisher LC6070).

Immunoprecipitation. Native whole-cell extracts or crosslinked nuclear extracts were incubated with 1 μg of DHX9 (polyclonal rabbit, see 'Antibodies' section) or of IgG (rabbit Santa Cruz sc-2017) antibody overnight at 4 °C and coupled to the ProtG Dynabeads (Life Technologies 10004D) for 1 h. Beads were washed in the IP buffer three times for 5 min each. Elution from the beads was performed in 2× protein loading dye by incubating for 10 min at 70 °C (or 95 °C for crosslinked samples) with shaking. DHX9 was detected with monoclonal mouse antibody (for the rest of the detected proteins see 'Antibodies' section).

Immunofluorescence. Cells were crosslinked with 4% methanol-free formaldehyde in PBS at room temperature for 10 min and permeabilized with 0.1% Triton-X and 1% BSA in PBS for 30 min at room temperature. Primary antibodies (see details in the Antibody section) were diluted (1:1000 for the DHX9 pRb, 1:500 for the SC-35 (SRSF2) and J2 antibodies) in PBS with 0.1% Triton-X and 1% BSA and incubated with fixed cells at 4 °C for ∼16 h. Fluorescently labelled secondary antibodies with the appropriate serotype were used reveal target proteins. Hoechst 33342 was used to stain DNA. Imaging was performed with a Leica SP5 confocal microscope.

J2 (dsRNA) pull-down. Cells were harvested on the third day of siRNA treatment (siRNA transfections were carried out as described above) in RIP buffer (25 mM HEPES pH 7.2, 75 mM NaCl, 5 mM $MgCl_2$, 0.1% Igepal CA-630, 1 U μl^{-1} RNasin), sonicated (Bioruptor, 5 min, 30 s ON, 30 s OFF) and centrifuged at 20,000*g* for 20 min at 4 °C. Clarified lysates were incubated with 25 μl of ProtG Dynabeads pre-coupled to 2 μg of J2 mAb (Scicons) or mouse-IgG (Santa Cruz) for 3 h at 4°C. The beads were washed three times with the RIP buffer and bound RNA was isolated using the RNA Clean and Concentrator columns (Zymo). Eluted RNA was reverse transcribed using SuperScript III with the following modifications:

RNA was incubated at 70 °C for 3 min to remove secondary structures, which is followed by reverse transcription at 50 °C for 15 min, 60 °C for 10 min and 70 °C for another 10 min. Quantitative real-time PCR was performed using the oligos listed in Supplementary Table 2 with FastStart SYBR Green Master (Roche 04 913 914 001), enrichments were calculated using the $2^{-\Delta\Delta C_t}$ method using 10% of input material as a reference for each immunoprecipitation.

Antibodies. DHX9 (monoclonal mouse, SantaCruz sc13183, polyclonal rabbit Abcam ab26271, monoclonal rabbit Abcam ab183731), ADAR (for the detection of human protein: Sigma SAB1401004, for the detection of mouse protein: Santa Cruz sc-73408), J2 antibody (Scicons, English and Scientific Consulting, Hungary), NONO (Sigma AV40715), ZFR (Sigma SAB2104153), HNRNPC (Santa Cruz sc-32308), KHDRBS1 (Sigma S9575), POL2 (4H8 Active Motif 101307, and 8WG16 Abcam ab817), CDK9 (Santa Cruz sc484), Flag-HRP (Sigma A8592), streptavidin-HRP (Pierce 21130), SPC24 (Bethyl, A304-260A), SRSF2/SC35 (Sigma S4045), MSL2 (Sigma HPA003413), MSL1 (polyclonal rabbit antibody generated by the Akhtar laboratory, previously described in ref. 32), MOF (Bethyl A300-992A).

Data accessibility. All the uvCLAP, FLASH and RNA-seq data in this study have been deposited to the Gene Expression Omnibus database under the accession number GSE85164.

30. Shin, Y. J. *et al.* Nanobody-targeted E3-ubiquitin ligase complex degrades nuclear proteins. *Sci. Rep.* **5,** 14269 (2015).
31. Ran, F. A. *et al.* Genome engineering using the CRISPR-Cas9 system. *Nat. Protocols* **8,** 2281–2308 (2013).
32. Chelmicki, T. *et al.* MOF-associated complexes ensure stem cell identity and Xist repression. *eLife* **3,** e02024 (2014).
33. Konig, J. *et al.* iCLIP--transcriptome-wide mapping of protein-RNA interactions with individual nucleotide resolution. *J. Vis. Exp.* **50,** 2638 (2011).
34. Faircloth, B. C. & Glenn, T. C. Not all sequence tags are created equal: designing and validating sequence identification tags robust to indels. *PLoS One* **7,** e42543 (2012).
35. König, J. *et al.* iCLIP reveals the function of hnRNP particles in splicing at individual nucleotide resolution. *Nat. Struct. Mol. Biol.* **17,** 909–915 (2010).
36. Dodt, M., Roehr, J. T., Ahmed, R. & Dieterich, C. FLEXBAR—flexible barcode and adapter processing for next-generation sequencing platforms. *Biology (Basel)* **1,** 895–905 (2012).
37. Langmead, B. & Salzberg, S. L. Fast gapped-read alignment with Bowtie 2. *Nat. Methods* **9,** 357–359 (2012).
38. Ibrahim, M. M., Lacadie, S. A. & Ohler, U. JAMM: a peak finder for joint analysis of NGS replicates. *Bioinformatics* **31,** 48–55 (2015).
39. Ramírez, F. *et al.* deepTools2: a next generation web server for deep-sequencing data analysis. *Nucleic Acids Res.* **44** (W1), W160–W165 (2016).
40. Afgan, E. *et al.* The Galaxy platform for accessible, reproducible and collaborative biomedical analyses: 2016 update. *Nucleic Acids Res.* **44** (W1), W3–W10 (2016).
41. Holmqvist, E. *et al.* Global RNA recognition patterns of post-transcriptional regulators Hfq and CsrA revealed by UV crosslinking *in vivo*. *EMBO J.* **35,** 991–1011 (2016).
42. Day, D. *et al.* Estimating enrichment of repetitive elements from high-throughput sequence data. *Genome Biol.* **11,** R69 (2010).
43. Novák, P., Neumann, P. & Macas, J. Graph-based clustering and characterization of repetitive sequences in next-generation sequencing data. *BMC Bioinformatics* **11,** 378 (2010).
44. Novák, P., Neumann, P., Pech, J., Steinhaisl, J. & Macas, J. RepeatExplorer: a Galaxy-based web server for genome-wide characterization of eukaryotic repetitive elements from next-generation sequence reads. *Bioinformatics* **29,** 792–793 (2013).
45. Kim, D. *et al.* TopHat2: accurate alignment of transcriptomes in the presence of insertions, deletions and gene fusions. *Genome Biol.* **14,** R36 (2013).
46. Liao, Y., Smyth, G. K. & Shi, W. featureCounts: an efficient general purpose program for assigning sequence reads to genomic features. *Bioinformatics* **30,** 923–930 (2014).
47. Robinson, M. D., McCarthy, D. J. & Smyth, G. K. edgeR: a Bioconductor package for differential expression analysis of digital gene expression data. *Bioinformatics* **26,** 139–140 (2010).
48. Anders, S., Reyes, A. & Huber, W. Detecting differential usage of exons from RNA-seq data. *Genome Res.* **22,** 2008–2017 (2012).
49. Dobin, A. *et al.* STAR: ultrafast universal RNA-seq aligner. *Bioinformatics* **29,** 15–21 (2013).
50. Steigemann, P. *et al.* Aurora B-mediated abscission checkpoint protects against tetraploidization. *Cell* **136,** 473–484 (2009).
51. Picardi, E. *et al.* REDIportal: a comprehensive database of A-to-I RNA editing events in humans. *Nucleic Acids Res.* **45,** D750–D757 (2017).

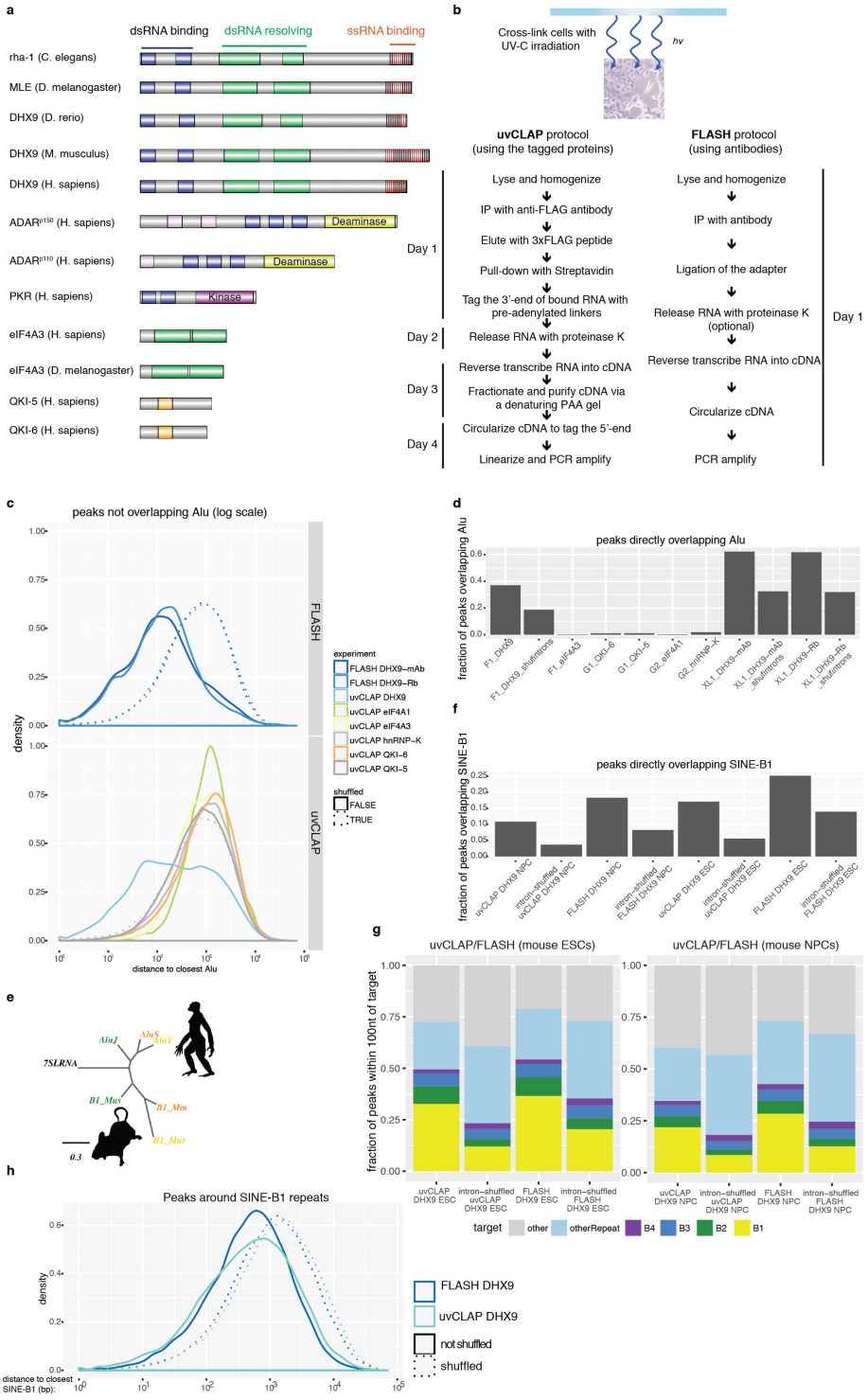

Extended Data Figure 1 | See next page for caption.

RESEARCH LETTER

Extended Data Figure 1 | uvCLAP/FLASH identifies DHX9 targets in humans and mice. a, The domain organization of *Drosophila*, human and mouse Mle/DHX9 is shown side by side with the other RNA-binding proteins, EIF4A3, QKI-5/6 used in uvCLAP, and the two other enzymatic-domain-containing dsRNA-binding proteins PKR and ADAR. Blue boxes show dsRNA-binding domains, green boxes show helicase-N and helicase-C domains, orange boxes show KH domains, pink box shows the Z-DNA-interacting domains of ADAR. Orange boxes with vertical lines show the RGG-repeats at the C-term of DHX9/Mle/RHA proteins that interact with single-stranded nucleic acids. **b**, The schematic representation of the two methods (uvCLAP and FLASH) developed for the identification of *in vivo* targets of RNA-binding proteins. **c**, The distance between peaks which do not directly overlap with an *Alu* repeat to the nearest *Alu* element for RNA-binding proteins EIF4A3, EIF4A1, HNRNPK, QKI-5 and QKI-6 is significantly further than similar peaks for DHX9. uvCLAP and FLASH data are shown separately which are put together in Fig. 1c. **d**, The fraction of peaks which are directly overlapping with an *Alu* element is depicted for DHX9 in comparison to peaks randomly placed in targeted regions within a sequencing library (shown as F1, G1, G2) and for EIF4A3, QKI-6, QKI-5, EIF4A1 and HNRNPK in uvCLAP and FLASH experiments (sequencing library XL1). **e**, The evolutionary divergence of primate and murine SINEs from the 7SL RNA. Scale bar, genetic distance (arbitrary units). **f**, The fraction of peaks which are directly overlapping with a SINE B1 repeat is depicted for DHX9 in comparison to peaks randomly placed in targeted regions. **g**, Fraction of uvCLAP and FLASH peaks in mouse embryonic stem (mES) cells and neural progenitor cells (NPCs) with a distance of at most 100 nucleotides from SINE B repeats is significantly enriched ($P < 2.2 \times 10^{-16}$; Fisher's exact test) for DHX9 in comparison to shuffled intron controls. **h**, The distances of DHX9 peaks in mES cells, which do not directly overlap with B1 repeats, to the nearest B1 repeats are shown. The distance is significantly smaller than the corresponding shuffled controls with median distances of 508 ($n = 33{,}686$) vs 1,312.5 ($n = 38{,}436$) nucleotides for uvCLAP and 514 ($n = 44{,}557$) vs 1,108.5 ($n = 51{,}272$) nucleotides for FLASH (all $P < 2.2 \times 10^{-16}$; one-tailed Mann–Whitney *U*-test). n = number of uvCLAP/FLASH peaks.

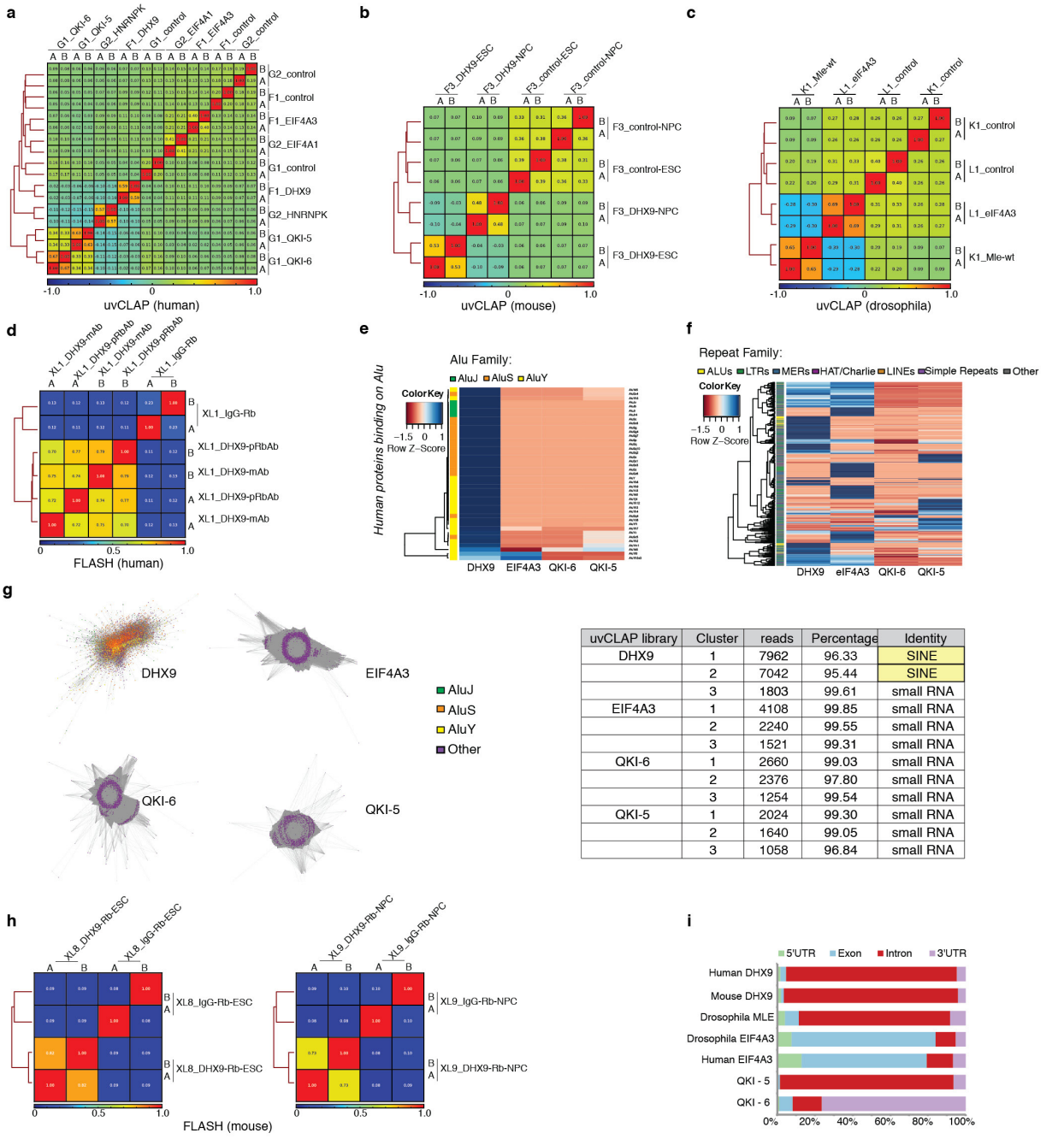

uvCLAP library	Cluster	reads	Percentage	Identity
DHX9	1	7962	96.33	SINE
	2	7042	95.44	SINE
	3	1803	99.61	small RNA
EIF4A3	1	4108	99.85	small RNA
	2	2240	99.55	small RNA
	3	1521	99.31	small RNA
QKI-6	1	2660	99.03	small RNA
	2	2376	97.80	small RNA
	3	1254	99.54	small RNA
QKI-5	1	2024	99.30	small RNA
	2	1640	99.05	small RNA
	3	1058	96.84	small RNA

Extended Data Figure 2 | See next page for caption.

Extended Data Figure 2 | Reproducibility of the replicates for each uvCLAP/FLASH library and enrichment of *Alu* repeat binding in human cells. a, Replicates (shown as A and B) in human uvCLAP sequencing libraries F1, G1 and G2 are compared to each other using Spearman correlation and similarity is represented as a heat map. Except for replicates the only other two profiles which correlate are of QKI isoforms. **b**, Replicates (shown as A and B) in mouse uvCLAP sequencing library F3, which is composed of DHX9 knock-in mES cells and NPCs, and BirA ligase control cell line, are compared to each other using Spearman correlation and similarity is represented as a heat map. Replicates of each experiment cluster together. **c**, Replicates (shown as A and B) in *Drosophila melanogaster* uvCLAP sequencing libraries K1 and L1, which are composed of Mle and Eif4a3 profiles, are compared to each other using Spearman correlation and similarity is represented as a heat map. Replicates of each experiment cluster together. **d**, Replicates (shown as A and B) in human FLASH sequencing library XL1 are compared to each other by using Spearman correlation. DHX9 library replicates as well as different antibody used in two independent library replicates cluster together, whereas IgG control is separated. **e**, Enrichments of *Alu* repeat subfamilies in uvCLAP data (see Methods). All subfamilies of *Alu* elements are highly enriched in the DHX9 uvCLAP experiment, compared to EIF4A3, QKI-5 and QKI-6. **f**, Enrichments of all human repeat families in uvCLAP data (see Methods). *Alu* elements are highly enriched in the DHX9 uvCLAP experiment, compared to EIF4A3, QKI-5 and QKI-6. **g**, Mapping-free clustering (see Methods) of repeated reads within uvCLAP libraries for human DHX9, EIF4A3, QKI-6 and QKI-5 reveals that only the top cluster of DHX9 library is composed of *Alu* elements. Right, a table view for the identity of the top three clusters (maximum reads) produced by graph based clustering of raw sequencing reads from different uvCLAP experiments. *Alu* elements bound by DHX9 form two distinct clusters (as depicted in the table) while the top three clusters in other samples (QKI-6, QKI-5 and eIF4A3) contain various small RNA families. **h**, Right, replicates (shown as A and B) in mouse FLASH sequencing library XL9 are compared to each other using Spearman correlation (see Supplementary Table 3 for mapping statistics and number of peaks). **i**, Binding frequencies of DHX9, EIF4A3 and QKI isoform crosslinking events on mRNA targets shown for UTRs, exons and introns.

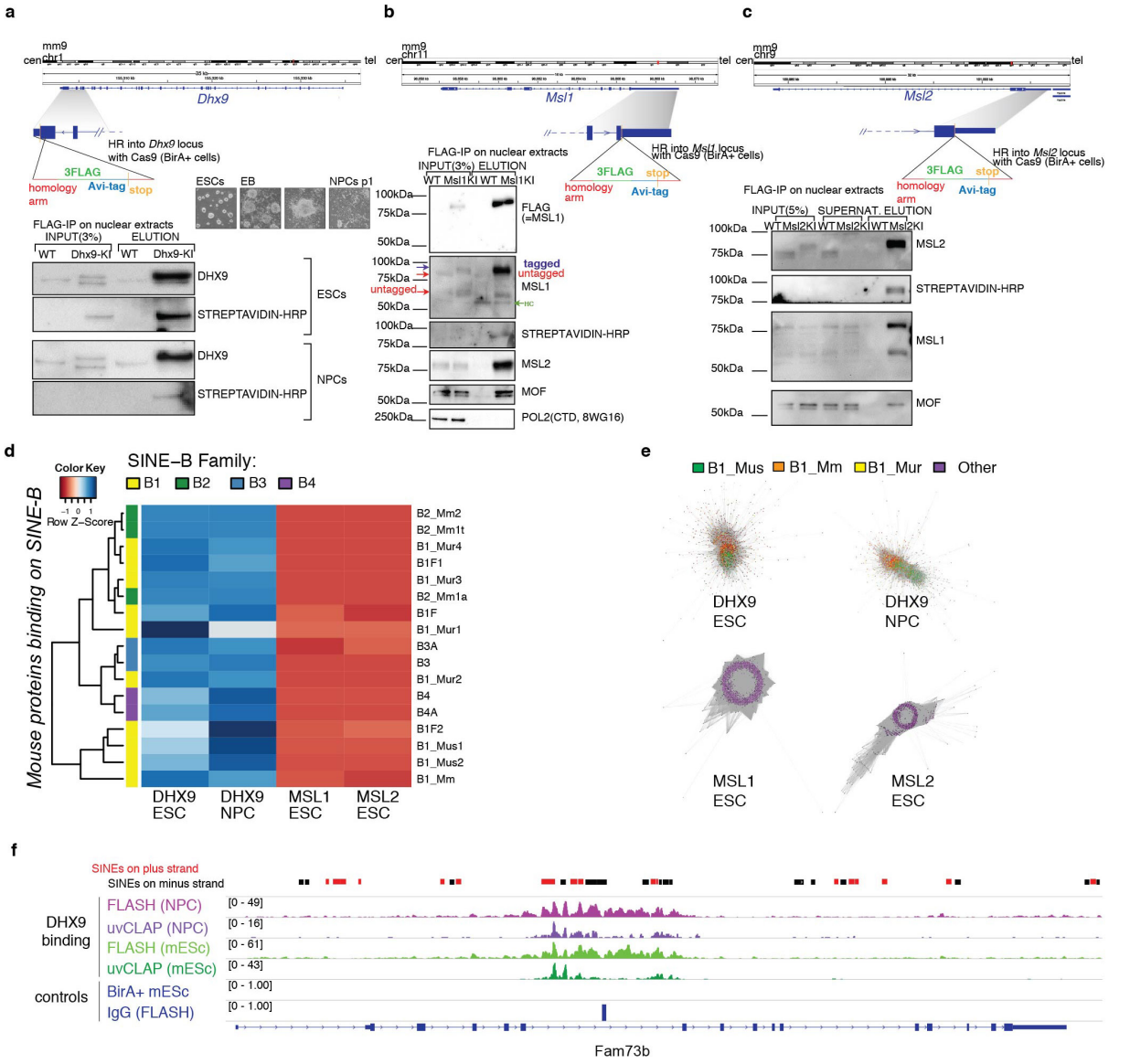

Extended Data Figure 3 | Mapping for DHX9-bound RNAs onto repeats reveals an enrichment of SINE B binding in mouse cells. **a**, Top, endogenous knock-in strategy is shown for the mouse *Dhx9* gene. Right, differentiation snapshots of the tagged mES cell line into NPCs. Bottom, the identity of the tagged protein and its biotinylation is shown by DHX9 and streptavidin blots from Flag immunoprecipitation (IP) carried in nuclear extracts both for mES cells and NPCs. **b**, Endogenous knock-in strategy is shown for the mouse *Msl1* gene. The integrity of the protein and its biotinylation is shown by MSL1 and streptavidin blots from Flag IP carried in nuclear extracts. The interaction ability of the tagged MSL1 protein with its known interaction partners (within MSL complex) is validated by this Flag IPs (performed on soluble nuclear extracts) by showing the co-IP for MOF (MYST1) and MSL2. POL2 (8WG16) is used as a loading control. **c**, Endogenous knock-in strategy is shown for the mouse *Msl2* gene. The integrity of the protein and its biotinylation is shown by MSL2 and streptavidin blots from Flag IP carried in nuclear extracts. The interaction ability of the tagged MSL2 protein with its known interaction partners (within MSL complex) is validated by this Flag IP (performed on soluble nuclear extracts) by showing the co-IP for MOF (MYST1) and MSL1. **d**, Enrichments of SINE repeat subfamilies in uvCLAP data (see Methods). All SINE B subfamilies are highly enriched in DHX9 uvCLAP experiment, both in mES cells and NPCs, compared to MSL1 and MSL2. **e**, Mapping-free clustering of reads (see Methods) within uvCLAP libraries (mES cells and NPCs) reveals that only the top cluster of mouse DHX9 library is composed of SINE B repeats. **f**, Snapshots of uvCLAP and FLASH binding events (both in mES cells and NPCs) within *Fam73b* gene show that the crosslinking sites of DHX9 reside on SINE B repeats on opposing strands. SINEs on the plus strand are shown with red boxes, SINEs on the minus strand are shown with black boxes. Biological replicates were merged in these representations (also see Extended Data Fig. 2 for reproducibility between biological replicates).

RESEARCH LETTER

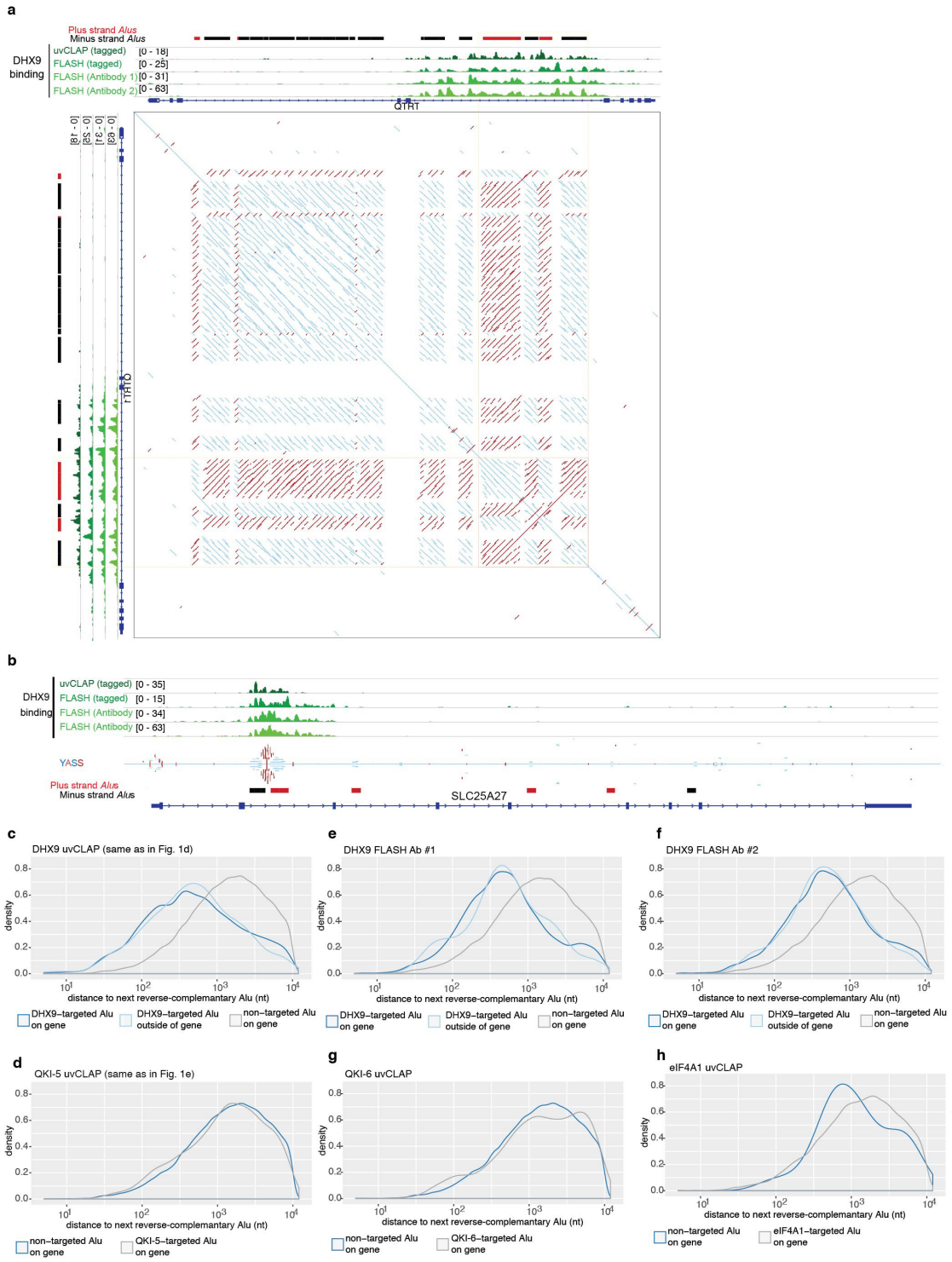

Extended Data Figure 4 | See next page for caption.

Extended Data Figure 4 | uvCLAP and FLASH reveal DHX9 binding on inverted-repeat *Alu* elements. a, A snapshot of DHX9 binding in the intron of the *QTRT1* gene. *Alu* elements are depicted with red (plus strand) or black (minus strand) boxes. Dot-plot generated by YASS (see Methods) showing that DHX9 binds to inverted repeats (structure-forming), shown by red lines, but not to direct repeats, shown by blue lines. **b**, A snapshot of DHX9 binding in the intron of the *SLC25A27* gene where there are *Alu* elements on opposite strands. YASS-generated dot-plots as in **a** (for simplicity only the diagonal of the YASS dot-plot is shown). **c**, Genome-wide analysis of uvCLAP DHX9 binding near paired *Alu* elements shows preferential targeting of *Alu* elements with nearby binding partners in both gene (dark blue) and outside gene (light blue) bound regions. **d**, Genome-wide analysis of uvCLAP QKI-5 binding near paired *Alu* elements (binding enriched in introns) shows no significant difference for closeness to nearest potential binding partner. **e**, Genome-wide analysis of FLASH DHX9 binding near paired *Alu* elements (Ab#1) shows a preferential targeting of *Alu* elements with nearby binding partners in both gene (dark blue) and outside gene (light blue) bound regions. **f**, Genome-wide analysis of FLASH DHX9 (Ab#2) binding near paired *Alu* elements shows a preferential targeting of *Alu* elements with nearby binding partners in both gene (dark blue) and outside gene (light blue) bound regions. **g**, Genome-wide analysis of uvCLAP QKI-6 binding near paired *Alu* elements shows no significant difference for closeness to nearest potential binding partner. **h**, Genome-wide analysis of uvCLAP EIF4A1 binding near paired *Alu* elements shows no significant difference for closeness to nearest potential binding partner.

RESEARCH LETTER

Extended Data Figure 5 | See next page for caption.

Extended Data Figure 5 | DHX9 depletion increases circular RNA formation and represses translation of reporters containing inverted-repeat *Alu* elements within the 3′ UTR. a, Left, the qPCR approach for detecting linear/circular RNAs with two sets of oligos indicated as divergent and convergent used for the detection of circular and linear RNAs, respectively. Right, quantitative real-time PCR analysis of previously reported circRNAs[23] in DHX9-siRNA-treated HEK293FT cells (error bars represent standard deviation between biological quadruplicates). **b**, Snapshot of a circRNA generated locus, PPP1CB with DHX9 crosslinking sites on inverted *Alu* repeats. Blue bar depicted as 'circPCR-PPP1CB' represents the qPCR scored region in (Fig. 2c). Biological replicates were merged in these representations (also see Extended Data Fig. 2 for reproducibility between biological replicates). **c**, Top, schematic drawing of pmirGlo insert cloning is shown. Bottom, 3′ UTRs used as inserts in luciferase assays. **d**, Top, genomic position of tested guide RNAs in CRISPR/Cas9 depletion of DHX9 is shown (see Supplementary Table 2 for guide RNA sequences). Bottom left, efficiency of guide RNA pairs is shown by DHX9 and tubulin western blots. Bottom right, description for the making of the constitutive DHX9-depleted clone. **e**, Expression check by western blot analysis of rescue cells used on two independent (different days) experiments. **f**, Luciferase assays show that DHX9-depletion does not alter the expression of 3′ UTR elements without inverted-repeat *Alu* elements. **g**, Luciferase assay results are shown carried in HEK293FT and HeLa cells upon siRNA knockdown of DHX9. Knockdown efficiency is validated by western blot analysis for DHX9 and tubulin. Similar to what is shown in Fig. 2d reporter expression from the constructs with an inverted-repeat *Alu* element in 3′ UTRs are affected upon DHX9 depletion. Error bars represent standard deviation of a total of 20 data points that come from one experiment carried out with biological quadruplicates for each cloned 3′ UTR insert (5 with and 5 without inverted-repeat *Alu* elements).

RESEARCH LETTER

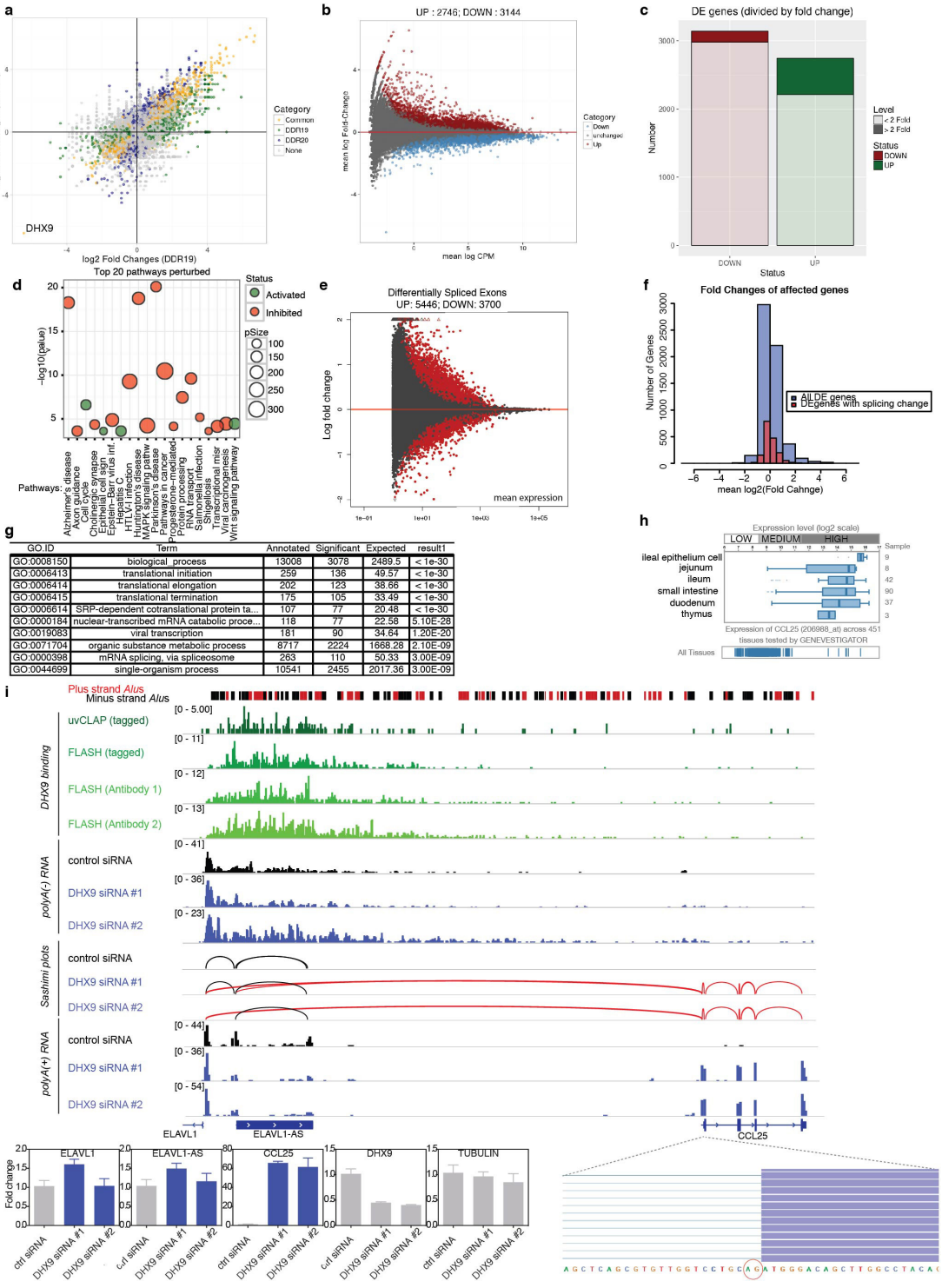

GO.ID	Term	Annotated	Significant	Expected	result1
GO:0008150	biological_process	13008	3078	2489.5	< 1e-30
GO:0006413	translational initiation	259	136	49.57	< 1e-30
GO:0006414	translational elongation	202	123	38.66	< 1e-30
GO:0006415	translational termination	175	105	33.49	< 1e-30
GO:0006614	SRP-dependent cotranslational protein ta...	107	77	20.48	< 1e-30
GO:0000184	nuclear-transcribed mRNA catabolic proce...	118	77	22.58	5.10E-28
GO:0019083	viral transcription	181	90	34.64	1.20E-20
GO:0071704	organic substance metabolic process	8717	2224	1668.28	2.10E-09
GO:0000398	mRNA splicing, via spliceosome	263	110	50.33	3.00E-09
GO:0044699	single-organism process	10541	2455	2017.36	3.00E-09

Extended Data Figure 6 | See next page for caption.

Extended Data Figure 6 | DHX9 depletion leads to changes in gene expression and exon usage. a, Reproducibility of gene-expression changes between cells treated with siRNA 1 (green) and siRNA 2 (blue) (both show that DHX9 is the most severely downregulated gene in these datasets). Genes with a significant change in their expression levels in both experiments are shown with yellow points. **b**, MA plot of genes that show a reproducible change in both RNAi experiments (yellow dots in **a**). **c**, The extent of gene expression changes in the reproducibly misregulated genes in **b**. **d**, Pathway perturbation analysis using the data in **b**. **e**, Differentially spliced exons that show a reproducible change in DHX9-depletion experiments (siRNA 1 and siRNA 2). **f**, Differentially expressed genes (DEgenes) with respect to their detected splicing changes shows 55% of the mis-spliced genes are downregulated. **g**, GO term analysis using data in **e**. **h**, Tissue expression database (Genevestigator) results for *CCL25* gene show its expression is specific to the intestine and thymus tissues. CCL25 is expressed at low levels every other tissue (in total 451 tissues). **i**, DHX9 binding in the *ELAVL1–CCL25* locus is shown together with the poly(A)$^-$ and poly(A)$^+$ RNA-seq data. Sashimi plots generated from control and DHX9-siRNA-treated samples show a new exon–exon junction from *ELAVL1*^{AS} to *CCL25* (depicted with red lines). For clarity, only plus strand data are shown. Biological replicates were merged in these representations (also see Extended Data Fig. 2 for reproducibility between biological replicates). Poly(A)$^+$ RNA-seq data show that an anti-sense transcript in the opposite direction to *ELAVL1* is now connected via a cryptic splice acceptor site to the first exon of *CCL25* upon DHX9 depletion (two independent siRNAs, four biological replicates each). Bottom, qPCR validation of the CCL25 upregulation upon RNA processing defects in DHX9 knockdown samples. We observe that CCL25 is ~60-fold upregulated in DHX9-depleted cells, while the expression of neither *ELAVL1* nor its accompanying anti-sense transcript change significantly. The cryptic splice acceptor site is enlarged on the bottom right.

RESEARCH LETTER

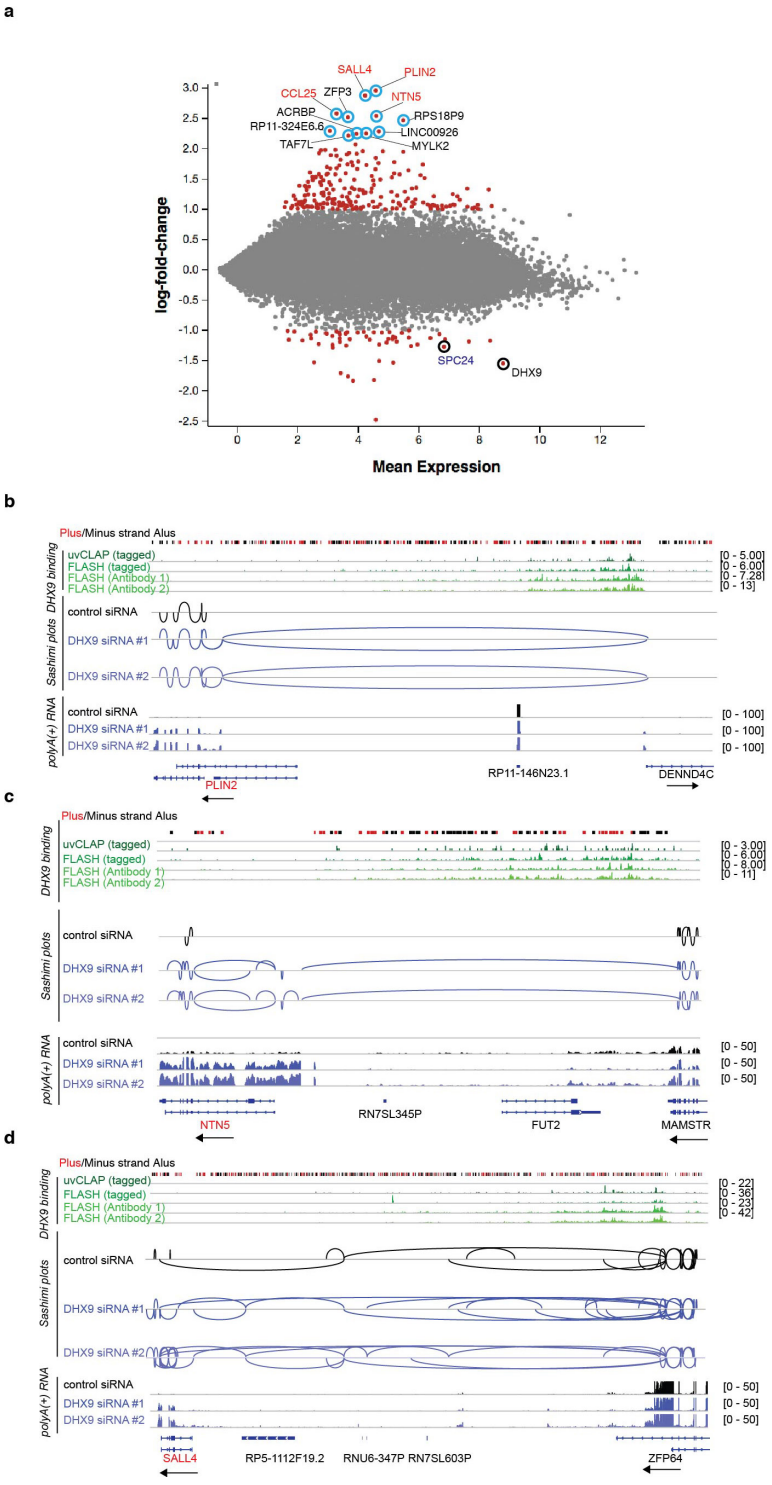

Extended Data Figure 7 | See next page for caption.

Extended Data Figure 7 | Many upregulated genes in DHX9 knockdown show RNA processing defects in their gene locus. a, Genes that were more than twofold up- or downregulated are marked with red dots. Top 11 upregulated genes, which show signs of transcription bleed-through from upstream genes are highlighted with blue circles. *CCL25*, *SALL4*, *PLIN2* and *NTN5* are further highlighted. **b**, DHX9 binding in the *PLIN2–RP11–146N23.1* gene locus on the nascent RNA originating from the antisense transcription of the *DENND4C* promoter and splicing defect upon DHX9 knockdown. Sashimi plots depicting the exon junctions of these genes are shown in blue for the DHX9 knockdown, whereas the control sample (shown with black lines) does not display such a joining event (threshold is set to five reads). Biological replicates were merged in these representations (also see Extended Data Fig. 2 for reproducibility between biological replicates). For clarity, only minus strand data are shown. **c**, DHX9 binding in the *NTN5–MAMSTR* gene locus on the nascent (bleed-through) RNA and splicing defect upon DHX9 knockdown. Sashimi plots depicting the exon junctions of these genes are shown in blue for the DHX9 knockdown, whereas the control sample (shown with black lines) do not display such a joining event (threshold is set to one read). Biological replicates were merged in these representations (also see Extended Data Fig. 2 for reproducibility between biological replicates). For clarity, only minus strand data are shown. **d**, DHX9 binding in the *SALL4–ZFP64* gene locus on the nascent (bleed-through) RNA and splicing defect upon DHX9 knockdown. Sashimi plots depicting the exon junctions of these genes are shown in blue for the DHX9 knockdown whereas the control sample (shown with black lines) displays a lower frequency of such joining events (threshold is set to 1 reads). Biological replicates were merged in these representations (also see Extended Data Fig. 2 for reproducibility between biological replicates). For clarity, only minus strand data are shown.

RESEARCH LETTER

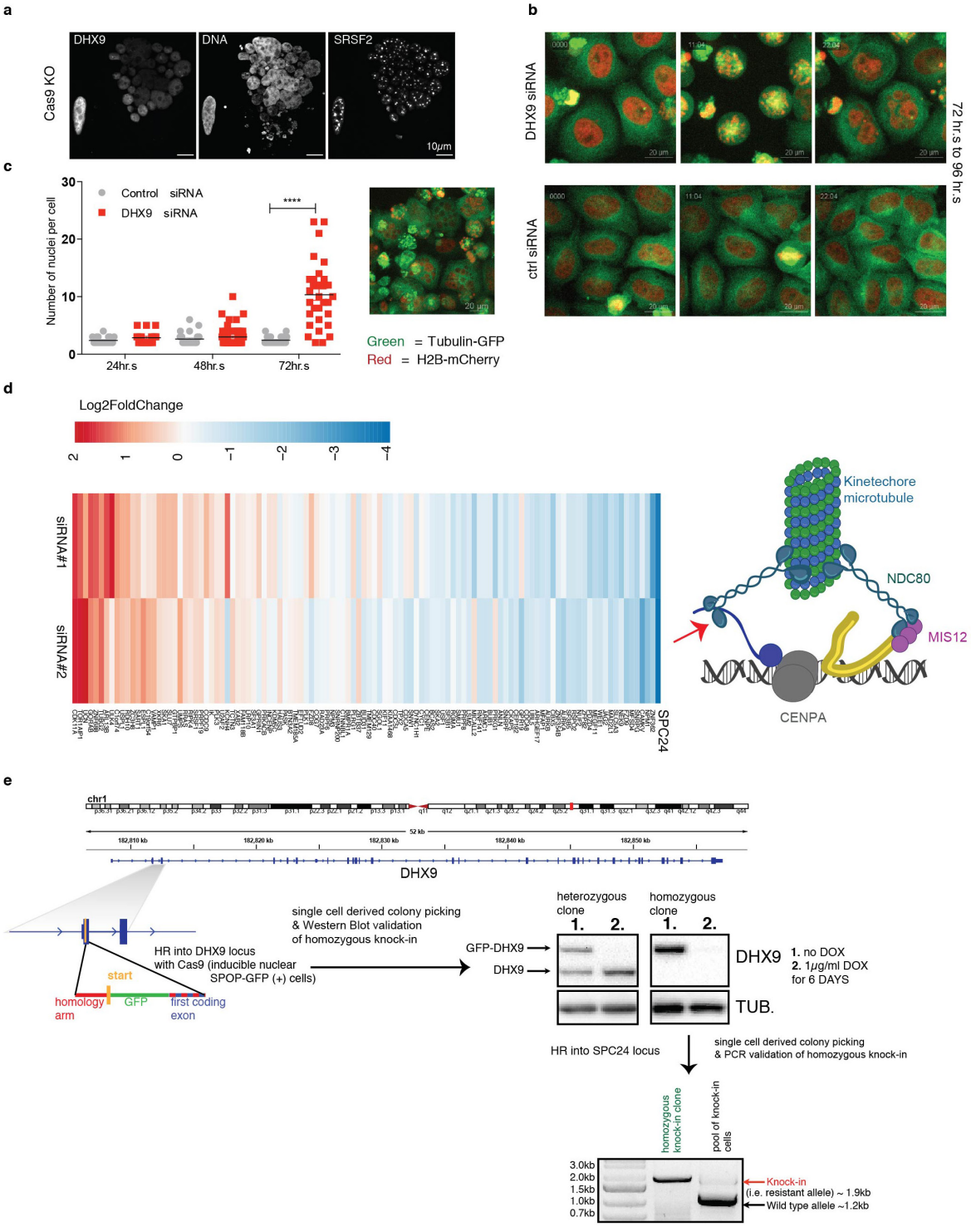

Extended Data Figure 8 | See next page for caption.

Extended Data Figure 8 | DHX9 depletion leads to a catastrophic disintegration of the nucleus. a, CRISPR–Cas9 DHX9-knockout cell (on the right side of the image) displays a multinucleated cell phenotype in comparison to a DHX9-expressing cell (on the left side of the image). Scale bar, 10 μm. **b**, Three still images from Supplementary Video 1 (control) and Supplementary Video 3 (knockdown) representing the start, middle and end point of 22-h-long live imaging for control or DHX9-siRNA-treated HeLa H2B–mCherry, tubulin–GFP cells. **c**, Quantification of the number of nuclei at the end point of live cell imaging (∼24 h imaging duration). Time points on the graph represent the start point of the imaging. All the imaged fields are taken into consideration and only the cells with more than one nucleus are included in the analysis. Statistical analysis performed with Kruskal–Wallis test shows that only the 72–96 h time point of DHX9-knockdown cells significantly differs from the rest with a $P < 0.0001$ (Kruskal–Wallis). Also see Supplementary Videos 2 and 7 for full field views of imaging and Supplementary Videos 5 and 6 for a second siRNA knockdown of DHX9. Right, multinucleated cells at the end point of imaging (at 96 h of DHX9 knockdown) in a different field from Supplementary Video 7. **d**, Left, expression levels for the Mitocheck Consortium Grape phenotype category genes (117 are expressed in the RNA-seq out of the 153 in total, mean counts per million > 0). Right, schematic view of the Ndc80 complex, red arrow points at the SPC24 protein. **e**, Left, experimental design of the homologous recombination of the GFP tag at the DHX9 locus is shown. Single-cell-derived heterozygously or homozygously GFP-tagged clones successfully deplete the GFP–DHX9 protein upon doxycycline induction of SPOP–GFP. Right, PCR-based screening of the knock-in allele is shown for pool of cells before the colony picking and the homozygous knock-in *Alu*-bypass SPC24 clone after isolation. Knock-in causes a size shift of the PCR product (from 1.2 to 1.9 kb). Correct insertion of the repair construct into the endogenous locus is further validated by Sanger sequencing (not shown).

RESEARCH LETTER

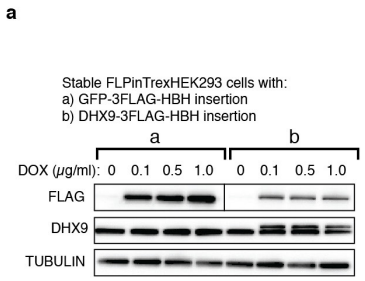

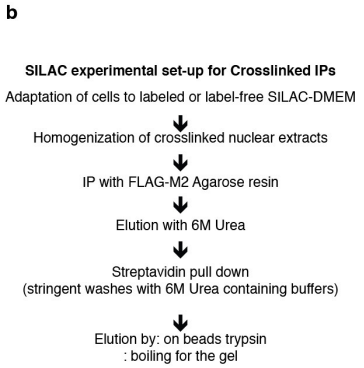

c

On-beads trypsin digest forward and reverse experiments

Gene names	Ratio H/L DHX9_E1_fw	Ratio H/L DHX9_E2_rev	INVERSE Ratio DHX9_E2_rev (L/H)	Average enrichment
DHX9	23.414	0.014	69.247	46.331
ADAR	5.847	0.076	13.106	9.476
DHX30	NaN	0.012	83.333	83.333
ZFR	9.158	0.043	23.017	16.087
ILF3	3.784	0.108	9.270	6.527
MATR3	7.751	0.038	26.501	17.126
SFPQ	10.324	0.031	32.687	21.506
HNRNPM	11.153	0.030	33.735	22.444
NONO	10.394	0.038	26.459	18.427
PSPC1	NaN	0.045	22.300	22.300
EIF4A3	4.165	0.121	8.267	6.216
HNRNPA1;HNRNPA1L2	9.413	0.034	29.036	19.224
ELAVL1	7.118	0.072	13.870	10.494
RALY	5.287	0.066	15.202	10.245
HNRNPC	11.750	0.026	38.814	25.282

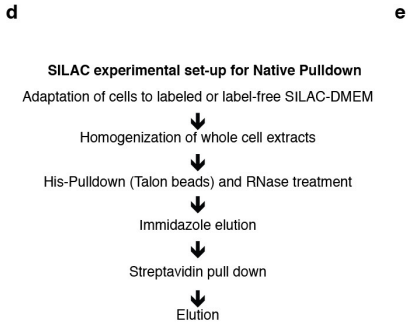

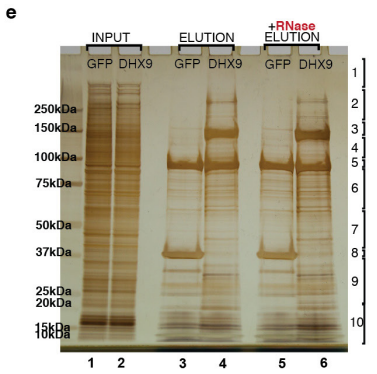

f

Gene names	INVERSE Ratio DHX9_E2_rev (L/H) no RNase	INVERSE Ratio DHX9_E2_rev (L/H) with RNase	Fold change upon RNase
DHX9	235.593	9.293	25.352
ADAR	41.596	14.547	2.859
DHX30	156.397	13.822	11.315
ZFR	Not detected	Not detected	N.A.
ILF3	28.891	12.895	2.240
MATR3	16.906	4.504	3.754
SFPQ	1.943	1.546	1.257
HNRNPM	35.845	5.828	6.150
NONO	1.761	1.260	1.398
PSPC1	2.078	Not detected	N.A.
EIF4A3	29.526	Not detected	N.A.
HNRNPA1;HNRNPA1L2	Not detected	Not detected	N.A.
ELAVL1	46.320	2.664	17.387
RALY	70.378	3.977	17.697
HNRNPC	177.450	2.451	72.385

mRNA stability related | NF45 interacting | Paraspeckles associated

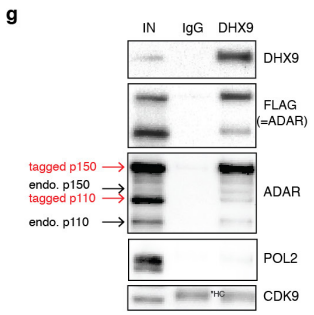

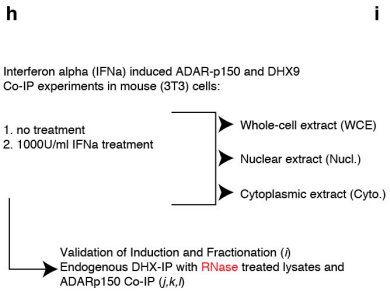

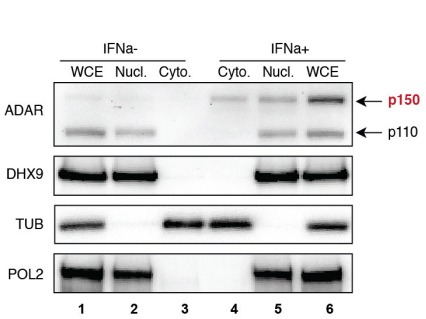

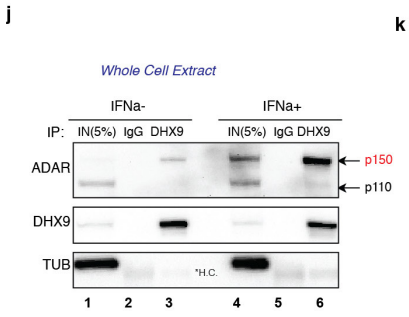

k (same as in Figure 4c)

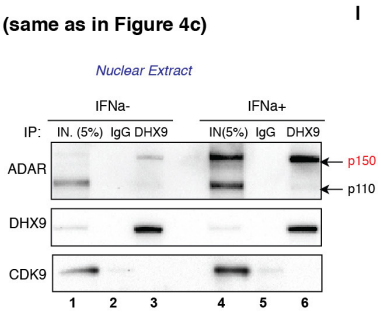

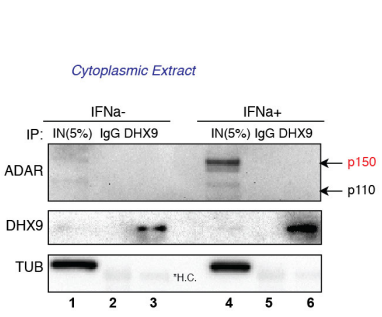

Extended Data Figure 9 | See next page for caption.

Extended Data Figure 9 | Tandem affinity purification of DHX9 from crosslinked nuclear extracts or native whole-cell extracts identifies a set of RNA-binding proteins that interact with DHX9. **a**, Induction test for the stable FLPinTrex HEK293 cell line with a single-copy C-terminal 3×Flag–6×His–biotin–6×His-tagged GFP or DHX9 protein. **b**, Experimental set-up for the SILAC quantified formaldehyde crosslinked DHX9 interactome (either loaded on gel or eluted from beads by trypsinization) obtained by tandem affinity purification. **c**, Fold enrichment values of on bead digested proteins from forward and reverse SILAC experiments (forward: DHX9 cells are grown in heavy isotope labelled SILAC medium and GFP cells are grown in unlabelled medium; reverse: DHX9 cells are grown in unlabelled medium and GFP cells are grown in heavy isotope labelled SILAC medium) for those proteins highlighted in Fig. 4a. **d**, Experimental set-up for the affinity tag pull-downs employing native whole-cell extracts that were used for in-gel digestion LC–MS. **e**, Silver-stain gel of native pull-down experiments, where lanes 1 and 2 show the input from GFP and DHX9 cell lines (DHX9 cells are grown in unlabelled medium and GFP cells are grown in heavy isotope labelled SILAC medium), lanes 3 and 4 are the final eluates of His-tag pull-down followed by streptavidin pull-downs from GFP and DHX9 cell lines, and lanes 5 and 6 are RNaseA-treated final eluates. The gel is cut into 10 slices as shown and both GFP and DHX9 lanes are combined (3 and 4 together; 5 and 6 together) prior to mass-spectrometry analysis. **f**, Fold enrichment values in the native purifications for the proteins highlighted in Fig. 4a, showing a depletion for most of these proteins upon RNase digestion. **g**, Validation of DHX9 interaction with ADAR is shown in a stable cell line for ADAR that can express both p110 and p150 isoforms. The doublet is detected with a blot for Flag after DHX9 IP in this stable cell line. POL2 and CDK9 blots serve as loading controls. **h**, The description of the experimental set-up for IFNα induction and DHX9–ADAR co-IP in different fractions of the mouse 3T3 cell line. **i**, Validation of fractionation with tubulin (lanes 3, 4) and RNA–POL2 blots (lanes 2, 5) and IFNα induction of ADAR(p150) (lanes 5 and 6). **j**–**l**, Mouse DHX9 interacts with ADAR(p150) in the whole cell (**j**, lanes 3 and 6) and nuclear extracts (**k**, lanes 3 and 6) but not in the cytoplasmic extracts (**l**, lanes 3 and 6).

RESEARCH LETTER

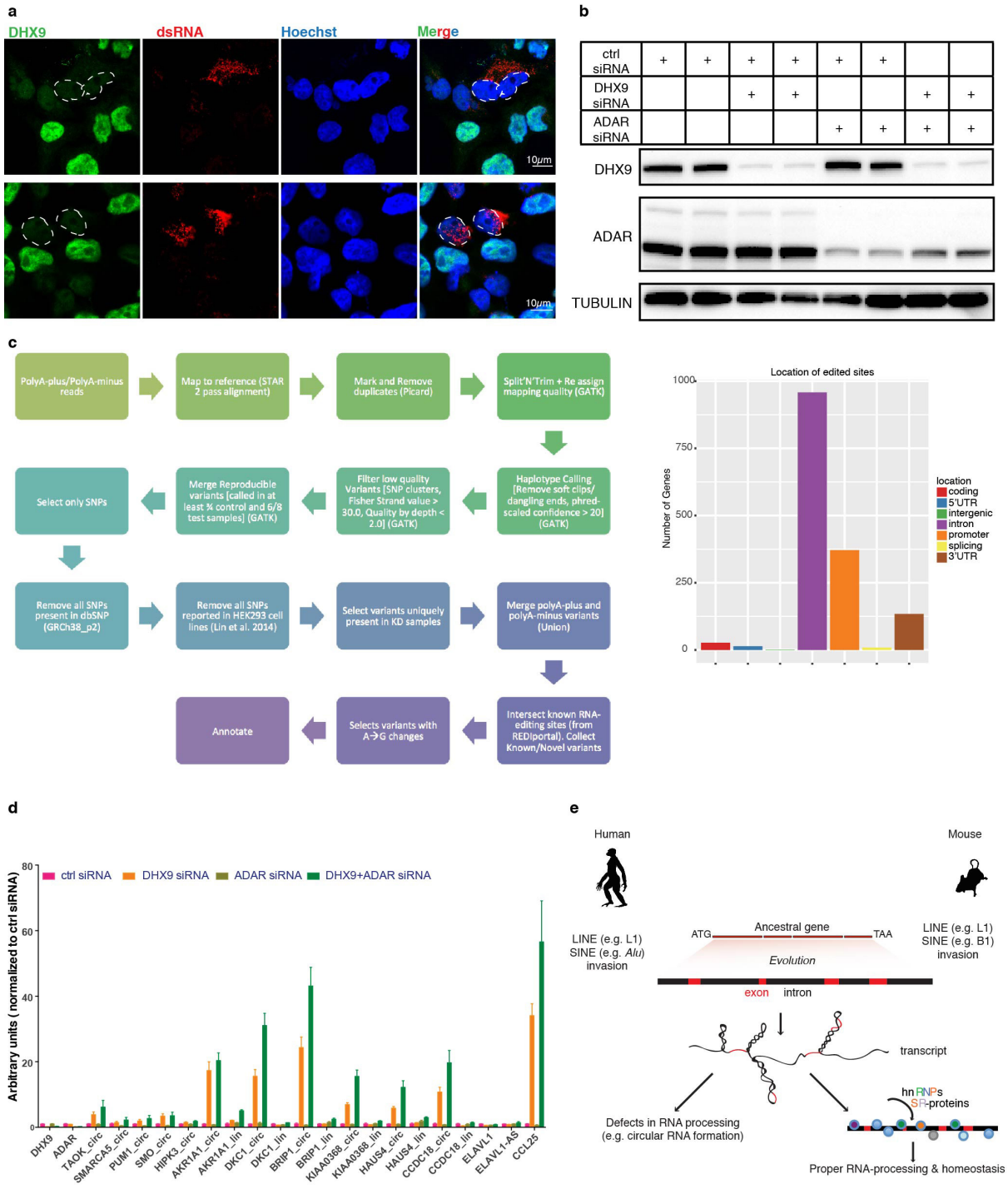

Extended Data Figure 10 | See next page for caption.

Extended Data Figure 10 | DHX9 and ADAR cooperatively work on large RNA secondary structures. a, Anti-DHX9 and J2 (dsRNA) antibody staining are shown for a mixed population of cells treated with control siRNA (DHX9 staining present, green) and DHX9 siRNA (DHX9 staining absent, for example, marked nuclei). DHX9-depleted cells accumulate dsRNA. **b**, The efficiency of knockdown in replicate experiments for J2 pull-down experiment displayed in Fig. 4e are shown by western blot. **c**, Left, analysis pipeline for detecting differential editing between control and knockdown RNA-seq libraries (both poly(A)$^+$ and poly(A)$^-$ considered). Right, distribution of differential A-to-I editing sites detected in DHX9 knockdown is shown. After filtering for known SNPs from dbSNP and HEK293 genome, 1,244 genes with 1,807 potential A-to-I RNA editing changes in DHX9-siRNA-treated samples were detected which were absent in controls. 48% of these sites have been reported previously[51]. 77% of genes showing editing changes have these changes within introns. Additionally, we observed that 21% of genes with intronic editing also showed splicing defects and 28% of genes with overall editing showed misregulation (differentially expressed) upon DHX9 knockdown. These genes are a small fraction of all the genes with splicing defects (4.5%) or expression changes (6%) observed in DHX9-depleted cells. **d**, Effect of DHX9, ADAR or double knockdown of DHX9 and ADAR on circular RNA generation and CCL25 upregulation is shown. ADAR depletion alone does not have an appreciable impact on circular RNA generation, whereas the effect of DHX9 depletion is augmented when it is combined with ADAR depletion. **e**, A summary model. *Alu* elements are the most abundant transposable elements making up >10% of our own genomes. These elements are potentially harmful to their host and are depleted entirely from 5′ UTRs of genes and developmentally important loci, such as the *HOXA–D* clusters but are found in abundance in intronic and intergenic regions. We show that DHX9, a highly conserved, very abundant nuclear RNA helicase, directly interacts with *Alu* elements *in vivo* and suppresses circular RNA formation, which is probably a symptom of *Alu*-mediated splicing defects. We propose that our cells have developed a dependency on DHX9 to remove strong secondary structures, such as the ones originating from *Alu* insertions in the transcribed parts of our genome. We also show that in mice, DHX9 interacts with SINE B elements that are the murine equivalent of *Alu* elements, underscoring the flexibility of DHX9-mediated control of retrotransposon toxicity throughout evolution.

A.5 Update of the deepTools toolkit for exploring deep-sequencing data

I contributed to the development of deepTools2 (led by Fidel Ramirez and Devon Ryan) through features and bugfixes, and to the testing and update of the documentation and the galaxy server. I helped with the writing and revision of the manuscript by Fidel Ramirez and other authors.

W160–W165 *Nucleic Acids Research, 2016, Vol. 44, Web Server issue* *Published online 13 April 2016*
doi: 10.1093/nar/gkw257

deepTools2: a next generation web server for deep-sequencing data analysis

Fidel Ramírez[1,†], Devon P Ryan[1,†], Björn Grüning[2], Vivek Bhardwaj[1,3], Fabian Kilpert[1], Andreas S Richter[1], Steffen Heyne[1], Friederike Dündar[4] and Thomas Manke[1,*]

[1]Max Planck Institute of Immunobiology and Epigenetics, 79108 Freiburg, Germany, [2]University of Freiburg, Department of Computer Science, 79110 Freiburg, Germany, [3]Faculty of Biology, University of Freiburg, 79104 Freiburg, Germany and [4]Weill Cornell Medical College, Applied Bioinformatics Core, Department of Physiology and Biophysics, New York, NY 10065, USA

Received February 02, 2016; Revised March 22, 2016; Accepted April 02, 2016

ABSTRACT

We present an update to our Galaxy-based web server for processing and visualizing deeply sequenced data. Its core tool set, deepTools, allows users to perform complete bioinformatic workflows ranging from quality controls and normalizations of aligned reads to integrative analyses, including clustering and visualization approaches. Since we first described our deepTools Galaxy server in 2014, we have implemented new solutions for many requests from the community and our users. Here, we introduce significant enhancements and new tools to further improve data visualization and interpretation. deepTools continue to be open to all users and freely available as a web service at deeptools.ie-freiburg.mpg.de. The new deepTools2 suite can be easily deployed within any Galaxy framework via the toolshed repository, and we also provide source code for command line usage under Linux and Mac OS X. A public and documented API for access to deepTools functionality is also available.

INTRODUCTION

The analysis of data from high-throughput DNA sequencing experiments continues to be a major challenge for many researchers. The rapidly increasing diversity of experimental assays using high-throughput sequencing has led to a concomitant increase in the number of analysis packages that allow for insightful visualization and downstream analyses (e.g. ChAsE (1), the ChIP-seq web server (http://ccg.vital-it.ch/chipseq), Genomation (2), Homer (3), ngs.plot (4)). Many of these tools require command line experience and input data, which is already quality controlled and properly normalized. As a result, many research groups still do not have the capacity to process and analyse the data generated with deep sequencing technologies. With this in mind, we developed deepTools, a modular suite of fast and user-friendly tools that we implemented within a publicly accessible Galaxy instance (5). deepTools support a wide range of functions, such as various quality controls, different normalization schemes and genome-wide visualizations. Since the original publication of deepTools, and motivated by frequent requests from biologists and bioinformaticians, we have published 10 releases with numerous performance improvements and expansions of scope. In the process, we rewrote large sections of the code, revised the documentation, and updated our server hardware. We added new ways to process and filter deep sequencing data, provided new tools for quality control and analysis, and updated our documentation and examples. Moreover, we have significantly increased the computational speed (sometimes up to 100-fold), extended automated testing for most components, and created an API allowing others to seamlessly incorporate deepTools' functionality into their own programs. Here, we present our latest release (deepTools2) and its associated web server, which is based on the well-known Galaxy platform (6). This ensures that users lacking access to specialized resources and servers can still benefit from a simple and flexible framework for reproducible analysis.

POWERFUL WEB SERVER FOR DEEP SEQUENCING ANALYSES

Our deepTools Galaxy server is freely available at http://deeptools.ie-freiburg.mpg.de. The deepTools suite supports four common tasks: (i) quality control, (ii) data processing and normalization, (iii) data integration and (iv) visualization (see Table 1). The package has been designed to take as input files some of the most established formats in the deep sequencing field, such as BAM for aligned reads, bigWig for scores (e.g. normalized read coverages) associated with genomic regions, and BED for coordinates of genome

*To whom correspondence should be addressed. Tel: +49 761 5108738; Fax: +49 761 5108 80738; Email: manke@ie-freiburg.mpg.de
†These authors contributed equally to the paper as first authors.

Nucleic Acids Research, 2016, Vol. 44, Web Server issue **W161**

regions. All tools come with a large number of options that can be used to fine-tune analyses or filter input datasets for faster data exploration. The visualizations and output files encompass highly customizable, publication-ready images as well as genome-wide scores in bigWig or bedGraph format and tab-separated summaries, e.g. of pairwise correlation metrics that can readily be used for further downstream analyses.

Users can upload data from their computers, e.g. via FTP, and can download additional files from the UCSC table browser (7). In addition, we have added more commonly used reference genomes and annotations to the web server's data library. Moreover, comprehensive test data is provided to allow users to easily explore the server's functionality without the need to upload their own data. Registered users can share data, histories and workflows with collaborators and reviewers. To support the increasing number of users, we have made substantial upgrades to our hardware, both in terms of the number of CPUs and available storage.

ADDITIONAL QUALITY CONTROLS

The first step of all analyses is quality control. In addition to the previously established GC-bias detection (*computeGCbias*) and the ChIP-specific assessment of enrichment (*plotFingerprint*), we have expanded the diagnostic capabilities of deepTools (Figure 1A). First, we have added a new program, *plotCoverage*, to inspect the genome-wide distribution of fragment coverage for several samples. This is crucial information for deciding whether the basic goals of the experimental design were met, particularly regarding the desired sequencing depth. For paired-end data, the new program *bamPEFragmentSize* provides a very sensitive quality check of whether the size distribution of sequenced fragments corresponds to the expectations based on the library preparation. The average fragment size of a sample is also an important parameter for many downstream analyses, such as peak calling (8,9).

Finally, we have enhanced the capacity for comparative quality control and replicate analysis over multiple samples. Users can now perform principal component analysis (PCA) of multiple samples and generate the corresponding plots with the program *plotPCA*. This tool takes as input a matrix, in which each column represents a sample-specific vector of fragment counts or any other genome-wide score. It can unveil unexpected patterns, such as batch effects, outliers or sample swaps. In a similar vein, *plotCorrelation* has been significantly updated to fine-tune the joint analysis of samples and visualization of the correlation structure. It is now also able to produce scatterplots. Previously, the correlation analysis was performed together with the data collection from BAM files by one tool, *bamCorrelate*. To improve both speed and flexibility, we have replaced this tool and separated the computationally demanding data retrieval from the actual visualization tasks (*plotCorrelation* and *plotPCA*). The data collection step can now be done using *multiBamSummary* or *multiBigwigSummary,* as described below.

ENHANCED PROCESSING FLEXIBILITY, SCOPE AND SPEED

Once the general quality controls have been carried out, researchers are faced with the actual processing of data, such as filtering, normalization and format conversions. Due to the sheer size of the aligned reads files, this is a non-trivial and cumbersome aspect of all deep sequencing workflows. Our web server supports this challenging part in two ways: (i) the Galaxy environment automatically keeps track of every analysis step, so that users can always and indefinitely identify the tools and parameters that were used to generate a file; (ii) deepTools can perform combined filtering, normalization and format conversion in a single framework, which has contributed to the appeal of deepTools even outside the web server. An important enhancement in this regard is the general support of all deepTools components for flexible filtering of alignments files (BAM) based on the SAM flag (10), in addition to the optional exclusion of duplicates and reads with low alignment scores. This is designed to prevent accumulation of large and unnecessary intermediate files that often occur when different filtering strategies are compared.

We have also enhanced the capability of deepTools to recognize and process new sequencing read types. For example, deepTools now parses CIGAR strings and spliced-read alignments. This is particularly important for *bamCoverage*, which can now properly handle spliced reads from strand-specific RNA-seq data and convert them into meaningful coverage tracks (Figure 1B). The same tool was also enhanced to accommodate MNase-seq data, which results in very high-resolution summaries for nucleosome positions.

Frequently, genome-wide data is available from large consortia and data portals, such as IHEC (http://ihec-epigenomes.org), ENCODE (https://www.encodeproject.org) and BLUEPRINT (http://www.blueprint-epigenome.eu). In most cases, the provided data has already been processed and normalized. Since this information is most commonly stored as bigWig files, most deepTools components now have the capacity to handle data stored in bigWig format. Importantly, the processing of bigWig files was sped up by up to 100-fold by using the new Python *pyBigWig* package (http://dx.doi.org/10.5281/zenodo.45238) and the *libBigWig* library written in C (http://dx.doi.org/10.5281/zenodo.45278), which were developed simultaneously as side projects. The command line versions of the tools additionally allow users to directly use remotely stored files without downloading them beforehand.

IMPROVED INTEGRATIVE ANALYSES AND VISUALIZATIONS

Following the normalization and aggregation of aligned reads, visualization of the data is a vital part of almost every bioinformatics analysis as it allows users to explore their data and generate hypotheses. In addition, downstream analyses and data interpretation often depend on the integration of multiple samples. One of the major changes for deepTools2 is the capability to process numerous signal (bigWig) and region files (BED) in a joint analysis, particularly for summarizing fragment coverages or other scores

W162 *Nucleic Acids Research, 2016, Vol. 44, Web Server issue*

Table 1. Typical applications of deepTools components and a summary of their main inputs and outputs

tool	application	input files	main output file(s)
quality control			
plotCorrelation	compute and visualize correlations between multiple samples	output from *multiBamSummary* or *multiBigwigSummary*	heatmap of correlation coefficients, pairwise scatterplots
plotPCA	compute and visualize the principal component analysis	output from *multiBamSummary* or *multiBigwigSummary*	PCA plot, scree plot
plotFingerprint (prev.: *bamFingerprint*)	assess enrichment strength of a ChIP-seq experiment	2 or more BAM	diagnostic plot
computeGCBias	calculate the expected and observed GC distribution of reads	1 BAM and one 2bit, optional: 1 BED	diagnostic plots, tabular output for *correctGCBias*
plotCoverage	compute the coverage distribution	1 or more BAM	diagnostic plot and tabular output
bamPEFragmentSize	compute distribution of fragment lengths for paired-end alignments	1 BAM	distribution plot and summary statistics
data processing and normalization			
multiBamSummary	count the number of overlapping reads per bin or genomic region across multiple samples	2 or more BAM, optional: 1 BED	compressed matrix data
multiBigwigSummary	calculate binned, genome-wide scores across multiple samples	2 or more bigWig, optional: 1 BED	compressed matrix data
bamCoverage	obtain the sequencing depth normalized read coverage of a single sample	1 BAM	bedGraph or bigWig
bamCompare	normalize the read coverage of 2 samples with a specific operation (e.g. log2ratio, difference)	2 BAM	bedGraph or bigWig
correctGCBias	obtain a BAM file with reads distributed according to the genome's GC content	1 BAM and tabular output from *computeGCbias*	GC bias-corrected BAM
computeMatrix	compute distribution of scores over aligned genomic regions	1 or more bigWig, 1 or more BED	compressed matrix data
heatmaps and summary plots			
plotHeatmap (prev.: *heatmapper)*	visualize pre-computed scores per genomic region	*computeMatrix* output	heatmap plot
plotProfile (prev.: profiler)	visualize score summaries over groups of genomic regions	*computeMatrix* output	summary plot ("meta-profile")
plotCoverage	assess the sequencing depth by way of calculating the frequencies of read coverages	1 or more BAM	diagnostic plots

Nucleic Acids Research, 2016, Vol. 44, Web Server issue **W163**

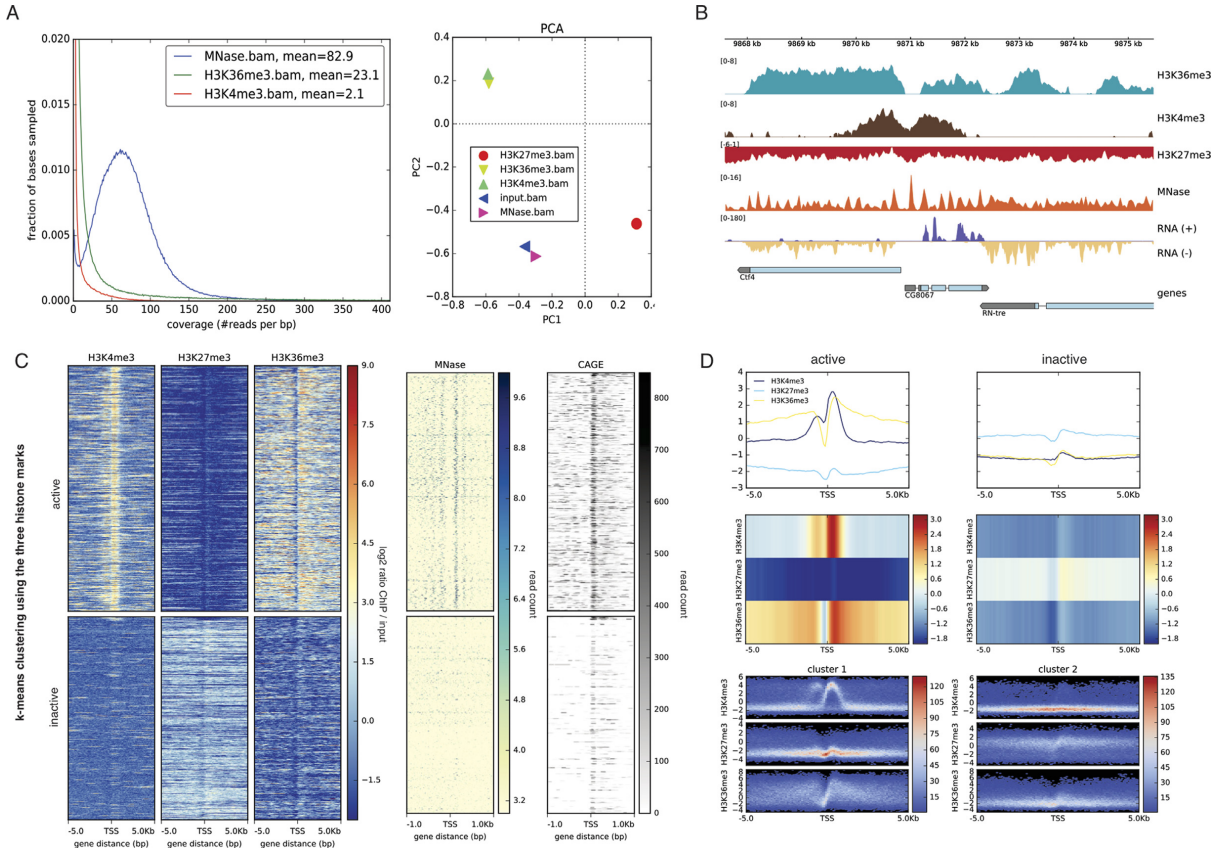

Figure 1. deepTools2 has enhanced features for quality control, data reduction, normalization and visualization of deeply sequenced data. (**A**) deepTools2 comes with two new quality control tools: *plotCoverage*, which displays sequencing depth distribution; and *plotPCA*, which plots the results of principal component analysis *(PCA)* on BAM or bigWig files. (**B**) Signal visualization by means of normalized bigWig tracks, produced by deepTools' *bamCompare* (ChIP-seq samples) and *bamCoverage*, which can now handle MNase- and strand-specific RNA-seq samples. In the genes track, the gray color represents untranslated regions and the thin lines represent introns. (**C**) *computeMatrix* and *plotHeatmap* were used to summarize and cluster multiple bigWig scores over genomic intervals. The image shows the resulting *k*-means clustering of ChIP-seq signals of three histone marks around the transcription start site of genes (with $k = 2$). Subsequently, the clustered regions were used to plot MNase-seq and CAGE read coverages. In the image, each row corresponds to the same genomic region. (**D**) *plotProfile* now offers additional means for visualization. The top panel shows the average signal for different samples and different cluster of regions (left and right plot). In the middle, the same profiles are represented as heatmaps. The bottom panel shows summary profiles where colors correspond to the observed frequency of the signal within each cluster. All data are from the *Drosophila melanogaster* S2 cell line and are publically available (see Section Accession numbers).

across genomic regions. The new tools *multiBamSummary* and *multiBigwigSummary* summarize the information from multiple samples into a single score for each region per sample. The resulting matrix can be used for correlation analyses, pairwise scatter plots and PCA (see above), or other downstream analyses.

Similarly, *computeMatrix* calculates the distribution of scores over selected genomic regions. Typical applications include the computation of signals around promoters or across gene bodies that are scaled to the same length. The primary purpose is to produce a matrix that can later be visualized. One of the most frequently requested features of deepTools was the extension of *computeMatrix* to allow for the combined analysis of multiple samples. Now, *computeMatrix* can aggregate regional scores from many different samples into a single matrix for subsequent visualization. Figure 1C illustrates this capability for 5 different signal files (H3K4me3, H3K27me3, H3K36me3, MNase, CAGE). Here, genome-wide scores were provided as five bigWig files, and a single BED file of annotated genes. From these inputs, *computeMatrix* generated a matrix file that was then visualized using *plotHeatmap* and *plotProfile*. Those tools have been extended to produce composite images of multiple heatmaps and summary profiles (Figure 1C and D). They also include options for unsupervised data analysis (*k*-means and hierarchical clustering), which are most useful if no prior grouping of regions is available. In the example of Figure 1C, two groups of regions were determined by *k*-means clustering of the signal profiles with $k = 2$. Alternatively, the user can provide multiple groups of predefined regions (multiple BED files) to *computeMatrix*. The tool will then output a structured matrix in which the rows are grouped according to the pre-defined regions, e.g. different sets of genes. Subsequent visualization corresponds

W164 Nucleic Acids Research, 2016, Vol. 44, Web Server issue

to a supervised analysis, where separate heatmaps and summary profiles are generated for each of the previously defined groups of interest. Both *plotHeatmap* and *plotProfile* now also offer many new options for customizing their output (Figure 1D).

IMPLEMENTATION AND ACCESS

Our deepTools web server has been implemented within the Galaxy framework (6). The software has been virtualized as a Docker container, which currently has access to 24 cores, 141GB memory and more than 8TB of disk storage. Our web server offers all deepTools' functionality for free and without registration. Users with more challenging requirements can access deepTools through multiple additional means:

Toolshed

For already existing local Galaxy instances, deepTools can be easily installed through the Galaxy toolshed (11).

Docker Image

For those wishing to use deepTools locally within the Galaxy framework, we have significantly simplified the way in which a deepTools Galaxy server can be deployed. Through incorporating everything in a single Docker container, users can now install a deepTools Galaxy web server on a desktop machine with a single command. Further details are available in our online documentation (http://deeptools.readthedocs.org/en/latest/content/installation.html).

Stand alone

deepTools can be installed through the Python package index (PyPi, https://pypi.python.org/pypi/deepTools), through GitHub (https://github.com/fidelram/deepTools) and in the bioconda channel of Anaconda (https://anaconda.org/bioconda/deeptools). More information can be found at http://deeptools.readthedocs.org/en/latest/content/installation.html.

API

Finally, deepTools are now fully available as a Python package. Numerous functions, such as the function for summarizing read counts from a BAM file per genomic region (countReadsPerBin), can easily be accessed in any Python script that imports the deepTools package. Usage details can be found at http://deeptools.readthedocs.org/en/latest/content/api.html.

EXTENSIVE TESTING, DOCUMENTATION AND COMMUNITY SUPPORT

deepTools have greatly benefited from transparent development as they are hosted on github.org, where users and collaborators can directly post issues, fork their own versions, and follow the changes to the code. All tools contain comprehensive and automatic tests that evaluate proper functioning after any modification of the code. We continuously update our documentation, and respond to questions sent to our mailing list (deeptools@googlegroups.com) and through the Galaxy bug report system. For this major update, we have reorganized the documentation with updated examples of tools usage, step-by-step protocols and FAQs. Also, detailed usage descriptions have been added to the Galaxy wrappers. To further improve our documentation, we migrated it to readthedocs.org, where we can offer versioned documentation and an easy way to export it as a composite PDF file. The most up-to-date documentation can now always be found at http://deeptools.readthedocs.org/en/latest/.

DISCUSSION AND OUTLOOK

The adoption of deep sequencing in many laboratories has created the need for accessible, efficient and transparent methods to process the data directly by the researchers. However, the ever-increasing throughput of deep sequencing technologies requires sophisticated bioinformatics solutions that are not always available to every lab. Via the deepTools web server, researchers can access a set of easy to use, yet powerful programs that cover quality control, normalization, integration and visualization of the data. Since deepTools employ a high level of parallelization for the computationally most expensive tasks, they are well suited to work with a large number of samples emerging from large-scale data production centers (12,13) or single-cell sequencing (14). The Galaxy framework is frequently used for establishing reproducible and standardized analysis workflows, even for groups where bioinformatics support is otherwise scarce. We have also found it to be a user-friendly environment that most biomedical scientists are comfortable with. This makes it a versatile platform for training workshops, as well as for sharing data and workflows among collaborators.

The modular design of deepTools has allowed us to significantly expand the scope of the analyses compared to its first release. More functionality can be added in the future, and since the software development is completely open and transparent, it will benefit from contributions from the wider community to incorporate new standards and best practices in this rapidly evolving field.

ACCESSION NUMBERS

The datasets used in Figure 1 were: H3K4me3 and H3K26me3 from GEO:GSE41440 (15), H3K36me3 from GEO:GSE27679 (16), MNase-seq from GEO:GSE58821 (17), CAGE from GEO:GSE52884 (18).

ACKNOWLEDGEMENTS

The authors would like to thank all users of deepTools for their constructive feedback and suggestions. We would further like to thank specific users for their valuable input: Peter Ebert, Sebastian Preissl and Ralf Gilsbach. We would also like to thank Abdullah Sahyoun for insightful discussions.

Nucleic Acids Research, 2016, Vol. 44, Web Server issue ***W165***

FUNDING

German Research Foundation [SFB 992, Project Z01]; German Epigenome Programme DEEP [01KU1216G]. Source of Open Access funding: own funds.
Conflict of interest statement. None declared.

REFERENCES

1. Younesy,H., Nielsen,C.B., Möller,T., Alder,O., Cullum,R., Lorincz,M.C., Karimi,M.M. and Jones,S.J.M. (2013) An interactive analysis and exploration tool for epigenomic data. *Comput. Graph. Forum*, **32**, 91–100.
2. Akalin,A., Franke,V., Vlahoviček,K., Mason,C.E. and Schübeler,D. (2015) Genomation: a toolkit to summarize, annotate and visualize genomic intervals. *Bioinformatics*, **31**, 1127–1129.
3. Heinz,S., Benner,C., Spann,N., Bertolino,E., Lin,Y.C., Laslo,P., Cheng,J.X., Murre,C., Singh,H. and Glass,C.K. (2010) Simple combinations of lineage-determining transcription factors prime cis-regulatory elements required for macrophage and B cell identities. *Mol. Cell*, **38**, 576–589.
4. Shen,L., Shao,N., Liu,X. and Nestler,E. (2014) ngs.plot: quick mining and visualization of next-generation sequencing data by integrating genomic databases. *BMC Genomics*, **15**, 284.
5. Ramírez,F., Dündar,F., Diehl,S., Grüning,B.A. and Manke,T. (2014) deepTools: a flexible platform for exploring deep-sequencing data. **42**, W187–W191.
6. Hillman-Jackson,J., Clements,D., Blankenberg,D., Taylor,J. and Nekrutenko,A.Galaxy Team (2012) Using Galaxy to perform large-scale interactive data analyses. *Curr. Protoc. Bioinformatics*, Chapter 10, Unit 10.5–10.5.47.
7. Speir,M.L., Zweig,A.S., Rosenbloom,K.R., Raney,B.J., Paten,B., Nejad,P., Lee,B.T., Learned,K., Karolchik,D., Hinrichs,A.S. *et al.* (2016) The UCSC Genome Browser database: 2016 update. *Nucleic Acids Res.*, **44**, D717–D725.
8. Feng,J., Liu,T., Qin,B., Zhang,Y. and Liu,X.S. (2012) Identifying ChIP-seq enrichment using MACS. *Nat. Protoc.*, **7**, 1728–1740.
9. Landt,S.G., Marinov,G.K., Kundaje,A., Kheradpour,P., Pauli,F., Batzoglou,S., Bernstein,B.E., Bickel,P., Brown,J.B., Cayting,P. *et al.* (2012) ChIP-seq guidelines and practices of the ENCODE and modENCODE consortia. *Genome Res.*, **22**, 1813–1831.
10. Li,H., Handsaker,B., Wysoker,A., Fennell,T., Ruan,J., Homer,N., Marth,G., Abecasis,G., Durbin,R. and 1000 Genome Project Data Processing Subgroup (2009) The sequence alignment/map format and SAMtools. *Bioinformatics*, **25**, 2078–2079.
11. Blankenberg,D., Von Kuster,G., Bouvier,E., Baker,D., Afgan,E., Stoler,N., Taylor,J., Nekrutenko,A. and Galaxy Team (2014) Dissemination of scientific software with Galaxy ToolShed. *Genome Biol.*, **15**, 403.
12. Bernstein,B.E., Birney,E., Dunham,I., Green,E.D., Gunter,C. and Snyder,M. (2012) An integrated encyclopedia of DNA elements in the human genome. *Nature*, **489**, 57–74.
13. Consortium,R.E., Kundaje,A., Meuleman,W., Ernst,J., Bilenky,M., Yen,A., Heravi-Moussavi,A., Kheradpour,P., Zhang,Z., Wang,J. *et al.* (2015) Integrative analysis of 111 reference human epigenomes. *Nature*, **518**, 317–330.
14. Klein,A.M., Mazutis,L., Akartuna,I., Tallapragada,N., Veres,A., Li,V., Peshkin,L., Weitz,D.A. and Kirschner,M.W. (2015) Droplet barcoding for single-cell transcriptomics applied to embryonic stem cells. *Cell*, **161**, 1187–1201.
15. Herz,H.-M., Mohan,M., Garruss,A.S., Liang,K., Takahashi,Y.-H., Mickey,K., Voets,O., Verrijzer,C.P. and Shilatifard,A. (2012) Enhancer-associated H3K4 monomethylation by Trithorax-related, the Drosophila homolog of mammalian Mll3/Mll4. *Genes Dev.*, **26**, 2604–2620.
16. Chen,Y., Negre,N., Li,Q., Mieczkowska,J.O., Slattery,M., Liu,T., Zhang,Y., Kim,T.-K., He,H.H., Zieba,J. *et al.* (2012) Systematic evaluation of factors influencing ChIP-seq fidelity. *Nat. Methods*, **9**, 609–614.
17. Ramírez,F., Lingg,T., Toscano,S., Lam,K.C., Georgiev,P., Chung,H.-R., Lajoie,B.R., de Wit,E., Zhan,Y., de Laat,W. *et al.* (2015) High-affinity sites form an interaction network to facilitate spreading of the MSL complex across the X chromosome in Drosophila. *Mol Cell*, **60**, 146–162.
18. Liang,J., Lacroix,L., Gamot,A., Cuddapah,S., Queille,S., Lhoumaud,P., Lepetit,P., Martin,P.G.P., Vogelmann,J., Court,F. *et al.* (2014) Chromatin immunoprecipitation indirect peaks highlight long-range interactions of insulator proteins and Pol II pausing. *Mol. Cell*, **53**, 672–681.

A.6 snakePipes enables reproducible epigenomic analysis

I developed the allele-specific and HiC workflows and contributed to DNA-mapping, ChIP-seq, ATAC-seq and RNA-seq workflows and documentation. I performed the analysis, prepared the figures and wrote the manuscript with input from all authors.

snakePipes enable flexible, scalable and integrative epigenomic analysis

Vivek Bhardwaj*[1,2], Steffen Heyne*[1], Katarzyna Sikora[1], Leily Rabbani[1], Michael Rauer[1], Fabian Kilpert[3], Andreas S Richter[4], Devon P Ryan[1#], Thomas Manke[1#]

[1]Max Planck Institute of Immunobiology and Epigenetics. Stübeweg 51, 79108 Freiburg Germany
[2]Faculty of Biology, University of Freiburg, Schänzlestraße 1, 79104 Freiburg, Germany
[3]Institutes of Neurogenetics & Cardiogenetics, University of Lübeck, Maria-Goeppert-Str. 1, 23562 Lübeck, Germany
[4]Genedata AG, Margarethenstrasse 38, 4053 Basel, Switzerland

* co-first authors (arranged alphabetically)
# Corresponding author
manke@ie-freiburg.mpg.de
+49 (0)761 5108738
ryan@ie-freiburg.mpg.de

Abstract

The scale and diversity of epigenomics data has been rapidly increasing and ever more studies now present analyses of data from multiple epigenomic techniques. Performing such integrative analysis is time-consuming, especially for exploratory research, since there are currently no pipelines available that allow fast processing of datasets from multiple epigenomic assays while also allow for flexibility in running or upgrading the workflows. Here we present a solution to this problem : snakePipes, which can process and perform downstream analysis of data from all common epigenomic techniques (ChIP-seq, RNA-seq, Bisulfite-seq, ATAC-seq, Hi-C and single-cell RNA-seq) in a single package. We demonstrate how snakePipes can simplify integrative analysis by reproducing and extending the results from a recently published large-scale epigenomics study with a few simple commands. snakePipes are available under an open-source license at https://github.com/maxplanck-ie/snakepipes.

Main

Epigenomics is a fast growing field, and due to the consistent fall in the price of sequencing, increase in multiplexing abilities, and multiple innovations in laboratory protocols, it has become increasingly convenient to perform multiple epigenomic assays within a project. However, a major bottleneck on the way to process and analyse this data in a reproducible way, particularly for novice analysts, is the availability of analysis pipelines. Next-generation sequencing (NGS) analysis pipelines are composed of a series of data processing steps, employ standardised processing parameters, and are usually scalable to large number of samples [1]. Due to such properties, most pipelines are currently developed and deployed for settings where standardized, large scale analysis is required. Examples are RNA-seq variant-calling pipelines deployed in clinical settings [2], or processing pipelines developed for large-scale consortia [3,4].

However, in a typical basic science research setting, researchers also seek to modify parameters, update tool versions or extend the workflows, while maintaining their scalability and ease-of-use. Conventional NGS pipelines, although scalable, do not allow for this flexibility. Options for exploratory and downstream analysis have been limited, resulting in various expert users developing their own custom pipelines suited to their needs. Computational frameworks such as Galaxy [5] and Nextflow [6] exist, but they still demand novice users to be trained and implement their workflows themselves from scratch. This leads to a conundrum, how can we provide a set of workflows following best-practices that are easy to install and run for the novice users, while still providing the flexibility of extending and upgrading the workflows to the expert users?

We developed snakePipes to address such requirements. snakePipes provide flexible processing as well as downstream analysis of data from the most common assays used in epigenomic studies: ChIP-seq, RNA-seq, whole-genome bisulfite-seq (WGBS), ATAC-seq, Hi-C and single-cell RNA-seq in a single package (Fig. 1b, Implementation Details). It employs snakemake [7] as a workflow language, which benefits from easy readability of the code, widespread adoption, and offers scalability using most cluster and cloud computing platforms. snakePipes also makes use of conda environments and the bioconda platform [8], which allow hassle-free installation and upgrade of tools (Fig. 1a, Implementation Details). Conda environments allow execution of tools avoiding dependency conflicts, and do not require root permissions to run. Due to a modular architecture, various tools are shared between workflows, which simplifies data integration since data from multiple technologies are processed using identical tool versions and genome annotations. The genome annotations and indices are shared by all workflows, and can also be generated directly via snakePipes, facilitating easy setup as well as integrative analysis. Finally, workflows in snakePipes employ extensive quality-checks and also produce reports using multiQC [9] and R, that inform the user of processing and analysis results.

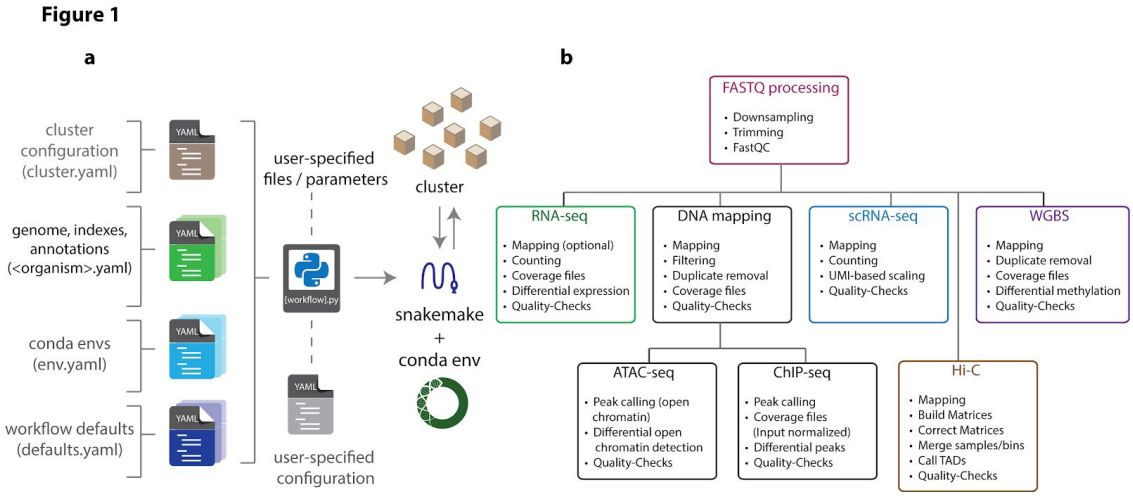

Figure 1. General architecture and available workflows in snakePipes. a. Configuration. *All configurable parameters for snakepipes are defined as YAML files. Organism-specific YAML files need to be configured once during setup, while the configuration of cluster, conda envs and workflow defaults is optional. After installation, the location of these files can be revealed by the snakePipes info command. Workflows are all executed using their command line wrappers. During execution user parameters and/or a user-provided YAML file can be used to override the workflow defaults and add flexibility to the processing/analysis.* ***b. Execution.*** *FASTQ files provided by the user first goes through FASTQ processing, followed by one of the workflows. Outputs from DNA mapping workflow can be further used as input for the ChIP-seq and ATAC-seq workflows. Only general processing steps are listed and each workflow includes workflow-specific quality-checks.*

Apart from conventional processing steps such as mapping, counting and peak calling, workflows in snakePipes also include various downstream analysis. All workflows (except scRNA-seq workflow) optionally accept a sample information (tab-separated) file that can be used to define groups of sample. This allows comparative analysis such as differential gene or transcript expression analysis for the RNA-seq workflow, differential peak calling for ChIP-Seq workflow, differential open chromatin detection for ATAC-seq workflow, and detection of differentially methylated regions (either de-novo or on user-specified regions) for WGBS workflow. The HiC workflow uses sample information to merge groups and can perform TAD calling with parameters adapted to the resolution of produced matrix (using HiCExplorer [10]). This preliminary analysis, combined with visualization-ready bed and bigwig files, allows users to quickly interpret their data.

Most workflows in snakePipes also allow processing and downstream analysis of data in an allele-specific manner. DNA-mapping and RNA-seq workflows utilize SNPSplit [11] to map data to a single or dual-hybrid genome, for samples coming from inbred mouse strains or from *Drosophila* SNP lines using the "allelic-mapping" mode. Single/dual hybrid genome indices can be provided externally, or can be created on the fly by simply providing a VCF file [12] and the name of desired strains. The workflows also generate allele-specific coverage files, QC reports, and performs allele-specific differential analysis using appropriate statistical design, without requiring any additional user intervention.

In order to demonstrate how snakePipes can simplify analysis and interpretation of data from multiple epigenomic assays, we downloaded and processed data from from a recently published study that investigated the role of Smchd1 protein on the mammalian X-chromosome [13]. The knock-out of Smchd1 in mouse neural progenitor cells (NPCs) affects the organization of inactive X-chromosome and leads to a loss of H3K27me3 domains along with a gain of H3K4me3 on various genes on the inactive X-chromosome. This results in de-repression of genes, seen as up-regulation in RNA-seq data. We observed the same effects upon re-analysis of the ChIP-Seq, RNA-seq and Hi-C data from the study, directly from the output of snakePipes, without further downstream analysis (Fig 2, Fig S1a-b). Further, we integrated this information with ATAC-seq data available online [14] to discover that the genes de-repressed upon Smchd1 knock-out display significantly higher open chromatin signal at their promoters in the wild-type NPCs, compared to down-regulated or unchanged, lowly expressed genes (Fig. S1c). Whole-genome bisulfite data obtained from another study (GSE101090) suggested that under wild-type conditions, promoters of the de-repressed genes show methylation levels slightly higher than the downregulated genes but significantly lower than unchanged, lowly expressed genes (Fig. S1d), corroborating previous [15] and recent [16] links between promoter CpG methylation and gene repression.

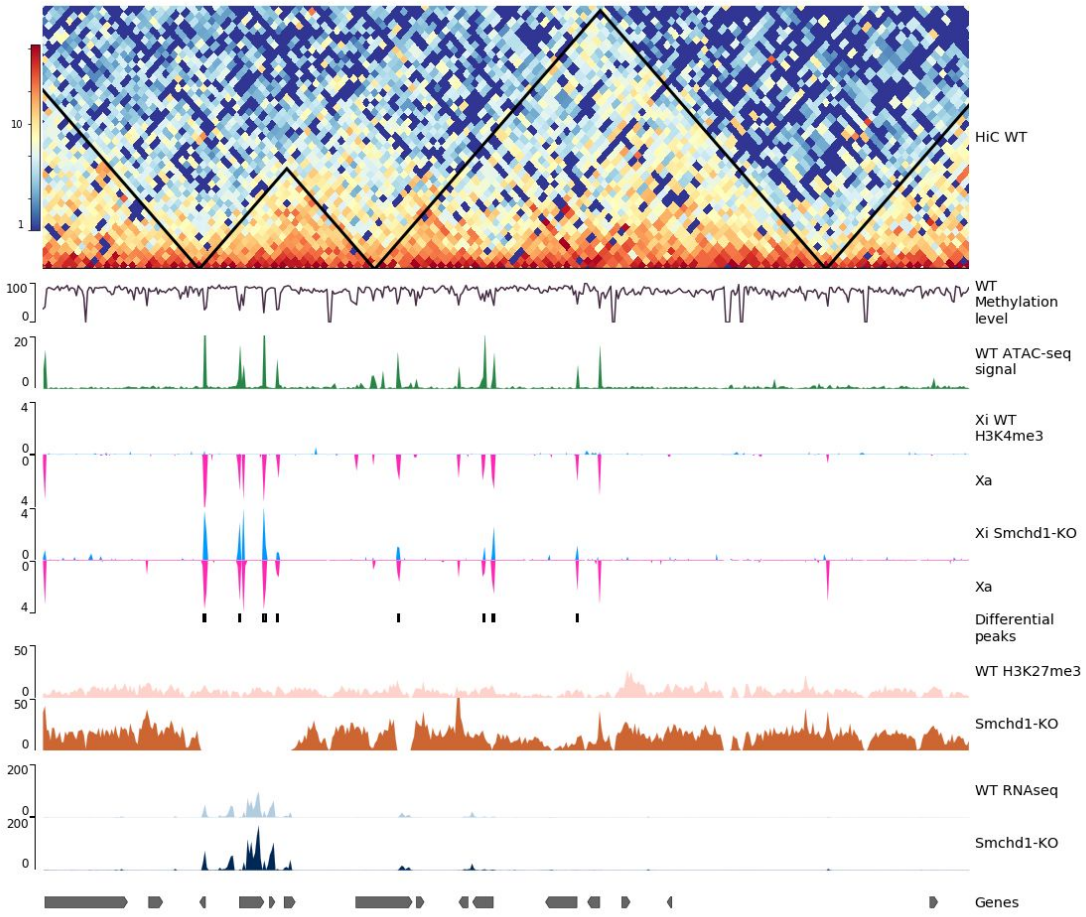

Figure 2. Outputs from snakePipes workflows quickly provide meaningful biological interpretation. *Genome tracks plotted using pyGenomeTracks [10]*. ***Top track:*** *output of HiC workflow with TADs (black triangles) on wild-type (WT) NPCs.* ***Tracks 2:*** *Methylation signal reported from the whole-genome bisulfite-seq (WGBS) workflow on wild-type NPCs. Gene promoters show demethylation.* ***Track 3****: Open chromatin signal from ATAC-seq workflow on wild-type NPCs.* ***Track 4-7 :*** *output of allele-specific ChIP-Seq workflow, Inactive X chromosome (Xi) tracks are in Blue while the active X chromosome (Xa) is shown in Pink. The knock-out (KO) of Smchd1 shows increase in H3K4me3 on Xi.* ***Track 8 :*** *Allele-specific differential peaks detected by the ChIP-Seq workflow in KO, over WT.* ***Track 9-10 :*** *H3K27me3 signal from the ChIP-Seq workflow. KO shows loss of H3K27me3 domains on certain genes.* ***Track 11-12 :*** *RPKM signal from RNA-seq workflow. Genes which loose H3K27me3 show up-regulation in KO.* ***Bottom track :*** *Genes.*

Our results demonstrate how a multi-assay epigenomic analysis toolkit like snakePipes could simplify data processing, reproduce previously published results, and allow new biological interpretations with minimal effort. snakePipes are under active development, open source and available via conda : `***conda install -c mpi-ie -c bioconda -c conda-forge snakePipes***`. Source code is available at https://github.com/maxplanck-ie/snakepipes and the documentation is hosted at https://snakepipes.readthedocs.io/en/latest/.

Implementation Details

General architecture of snakePipes

The general architecture of snakePipes is summarized in Fig. 1a. snakePipes utilizes conda and bioconda for setup and execution of workflows. All information required for workflow execution is stored in easy-to-edit YAML (Yet Another Markup Language) files. The **cluster.yaml** file defines the command used to execute each process on a cluster (assuming HPC cluster infrastructure like Slurm or SGE has been set up). For each organism of interest, the **<organism>.yaml** file describes the location of genome fasta, (mapping) indices and annotations. This allows running different workflows on exactly the same version of genome and annotations. The conda **env.yaml** file is used to specify version number of required tools for each workflow. The required tools are then fetched and setup automatically via the conda and bioconda repositories either during workflow setup, or execution. The **defaults.yaml** file specifies reasonable default parameter for each workflow according to the best practices for the most common sequencing protocols. These files are used by the command line wrappers, that use snakemake to execute the workflows on the cluster. In the absence of cluster setup, workflows can also be executed locally. Each step of a workflow is defined as a snakemake “rule”, which is executed in it’s own virtual environment, avoiding conflicts between tools. All log files, including user-supplied commands are written in the working directory, along with (optionally) a graph of executed steps. This allows users to easily reproduce and communicate their analysis in the future.

Running and testing the workflows

Comprehensive documentation for snakePipes can be found online: https://snakepipes.readthedocs.io/ and the test datasets are available on zenodo : https://zenodo.org/record/1346303 . snakePipes also provide a `***createIndices***` workflow that creates genome indices and annotations (contents of <organism>.yaml) from a user-specified genome fasta file or URL.

Workflows in snakePipes

snakePipes provide DNA-mapping, ChIP-seq, ATAC-seq, RNA-seq, whole-genome bisulfite-seq (WGBS), HiC and single-cell RNA-seq workflows. All workflows make use of the common fastq downsampling (via seqtk (https://github.com/lh3/seqtk)) and trimming (via cutadapt [17] and Trim Galore! (https://www.bioinformatics.babraham.ac.uk/projects/trim_galore/)) module. All workflows also produce an interactive report using multiQC [9] that summarizes outputs from multiple workflow steps and samples.

In the **DNA-mapping** workflow, the fastq files are aligned to the genome via Bowtie2 [18] and filtering can be performed via samtools [19] using user-provided parameters. Various quality-checks are performed via SamBamba [20], Picard [21], deepTools [22] and (optionally) qualimap [23]. Coverage files (bigwigs) are generated via deepTools. The output of DNA-mapping workflow can then be used for ChIP-Seq or ATAC-seq workflows. DNA-mapping workflow handles both single and paired-end files and could also be used for whole-genome alignments.

The **ChIP-seq** workflow takes information about the samples (corresponding input controls, expected broad/sharp mark) using a yaml file, and performs ChIP-specific quality-checks via deepTools. It also generates input-normalized bigwig files and performs peak calling for both sharp (via MACS2 [24]) and broad (via histoneHMM [25]) marks. The **ATAC-seq** workflow takes paired-end DNA mapping output and performs quality-checks and filtering useful for ATAC-seq samples. It then performs detection of open chromatin using MACS2. Both ChIP-Seq and ATAC-Seq workflows can perform detection of differential peaks or differential open chromatin regions between groups of samples using CSAW [26], if a sample sheet is provided.

The **RNA-seq** workflow can be run in "alignment" or "alignment-*free*" mode. In the alignment mode, fastq files are aligned to the genome via user-selected aligner (STAR [27] or HISAT2 [28]) and high-quality primary alignments are counted via featureCounts [29]. In the alignment-free mode, the transcripts are directly quantified via Salmon [30]. Transcripts can be filtered for various features before quantification. Additionally, the "*deepTools_qc*" mode can be added, which performs various quality-checks via deepTools and produces normal and depth-normalized (RPKM) coverage files. Differential gene and transcript expression analysis could then be performed using DESeq2 [31], wasabi (https://github.com/COMBINE-lab/wasabi) and Sleuth [32].

The **scRNA-seq** workflow performs mapping and counting of data obtained from the CEL-Seq2 protocol [33]. Fastq files are first preprocessed by moving cell barcodes and unique molecular indices (UMIs) to read headers and then mapped using STAR (Dobin et al.). Quantification is then performed per-cell by accounting for UMIs and the resulting counts corrected for Poisson sampling. A variety of quality control steps are also taken, such as computing a heatmap per well-plate of obtained transcript counts and the correlation between reads and UMIs. After the workflow is finished the resulting counts files are ready for custom downstream analysis (e.g., clustering or differential expression).

The **Hi-C** workflow performs read mapping of paired-end HiC data using BWA [34]. It then uses HiCExplorer [10] to build and correct the Hi-C matrices using the iterative correction (ICE) method [35]. Matrices can be built at a user-specified resolution or at restriction fragment resolution by simply specifying the name of the restriction enzyme. The corrected HiC matrices can then be used for detection and visualization of topologically associated domains (TADs) [36]. Quality reports are produced using HiCExplorer and are then summarized by MultiQC for comparison of samples.

The **WGBS** (whole-genome bisulfite-seq) workflow performs mapping of paired-end WGBS-seq data on a bisulfite converted genome using bwa-meth [37]. To help assess the quality of the experiment, several metrics, including bisulfite conversion rate and coverage of random CpGs, are collected in a report. Counting of reads supporting methylated and unmethylated cytosines is performed with MethylDackel (https://github.com/dpryan79/MethylDackel). De novo discovery

of differentially methylated regions (DMRs) can also be performed using Metilene [38] if a sample sheet is provided.

Methods

Processing of Online data

HiC, ChIP-Seq, and RNA-seq data for Smchd KO and wild-type Neural Progenitor Cells (NPCs) was downloaded from GSE99991. ATAC-Seq data for wild-type NPCs was downloaded from GSE71156 and WGBS data for wild-type NPCs was downloaded from GSE101090. All data was processed with snakePipes (version 1.0.0alpha5) on mouse genome GRCm38 (mm10).

The parameters specified for processing the data are as follows:

ATAC-Seq

DNA-mapping performed on mouse genome with parameters : *`-m allelic-mapping -j 30 --gcbias --mapq 5 --dedup --fastqc --trim --properpairs*

ATAC-seq performed on DNA-mapping output with parameters : `*--bw-binsize 10*`. By default, fragments longer than 150 nt are removed from peak calling `*--atac-fragment-cutoff 150*`.

ChIP-Seq

DNA-mapping performed on a dual hybrid (129S1/CAST) mouse genome with parameters : *`-m allelic-mapping --trim --fastqc --bw-binsize 10 --plotFormat pdf --dedup --mapq 10 --SNPfile <snp_positions.txt> --Nmasked_index <bowtie2_index.bt2>* `

ChIP-Seq performed on DNA-mapping output with parameters : `--bw-binsize 10` with *chip_sampleInfo.yaml* file which specified the corresponding input controls and peak-type.

H3K4me3 samples were specified as `*sharp*` while the H3K27me3 samples were described as `*broad*`

RNA-Seq

RNA-seq workflow was run with parameters : `--fastqc --trim -m alignment,deepTools_qc --DE sampleinfo.tsv` where sampleinfo.tsv file defined groups with replicates (5 control and 5 knock-out samples). One of the knock-out samples was removed after inspecting PCA output (Fig. S1A) and workflow was re-run to obtain differentially expressed genes (Fig. S1B).

Hi-C

Hi-C workflow was run with parameters : `*--merge_samples --sampleInfo sampleinfo.tsv --distVsCount --bin_size 10000 --trim --fastqc*` where sampleinfo.tsv was used to define the two Hi-C replicates.

WGBS

WGBS workflow was run with all default parameters.

Downstream analysis

Plotting of ATAC-seq signal on up-regulated, down-regulated and 500 lowly expressed, un-affected genes was performed by subsetting gene sets from DESeq2 output of snakePipes RNA-seq module, followed by deepTools computeMatrix with options : *-a 5000 -b 5000*, and plotHeatmap with option *--plotType se* . For WGBS data, bedgraph output of CpG methylation signal from WGBS pipeline was converted to bigWig using *UCSCtools bedGraphToBigWig* and plotting using computeMatrix (--binsize 100) and plotHeatmap.

Code availability

snakePipes is open-source and freely available on GitHub : https://github.com/maxplanck-ie/snakepipes

Acknowledgements

Authors acknowledge the contribution of Gina Renschler and Jana Böhm on testing of workflows. We also thank Chen-Yu Wang for useful comments on our preprint. TM acknowledges funding from the German Science Foundation (CRC992 “Medical Epigenetics”).

Availability of data and materials

Online datasets re-analysed during this study are available in GEO with accession numbers : GSE99991, GSE71156 and GSE101090

Competing interests

The authors declare no competing interests.

Authors' contributions

VB developed the allele-specific and HiC workflows and contributed to DNA-mapping, ChIP-seq, ATAC-seq and RNA-seq workflows and documentation. SH developed the scRNA-seq workflow and documentation and contributed to DNA-mapping, ChIP-seq and RNA-seq workflows. DPR improved the wrapper design, integrated installation and conda support, contributed to the documentation and bug fixes to various workflows. KS developed the WGBS workflow and documentation. LR contributed to HiC workflow and documentation. MR developed ATAC-seq workflow. FK contributed to RNA-seq workflow. AR contributed to DNA-mapping and ChIP-seq workflow. FK, SH and AR contributed to the general design of snakePipes and wrote the early version of the wrappers. VB performed the analysis and wrote the manuscript with input from all authors. TM conceived the project and supervised the development of snakePipes.

References

1. Leipzig, J. A review of bioinformatic pipeline frameworks. *Brief. Bioinform.* **18,** 530–536 (2017).
2. Blanca, J. M., Pascual, L., Ziarsolo, P., Nuez, F. & Cañizares, J. ngs_backbone: a pipeline for read cleaning, mapping and SNP calling using next generation sequence. *BMC Genomics* **12,** 285 (2011).
3. Roadmap Epigenomics Consortium *et al.* Integrative analysis of 111 reference human epigenomes. *Nature* **518,** 317–330 (2015).
4. Fernández, J. M. *et al.* The BLUEPRINT Data Analysis Portal. *Cell Syst* **3,** 491–495.e5 (2016).
5. Goecks, J., Nekrutenko, A., Taylor, J. & Galaxy Team. Galaxy: a comprehensive approach for supporting accessible, reproducible, and transparent computational research in the life sciences. *Genome Biol.* **11,** R86 (2010).
6. Di Tommaso, P. *et al.* Nextflow enables reproducible computational workflows. *Nat. Biotechnol.* **35,** 316–319 (2017).
7. Köster, J. & Rahmann, S. Snakemake--a scalable bioinformatics workflow engine. *Bioinformatics* **28,** 2520–2522 (2012).
8. Grüning, B. *et al.* Bioconda: sustainable and comprehensive software distribution for the life sciences. *Nat. Methods* **15,** 475–476 (2018).
9. Ewels, P., Magnusson, M., Lundin, S. & Käller, M. MultiQC: summarize analysis results for

multiple tools and samples in a single report. *Bioinformatics* **32,** 3047–3048 (2016).

10. Ramírez, F. *et al.* High-resolution TADs reveal DNA sequences underlying genome organization in flies. *Nat. Commun.* **9,** 189 (2018).
11. Krueger, F. & Andrews, S. R. SNPsplit: Allele-specific splitting of alignments between genomes with known SNP genotypes. *F1000Res.* **5,** 1479 (2016).
12. Danecek, P. *et al.* The variant call format and VCFtools. *Bioinformatics* **27,** 2156–2158 (2011).
13. Wang, C.-Y., Jégu, T., Chu, H.-P., Oh, H. J. & Lee, J. T. SMCHD1 Merges Chromosome Compartments and Assists Formation of Super-Structures on the Inactive X. *Cell* **174,** 406–421.e25 (2018).
14. Giorgetti, L. *et al.* Structural organization of the inactive X chromosome in the mouse. *Nature* **535,** 575–579 (2016).
15. Schübeler, D. Function and information content of DNA methylation. *Nature* **517,** 321–326 (2015).
16. Korthauer, K. & Irizarry, R. A. Genome-wide repressive capacity of promoter DNA methylation is revealed through epigenomic manipulation. *bioRxiv* 381145 (2018). doi:10.1101/381145
17. Martin, M. Cutadapt removes adapter sequences from high-throughput sequencing reads. *EMBnet.journal* **17,** 10–12 (2011).
18. Langmead, B. & Salzberg, S. L. Fast gapped-read alignment with Bowtie 2. *Nat. Methods* **9,** 357–359 (2012).
19. Li, H. *et al.* 692 (2009). The Sequence Alignment/Map format and SAMtools. *Bioinformatics* **25,** 2078–2693
20. Tarasov, A., Vilella, A. J., Cuppen, E., Nijman, I. J. & Prins, P. Sambamba: fast processing

of NGS alignment formats. *Bioinformatics* **31,** 2032–2034 (2015).

21. McKenna, A. *et al.* The Genome Analysis Toolkit: a MapReduce framework for analyzing next-generation DNA sequencing data. *Genome Res.* **20,** 1297–1303 (2010).
22. Ramírez, F. *et al.* deepTools2: a next generation web server for deep-sequencing data analysis. *Nucleic Acids Res.* **44,** W160–5 (2016).
23. García-Alcalde, F. *et al.* Qualimap: evaluating next-generation sequencing alignment data. *Bioinformatics* **28,** 2678–2679 (2012).
24. Feng, J., Liu, T., Qin, B., Zhang, Y. & Liu, X. S. Identifying ChIP-seq enrichment using MACS. *Nat. Protoc.* **7,** 1728–1740 (2012).
25. Heinig, M. *et al.* histoneHMM: Differential analysis of histone modifications with broad genomic footprints. *BMC Bioinformatics* **16,** 60 (2015).
26. Lun, A. T. L. & Smyth, G. K. csaw: a Bioconductor package for differential binding analysis of ChIP-seq data using sliding windows. *Nucleic Acids Res.* **44,** e45 (2016).
27. Dobin, A. *et al.* STAR: ultrafast universal RNA-seq aligner. *Bioinformatics* **29,** 15–21 (2013).
28. Kim, D., Langmead, B. & Salzberg, S. HISAT2: graph-based alignment of next-generation sequencing reads to a population of genomes. (2017).
29. Liao, Y., Smyth, G. K. & Shi, W. featureCounts: an efficient general purpose program for assigning sequence reads to genomic features. *Bioinformatics* **30,** 923–930 (2014).
30. Patro, R., Duggal, G., Love, M. I., Irizarry, R. A. & Kingsford, C. Salmon provides fast and bias-aware quantification of transcript expression. *Nat. Methods* **14,** 417–419 (2017).
31. Love, M. I., Huber, W. & Anders, S. Moderated estimation of fold change and dispersion for RNA-seq data with DESeq2. *Genome Biol.* **15,** 550 (2014).
32. Pimentel, H., Bray, N. L., Puente, S., Melsted, P. & Pachter, L. Differential analysis of RNA-seq incorporating quantification uncertainty. *Nat. Methods* **14,** 687–690 (2017).

33. Hashimshony, T. *et al.* CEL-Seq2: sensitive highly-multiplexed single-cell RNA-Seq. *Genome Biol.* **17,** 77 (2016).
34. Li, H. Aligning sequence reads, clone sequences and assembly contigs with BWA-MEM. *arXiv [q-bio.GN]* (2013).
35. Imakaev, M. *et al.* Iterative correction of Hi-C data reveals hallmarks of chromosome organization. *Nat. Methods* **9,** 999–1003 (2012).
36. Dixon, J. R. *et al.* Topological domains in mammalian genomes identified by analysis of chromatin interactions. *Nature* **485,** 376–380 (2012).
37. Pedersen, B. S., Eyring, K., De, S., Yang, I. V. & Schwartz, D. A. Fast and accurate alignment of long bisulfite-seq reads. *arXiv [q-bio.GN]* (2014).
38. Jühling, F. *et al.* metilene: fast and sensitive calling of differentially methylated regions from bisulfite sequencing data. *Genome Res.* **26,** 256–262 (2016).

Figure S1

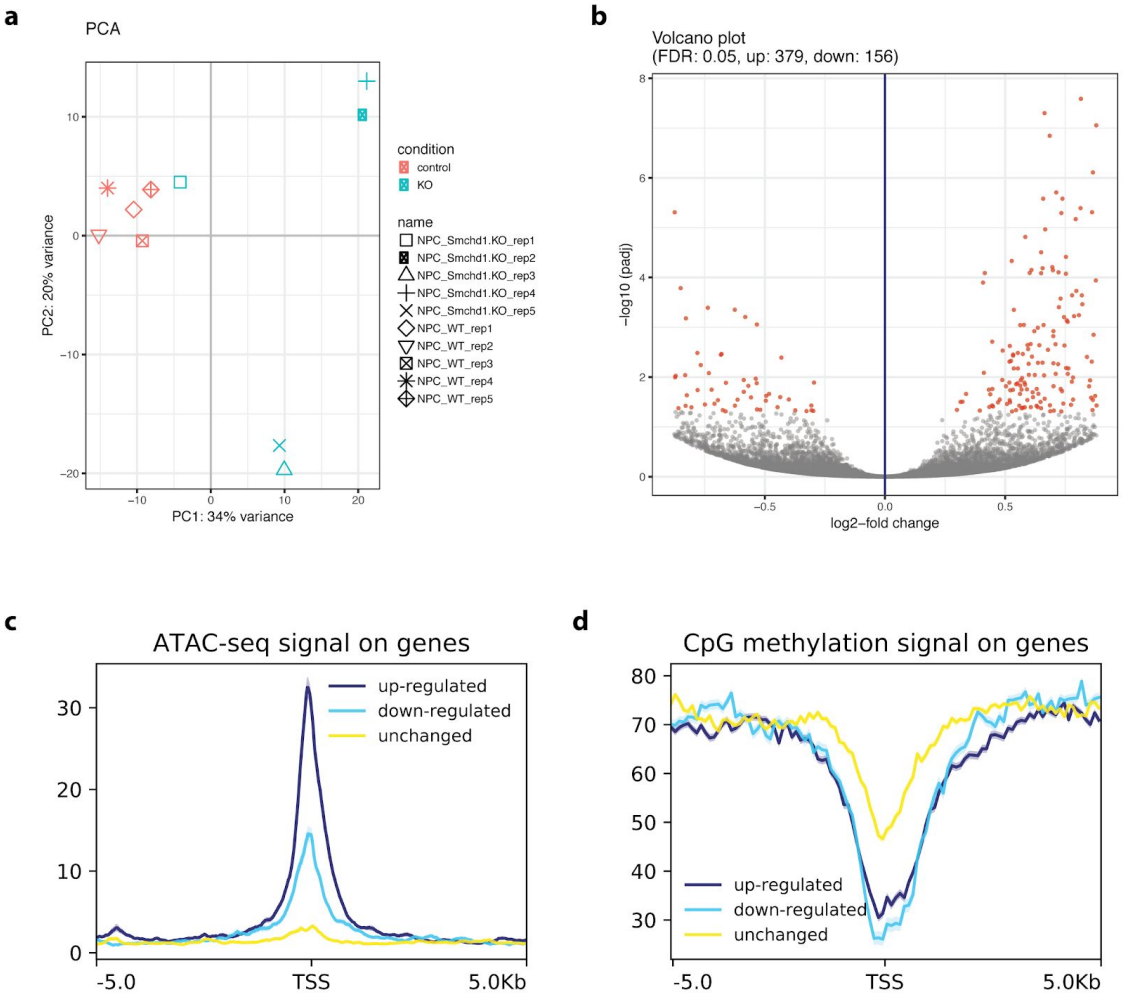

Figure S1. Analysis of de-repressed genes upon Schmd1 knock-out. A. *PCA output from snakepipes suggested that one knock-out sample (replicate1) behaves differently. This sample was later revealed to be the XO clone which lost it's inactive X chromosome. The sample was removed for DESeq2 analysis and the workflow was re-run.* ***B.*** *Volcano plot for DESeq2 output from snakePipes (knock-out replicate 1 excluded), shows an increase in up-regulated genes, indicating de-repression upon knock-out.* ***C.*** *Wild-type ATAC-seq signal on UP, DOWN and unchanged (NONE) genes, gene lists were extracted from DESeq2 output of RNA-seq workflow and depth-normalized bigwigs from ATAC-seq workflow was used for plotting.* ***D.*** *Wild-type methylation level reported by the WGBS workflow on UP, DOWN and unchanged (NONE) genes. (TSS = Transcription Start Site)*

B. Supplemental information

C. Academic Vita

References

Angel, E. (2000). *Interactive computer graphics : A top-down approach with opengl*. Boston, MA: Addison Wesley Longman.

Angel, E. (2001a). *Batch-file computer graphics : A bottom-up approach with quicktime*. Boston, MA: Wesley Addison Longman.

Angel, E. (2001b). *Test second book by angel*. Boston, MA: Wesley Addison Longman.